THE EFFECT OF STRAIN AND PATH CHANGE ON THE MECHANICAL PROPERTIES AND MICROSTRUCTURAL EVOLUTION OF ULTRAFINE GRAINED INTERSTITIAL FREE STEEL DURING EQUAL CHANNEL ANGULAR EXTRUSION (ECAE)

A Thesis

by

STEVEN GEORGE SUTTER

Submitted to the Office of Graduate Studies of
Texas A&M University
in partial fulfillment of the requirements for the degree of

MASTER OF SCIENCE

December 2005

Major Subject: Mechanical Engineering

THE EFFECT OF STRAIN AND PATH CHANGE ON THE MECHANICAL PROPERTIES AND MICROSTRUCTURAL EVOLUTION OF ULTRAFINE GRAINED INTERSTITIAL FREE STEEL DURING EQUAL CHANNEL ANGULAR EXTRUSION (ECAE)

A Thesis

by

STEVEN GEORGE SUTTER

Submitted to the Office of Graduate Studies of
Texas A&M University
in partial fulfillment of the requirements for the degree of

MASTER OF SCIENCE

Approved by:

Chair of Committee, Ibrahim Karaman
Committee Members, Richard Griffin
Karl Hartwig
Amy Epps-Martin
Head of Department, Dennis O'Neal

December 2005

Major Subject: Mechanical Engineering

ABSTRACT

The Effect of Strain and Path Change on the Mechanical Properties and Microstructural
Evolution of Ultrafine Grained Interstitial Free Steel during Equal Channel Angular
Extrusion (ECAE). (December 2005)
Steven George Sutter,
B.S., Texas A&M University
Chair of Advisory Committee: Dr. Ibrahim Karaman

The objectives of this study were to examine the effect of strain and path change on the microstructural evolution of ultrafine grained interstitial free (IF) steel during equal channel angular extrusion (ECAE); to determine the mechanical properties; to observe the resulting texture; and to perform optical and electron microscopy of the resulting material. The effects of different routes of extrusion (A, B, C, C' and E), heat treatment and plastic strains from 1.15 to 18.4 were examined. Monotonous tensile testing was used to determine mechanical behavior of processed materials. X-ray diffraction and TEM analyses were performed to evaluate the effect of processing on texture and grain morphology. Hardness measurements were performed to determine recrystallization behavior of the processed material. Optical microscopy was conducted on heat treated samples to determine their grain size and refinement.

Monotonous tensile testing of processed materials showed that there was significant strengthening after the first extrusion. Further processing resulted in increasing values of yield strength and ultimate tensile strength, with ductility at failure varying depending upon which processing route was used. The best tensile strength results were obtained after processing Routes 8C’ and 16E, due to the significant grain refinement these routes produced.

X-ray diffraction revealed increases in strength of preferred texture along the directions [111] and [001], perpendicular to the transverse plane, for all specimens that were processed using ECAE. TEM observations showed a consistent refinement of grain size as the amount of processing increased, especially within Routes C’ and E.

Hardness measurements of heat treated specimens showed that the onset of recrystallization occurred at approximately the same temperature of recrystallization as that of pure iron, 450°C. The recrystallization curves for all samples showed that grain growth begins at a temperature of around 700°C.

The low carbon content of IF steel made optical microscopy challenging. The grain size of annealed materials becomes finer and more uniform, ranging between 60 and 90 μm^2, at high strain levels under Routes C’ and E, due to the many potential nucleation sites developed in highly worked material.

TABLE OF CONTENTS

LIST OF FIGURES

Page

Page

Page

Page

Page

Page

Page

Page

Page

Page

LIST OF TABLES

Page

1. INTRODUCTION

Material properties are dependent upon material microstructure, crystal structure, and crystallographic texture. Crystallographic texture describes how grains are oriented with respect to a sample coordinate grame. The materials properties and mechanical performance are closely related to its microstructure. Manipulating the microstructure of a material through mechanical deformation, processing, and heat treatment, i.e. thermomechanical treatments, can be used to change material properties.

There are a number of different thermomechanical treatments for changing the microstructure of a material. One commonly used method, rolling, involves reducing one dimension of a materials cross-section by feeding it through a set of rollers. The resulting textures are sometimes called "sheet texture" characterized by a planar structure that runs parallel to the rolling direction. Drawing of a material, in which the material is pulled through a die, can produce wire. The textures associated with drawing are fibrous and are oriented in the direction of drawing. There are many other methods of working a material, including torsion and compression, but one method that is receiving much interest is severe plastic deformation, in particular a special form of extrusion known as equal channel angular extrusion.

The mode of deformation in equal channel angular extrusion (ECAE) is mainly simple shear. This is made possible by subjecting a sample of material, known as a billet, to a high load, forcing the billet through an angled channel. In the case of a

---

The journal model is Acta Materialia.

perfect 90° angled die, it is within this angled channel that the simple shear occurs, causing a change in the materials microstructure across the entire cross-sectional area of the billet. The material that emerges from the process has the same cross-section as the material that entered. This is one of the benefits of the ECAE processing technique. Another benefit offered by ECAE processing is the ability to control the resulting microstructures during subsequent extrusions, by changing the orientation of the billet, rotating it along the long axis.

Post-processing heat treatments permit further modification of the material's grain structure. Recrystallization within the processed billets relieves some of the internal stresses and restores ductility.

The present research focuses upon the effect of severe plastic deformation strain and path change on the microstructural evolution of a material that has been subjected to equal channel angular extrusion. Multiple extrusion routes and passes through the die were performed, all at a fixed room temperature. Microstructural analysis was conducted to help determine grain size, deformation structure and orientation. The objectives and parameters of this research are: 1) to examine mechanical performance of post-process material through the use of room temperature monotonic tensile tests; 2) determine its hardness using microhardness tests; 3) observe microstructural features through optical microscopy and TEM visualization; 4) examine the texture changes that occur during the processing, both before and after heat treatment, using XRD texture analysis; and 5) examine the recrystallization behavior of the material for different temperatures and a fixed time. The material in question is known as interstitial free (IF) steel, a variant of the steel commonly used in the automotive industry for body panels and other “non-exposed” or painted surfaces. To date there have been very few studies of this kind conducted on IF steel at room temperature.

2. LITERATURE REVIEW

2.1. Properties and Application of Interstitial Free Steel

Interstitial free steel was selected for this study due, in part, to its excellent deep drawing characteristics. Such properties lend this material to wide application in fields ranging from the automobile industry to architectural applications.

As stated previously the automotive industry uses IF steel for body panels and other painted components. Known as "bake hardening" steel, this metal is very easily formed into complex contours using pressing machines. During the forming process dislocations are created within the steel, and are subsequently pinned in place by the few remaining carbon atoms during the paint curing stage of part fabrication. The pinned dislocations make the metal stronger, and the processing stage where this takes place is what gives the metal its name. The use of IF steel in architecture is based upon similar logic: the metal is easily formed into complex shapes. This permits builders to create structures that are more organic in form than previously possible.

2.2. Equal Channel Angular Extrusion

The severe plastic deformation technique known as equal channel angular extrusion (ECAE) was pioneered in Soviet Russia in 1972 by V. M. Segal [1, 2]. This processing technique allows the creation of ultra-fine or nano-scale structures within a material by imparting a nearly uniform simple shear load in large billets. Billet dimensions do not change much between the beginning and end of the process (Figure 1). Repetitive extrusions make it possible to control the evolution of the resulting billet microstructure.

The process of ECAE is accomplished by pressing a lubricated billet through two intersecting channels of equivalent cross section. The angle of intersection of these angles may vary, but is typically either 90-degrees or 120-degrees. In the present work the ECAE intersection angle was 90-degrees. Pressing forces and temperature are sometimes varied for research purposes, but for this research the press force was 500,000 pounds, performed at room temperature. Billet lubricant for the ECAE machine used is typically a thin wrapping of Teflon sheet, with the moving parts lubricated by an anti-seize compound that can tolerate high temperatures.

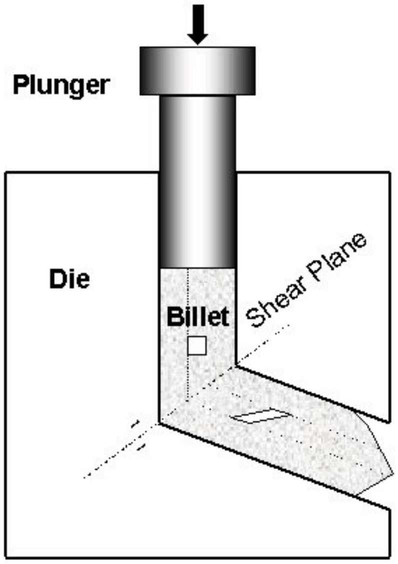

Figure 1: Schematic of the ECAE process [38]

Figure 2 shows the slip line field and velocity vectors associated with a billet during extrusion. Some assumptions, namely that the billet moves with a constant velocity inside both channels, and that the zone of plasticity is a single β-slip line, lead to some basic operating equations for ECAE. If there is no other force acting upon the transverse plane – that is, the plane that is parallel to the driving punch – then it is possible to calculate the average stress σ along the line OA, as well as the punch pressure *p*.

$$\sigma = -k\cot\theta$$
$$p = 2k\cot\theta$$

The variable *k* in the above equations represents the material shear stress, while *θ* is the angle between channels.

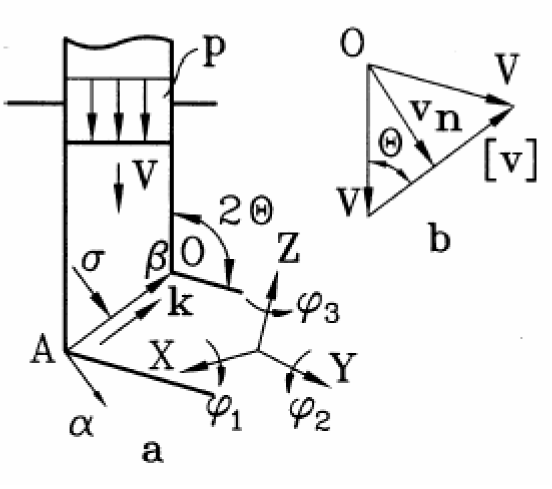

Figure 2: (a) ECAE slip line diagram; (b) velocity vector diagram [2]

In the event of contact friction between the billet and the die channel walls, the situation becomes a bit more complex. Given a contact friction τ, the slip line field becomes more of a fan, and includes a central fan AOB, a zone of rigid metal AO_1B, and a zone of uniform stress BOC. These zones are illustrated in Figure 3a and Figure 3b.

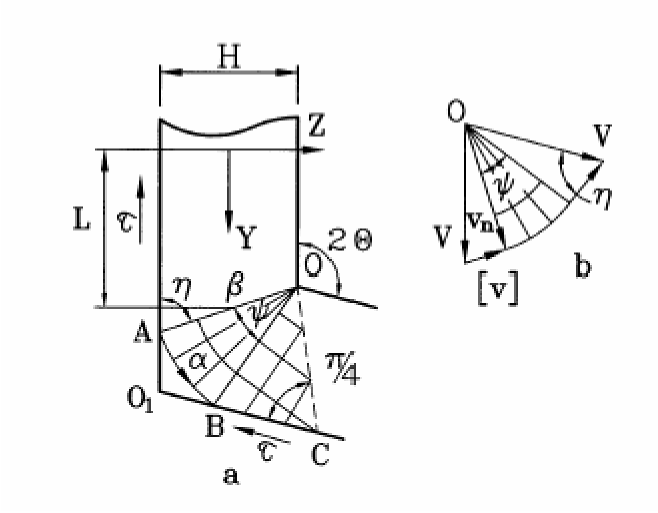

Figure 3: (a) Slip line fan with friction forces, (b) velocity diagram [2]

The angle ψ, the fan angle, is calculated using:

$$\psi = 2(\eta - \theta)$$

where $\eta=\pi/2-1/2$ Arccos (τ/k) is an angle between slip lines AO and BO. These equations are true when $\tau>k \cos 2\theta$. With a ratio of length to thickness (L/H), the punch pressure may be calculated as:

$$p = 2k[\cot\eta + 2(\eta - \theta)] + \tau[\sin\eta(\sin\eta + \cos\eta)]^{-1} + \frac{2\tau L}{H}$$

Material strain is focused primarily in the fan shape of AOB in Figure 3, and also across the lines AO and BO. The shear within these regions is a simple shear in the direction of the β-slip lines, and may be calculated using:

$$\gamma_\beta = \frac{[v]}{v_n} = \cot\eta$$

After passing through the area AOB the accumulated shear is:

$$\gamma_\alpha = \psi \text{ (rad)}$$

with α-slip lines making up the flow lines and indicating the direction of simple shear within the region AOB.

Segal's work [2] describes the history of a square element within a fictitious billet of material that is undergoing ECAE. The element, confined between flow lines 1-1 and 2-2 (see Figure 4) undergoes repeated stages of simple shear along the line AO, simple shear along the α-slip lines within the AOB region, and simple shear along the slip line BO. The dashed lines and vectors show that the deformation process is not one of a single step of simple shear, but rather a more complex series of different macroslip planes. Full distortion of the element is given by:

$$\tan\varphi = 2\cot\eta + \frac{\psi}{\sin^2\eta}$$

This equation, however, does not correspond to simple shear in the flow direction. There are two limiting cases worth noting. First, when $\eta<\theta$, $\psi=0$, as shown in Figure 2, and the element distortion and shear strain are given by:

$$\gamma = 2\gamma_\beta = \tan\varphi = 2\cot\theta$$

while shear planes are involved with the β-slip line AO.

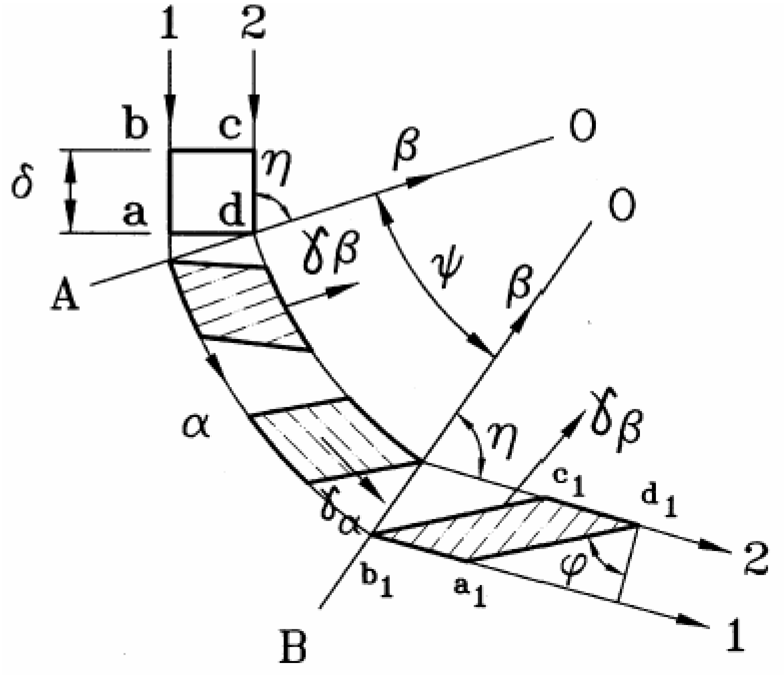

Figure 4: Deformation history of a square element [2]

In the second case, $\eta = \pi/2$ and distortion is given by:

$$\gamma = \gamma_\alpha = \tan\varphi = \psi$$

These two cases may correspond to situations of both low and high contact friction.

Segal's work uses the axes *x, y, z* to represent the directions perpendicular to the flow, transverse and longitudinal planes, respectively. The angles associated with these axes, φ_1, φ_2, and φ_3, are the three possible angles of rotation about the flow, transverse and longitudinal axes.

For cases in which $\varphi_1 = \varphi_2 = \varphi_3 = 0$ or when those three angles are divisible by 180°, the flow is plastic and planar. Structural elements will receive distortion into the plane in these cases. The accumulation of shear may increase continuously, as in the case of Route A (no rotations between extrusions), or alternate between their destruction and creation, as in Route C (+180° rotation on even passes, -180° on odd passes). An equation that yields the orientation of any shear plane of Route A at the n^{th} pass out of N total passes is given by:

$$\tan \varphi_n = 2(N + 1 - n)\cot \theta$$

and is visually represented in Figure 5.

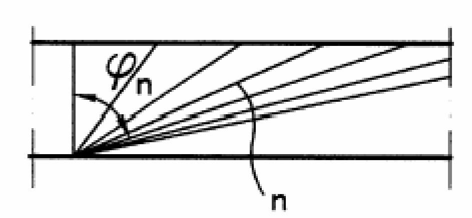

Figure 5: Shear planes of Route A [2]

In the case of Route C, the angle φ_2 alternates between ± 180°, causing the shear planes to alternate across the same shear plane. Structural elements are alternatively destroyed and restored between odd and even passes, respectively. Visually, the shear planes of Route C are presented in Figure 6.

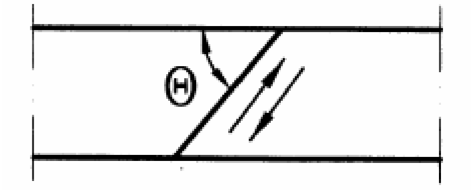

Figure 6: Shear planes of Route C [2]

It is possible to rotate the angle φ_2 by 90° or even 270°, and these rotations are the basis of Routes B and C'. Routes B and C' are made up of superpositioning shear vectors, as seen in Figure 7. In the case of two rotations of φ_2=90°, the first pass performs a simple shear γ_1 in the plane *yoz*, with line 1 indicating the unit element's displacement.

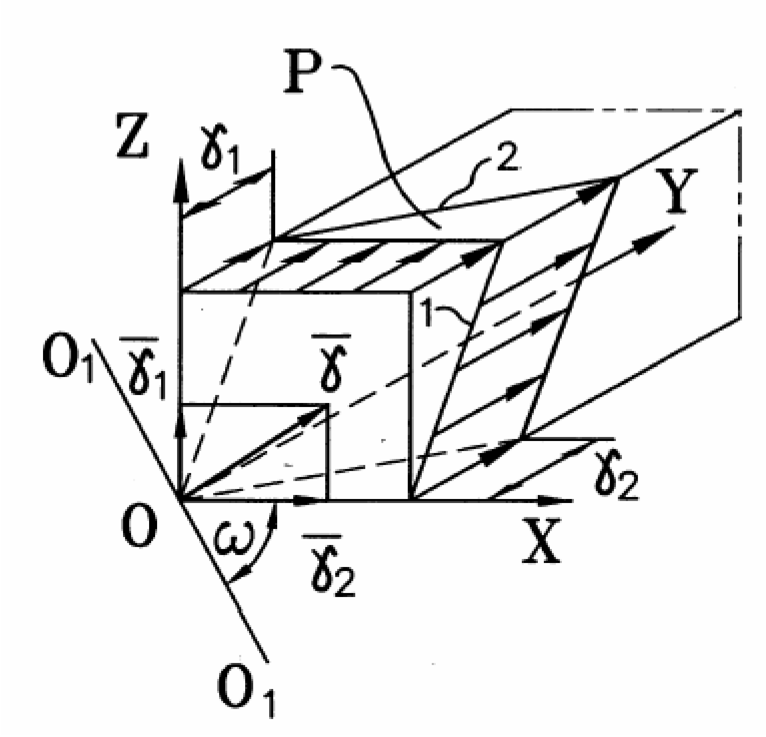

Figure 7: The superposition of shear vectors [2]

The second operation induces a second shear, γ_2, on the plane *xoy*, with line 2 indicating the displacement. Adding these vectors gives the equivalent shear:

$$\gamma = \sqrt{\left(\gamma_1^2 + \gamma_2^2\right)}$$

which lies within plane P, and has a trace O_1 O_1 at the transverse section *zox*.

$$\tan\omega = \frac{\gamma_1}{\gamma_2}$$

When a billet is alternated between φ_2= ±90°, it is following Route B. The billet's original position is returned after even numbers of passes. The distortion within a billet following Route B is shown in Figure 8 for up to 4 passes in a tool with a die angle of 2θ=90°.

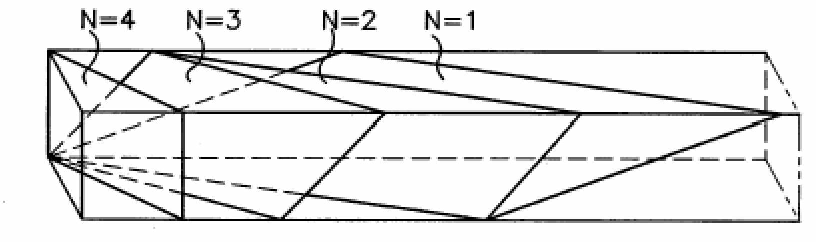

Figure 8: Shear plane orientations within a billet following Route B [2]

For Route C', the billet is rotated by φ_2=+90° after each pass. This has the end effect of returning the billet to its original position after four passes. It should be noted that because subsequent passes are performed upon the previous shear planes, all passes of Route C' occur on four spatially separate planes. Figure 9 shows the orientation of the shear planes for a billet following Route C' after four passes through a die angle of 2θ=90°.

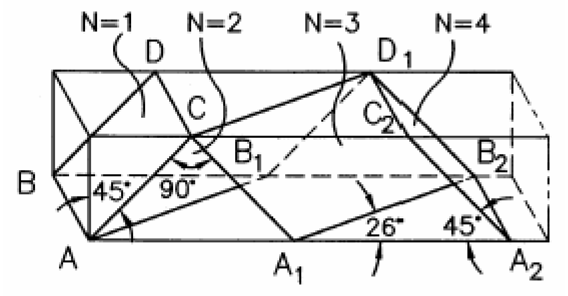

Figure 9: Shear plane orientation within a billet following Route C' [2]

During multi-pass ECAE, the ends of the billets are subject to "end effects," which are zones of rigid metal that have not been subjected to the same amount of working as the rest of the billet. Figure 10 (a) and (b) shows process simulations, and Figure 10 (c) and (d) actual billets of aluminum alloy 3003 that have been processed up to Route 4A through a die with an angle of 2θ=90°, the billets having been macroetched to better show the end effects, which vary between route.

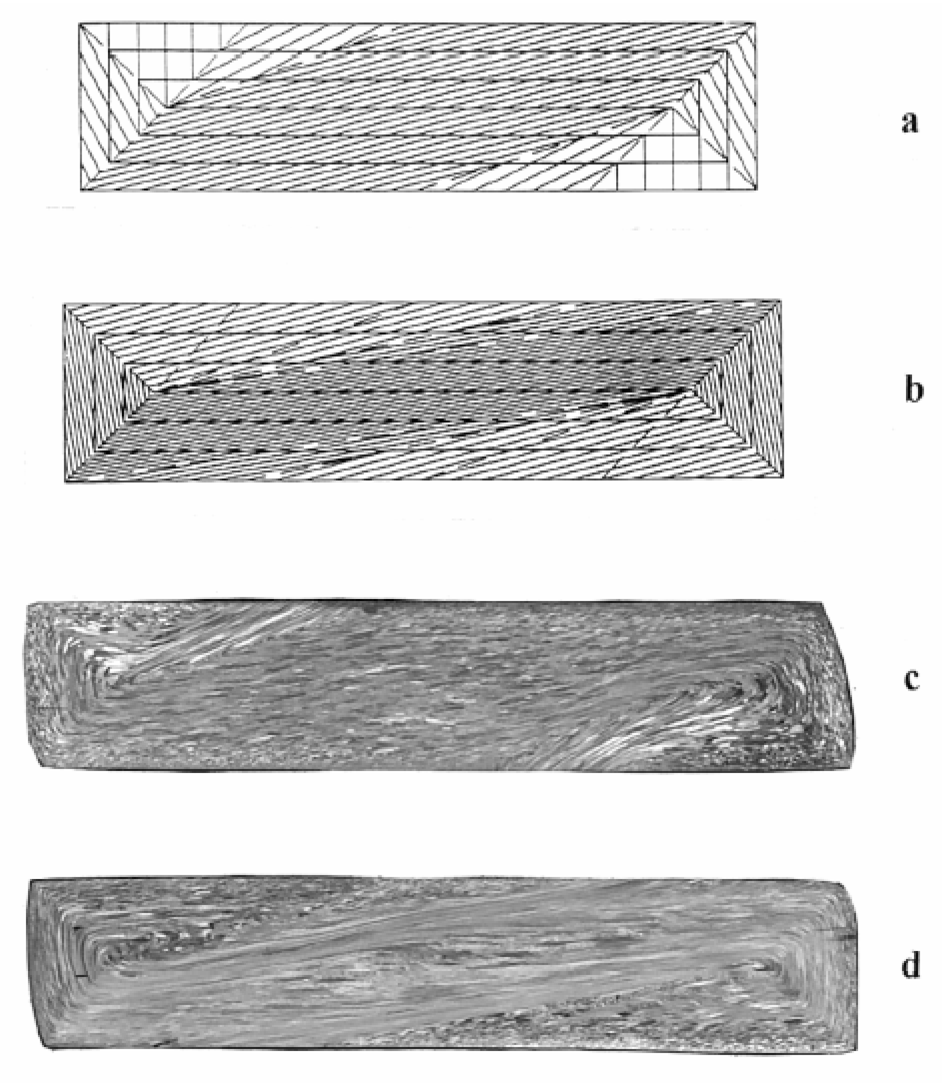

Figure 10: (a) Process simulation of two passes; (b) process simulation of four passes; (c) macroetched Al billet after two passes; (d) macroetched Al billet after four passes [2]

In the case of Route A, the end effect development is fairly easy to visualize and understand. Route C has localized end effects, and there is a periodic repetition of the coordinate grid distortion between odd and even-numbered passes. Route B's end effects are somewhat similar to Route A's, except that the areas of non-uniformity are turned on an angle of ω=45° about the y-axis, and are symmetrically arranged on the other end of the billet. Route C' has a more complex distribution of end effects, as after four passes the rigid zones at the billet ends are only partially restored, and are partially distributed across the billet volume.

End effects can impact the amount of fully processed material that a billet can yield, and must be taken into consideration during processing.

When comparing a process such as ECAE to other, more conventional operations, some important differences emerge. Since ECAE is not coupled with a change in geometry there must be some discussion of equivalence. Segal's work uses equivalence of spent energy through effective stress (σ_i) and strain (ε_i). In the case of ECAE simple shear with no friction, effective stress, strain and punch pressure can be calculated using:

$$\begin{aligned} \sigma_i &= \sqrt{3}k \\ \varepsilon_i &= 2N\cot\theta/\sqrt{3} \\ p &= 2k\cot\theta \end{aligned}$$

For standard extrusion, the equations for "ideal" forming without friction are:

$$\begin{aligned} \sigma_i &= \sqrt{3}k \\ \varepsilon_i &= \ln\lambda \\ p &= \sqrt{3}k\ln\lambda \end{aligned}$$

with $\lambda=F_o/f$ representing the cross-sectional area reduction from F_o to f. The equivalent extrusion reduction, based upon the effective strain calculations above, is:

$$\lambda_E = \exp\left(2N\cot\theta/\sqrt{3}\right)$$

The equivalent extrusion reduction provides the same spent energy as N passes of ECAE. The ideal conventional extrusion of like final products would require N times higher pressure, and $N\lambda_E$ times larger load than the equivalent ECAE process. In the event of extremely high values of *N*, ECAE may be used to achieve very large effective strains under low pressures and loads.

The evolution of texture under ECAE processing was also studied [36]. The researchers observed the evolution of texture in a high purity Al0.5Cu alloy based upon the processing route, the number of passes and the initial texture of the specimen. It was discovered that processing route and number of passes have a very important impact on texture evolution.

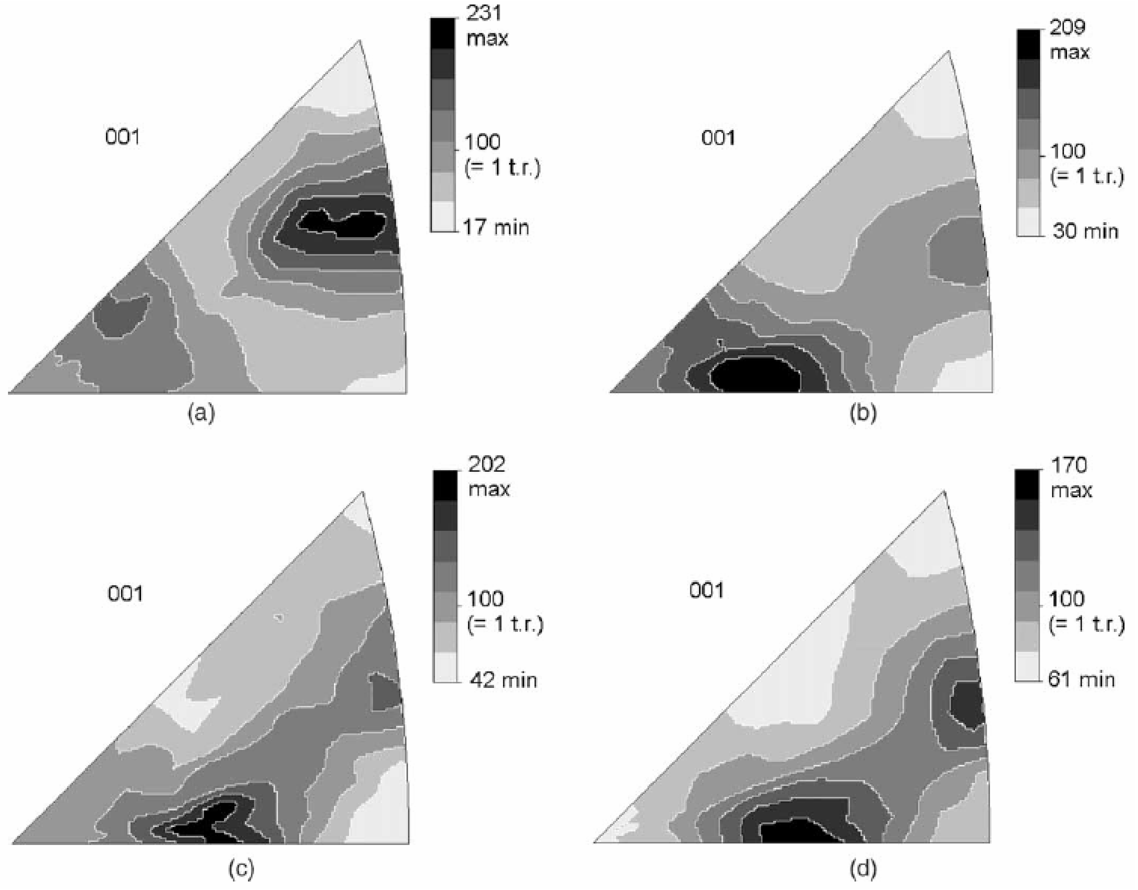

Figure 11: Inverse pole figures for Route C' after two passes for strong (a) and weak (b) initial texture, after four passes for strong (c) and weak (d) initial texture [36]

Figure 11 shows how the beginning texture impacts the texture results at low numbers of ECAE pass. In the case of Figure 11 (c) and (d), the influence of initial texture begins to decrease. The researchers discovered that, as a general rule, the texture strength shows a decrease as the number of ECAE passes increases. Routes A, B and C' showed a continuous decrease in texture strength, with Routes A and C' being most effective for randomizing the texture after four passes. Given a strong starting texture Route B yields a moderately strong texture after six and even eight passes. Route C exhibits a cyclic evolution in texture strength, with odd-numbered passes showing very weak textures and even numbered passes showing strong textures, as in Figure 12.

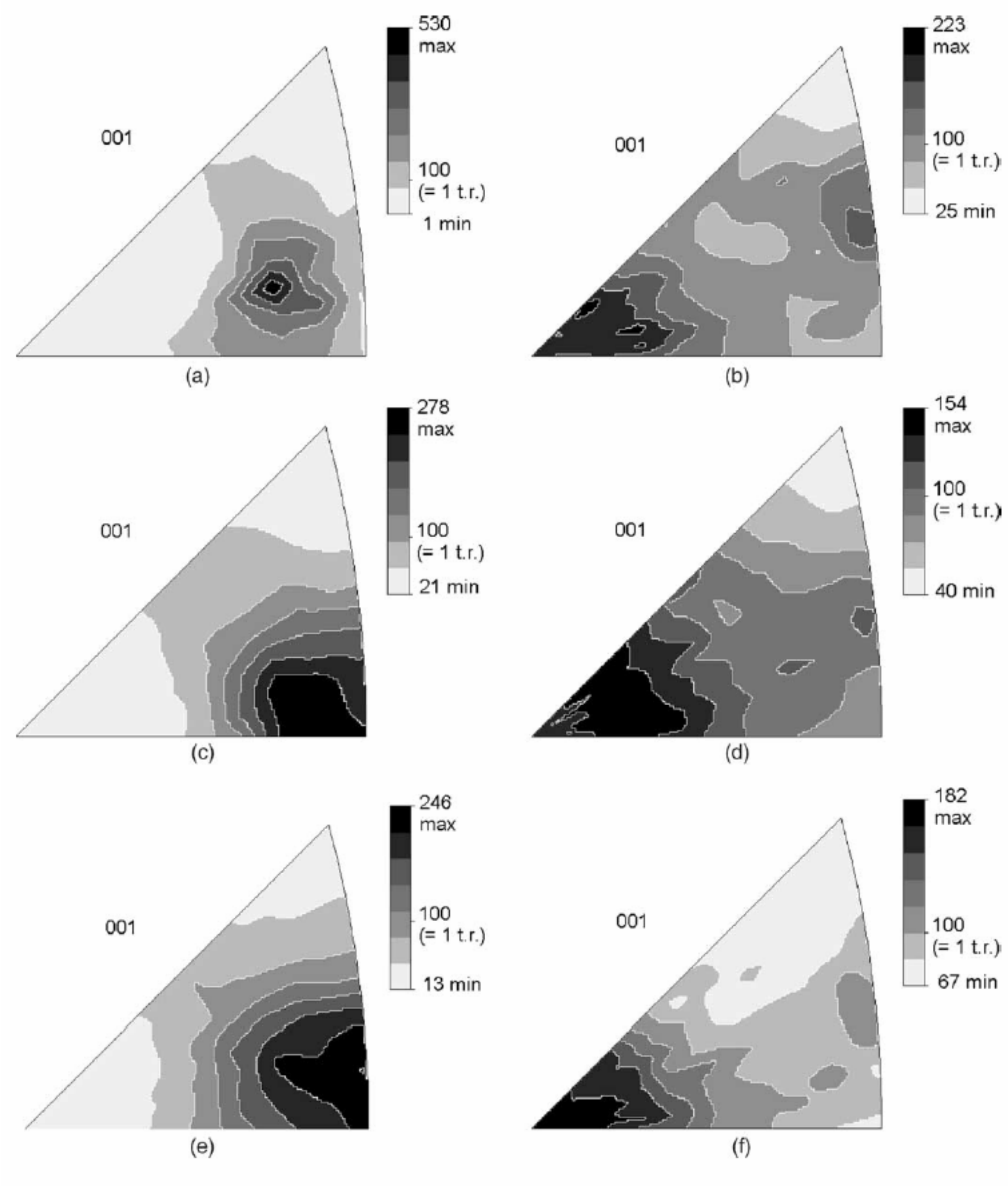

Figure 12: Inverse pole figures of Route C after two (a), three (b), four (c), five (d), six (e) and seven (f) passes [36]

2.3. The Mechanical Behavior of Metals Subjected to ECAE

When processing metallic materials through a technique such as equal channel angular extrusion, certain changes in mechanical behavior are commonly observed. As ECAE strain levels increase, so too follows the yield stress of the metal [4], while the ductility typically decreases, sometimes significantly [3]. Figure 13 shows the mechanical behavior of 0.15%C steel after having been processed using ECAE.

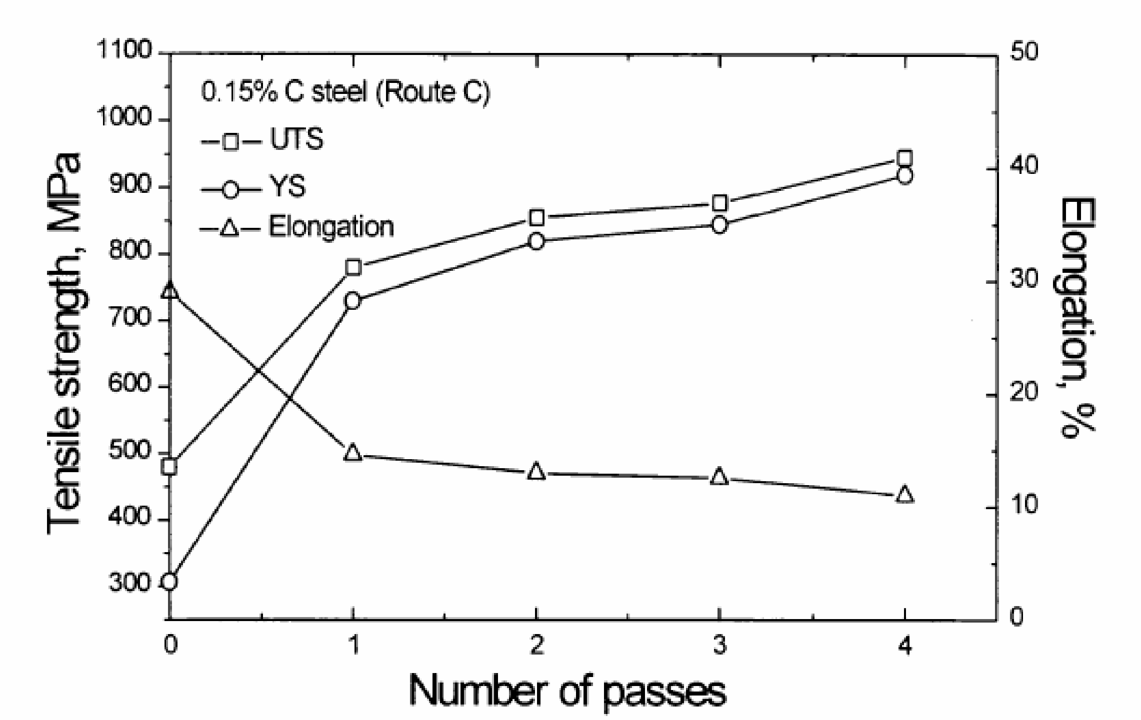

Figure 13: Tensile properties vs. pass number for ECAE processed 0.15%C steel [19]

The increase in tensile strength is most noticeable at the initial stage of ECAE processing. After the first pass through the die, the increase in both yield strength and ultimate tensile strength decreases. Grain refinement is also most pronounced after the initial stage of ECAE [18], with less significant refinement as the processing is continued, but an increase in high-angle boundaries. Figure 14 shows a series of TEM images of low-carbon steel subjected to increasing passes of ECAE.

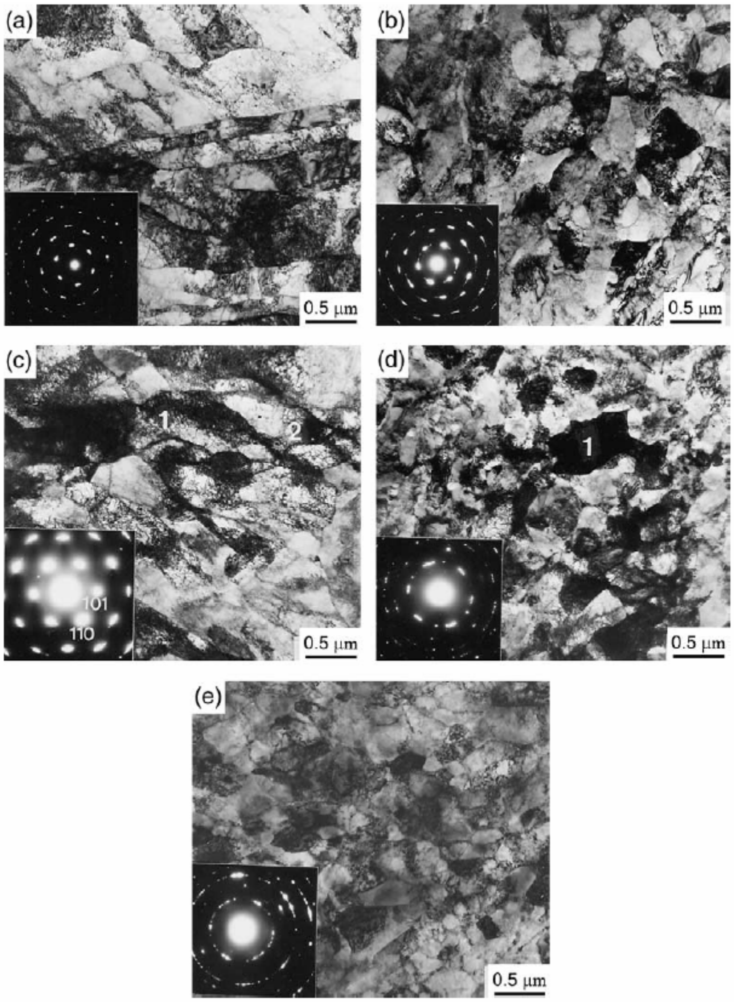

Figure 14: Low-carbon steel processed via ECAE Route C: (a) one passes; (b) two passes; (c) two passes, in a different region; (d) four passes; (e) eight passes. Numerals within the figures reference features relevant to the researcher's study [18]

To recover some of an as-processed material's ductility, an annealing heat treatment may be used. During annealing, the sample is placed in a furnace at elevated temperatures for an extended period of time, ranging from as little as one hour to as long as 72 hours. At the elevated temperatures of the annealing process, stored internal strain energy from severe plastic deformation is relieved as a result of increased atomic diffusion. Recrystallization, in which new, low strain, equiaxial grains grow, occurs at a certain point during the annealing heat treatment. As recrystallization progresses and crystal grains grow, the mechanical properties associated with the severe plastic deformation revert to a state that is closer to the pre-deformation material; the yield strength and ultimate tensile strength decrease, along with the material's hardness, while ductility is recovered. Research into the use of annealing after ECAE [4, 7] indicates that samples that are processed using ECAE and then annealed for various lengths of time show superior performance when compared to unprocessed samples. Figure 15 shows this in the case of 0.15 wt.% C steel that has been processed using four passes of Route C.

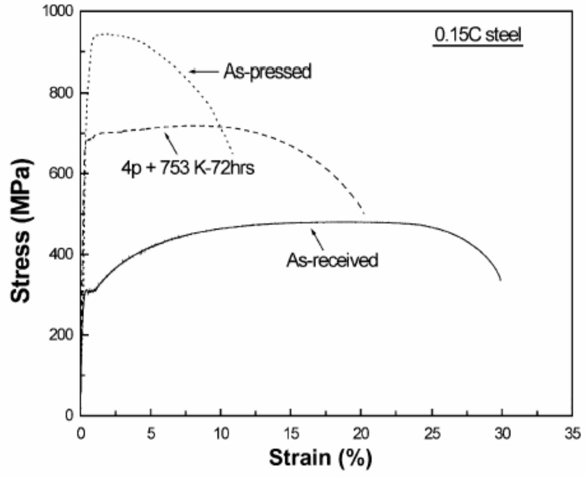

Figure 15: Stress-strain curves of 0.15C steel, as-received, post ECAE ("As-pressed"), post ECAE (4 passes) and annealed at 753K for 72 hours [7]

3. EXPERIMENTAL PROCEDURES

3.1. Material

This research was conducted using titanium-stabilized interstitial free steel that was obtained from US Steel Research, Monroeville, Pennsylvania. The chemical composition of this material is shown in Table 1. The raw material used in this research came from US Steel Research in the form of a 21” x 8” x 1” plate. The plate was hot rolled and allowed to slow cool, permitting the IF steel to fully recrystallize.

Table 1: Chemical composition of the IF steel used in the present research

Element	Atomic Weight	Weight Percent	Atomic Percent
Fe	55.85	Balance	Balance
C	12.01	0.0023	0.0107
S	32.07	0.0077	0.0134
N	14.01	0.0018	0.0072
O	16	0.002	0.007
Ti	47.9	0.065	0.0758
Nb	92.91	0	0
Al	26.98	0.05	0.1035

3.2. ECAE Procedures

The billets of IF steel were first rough cut from the bulk plate, and then machined on a mill to the dimensions of 1”x1”x6” in preparation for extrusion. The longitudinal axis of each billet corresponded to the rolling direction. The original plate was hot rolled and allowed to slowly cool and recrystallize, and so was not cold worked. The texture of the as-received material indicated a strong texture in the [111] and [001] directions of the transverse plane of the billets. All billets were extruded at room temperature at a rate of 0.1 inch per second, using a variety of routes and passes. Table 2 shows the routes and number of passes used in this study. Graphical representations of the billet rotations for each route are provided in the Appendix.

Table 2: Processing routes

Sample Group Number	Extrusion Route
0 / As-Received	No Extrusions Performed
1	Route 1A
2	Route 2A
3	Route 2B
4	Route 2C
5	Route 4A
6	Route 4B
7	Route 4C’
8	Route 4C
9	Route 4E
10	Route 8C’
11	Route 8C
12	Route 8E
13	Route 16E

Prior to extrusion, anti-seize lubrication was applied to both the billet and the moving surfaces of the extrusion machine in an effort to reduce the friction during the extrusion process. IF steel is easily extruded at room temperature with a punch speed of 0.1 inches per second.

The formation of flash was a common side-effect of the extrusion process because of the wearing of the tool over time. Flash occurred along most corners of the billet, and at the point of contact between the punch and the billet. The flash was easily removed using a high speed rotary grinder. The extrusion process caused some dimensional changes from the norm as a result of friction and tool wear, and these were addressed using a combination of rolling (performed on the flow faces) and milling (performed on the longitudinal faces) to make the billet ready for further processing. Recrystallization does not occur until approximately 500°C in IF steels, so the process of machining a billet was not expected to cause a significant recovery or recrystallization.

3.3. Tension Testing

Tension testing was performed to examine the mechanical behavior of ECAE processed IF steel. Tension tests were conducted on specimens that were both as-processed and post-process annealed, to examine the impact of recrystallization on mechanical response. The tension tests in this study were conducted until failure occurred. To obtain the tension test specimens, cubes of approximately 1” x 1” x 1” were first cut from processed billets on a diamond saw, and the tension sample profiles were cut using wire EDM. The tension sample profile is shown in Figure 16. Once the bulk tension profile was cut, the individual specimens were sliced from the bulk profile, again using wire EDM. Every tension specimen was cut such that the profile face corresponded to the flow plane of the billet and load direction was parallel to the extrusion direction. The thickness of each tension specimen was two millimeters, with the exception of the tension specimens from Routes 4A and 4B, which were cut to 1.5 mm thickness.

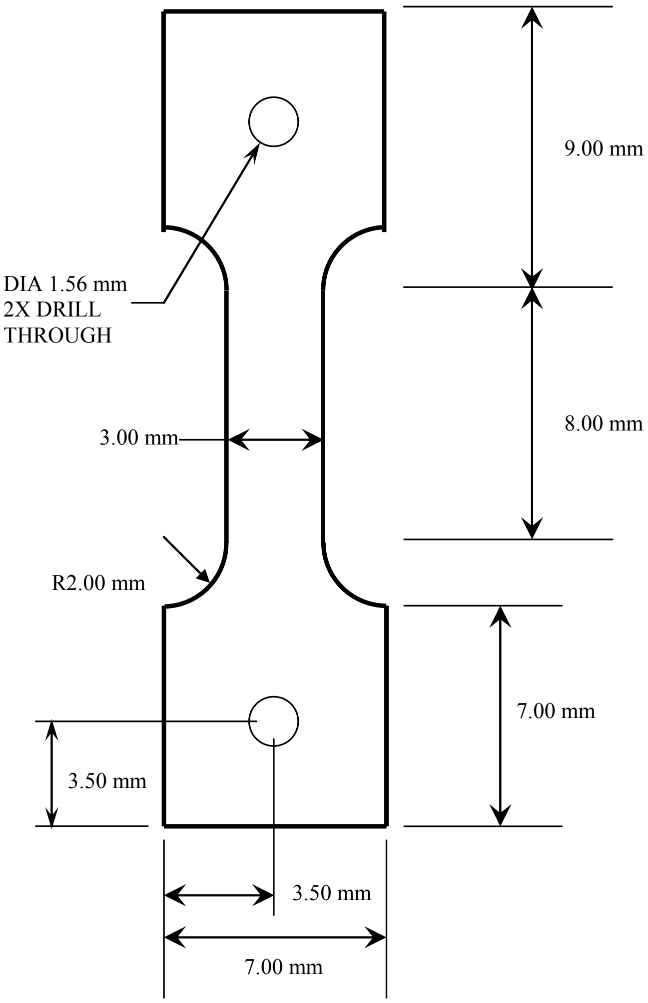

Figure 16: Schematic of the tension sample profile

The samples were all coated with a thin film of residue that is normal for EDM processing. This thin film was removed by hand-sanding each specimen first with a

600-grit pad, and then finished off with an 800-grit pad. The objective was to remove any surface imperfections that could interfere with the extensometer during tension testing and cause stress concentration areas.

Tension testing was performed on an MTS brand machine with a computer recording the output data. Simple experiments were conducted to check the modulus of the samples before each tension test to verify measurement accuracy. The strain rate was 0.004 sec^{-1} for all experiments. The data collected from the test series was then evaluated using programs such as Microsoft Excel and Igor Pro. Of particular interest were the shape of the complete stress-strain response, the yield and ultimate tensile strengths, and the ductility at failure of each specimen. To check for repeatability, two or three companion specimens from each case were tested.

The annealed tension specimens were tested and evaluated in the same manner as the as-processed specimens. A light hand-sanding of each specimen was performed prior to the tension tests so as to remove any residue that may have collected during the annealing heat treatment. Of particular interest was how the annealing process influenced the ductility of the material, or the level of strain on a material just prior to failure.

3.4. TEM

The transmission electron microscopy done in this research was conducted at the University of Paderborn, Germany. IF steel was processed into foils for use in the TEM system. First, a slice of about 1 mm to 1.5 mm thickness was cut from the original sample. This slice was then polished using SiC paper to a grit of 4000, and then finished with twin-jet electropolishing.

Transmission electron microscopes resolve images by emitting a beam of electrons through a specially prepared specimen. Internal microstructural details are resolved, and contrasts in the image are produced by beam scattering and diffraction off of the microstructure or defect. Solid materials are very absorptive to electron beams, so the specimen being imaged must be a very thin foil. Once the beam penetrates through the specimen, it is projected onto a fluorescent screen or photographic film for viewing [39].

3.5. Heat Treatment and Construction of Recrystallization Curves

A diamond saw was used to cut out sections of ECAE-processed billets for use in constructing recrystallization curves. The cuts were done such that the largest surface was that of the flow plane. In order to construct these curves each sample was annealed for 90 minutes at temperatures ranging from 100°C to 700°C, then mounted into epoxy, ground to a surface finish of 800-grit, and finally tested for hardness. Heat treatments were performed in air inside a Lindberg/Blue brand box furnace, followed by quenching in water at the end of annealing. The schedule for the heat treatments conducted in this study is shown in Table 3.

Table 3: Annealing schedule for the ECAE processed IF steel samples

Annealing Temperature (°C)	Annealing Time (minutes)
100	90
200	
300	
350	
400	
450	
500	
550	
600	
700	

For each temperature, ten microhardness measurements were taken on each sample. All results will be presented in the experimental results section.

3.6. Texture

All texture measurements were performed at the University of Paderborn, Germany. The planes under examination are identified as 1, 2, 3, and correspond to the flow plane, longitudinal plane, and transverse plane, respectively.

Obtaining a pole figure requires the use of X-ray diffraction systems. X-ray diffraction systems make use of alignment characteristics of the crystal lattice in regards to the reflection of incident rays of radiation with varying wavelength off of crystallographic surfaces. Using the Bragg law, which governs how waves of radiation are diffracted from the parallel atomic planes of crystals, it is possible to generate a map of the arrangement of crystals within a specimen. In equation form, the Bragg law appears as

$$n\lambda = 2d \sin\theta$$

where n is an integer, λ is the wavelength (in nanometers), d is the interplanar distance within the crystal, and θ is the angle of incidence or reflection of the radiation.

X-ray diffractometers use devices such as Geiger countertubes or ionization chambers instead of photographic plates to detect the reflected radiation from a sample [32]. These machines, at the basic level, consist of a source of parallel X-rays, a rotating sample holder that is held at an angle of incidence θ to the X-ray source, and a Geiger countertube that is held at an angle 2θ from the incident X-rays. Both the sample holder and the Geiger countertube rotate, with the Geiger counter tube always rotating at twice the speed of the specimen holder. This doubling of speed is necessary if the Geiger countertube is to remain in position for receiving the reflected radiation from the specimen.

A schematic of a standard X-ray diffractometer is shown in Figure 17.

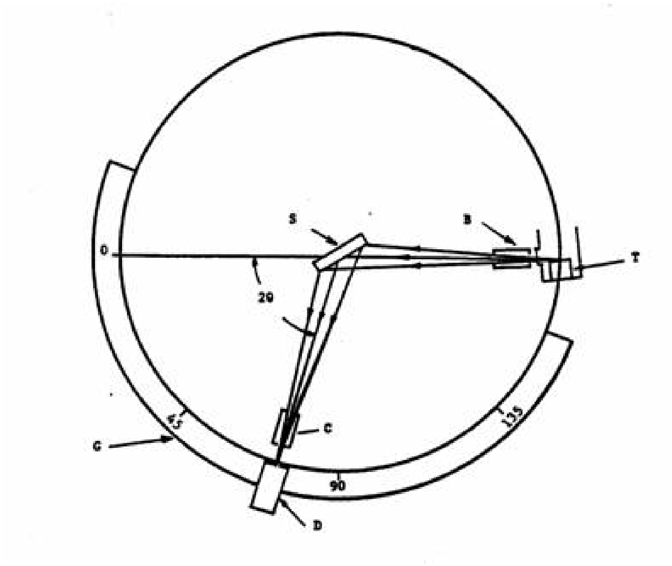

Figure 17: Schematic of an X-ray diffractometer [40]

In Figure 17, *T* represents the target emitting X-rays, *B* and *C* are slits and collimator assemblies, *S* is the specimen holder, *D* is the X-ray detector, and *G* is a goniometer scale graduated in degrees.

3.7. Hardness Measurements

One method of determining the recrystallization temperature is to measure the change in hardness of a specimen. There is a significant drop in hardness due to softening of the material during recovery and recrystallization. Hardness, or the resistance of a material to penetration or indentation, is determined by applying a constant force on the material's surface via an indenter. For the hardness measurements in this study, Vickers microhardness was measured. Vickers hardness makes use of a square shaped diamond indenter, which leaves a pyramidal indentation in the surface of the sample. The diagonal dimensions of this pyramid indentation are measured, and from that the hardness value is calculated. Vickers hardness, or HV, is the ratio of applied load to the surface area of the indentation left on the sample's surface.

The hardness testing machine used in this research was a Buehler Micromet II Digital Micro Hardness Tester. A load of 1000 grams (g) was applied for a duration of 15 seconds. Such test conditions permitted a well-defined indentation to form, allowing more accurate readings. It is important to have a smooth, flat surface on the specimen, in order to better identify the contours of the indentation. Every sample used in this research was given an initial rough grinding on 240-grit paper, and then transferred in groups of six samples to the automatic grinding machine for further grinding with 400-grit, ending with 800-grit paper. The samples were then rinsed with water, followed by alcohol, and then dried under a heated blower. All hardness measurements were performed on the flow plane for each route studied. When performing the hardness measurements, the recommended spacing between adjacent indentations was at least three times the average indentation diameter. The rationale behind this spacing is that for each load applied to the surface, there may be a zone around the indentation where material stresses have increased; therefore, each indentation must be made outside of this zone of stress. In measuring the recrystallization curves, ten measurements were recorded for each specimen. The highest and lowest microhardness values were ignored in order to obtain a better calculation of the average hardness.

3.8. Metallography

To examine the microstructure of the specimens using optical metallography, the specimens were subjected to the following processes: sectioning, mounting, polishing and etching. These processes are described in the following paragraphs.

Cutting specimens out of the as-processed billets is an important step, and should therefore be done with care and attention to detail. If done properly, a good sectioning will not interfere with hardness measurements. Carelessness can lead to improper mechanical loading, which could damage the diamond blade, introduce mechanical hardening, or cause localized annealing due to heat buildup. Standard cutting techniques tend to introduce an inclination of the specimen, leading to misorientation of the desired surface. To maintain as precise an orientation as possible, the sections were cut using a Buehler Isomet 1000 diamond saw, which was cooled with an oil-water lubricant to keep cutting temperatures low.

All specimens were mounted in Buehler Epoxicure epoxy. Epoxy mounting was used first because of its low curing temperature, and second because it cures clear, making it possible to insert identifying labels into each specimen for quick reference.

The grinding of the specimens was performed via the traditional method of abrasive removal of material from the surface. Typically this is accomplished through the use of a grinding wheel with an attached grinding pad. This wheel rotates at a set rate, and the sample is pressed against the grinding pad, initiating the surface grinding. To improve the surface finish of the specimen, successive grinding stages make use of smaller abrasive particle sizes. Once a small enough particulate size is reached, the process becomes known as polishing, and makes use of liquid abrasive solutions and polishing pads. The stages of grinding and polishing are performed in order to prepare the specimen's surface for microstructural evaluation and hardness testing. It is important to obtain as smooth a surface as possible, since scratches may negatively impact the results of optical microscopy. The use of automated grinding and polishing machines has made this stage of sample preparation more efficient, since multiple samples can be ground and polished at the same time.

All of the specimens used in this phase of the research were given an initial rough grinding treatment by hand. This was performed on a Buehler Ecomet 3 machine, using rough 240-grit grinding disks. First a chamfer with an angle of approximately 45° was ground into the epoxy in order to reduce grinding friction during the later stages of surface preparation. Next the sample was subjected to a rough grinding to remove any thin film of epoxy that might exist on the surface of the sample. Once the rough grinding was completed, the samples were gathered into groups of six for further surface preparation using a Buehler automatic grinding machine. The automatic grinding machine allowed adjustments in grinding time, downward force during grinding, and direction of circular rotation during the grinding cycle. For the purposes of this research, the grinding time was kept as 10 minutes, the downward force was 24 pounds, and the platter rotated in a counter-clockwise direction. Initial grinding on the automatic grinding machine was performed with disks of 400-grit surfaces, then finished with 800-grit disks. Upon completion of the final grinding step, the platter was removed from the power head and rinsed under running water, sprayed with alcohol to prevent watermark formation, and dried under a heater. The resulting surface finish was acceptable for microhardness testing of the various samples.

To obtain a good optical image, the surface finish must be of high enough quality to reflect back large amounts of light. Good results in microscopy also require a flat, scratch free surface finish on the sample in question. Using the correct polishing surface and abrasive compound, it is possible to obtain a mirror-like surface finish on a specimen. Unlike grinding, where the abrasive is bonded onto the surface of the grinding disk, the abrasive particles used in polishing are so small they must be held in a suspension, typically in the form of liquid slurry or as a paste that is then applied to a soft polishing wheel.

For IF steel, a regimen of progressively finer grit polishing compounds is applied to clean polishing cloths. The polishing begins with an initial surface grind at 240-300 rpm, under moderate pressure, using 320-grit SiC paper for one minute. The next phase, lasting five minutes and rotated opposite the direction of the polishing wheel, is performed at 120-150 rpm, with moderate pressure, using 9-μm diamond paste applied to an Ultra-Pol cloth, and Metadi Fluid as a lubricant. After cleaning the specimens, a four minute polish at 120-150 rpm, using 3-μm diamond paste and Metadi Fluid lubricant on a Trident cloth is performed. A similar polish using 1-μm diamond paste is recommended for materials such as IF steel. The final polishing stage is performed for 2-3 minutes using 0.05-μm Masterprep Alumina slurry on a wet MicroCloth polishing cloth.

It is important to maintain a high level of cleanliness during the polishing stage. Routine distilled water rinses are used during the polishing stage, sometimes followed up with ultrasonic cleaning if there are any pockets of foreign material trapped between the specimen and the epoxy. A thorough rinse with alcohol prevents any staining during the drying stage.

Before any etching was performed, the specimens were examined under an optical microscope. This preliminary examination was done to identify any defects, such as pores, pits, inclusions or scratches, which could result in a possible adverse reaction during etching.

Even after polishing is complete, the final surface of the IF steel samples will not have any visible microstructure under optical microscopy. This is because the incoming light is uniformly reflected. To expose grain boundaries and produce contrast between grains a chemical etch is employed. Since IF steel has such a low carbon content, conventional etchants such as Nital can not be used. Instead a mixture of Marshall's reagent and hydrofluoric acid is used. The composition of the Marshall's reagent is presented in Table 4.

Table 4: The composition of the Marshall's reagent used to reveal grain boundaries in IF steels

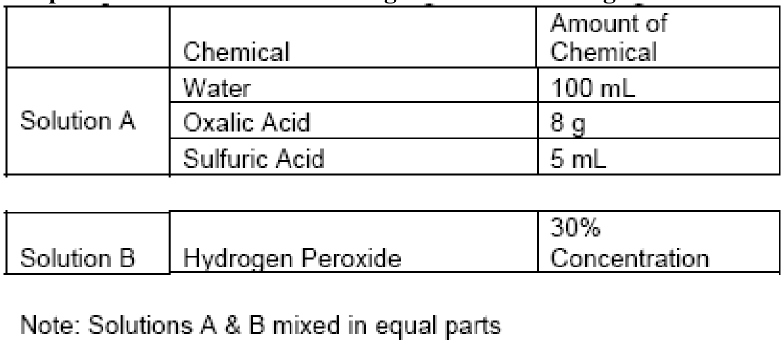

	Chemical	Amount of Chemical
Solution A	Water	100 mL
	Oxalic Acid	8 g
	Sulfuric Acid	5 mL
Solution B	Hydrogen Peroxide	30% Concentration

Note: Solutions A & B mixed in equal parts

The recommended mixture of Marshall's reagent to hydrofluoric acid is 100:1 ml, with the etching performed through immersion of the sample. Marshall's reagent works well for exposing the grain structure of low carbon steels, such as IF steel.

4. EXPERIMENTAL RESULTS AND DISCUSSION

4.1. Tensile Testing

Tensile testing is a standard method of examining the mechanical behavior of materials. Of interest in this study were the value of ECAE-processed IF steel's yield strength, ultimate tensile strength, and ductility. The description of the tensile testing performed in this study was presented in Section 3.3. A summary of the values of yield strength, ultimate tensile strength and ductility for each sample used in the as-processed tests is shown in Table 5. The values are presented as true-stress for YS and UTS, and engineering-strain for % ductility. Engineering-strain was chosen because the equations for converting to true-stress and true-strain do not apply after plastic deformation begins.

Table 5: Summary of tensile test results

Tensile Test Results			
Sample	YS (MPa, true)	UTS (MPa, true)	Ductility at Failure (%, Engineering)
As Received	70.7	282.3	60.3
1A	442.7	467.8	29.3
2A	496.3	526.3	10.7
2B	532	571.2	45.2
2C	522.7	561.6	45.6
4A	593.1	636.3	27.1
4B	590.9	634.8	18.8
4C'	602	678.2	41.5
4C	552.7	588.3	16
4E	555.5	651.2	41.7
8C'	681.2	776.3	43.4
8C	575.4	634.6	41.9
8E	613.2	704.7	39.6
16E	654.2	758.9	44.7

A comparison of these values makes it possible to see, at a glance, the impact ECAE has on the mechanical performance of IF steel (Figure 18). Yield strength shows a dramatic improvement at the first pass through the press. In the case of Route A, there is a steady increase in the yield strength as the number of passes increases. The same increase is observed in Route B, although the increase is not as noticeable. In the case of Route C the increase in yield strength is very slight, especially between ECAE 4C and ECAE 8C. For Route C' the increase in yield strength is more noticeable; ECAE 8C' has the highest yield strength of all of the processing routes used in this study. Route E shows some degree of yield strength enhancement, though it is not as great as Route C'.

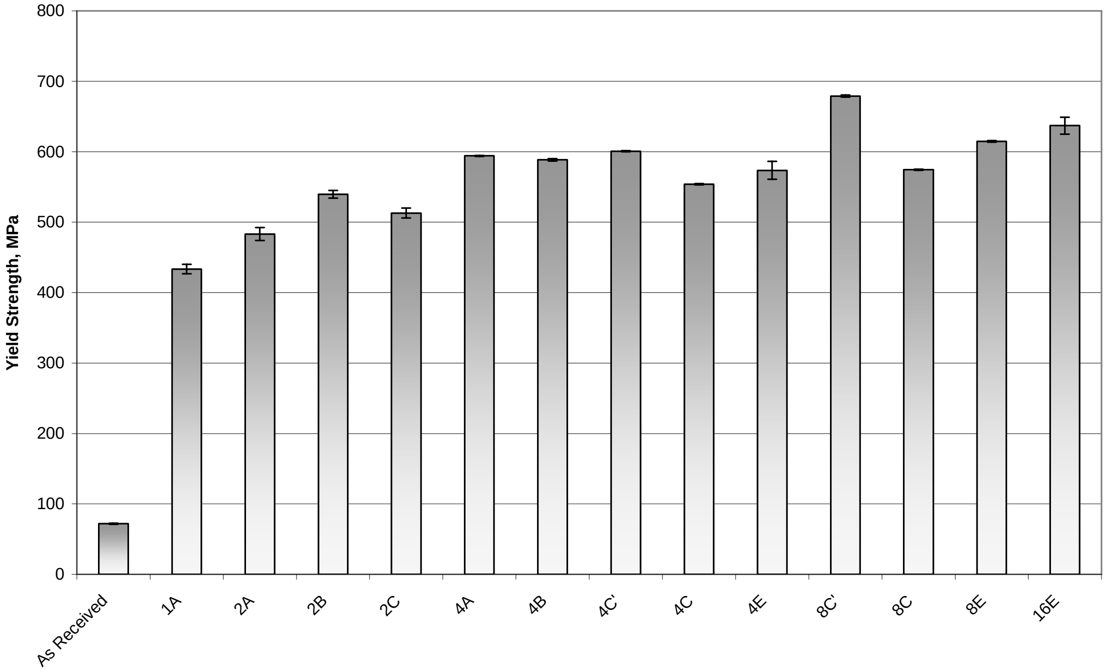

Figure 18: A comparison of yield strength of as-processed IF steel

In Figure 19 a comparison of tensile strength across the various routes is made. Route A shows a steady increase in the value of UTS from ECAE 1A to ECAE 4A. Route B shows a less significant increase in comparison to Route A. The increase in ultimate tensile strength in Route C as the number of passes increase is very slight. Route C' shows a significant increase in ultimate tensile strength, and again ECAE 8C' has the highest recorded values for ultimate tensile strength. Route E shows a steady increase in its UTS values, with ECAE 16E having the second-highest ultimate tensile strength recorded.

The ductility of the IF steel tension test samples is presented in Figure 20 so as to allow a comparison between the routes that were examined in this study. Comparisons of ductility at failure across the different routes show unusual results. In the case of Route A, the first specimens showed a decrease from ECAE 1A to ECAE 2A, and then an increase to ECAE 4A. Route C showed a similar behavior. The ductility of Route B decreased as the number of passes increased. The opposite is true for Routes C' and E: their ductility increased as the number of passes rose.

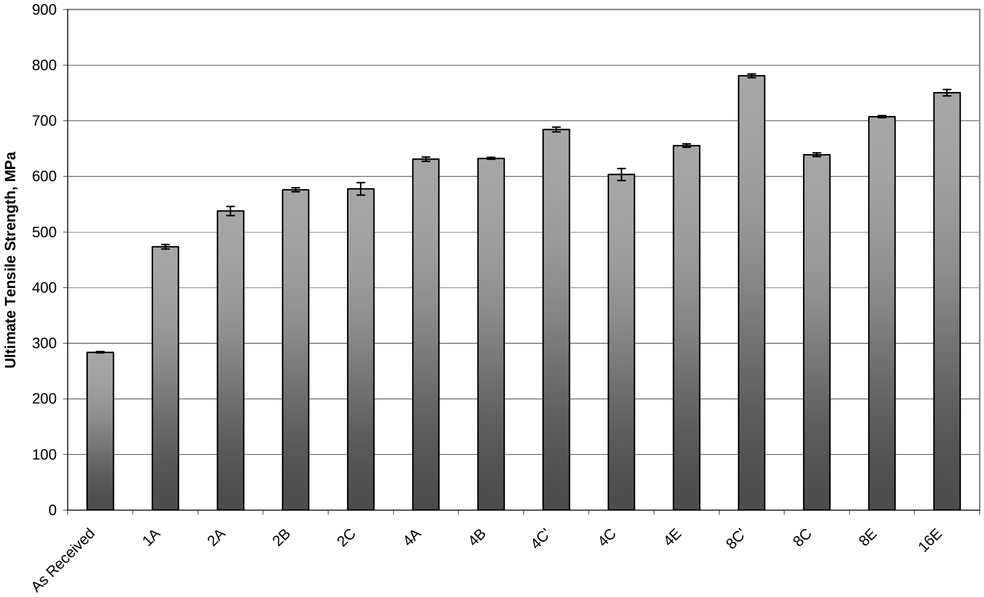

Figure 19: A comparison of ultimate tensile strength of as-processed IF steel

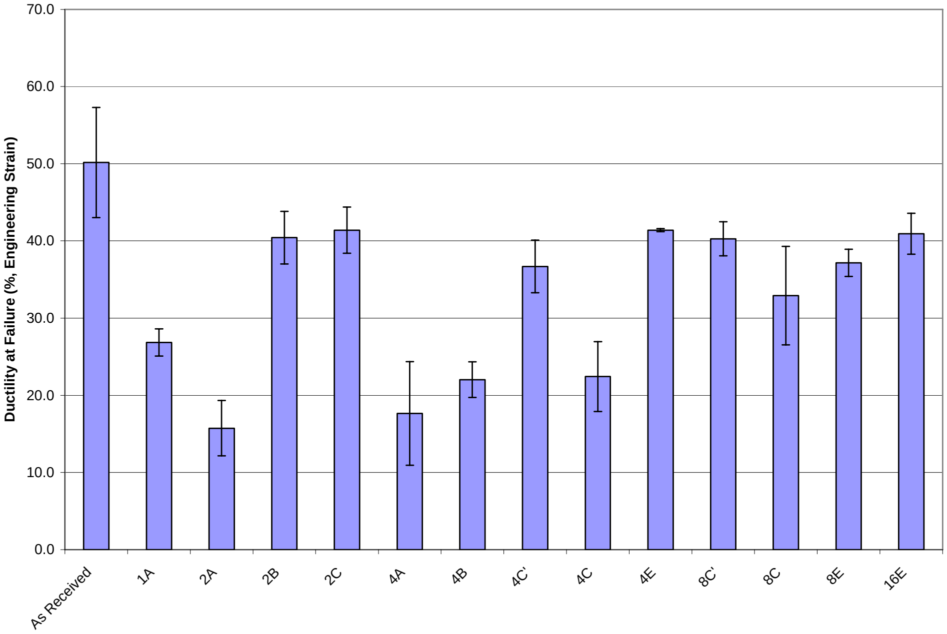

Figure 20: A comparison of ductility at failure of as-processed IF steel (Engineering-strain)

The summaries that were presented in Figures 18 – 20 present only the yield strength, ultimate tensile strength and ductility values of the specimens tested. They do not show the actual true-stress versus true-strain curves obtained from the test data. The ductility data presented in Figure 20 is taken from engineering strain values. Plots of the true-stress versus true-strain performance of the different routes examined in this study are presented in Figures 21 – 25 on the following pages. In each case the as-received material true-stress versus true-strain curves are shown for comparison purposes. Because the values for true-stress and true-strain were obtained using the equations

$$\begin{aligned} \sigma_{true} &= \sigma_{engineering}\left(1 + \varepsilon_{engineering}\right) \\ \varepsilon_{true} &= \ln\left(1 + \varepsilon_{engineering}\right) \end{aligned}$$

the strain values after the ultimate tensile strength should not be considered accurate by the reader.

True-stress versus true-strain behavior for specimens processed using Route A is shown in Figure 21. True-stress versus true-strain behavior for specimens processed using Route B is shown in Figure 22. True-stress versus true-strain behavior for specimens processed using Route C is shown in Figure 23. True-stress versus true-strain behavior for specimens processed using Route C’ is shown in Figure 24. True-stress versus true-strain behavior for specimens processed using Route E is shown in Figure 25.

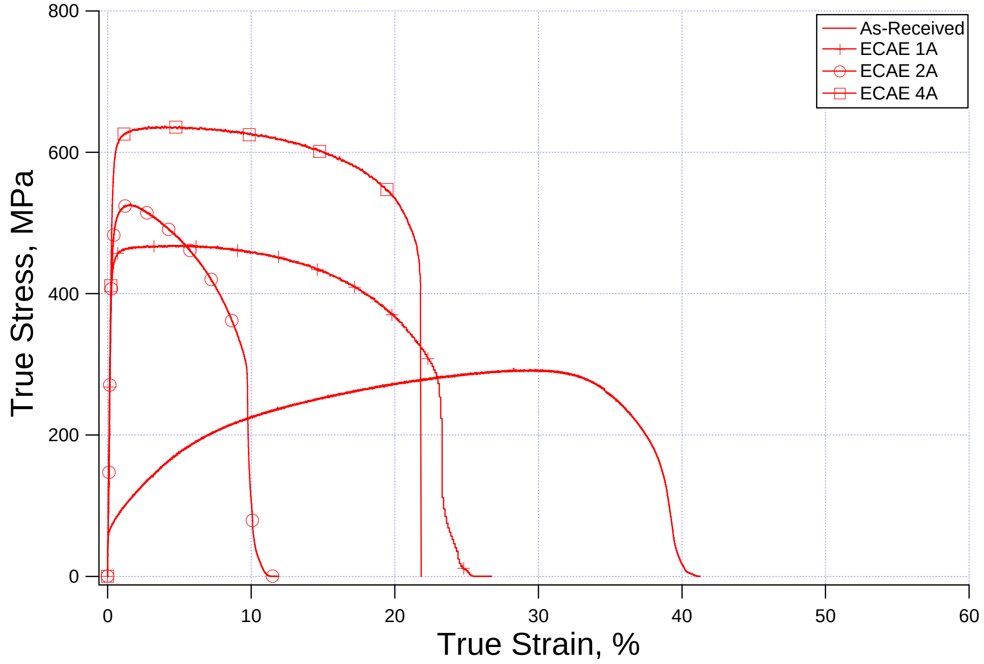

Figure 21: True-stress vs. true-strain comparison of IF steel processed using Route A

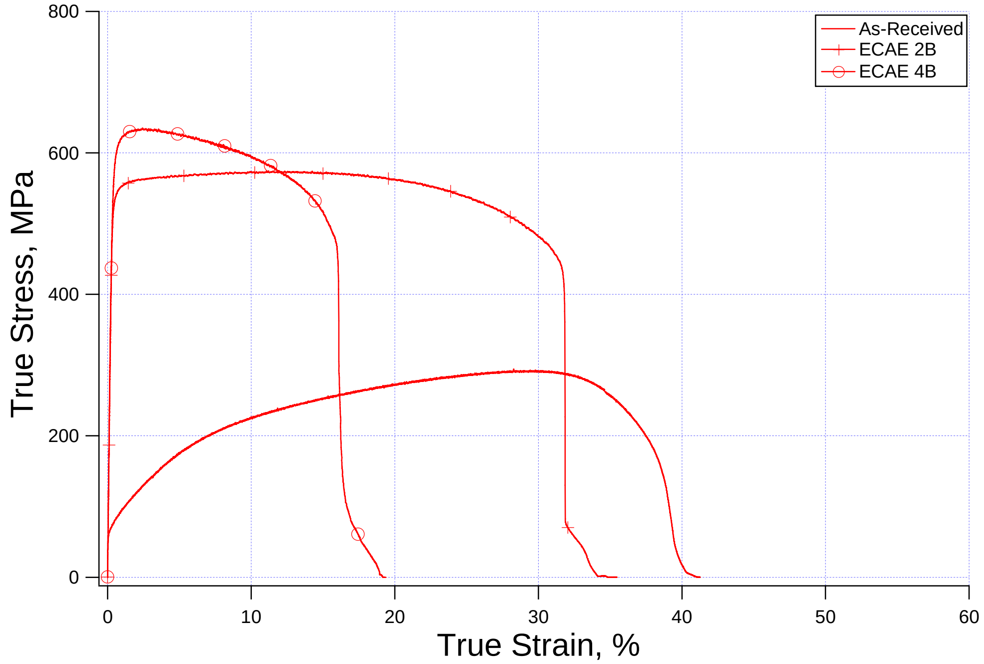

Figure 22: True-stress vs. true-strain comparison of IF steel processed using Route B

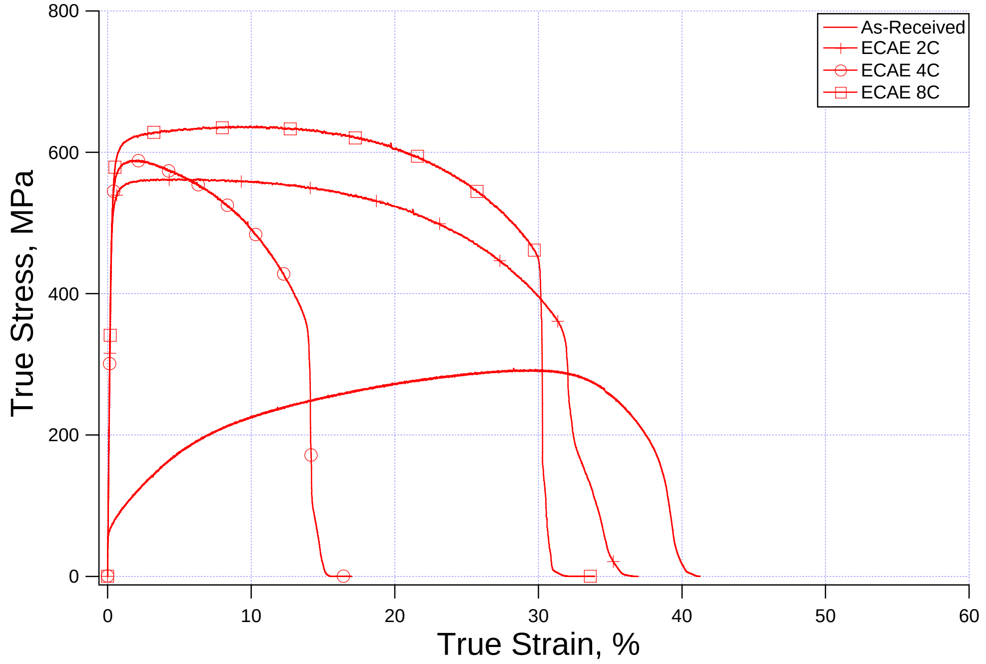

Figure 23: True-stress vs. true-strain comparison of IF steel processed using Route C

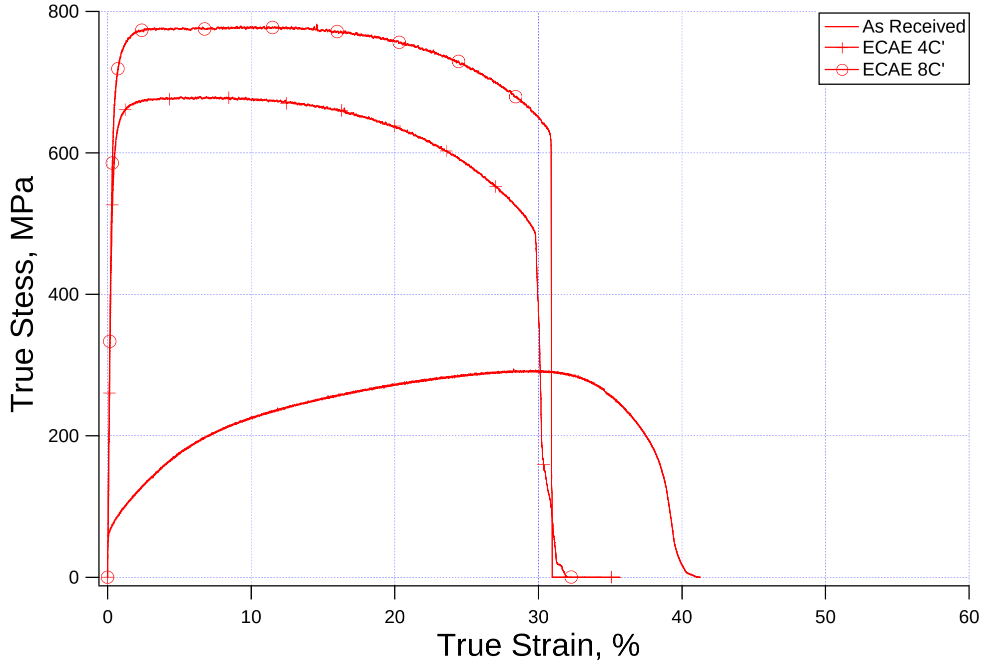

Figure 24: True-stress vs. true-strain comparison of IF steel processed using Route C’

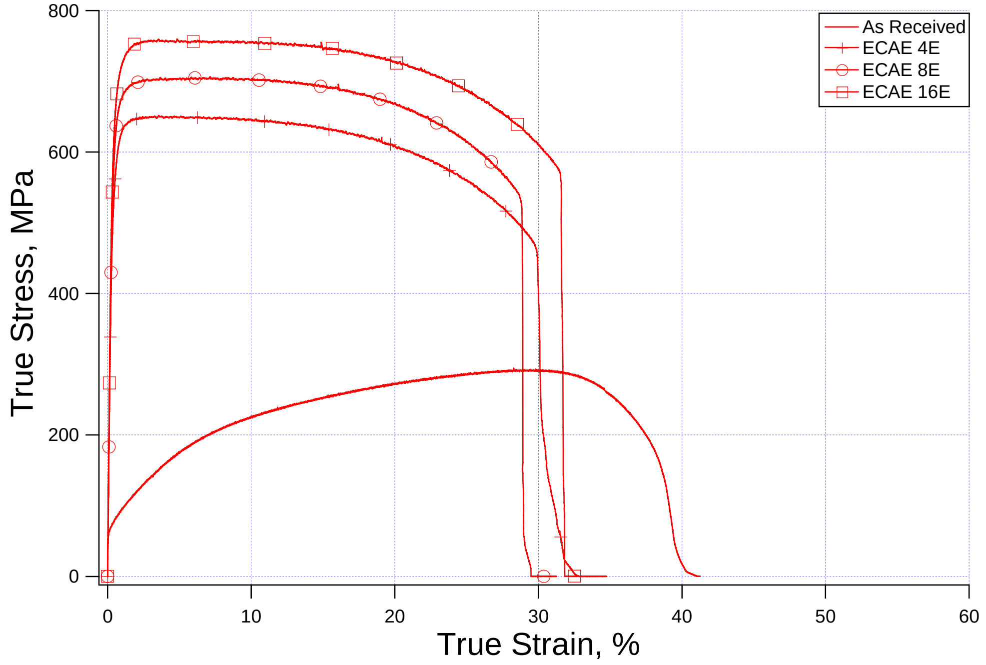

Figure 25: True-stress vs. true-strain comparison of IF steel processed using Route E

The data plots shown in Figures 21 – 25 are useful for examining how the mechanical properties of as-processed IF steel change as the number of passes increase in a given route. A comparison of the routes, given a constant number of passes, allows an examination of the impact routes have upon mechanical performance. In all cases, the true-stress vs. true-strain behavior of the as-received material is included for reference purposes.

The plot comparing routes given two passes (Figure 26) shows that ECAE 2A yields poor YS and UTS when compared to ECAE 2B and ECAE 2C. In the cases of ECAE 2B and ECAE 2C, their YS is virtually identical, and their UTS values are also quite similar.

When four passes are considered (Figure 27), there are more routes available for examination: ECAE 4A, ECAE 4B, ECAE 4C, ECAE 4C' and ECAE 4E. Of these, ECAE 4C' and ECAE 4E show the highest values of YS and UTS.

In the case of eight passes (Figure 28), there are three routes that can be compared: ECAE 8C, ECAE 8C' and ECAE 8E. It is shown that the mechanical performance of ECAE 8C' is superior to the other routes in this instance. The UTS of ECAE 8C' is the highest recorded in this study.

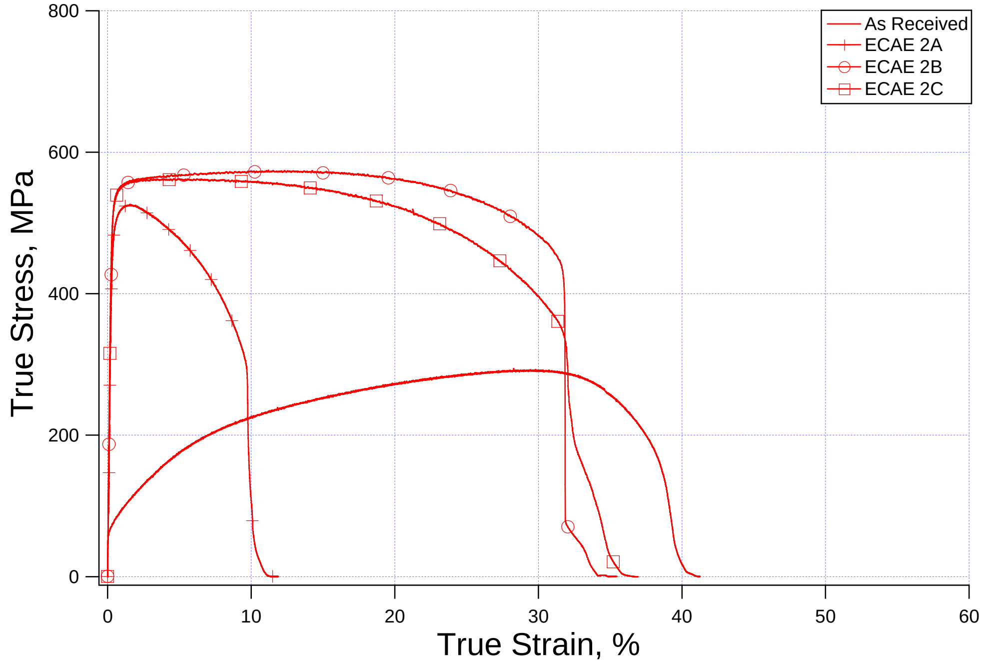

Figure 26: Comparison of routes at two passes for as-processed IF steel

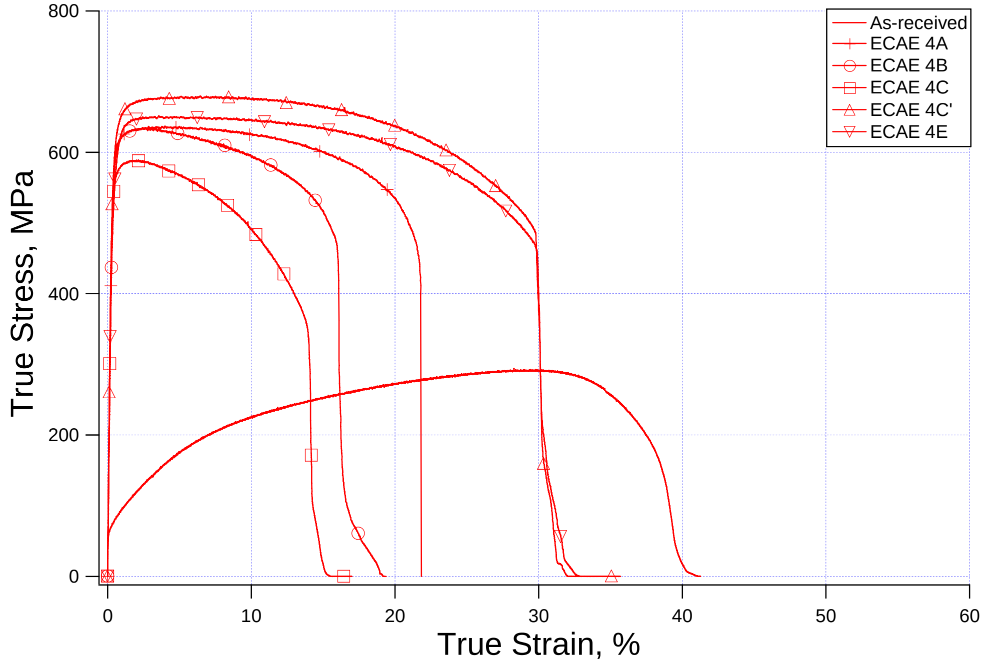

Figure 27: Comparison of routes at four passes for as-processed IF steel

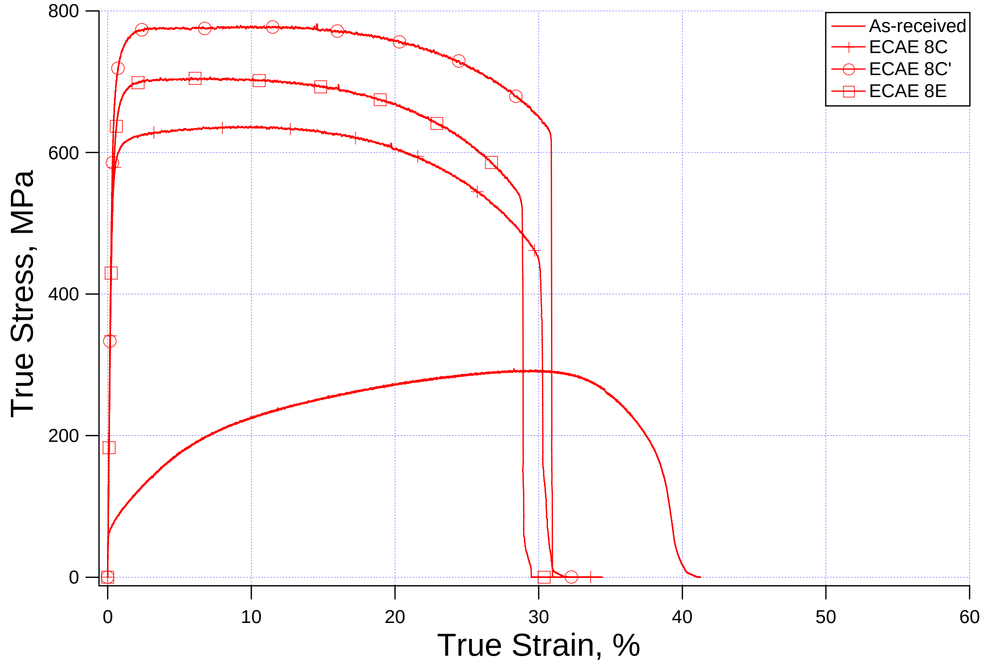

Figure 28: Comparison of routes at eight passes for as-processed IF steel

To examine the impact of annealing on as-processed IF steel, tension specimens from three ECAE processing routes were annealed and tested. The annealing temperatures chosen corresponded to those of the early and middle stages in recrystallization, between 400°C and 600°C, with annealing times ranging from five to 90 minutes. In the case of ECAE 4A, three samples were annealed; one at 500°C for five minutes, one at 600°C for five minutes and the last at 600°C for 15 minutes. In the case of ECAE 4E, two specimens were annealed for 90 minutes each, one at 450°C and the other at 500°C. In the case of ECAE 8E, three specimens were annealed for 90 minutes each, one at 400°C, another at 500°C and the last at 600°C.

True-stress vs. true-strain plots from these annealed specimens are shown in Figures 29 – 31.

The plot for ECAE 4A (Figure 29) shows that a short anneal of 15 minutes at 600°C significantly reduces both YS and UTS values. The true-stress vs. true-strain curve for ECAE 4A that has been annealed at 500°C for five minutes shows inferior values of YS and UTS. When annealed for 600°C for five minutes, the true-stress vs. true-strain plot shows a decrease in YS and UTS in comparison to the as-processed sample. The YS and UTS of the sample annealed for five minutes at 600°C is lower than those values for the sample annealed at 500°C for the same time.

In the case of ECAE 4E the true-stress vs. true-strain plots of Figure 30 show a steady decrease in YS and UTS as the 90-minute annealing temperature increases.

The true-stress vs. true-strain results for ECAE 8E are shown in Figure 31. All of the tension specimens were annealed for 90 minutes in this case. When annealed at

400°C the YS is slightly lower than the as-processed material, but the UTS values are both lower than the as-processed curves. At 500°C the sample displays a YS lower than that of the 400°C sample, with a UTS that is almost identical to the YS. At the highest annealing temperature, 600°C, the true-stress vs. true-strain curve shows similar behavior to the as-received curve. At 600°C the ECAE 8E tension specimen displays somewhat improved YS and UTS, in comparison to the as-received sample.

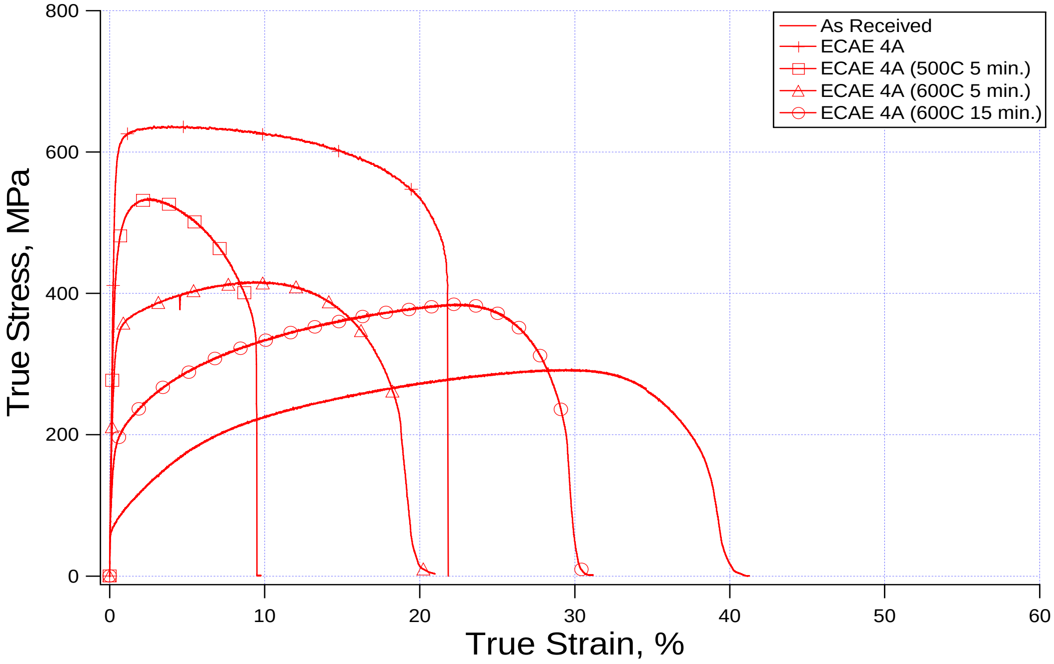

Figure 29: True-stress vs. true-strain behavior of as-processed and annealed ECAE 4A IF steel

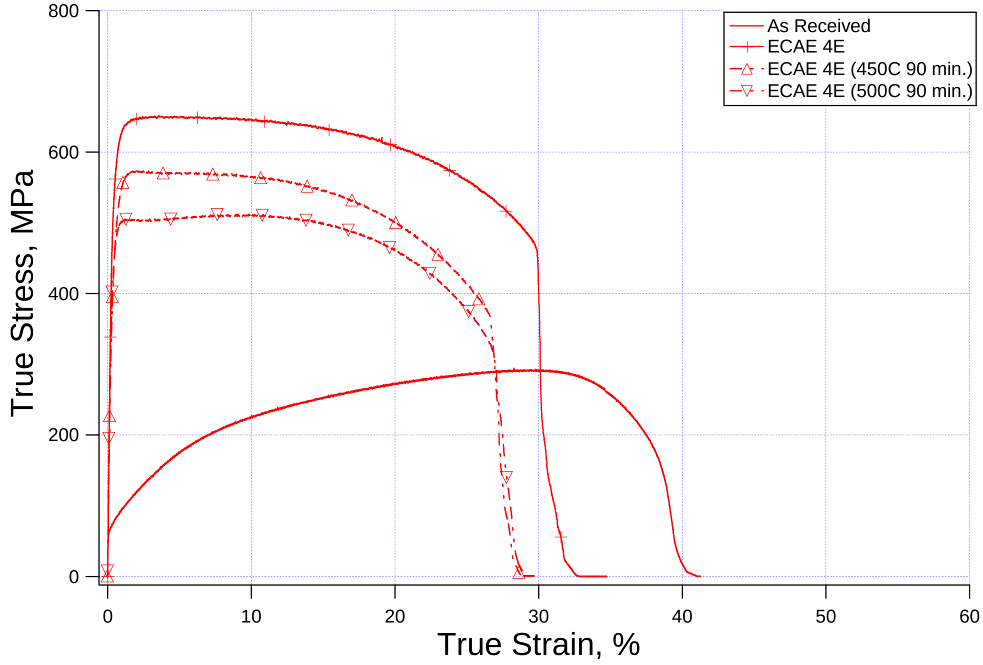

Figure 30: True-stress vs. true-strain behavior of as-processed and annealed ECAE 4E IF steel

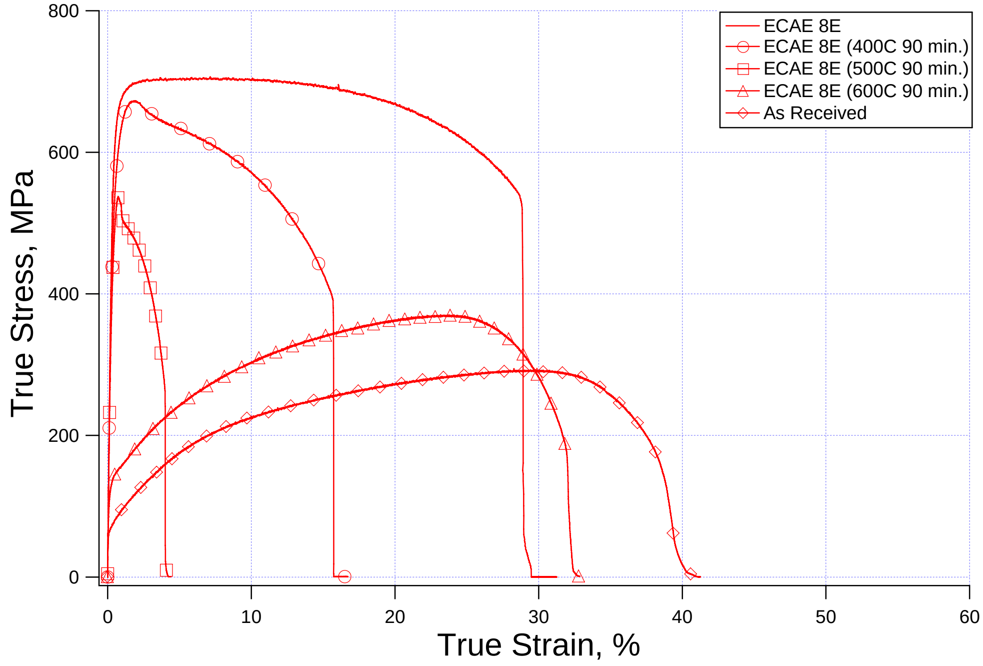

Figure 31: True-stress vs. true-strain behavior of as-processed and annealed ECAE 8E IF steel

4.2. Hardness

Vickers hardness measurements are taken for two reasons: first, to determine how different ECAE processing routes impacts the mechanical behavior of IF steel; second, to identify the temperature at which recrystallization occurs within the processed billets.

4.3. Texture

The objective of the texture analysis was to examine how different processing routes of ECAE impacted the preferred grain orientation in IF steel, and whether this preferred grain orientation might be responsible for some of the anisotropy we observe in mechanical properties.

Pole figures and inverse pole figures are standard methods of visualizing textures. Inverse pole figures may be used to locate certain billet planes, such as the longitudinal, flow and transverse planes, with respect to the poles [001], [101], and [111]. All pole figures are oriented with the flow plane (1) normal to the bottom, the longitudinal plane (2) normal to the right, and the transverse plane (3) normal to the center. In Figure 32 these orientations are depicted in relation to a billet.

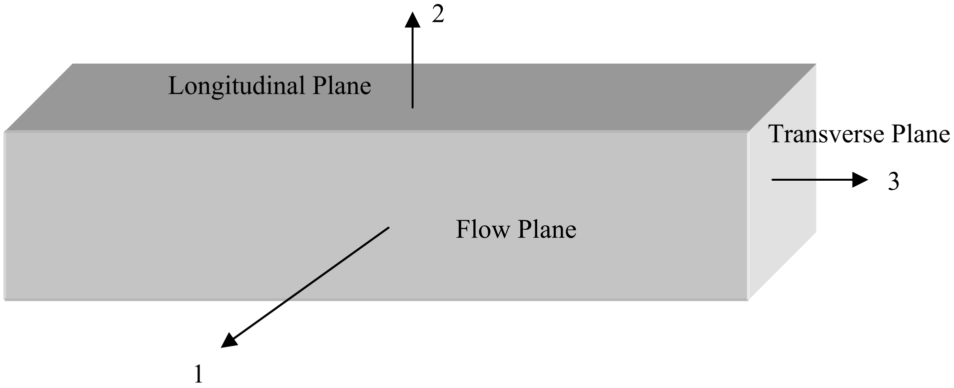

Figure 32: Notations of billet orientation used in texture analysis

To obtain a baseline for comparison purposes, IF steel in its as-received condition was subjected to a texture analysis. The pole figures of the as-received IF steel are shown in Figures 33 – 35.

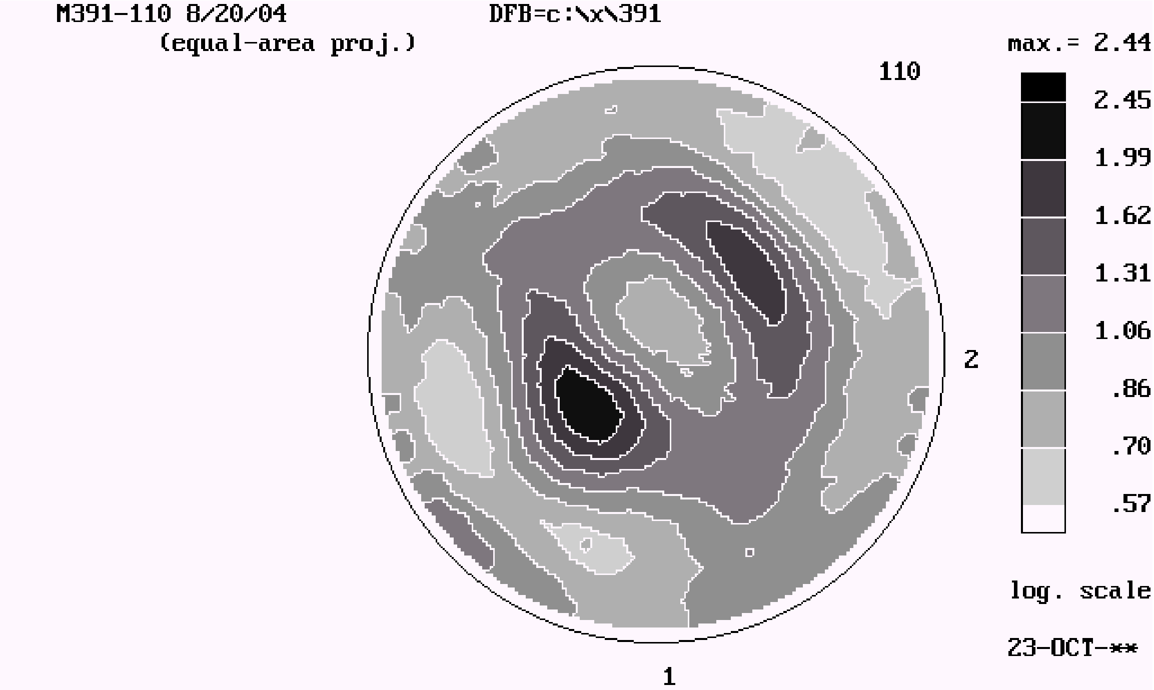

Figure 33: (110) Pole figure for as-received IF steel, direction 3 normal to plane of page

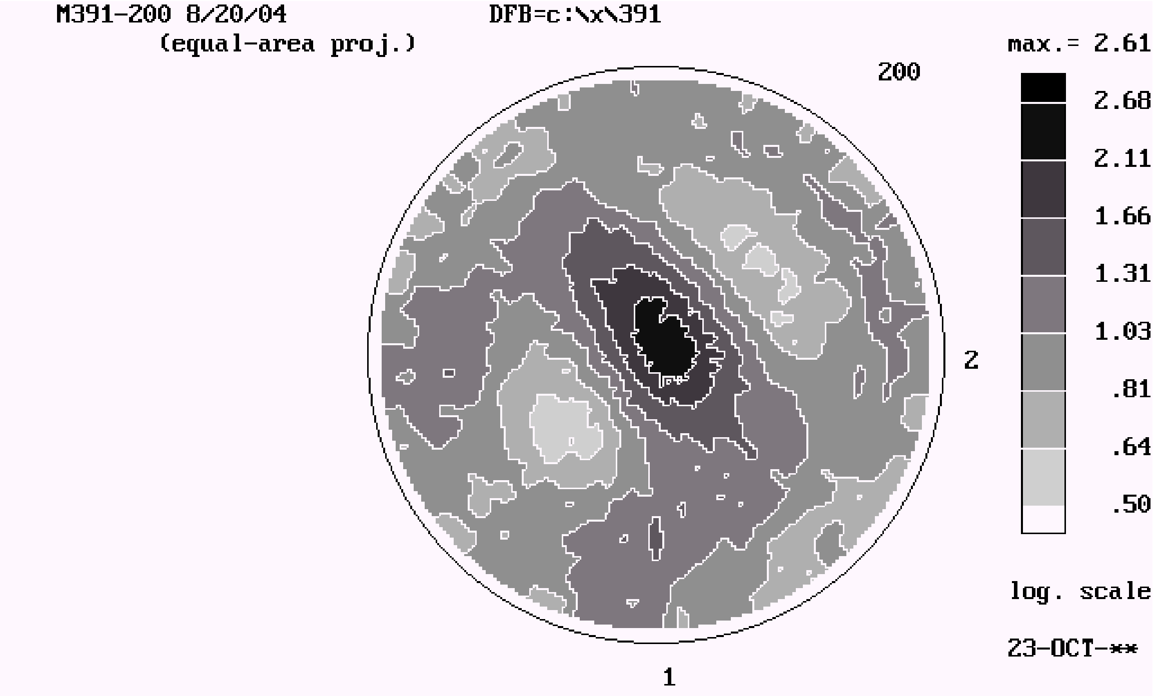

Figure 34: (200) Pole figure for as-received IF steel, direction 3 normal to plane of page

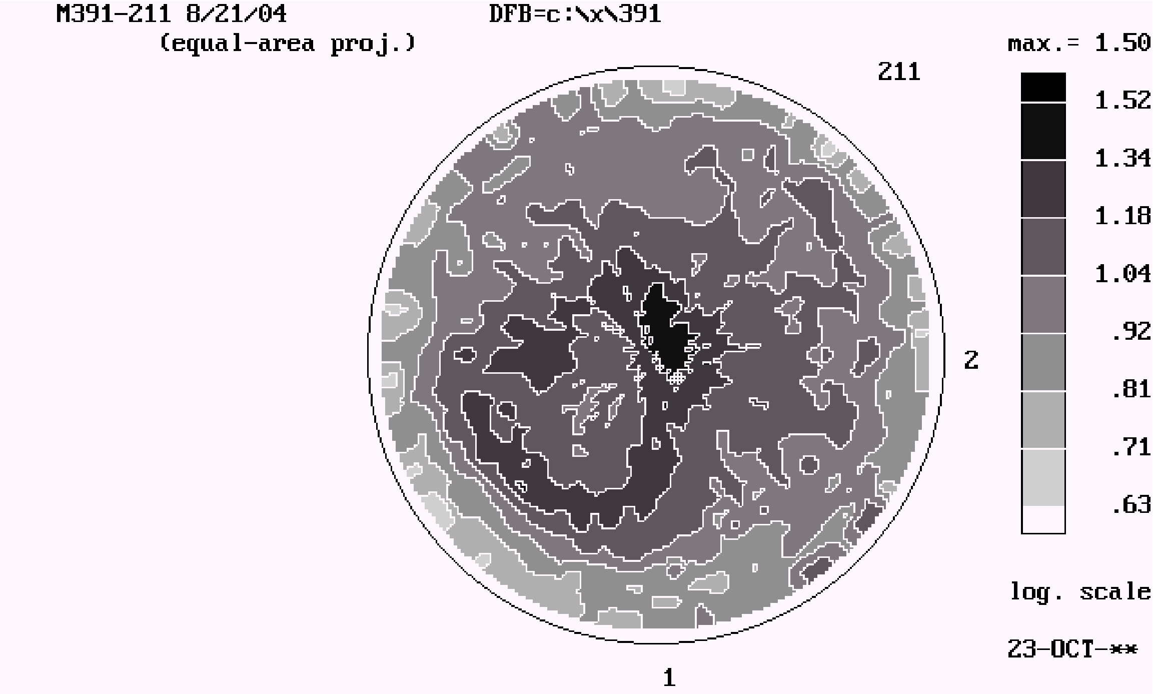

Figure 35: (211) Pole figure for as-received IF steel, direction 3 normal to plane of page.

The inverse pole figures for the as-received material are shown in Figure 36. There is a strong texture in the [111] and [001] orientation along axis 3, the transverse plane.

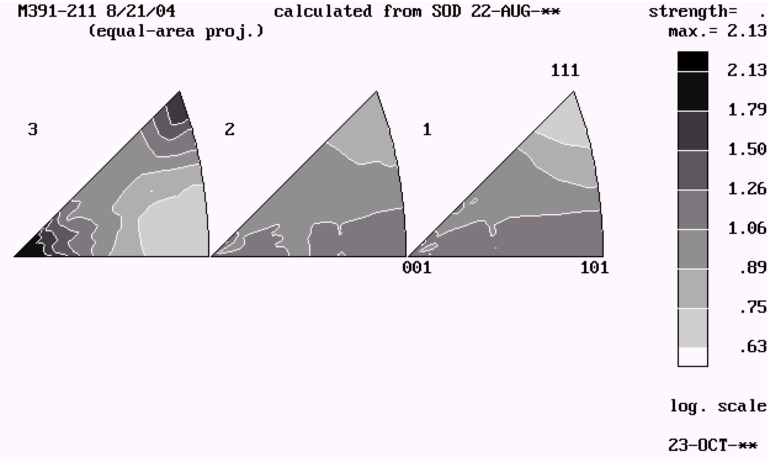

Figure 36: Inverse pole figures for as-received IF steel

This study had three samples of IF steel that were processed following Route A: ECAE 1A, ECAE 2A and ECAE 4A. A sample processed using Route A does not undergo any rotation between passes.

The [110] pole figures are shown in Figures 37 – 39. The textures appear rotated by 90° from the as-received specimen for the cases of ECAE 1A and ECAE 2A. As processing continues, the intensity of the preferred texture increases. In the case of ECAE 4A, the orientation of the texture of [110] appears similar, but is of a higher intensity, than that of the as-received sample.

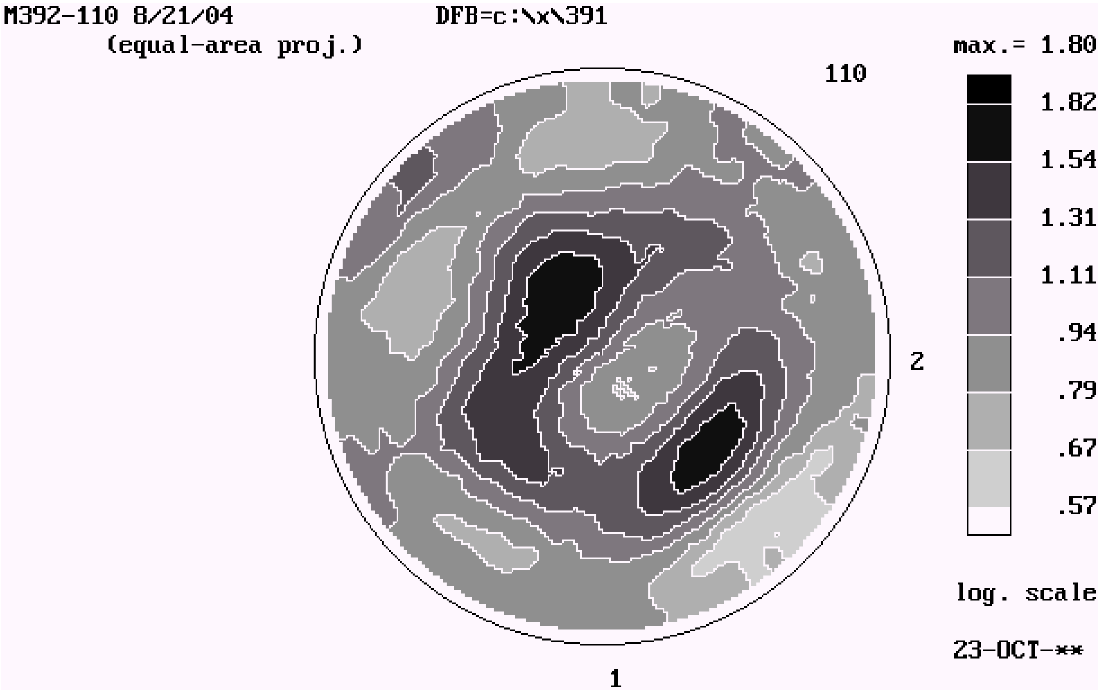

Figure 37: (110) Pole figure of ECAE 1A IF steel, direction 3 normal to plane of page

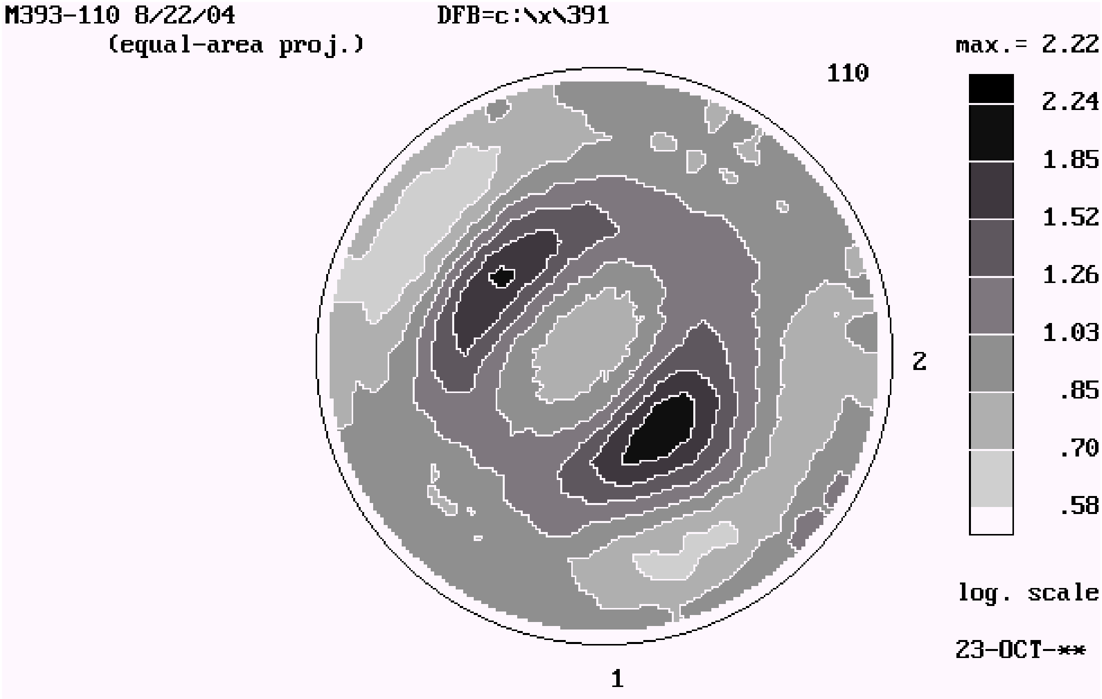

Figure 38: (110) Pole figure for ECAE 2A IF steel, direction 3 normal to plane of page

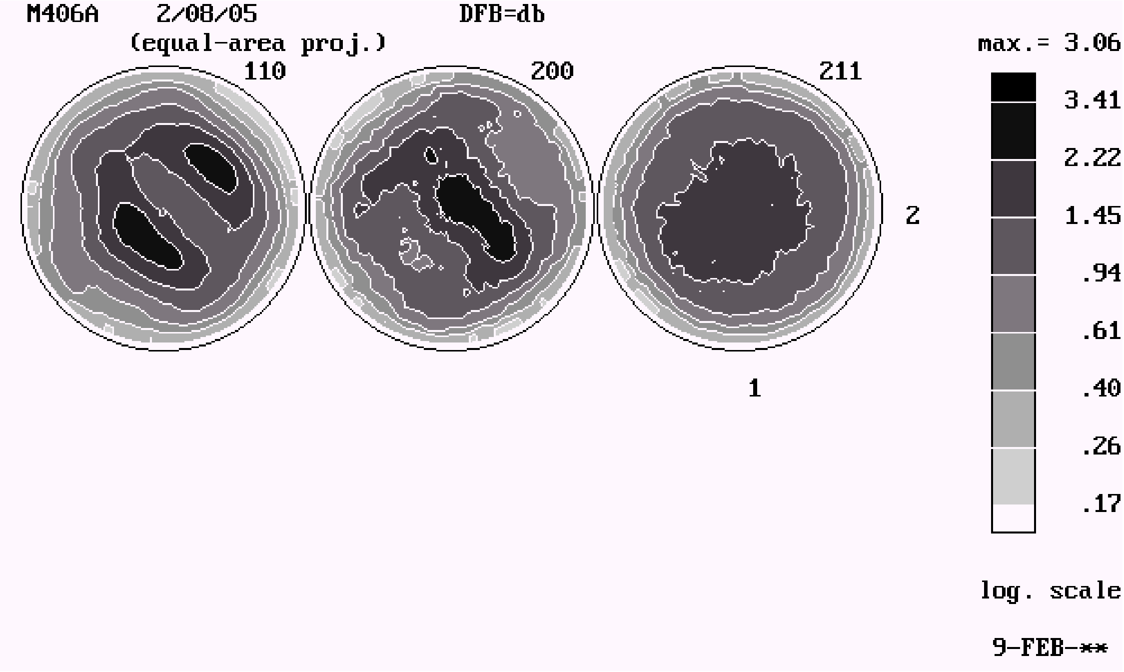

Figure 39: Pole figures for ECAE 4A IF steel (all orientations), direction 3 normal to plane of page

For [200] there is little change in the preferred texture orientation from the as-received specimen. In Figures 39 – 41 the texture shows a general increase in peak magnitude as the number of passes increases.

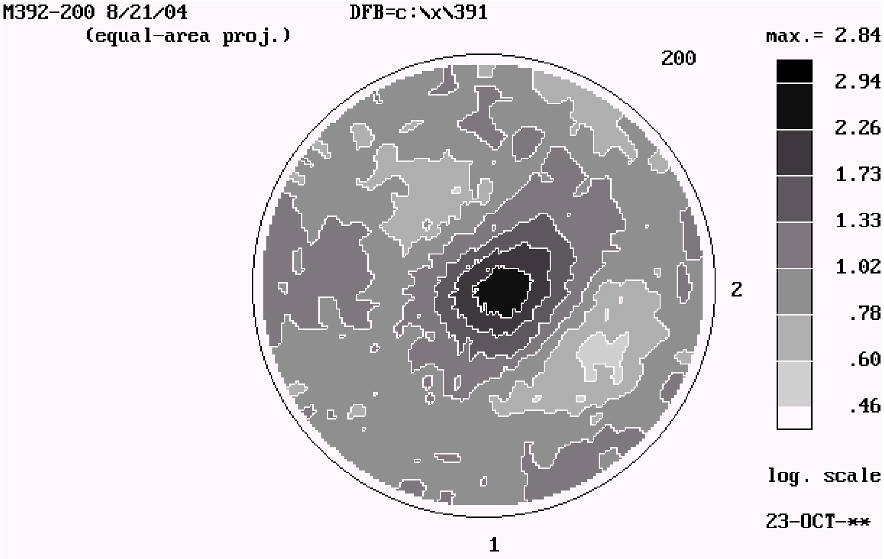

Figure 40: (200) Pole figure for ECAE 1A IF steel, direction 3 normal to plane of page

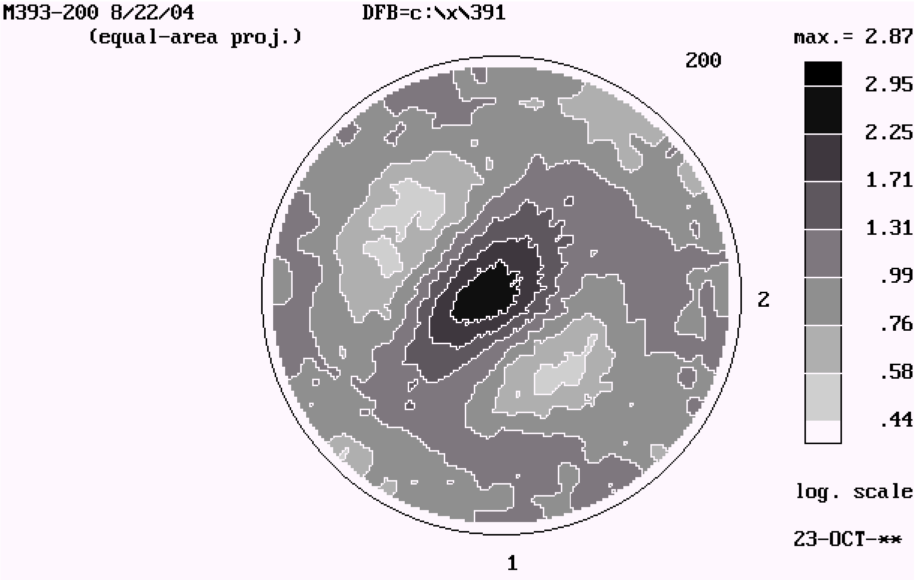

Figure 41: (200) Pole figure for ECAE 2A IF steel, direction 3 normal to plane of page

For [211] the texture does not show a great deal of change from one case to another. Figures 42, 43 and 39 show the texture results for ECAE 1A, ECAE 2A and ECAE 4A, respectively. Texture becomes stronger as the number of passes increase.

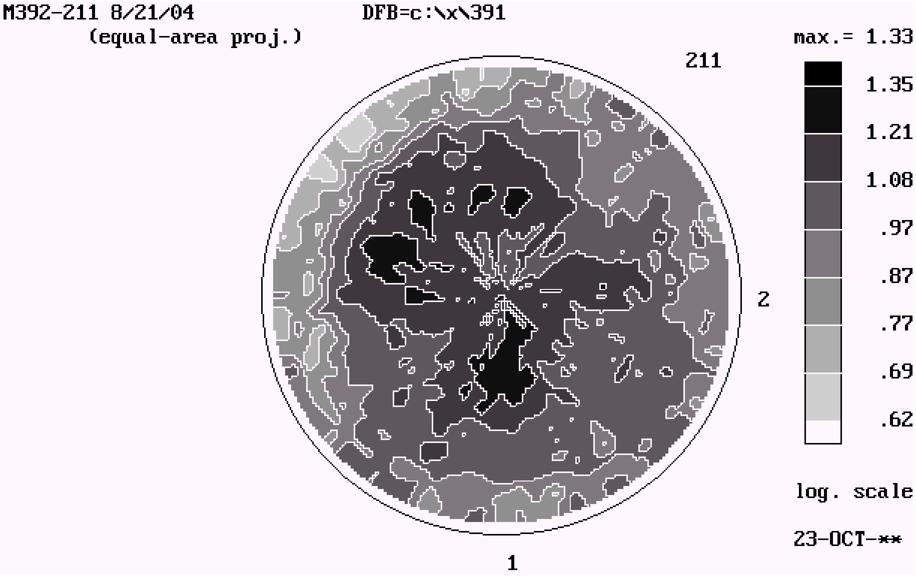

Figure 42: (211) Pole figure for ECAE 1A IF steel, direction 3 normal to plane of page

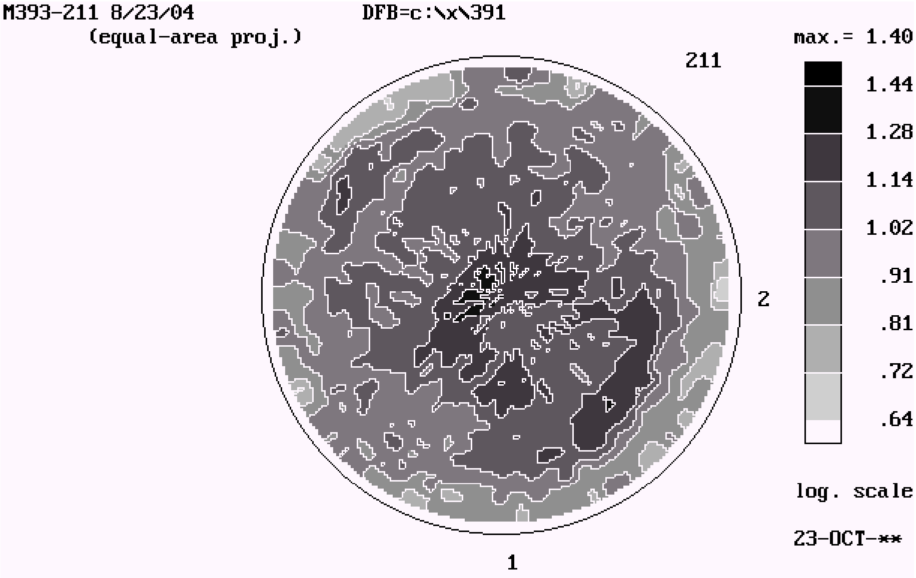

Figure 43: (211) Pole figure for ECAE 2A IF steel, direction 3 normal to plane of page

Inverse pole figures for the three samples processed using Route A are presented in Figures 44 – 46. The inverse pole figures show a consistent strengthening in the textures of [001] and [111] on the transverse plane. There is also a gradual strengthening of the texture corresponding to [001] and [101] in both the flow and longitudinal planes. The strength of the textures increased with the number of passes performed.

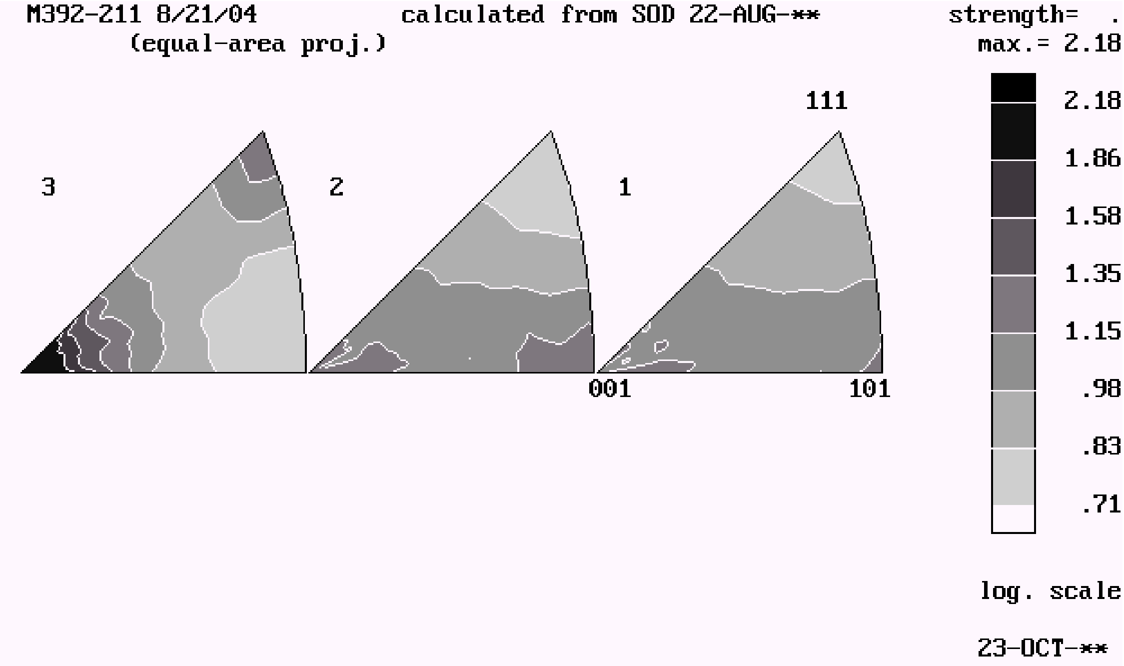

Figure 44: Inverse pole figure for ECAE 1A IF steel

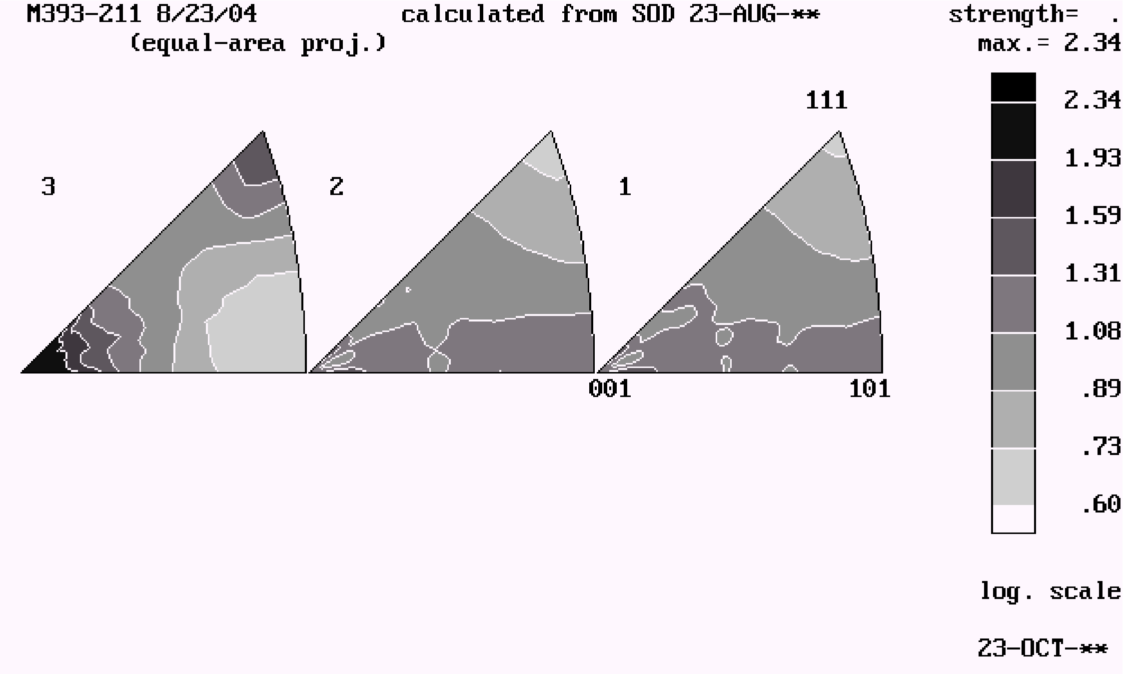

Figure 45: Inverse pole figure for ECAE 2A IF steel

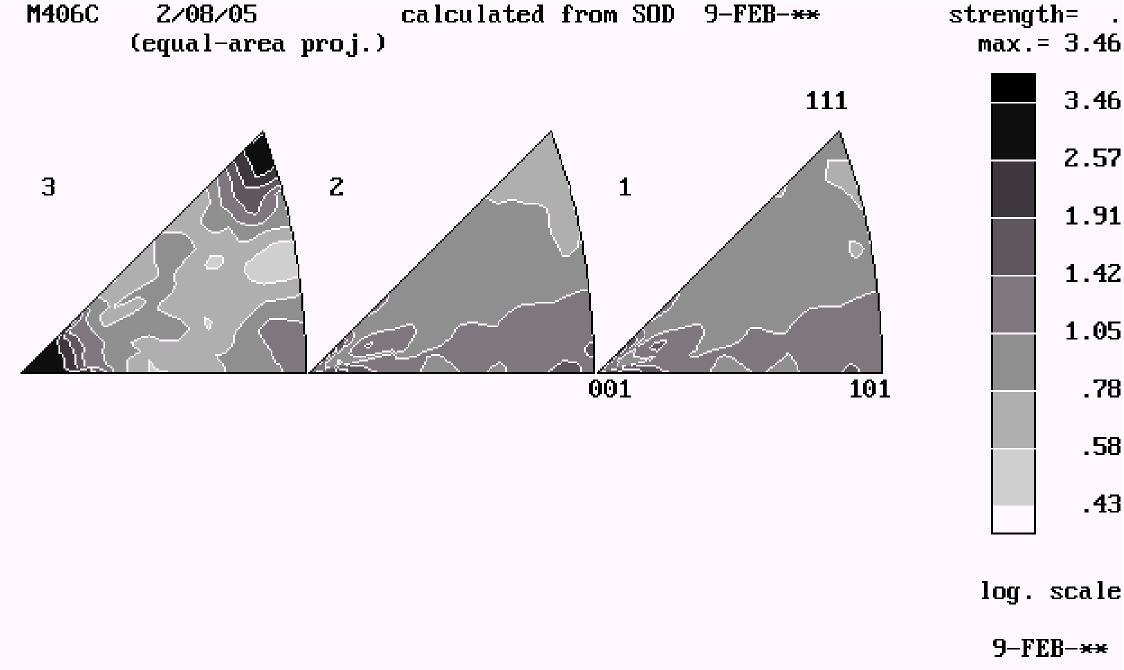

Figure 46: Inverse pole figure for ECAE 4A IF steel

Two samples, ECAE 2B and ECAE 4B, were processed using Route B. After the first extrusion pass, samples processed according to Route B are rotated +90° on the even-numbered passes, and -90° for the odd-numbered passes.

The [110] pole figures for Route B are shown in Figures 47 – 48. The preferred texture for ECAE 2B [110] shows a higher strength and is rotated 45° from the as-received material. The preferred texture for ECAE 4B [110] is the strongest, and shows a counter-rotation, back to the as-received orientation.

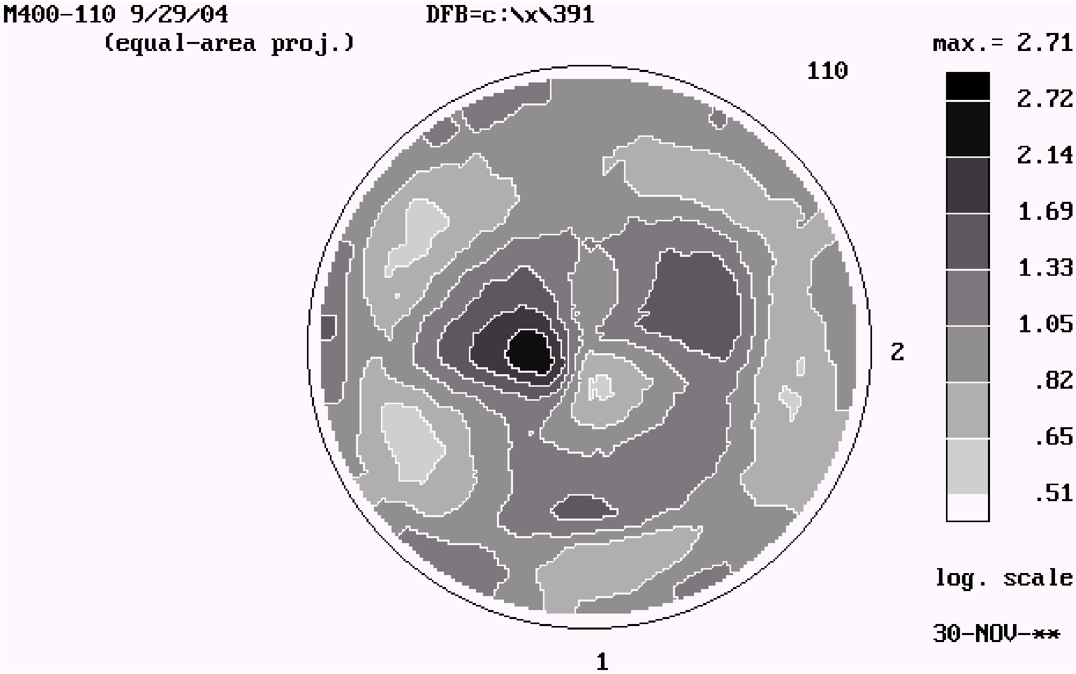

Figure 47: (110) Pole figure for ECAE 2B IF steel, direction 3 normal to plane of page

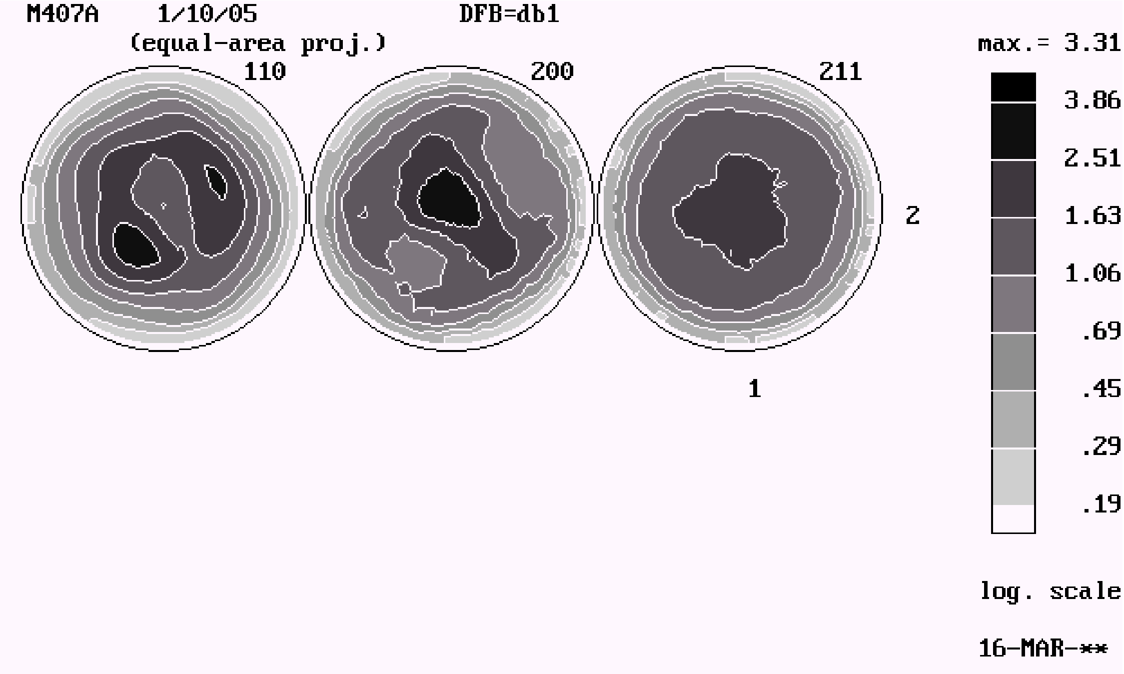

Figure 48: Pole figures for ECAE 4B IF steel, direction 3 normal to plane of page

Texture for [200] is shown in Figures 48 – 49 and shows a significant increase in texture strength between four and two passes, respectively, as well as a consolidation of texture.

The pole figure for ECAE 2B [200] shows three separate preferred texture zones, while the pole figure for ECAE 4B [200] shows only a single, very strong region of preferred texture.

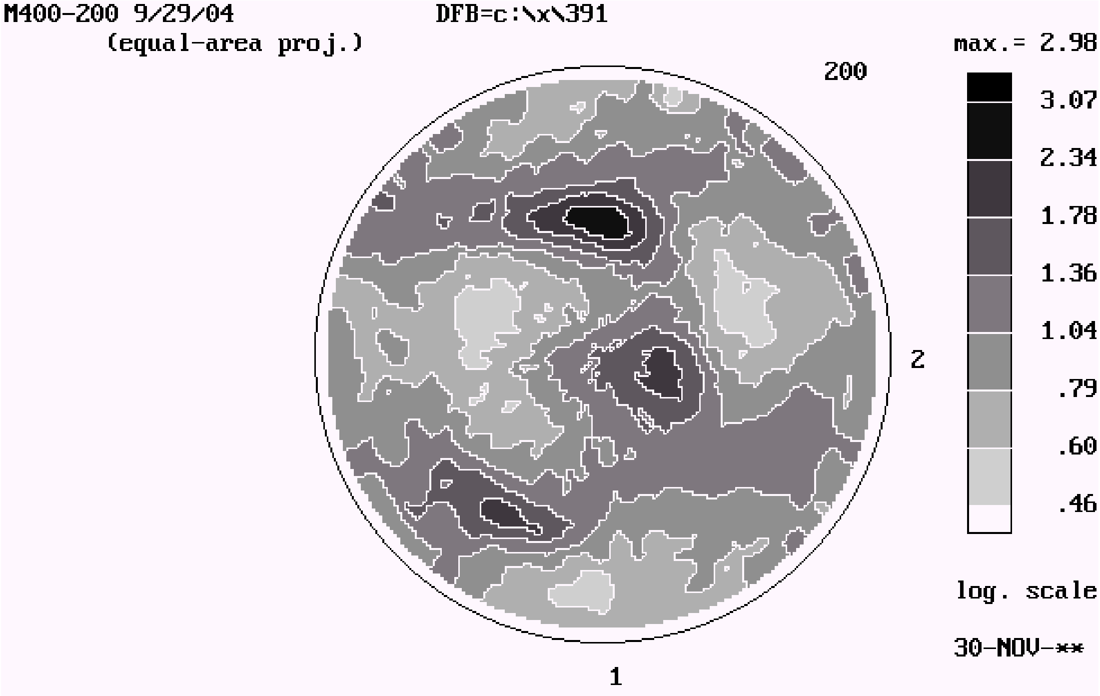

Figure 49: (200) Pole figure for ECAE 2B IF steel, direction 3 normal to plane of page

The pole figures for [211] of the Route B samples are shown in Figure 48 and Figure 50 for ECAE 4B and ECAE 2B, respectively.

Two passes following Route B results in a fragmented texture of increased strength when compared to the as-received material. Four passes following Route B results in a single [211] texture of greater magnitude.

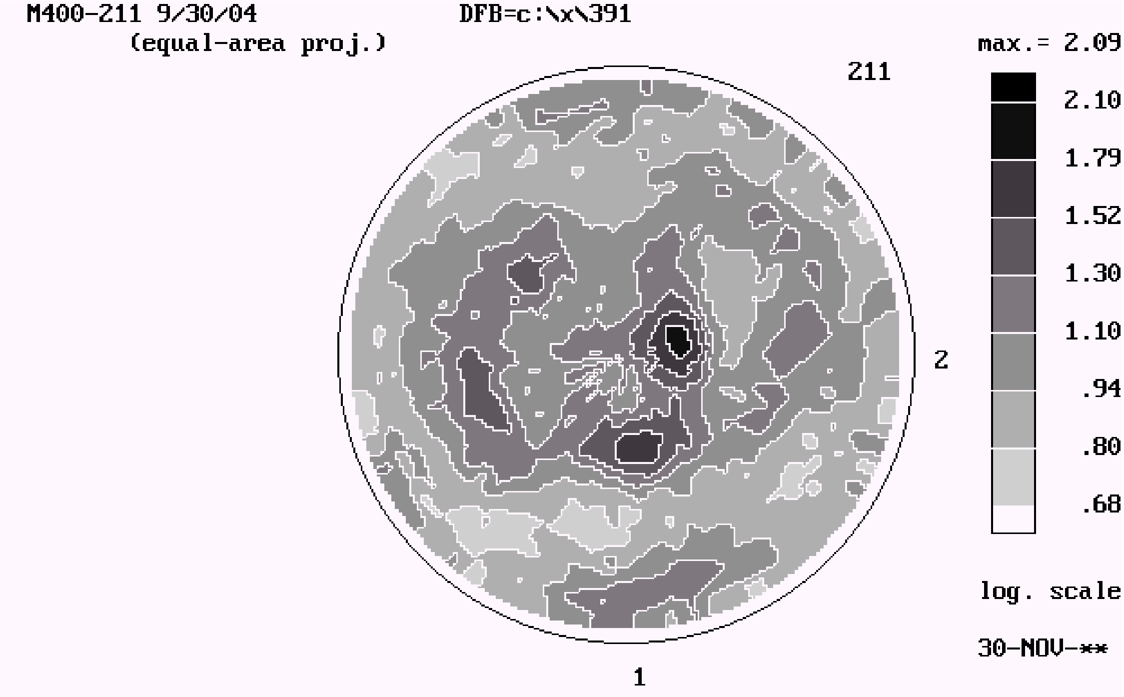

Figure 50: (211) Pole figure for ECAE 2B IF steel, direction 3 normal to plane of page

The inverse pole figures for ECAE 2B and ECAE 4B are shown in Figure 51 and Figure 52, respectively.

Two passes using Route B produces preferred textures on the transverse plane in the [001] and [111] directions. There is also a preferred texture on the longitudinal plane corresponding to [111], and a small zone of preferred texture on the flow plane near [101].

Four passes using Route B produces strong preferred textures on the transverse plane in the [001] and [111] directions. Both the flow plane and longitudinal plane of ECAE 4B show a some texture strengthening around [101].

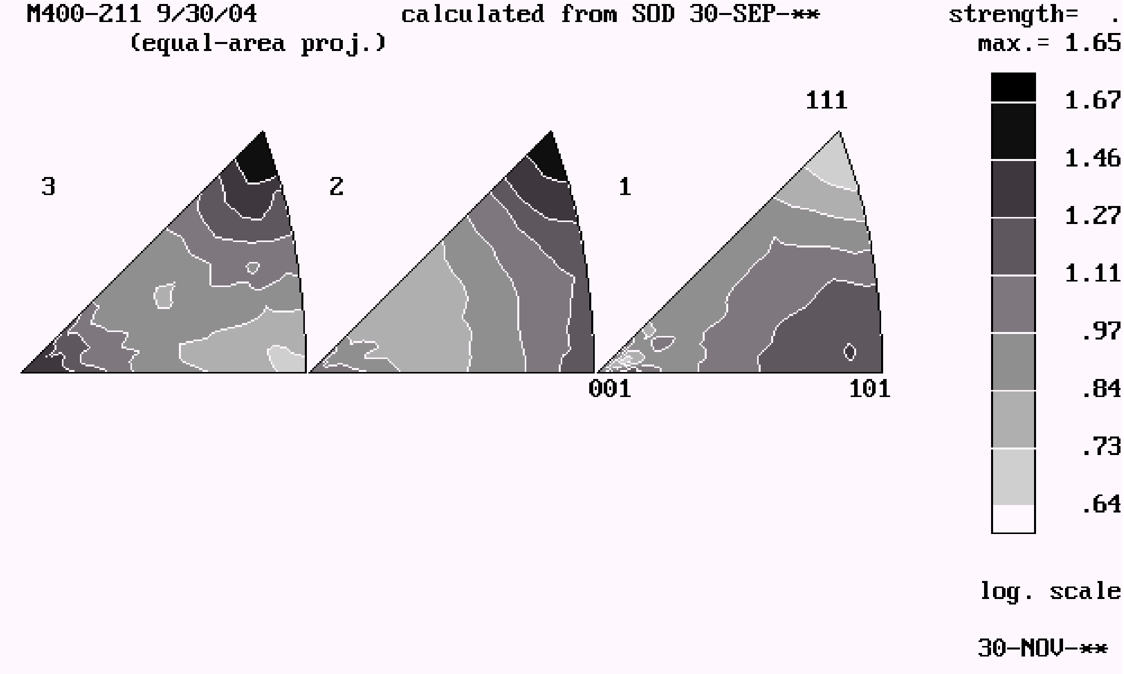

Figure 51: Inverse pole figures for ECAE 2B IF steel

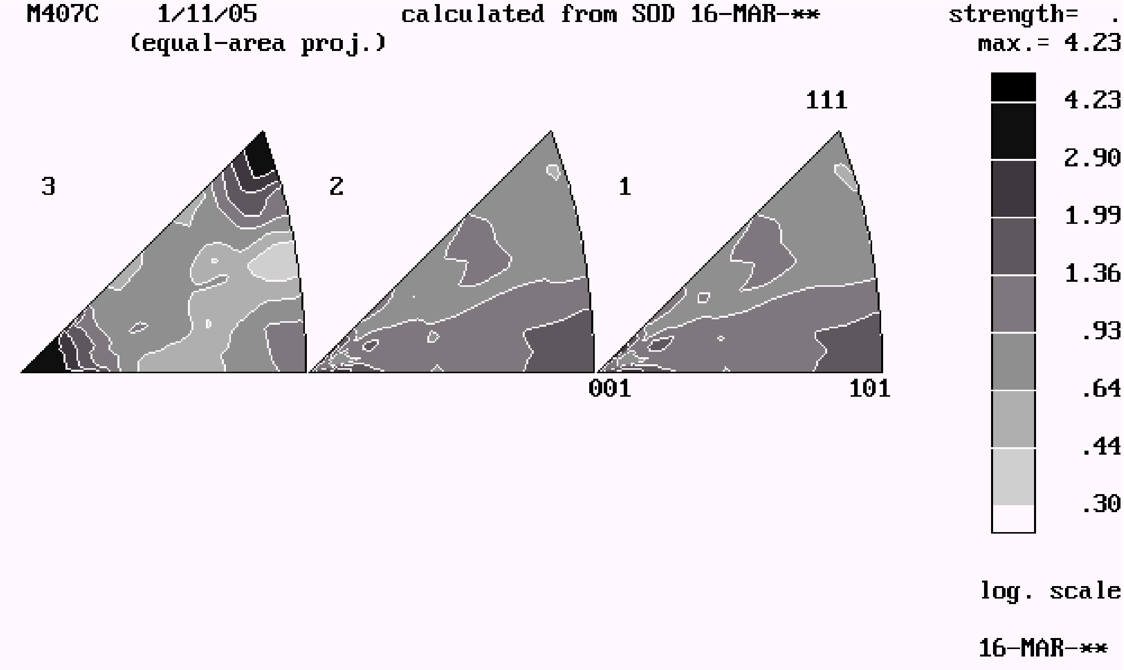

Figure 52: Inverse pole figures for ECAE 4B IF steel

Three samples, ECAE 2C, ECAE 4C and ECAE 8C, were processed following Route C. After the first pass, the sample is rotated +180° on the even-numbered passes, and -180° on the odd-numbered passes.

The pole figures for [110] are shown in Figures 53 – 55. The texture associated with ECAE 2C [110] is rotated 45° from the as-received condition, and is not as strong as the as-received texture. The texture orientations for ECAE 4C and ECAE 8C are nearly identical to the as-received material, but show significant increases in strength.

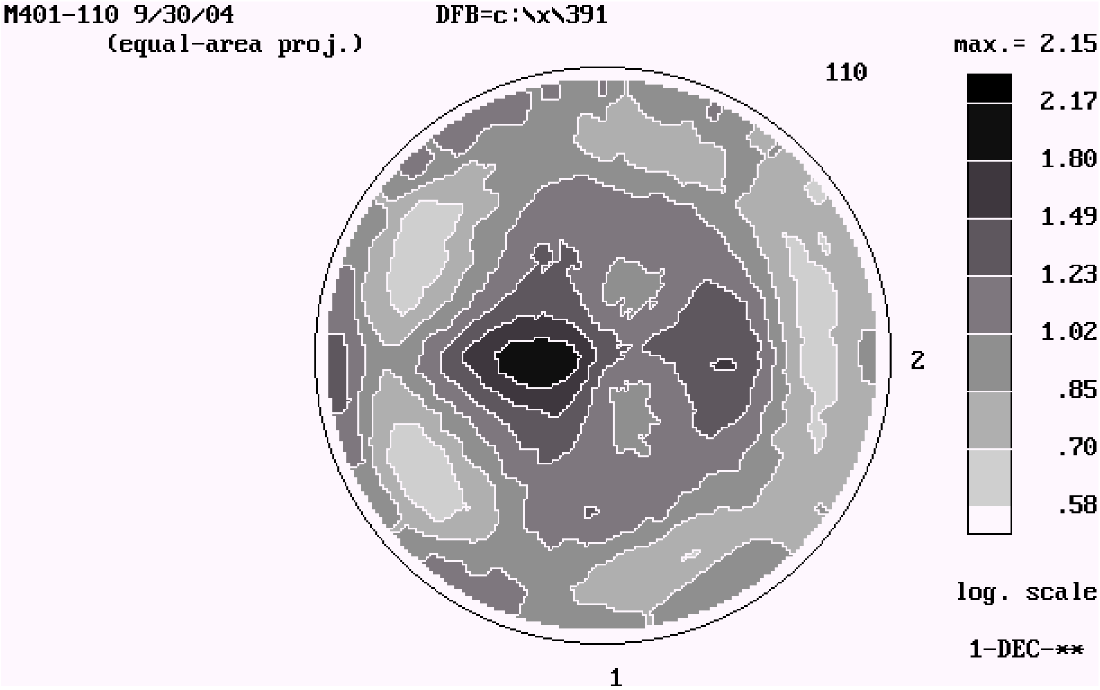

Figure 53: (110) Pole figure for ECAE 2C IF steel, direction 3 normal to plane of page

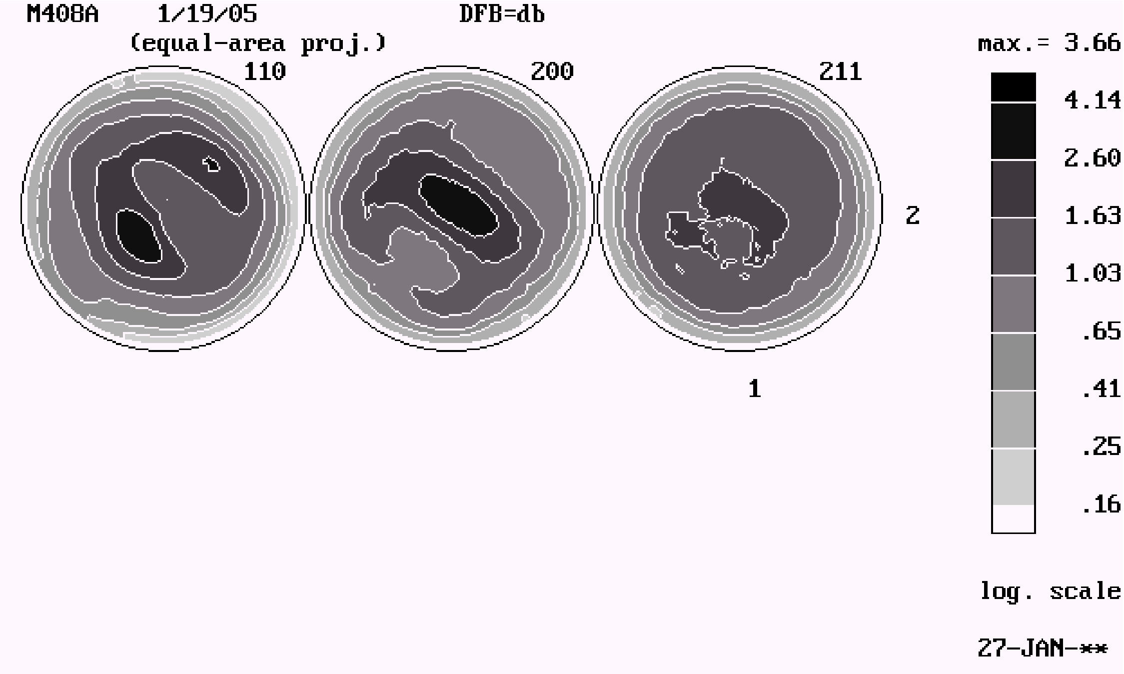

Figure 54: Pole figures for ECAE 4C IF steel (all orientations), direction 3 normal to plane of page

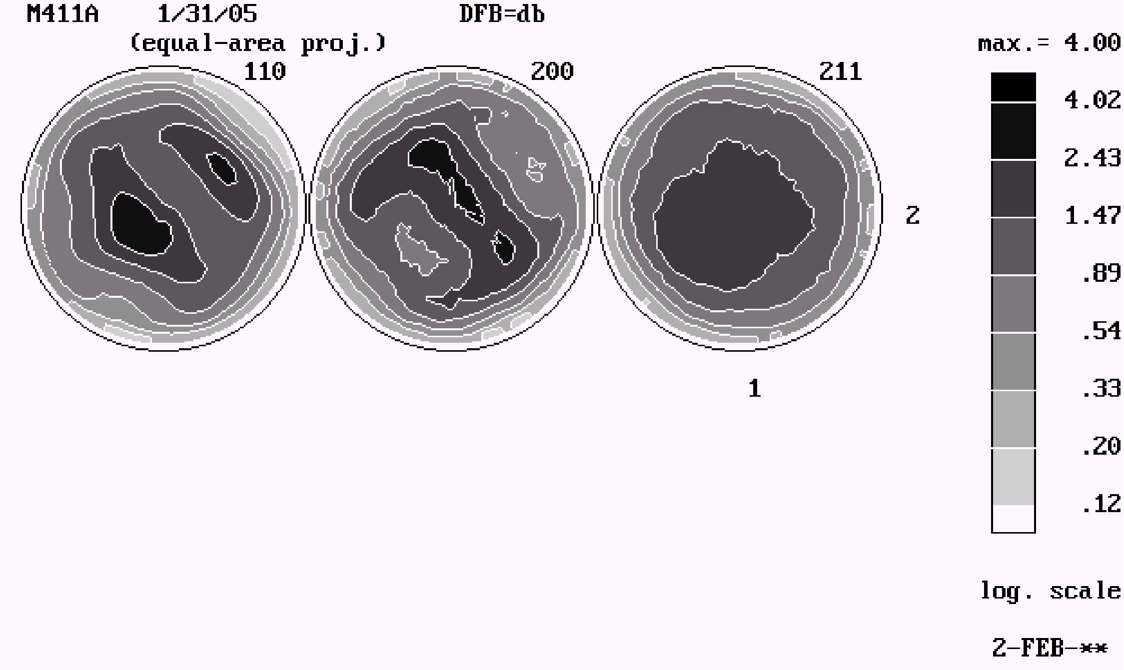

Figure 55: Pole figures for ECAE 8C IF steel (all orientations), direction 3 normal to plane of page

The pole figures for [200] (Figures 54 – 56) show two distinct regions of preferred texture in the case of ECAE 2C, as well as a decrease in the maximum recorded texture. The pole figures for ECAE 4C and ECAE 8C show a formation similar to that of the as-received material, and a strengthening of the recorded texture strength.

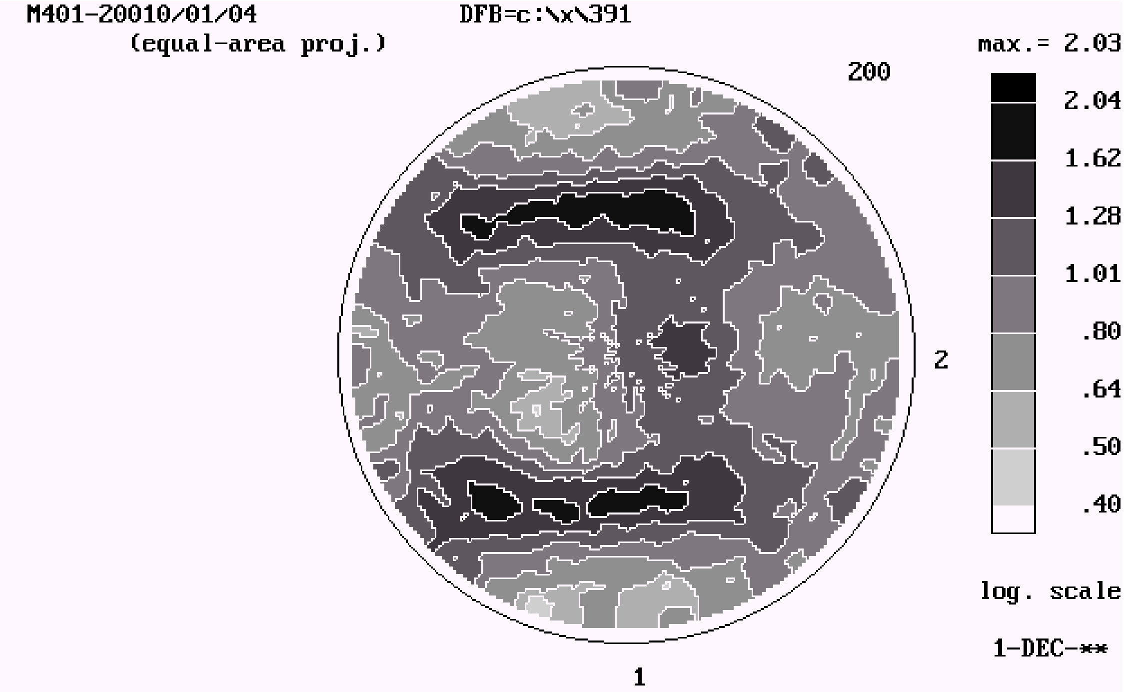

Figure 56: (200) Pole figure for ECAE 2C IF steel, direction 3 normal to plane of page

The [211] pole figures for Route C show a consistent trend in preferred texture growth and strengthening. The texture for ECAE 2C (Figure 57) is very similar to that of the as-received material and shows little strengthening. In the case of ECAE 4C (Figure 54), the texture has consolidated and strengthened, a behavior that is continued with the texture of ECAE 8C (Figure 55).

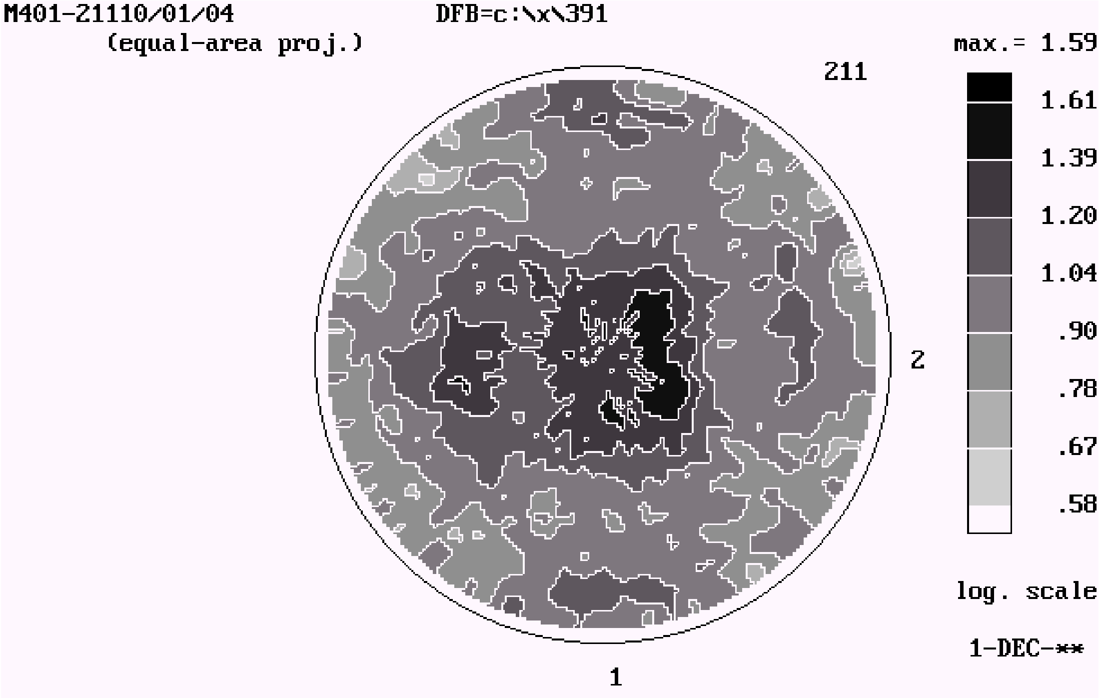

Figure 57: (211) Pole figure for ECAE 2C IF steel, direction 3 normal to plane of page

The inverse pole figures for Route C are shown in Figures 58 – 60. Preferred textures are apparent on the transverse plane in all cases to a varying degree. The strength of the preferred texture on the transverse plane in ECAE 2C is lower than that of the as-received material in general, and in particular around [001]. A single spot of preferred texture is observed on the longitudinal plane of ECAE 2C around [111] that is not found on any of the other specimens followed Route C. Strong preferred texture signatures are visible on the transverse planes of ECAE 4C and ECAE 8C around [111] and [001]. The strength of the preferred texture observed in ECAE 8C is not as great as that of ECAE 4C.

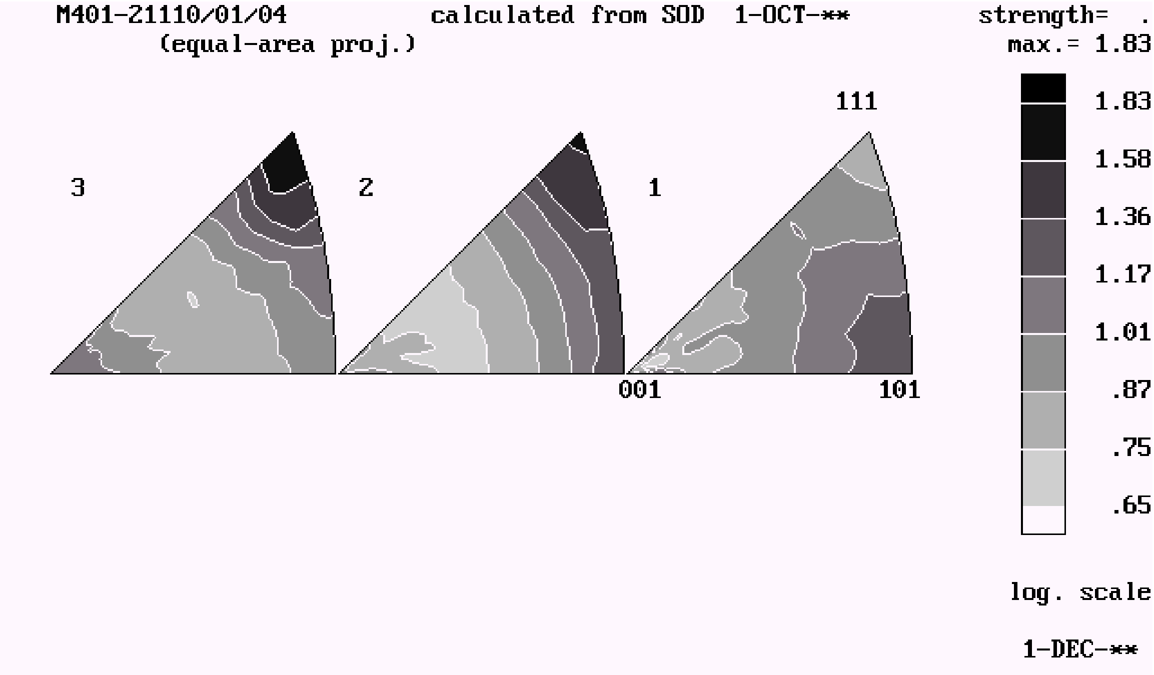

Figure 58: Inverse pole figures for ECAE 2C IF steel

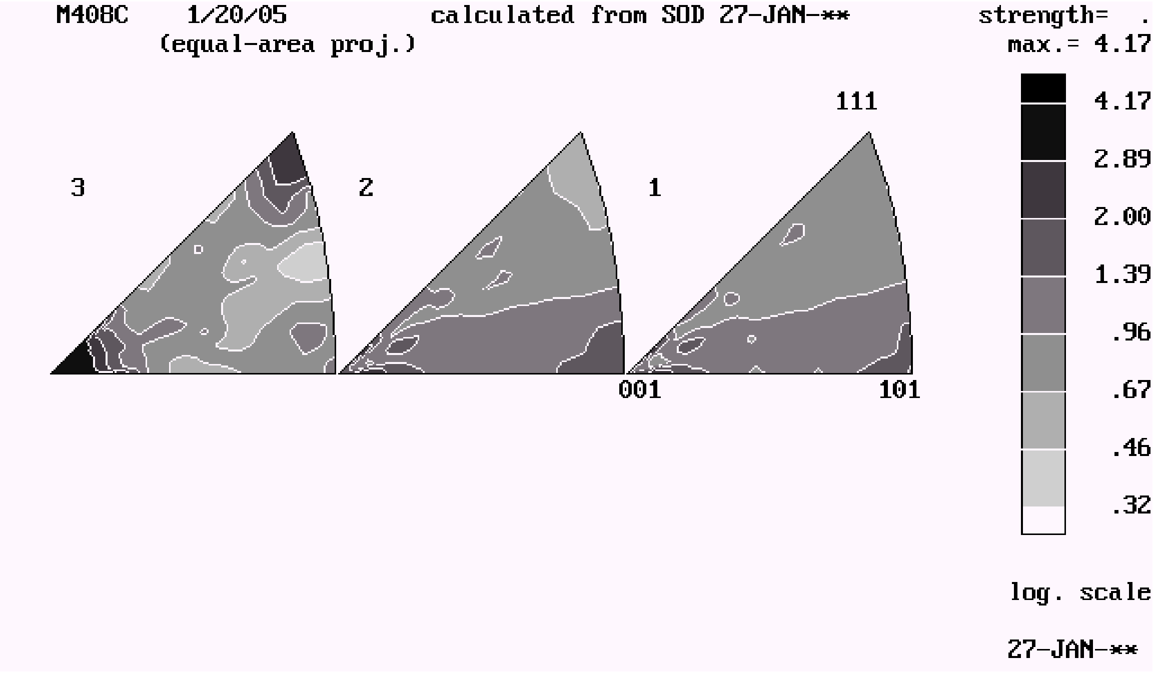

Figure 59: Inverse pole figures for ECAE 4C IF steel

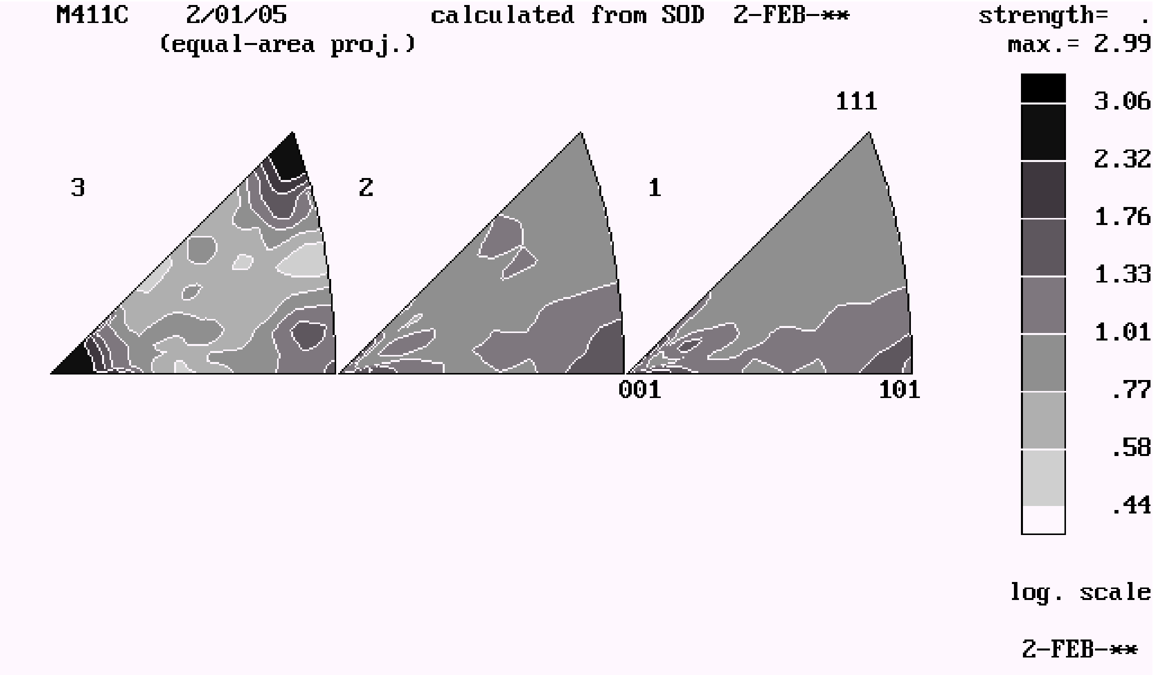

Figure 60: Inverse pole figures for ECAE 8C IF steel

Two samples, ECAE 4C’ and ECAE 8C’, were processed according to Route C’. According to this method of processing, after the initial pass the sample is rotated +90° for each additional pass.

The pole figures for Route C’ are shown in Figures 61 – 62. The [110] texture shows a 45° rotation from the as-received sample to the ECAE 4C’ and then ECAE 8C’ sample. The strength of the [110] texture shows a steady increase as the number of passes increases. For the texture of [200] there is no change in structure from as-received to ECAE 4C’ and ECAE 8C’, and the texture strength does not increase dramatically. The texture of [211] shows a great deal of consolidation and strengthening as the number of Route C’ passes increase from the as-received condition.

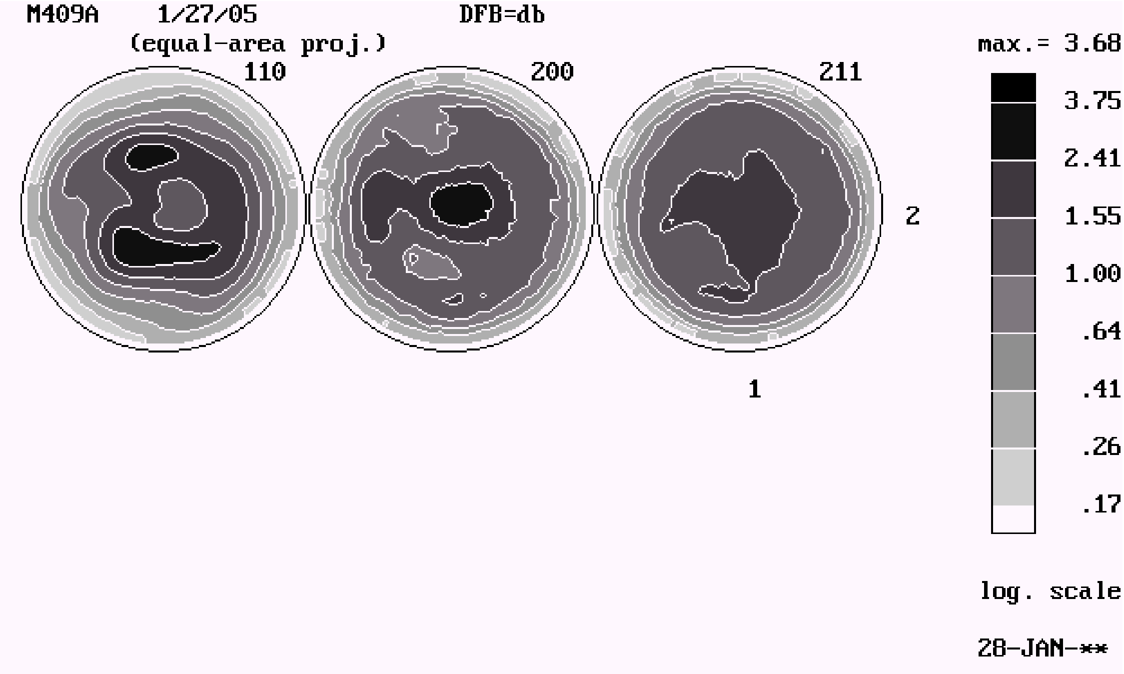

Figure 61: Pole figures for ECAE 4C' IF steel (all orientations), direction 3 normal to plane of page

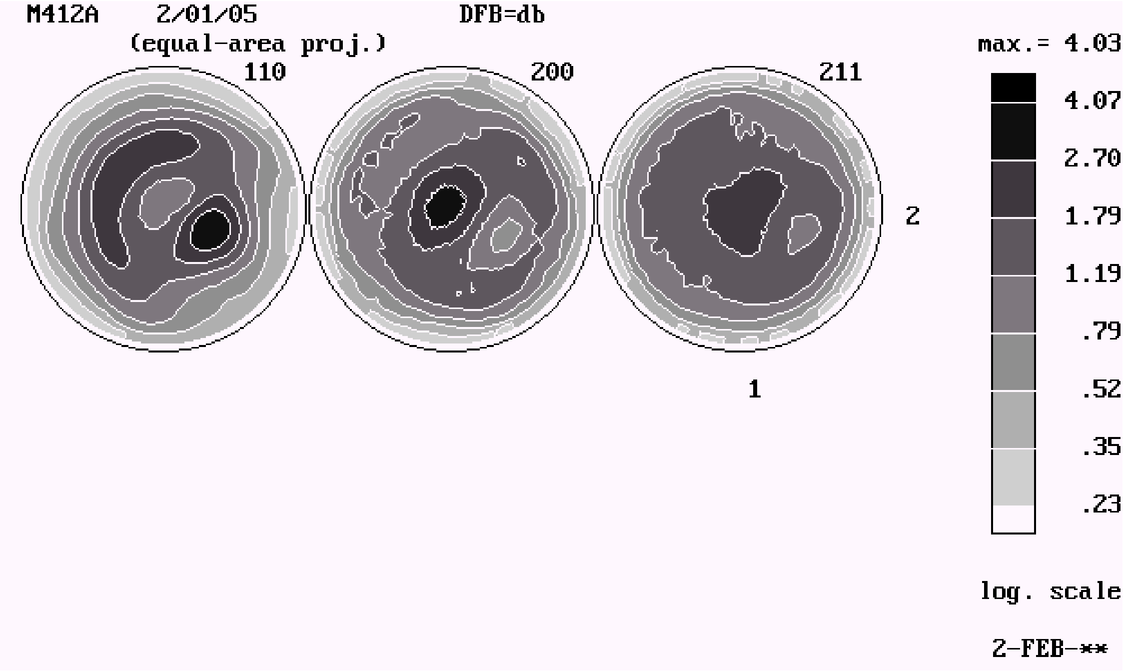

Figure 62: Pole figures for ECAE 8C' IF steel (all orientations), direction 3 normal to plane of page

The inverse pole figures for Route C' are shown in Figures 63 – 64. Texture strength on the transverse plane around [001] and [111] is significantly stronger in ECAE 4C' than ECAE 8C', though both are stronger than the as-received material. The flow plane and longitudinal plane do not show a great deal of strengthening, although the regions around [001] and [101] seem to be developing a preferred texture.

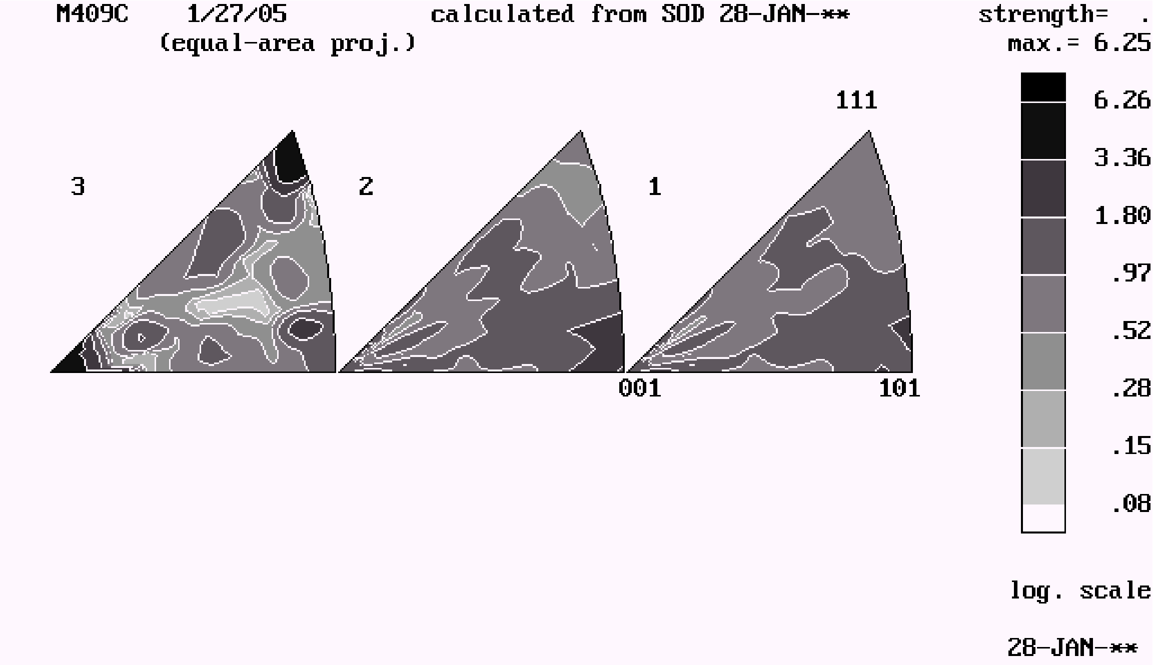

Figure 63: Inverse pole figures for ECAE 4C' IF steel

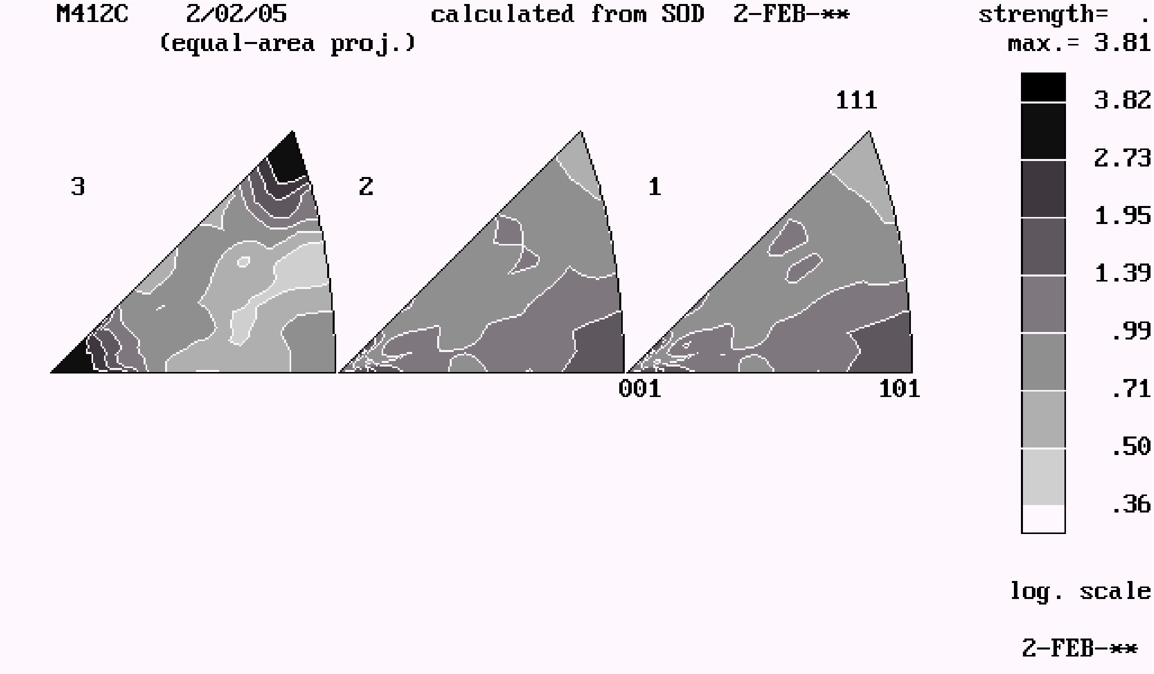

Figure 64: Inverse pole figures for ECAE 8C' IF steel

The pole figures for Route E are shown in Figures 65 – 67. Three samples, ECAE 4E, ECAE 8E and ECAE 16E, were processed using Route E. The processing of Route E involves rotating the billet +180° after the initial pass and for the even-numbered passes, then -90° for the odd-numbered passes.

The pole figures for Route E [110] show little change in orientation from one specimen to the next, and all of the samples using this processing route have a stronger preferred texture when compared to the as-received sample. The highest recorded preferred texture was observed in ECAE 8E, with the other two samples being somewhat weaker, but of similar value to each other.

Examination of the texture of [200] shows no major changes in texture orientation from one sample to the next. There appears to be a general consolidation and strengthening in texture as the number of passes increase.

In the case of [211] the texture undergoes a noticeable evolution and strengthening beginning with ECAE 4E and ending with ECAE 16E. A somewhat diffuse preferred texture can be observed in ECAE 4E, which develops and strengthens into ECAE 8E. The texture for ECAE 16E shows a large area of preferred texture, as well as a surrounding zone of strong texture.

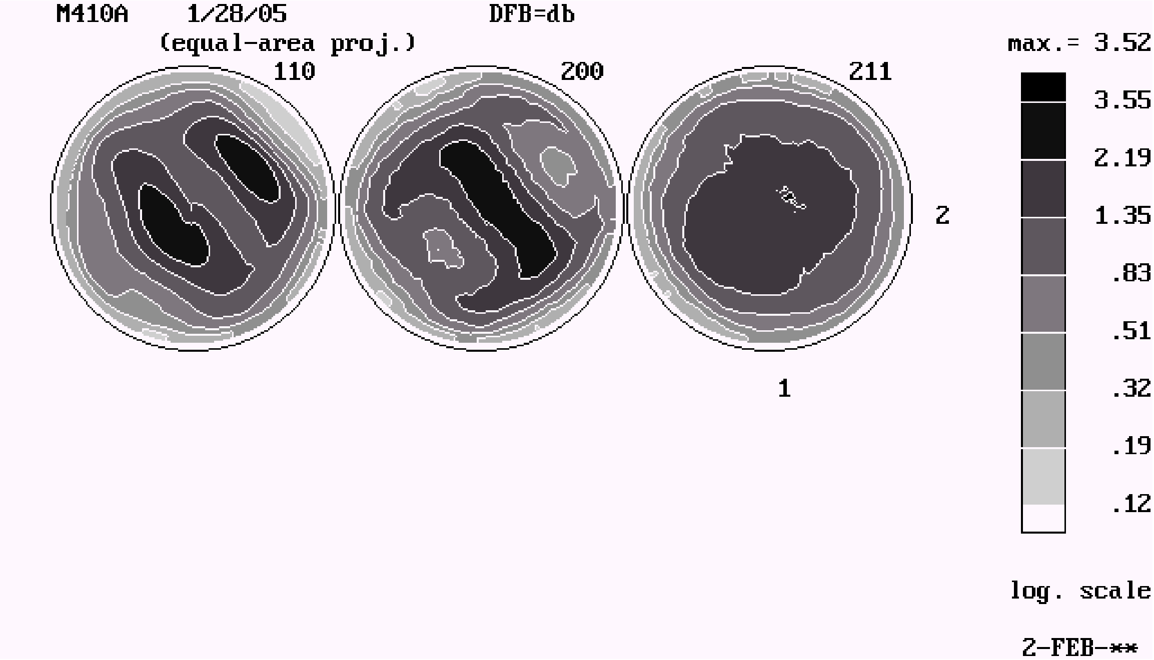

Figure 65: Pole figure for ECAE 4E IF steel (all orientations), direction 3 normal to plane of page

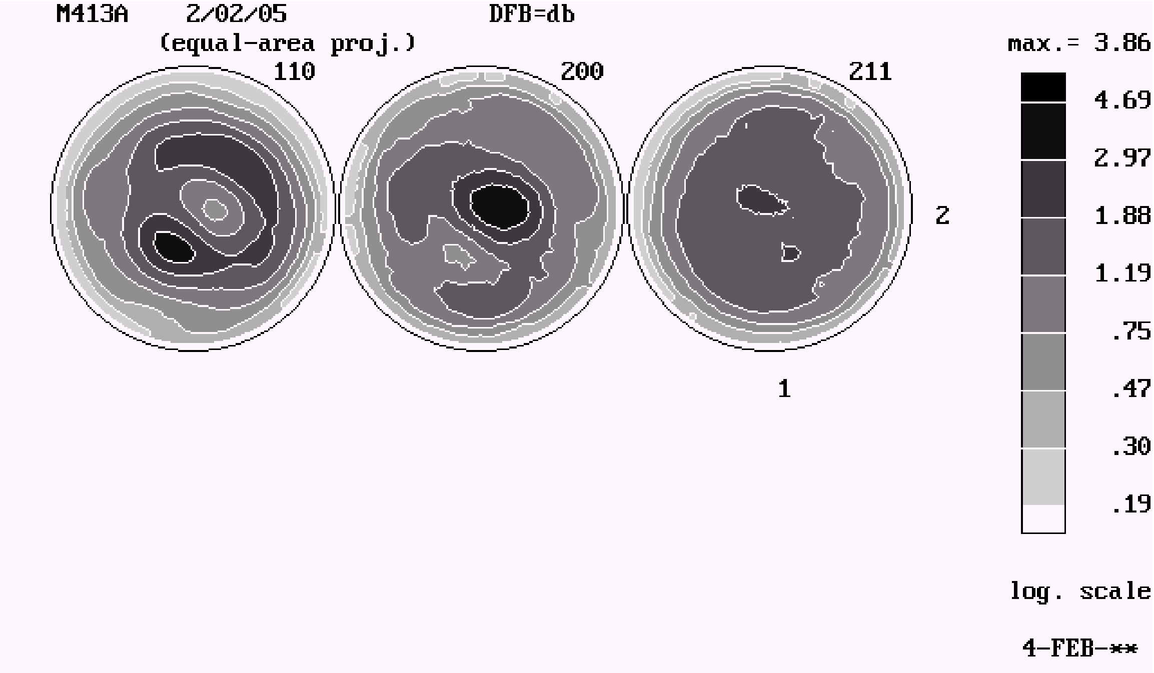

Figure 66: Pole figures for ECAE 8E IF steel (all orientations), direction 3 normal to plane of page

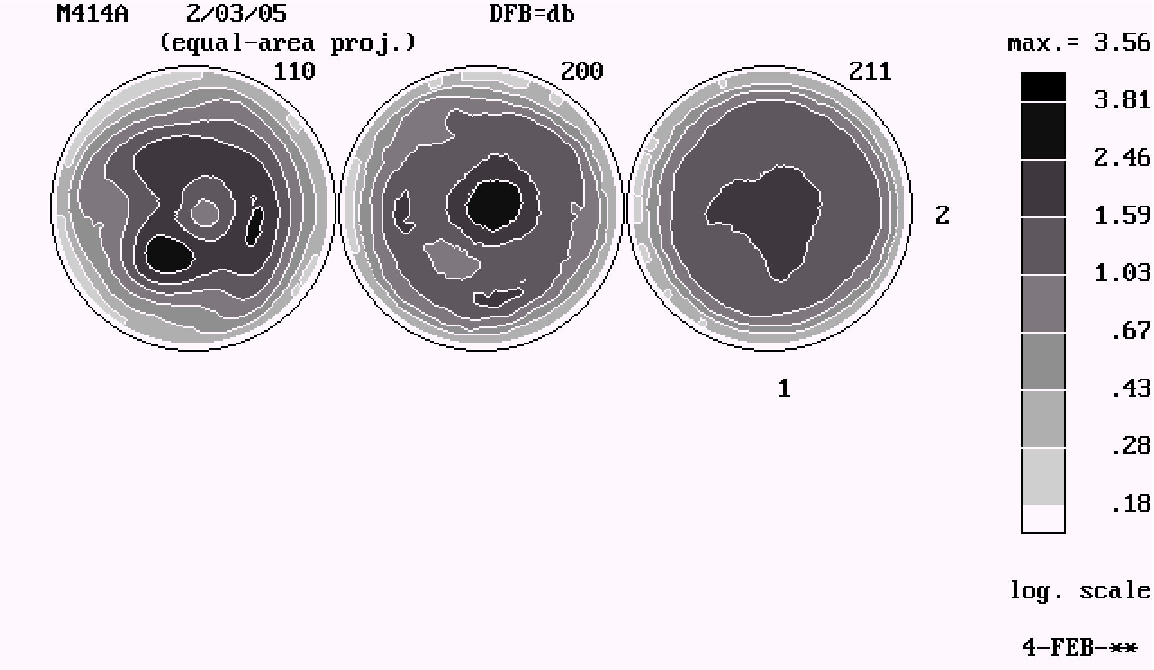

Figure 67: Pole figures for ECAE 16E IF steel (all orientations), direction 3 normal to plane of page

The inverse pole figures for Route E are presented in Figures 68 – 70. Strong preferred textures exist on the transverse plane around [001] and [111], with the strongest textures belonging to ECAE 8E, then ECAE 16E and finally ECAE 4E. Some degree of texture formation may be observed on both the flow and longitudinal planes around [001] and [101], though these textures do not display the strength or concentration as those seen on the transverse plane.

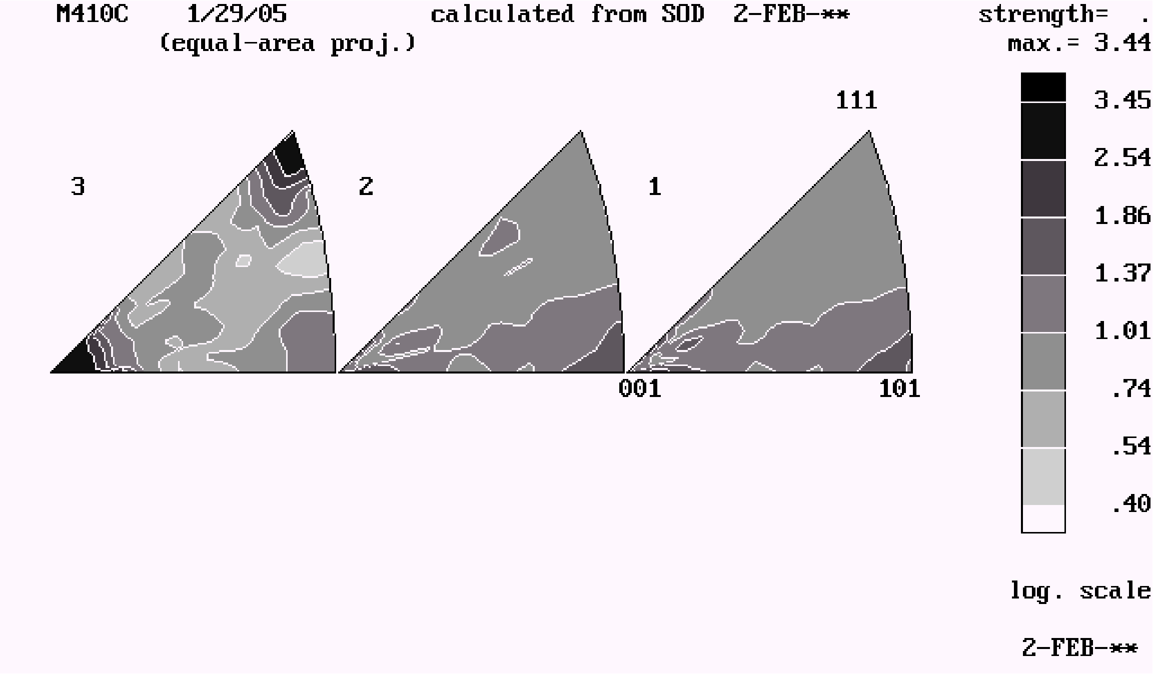

Figure 68: Inverse pole figures for ECAE 4E IF steel

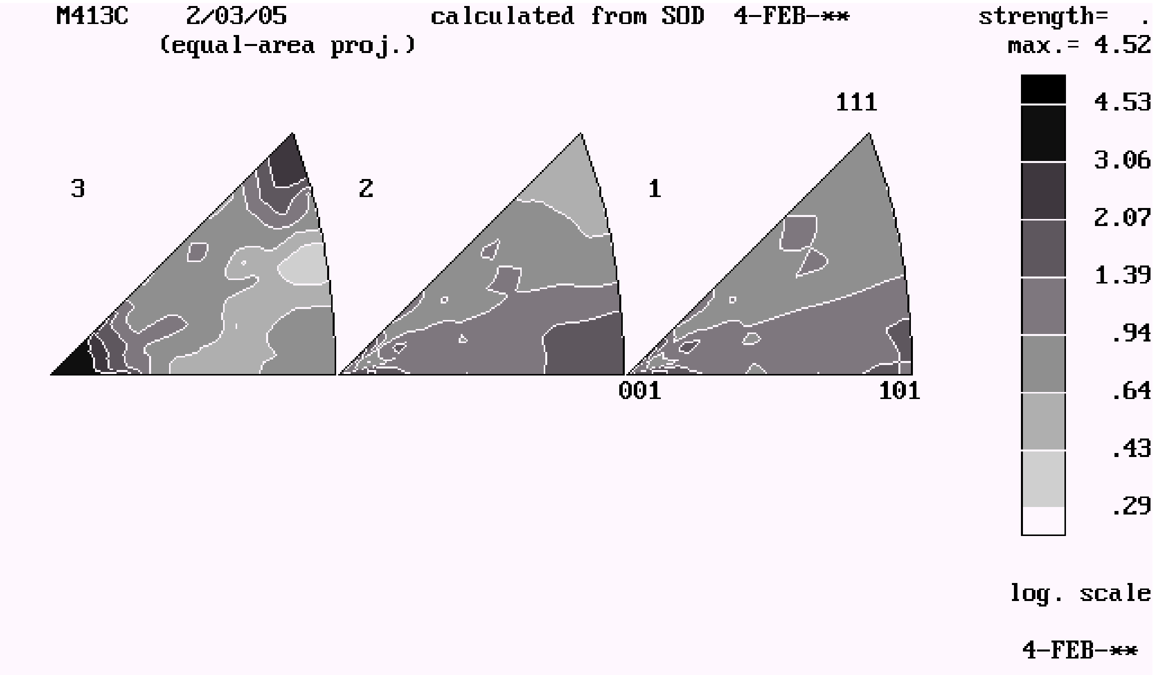

Figure 69: Inverse pole figures for ECAE 8E IF steel

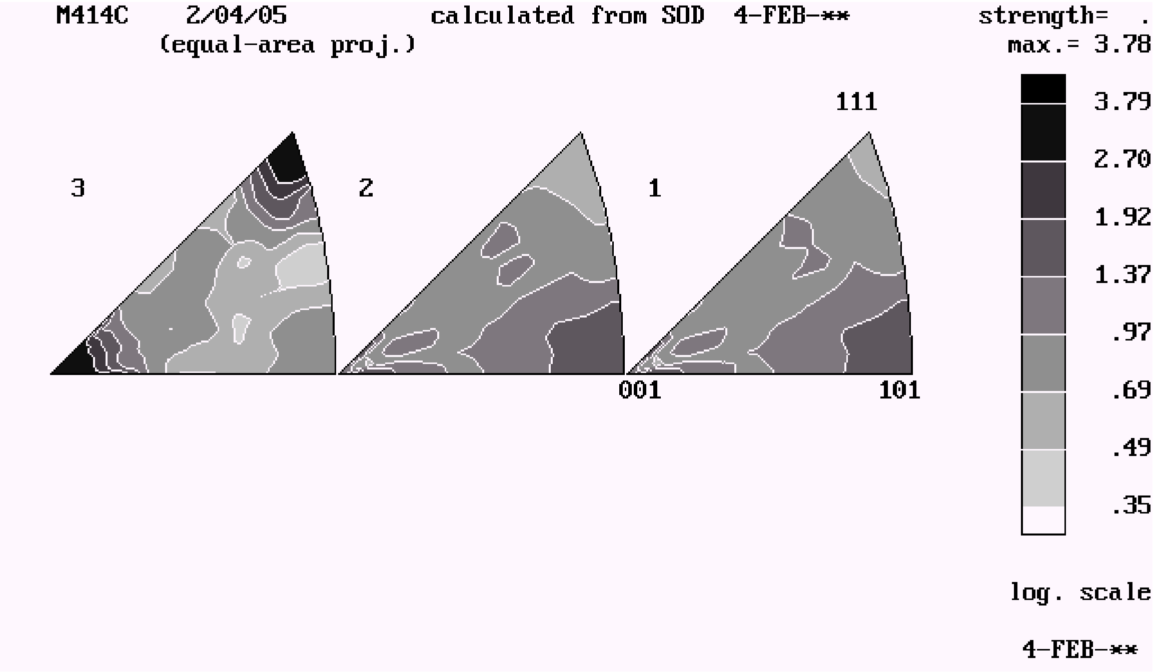

Figure 70: Inverse pole figures for ECAE 16E IF steel

In summary, the texture data indicates ECAE processing of IF steel produces strong texture in the [111] and [001] directions on the transverse plane.

4.4. Electron Microscopy

The use of transmission electron microscopy makes possible an examination of the internal structure of the materials used in this study. Thin foils of the different bulk samples are prepared by first grinding and then electropolishing the material. Foil thickness is dictated by the amount of energy the incoming electrons possess. Thin foils from each sample used in this study were evaluated using transmission electron microscopy.

Electron microscope images of the as-received IF steel are presented in Figures 71 – 72. The grain size in the as-received material is so large that the TEM could not observe a whole grain, even at the lowest magnification. At intermediate magnification (Figure 72) it was possible to observe dislocations in the as-received material. Some features which resemble “dark spots” may be artifacts from sample preparation, carbide precipitates, or some dislocation phenomenon. Such features deserve further study.

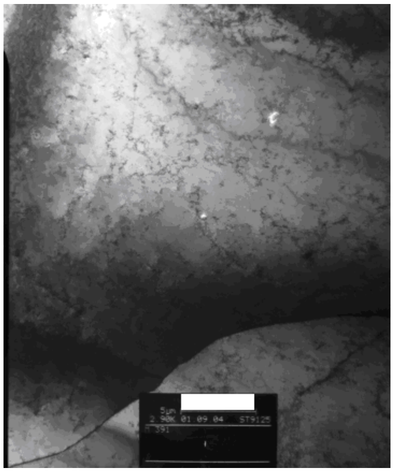

Figure 71: Low magnification TEM image of as-received IF steel (white bar = 5 µm)

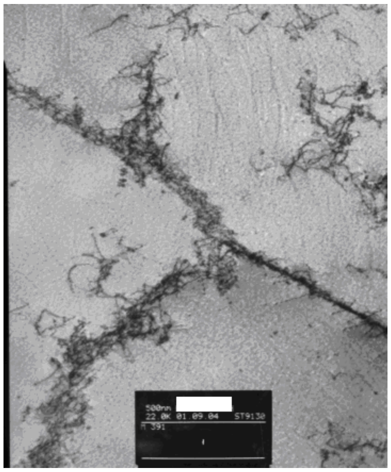

Figure 72: Medium magnification TEM image of as-received IF steel showing dislocations (white bar = 500 nm)

Electron micrographs of ECAE 1A IF steel are shown in Figures 73 – 76. At low magnification (Figure 73) an elongated subgrain structure, the result of ECAE processing, is clearly visible. The subgrain size is on the order of 500 nm.

An electron micrograph from another region of the sample (Figure 74) with slightly higher magnification shows similar elongated subgrains. The significant change in contrast show large misorientation between the regions that may correspond to microshear banding. In each region, further contrast change is visible, which is an indication of small misorientation. This small misorientation between the regions, on the order of a few hundred nm in size, corresponds to subgrain or cell formation in each microshear banding.

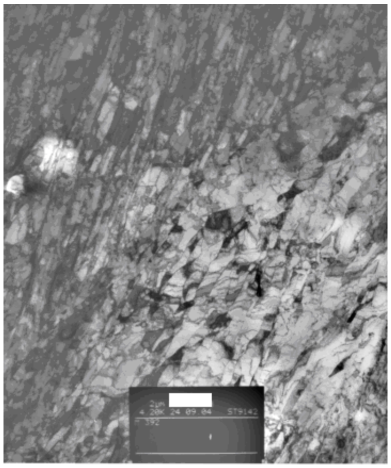

Figure 73: Low magnification TEM image of ECAE 1A IF steel (white bar = 2 μm)

Figure 74: Low magnification TEM dark field image of ECAE 1A IF steel (black bar = 1 μm)

Structures within the zones of high dislocation density begin to appear as the magnification is increased (Figure 75). These appear as speckles or “spots” within the dark, high dislocation density zones in the electron micrographs, and are visible inside the circled region of Figure 75.

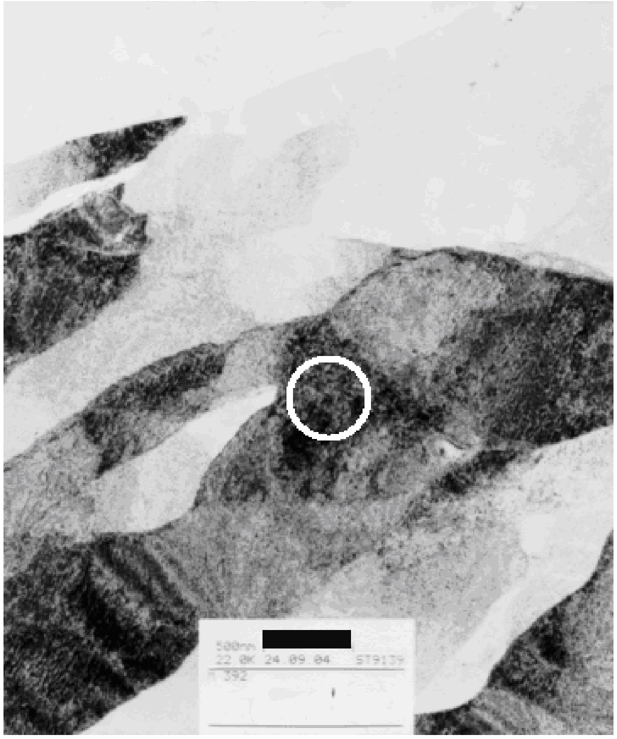

Figure 75: TEM dark field image of high dislocation density zones within ECAE 1A IF steel (black bar = 500 nm). Circled region contains “dark spots”

At even higher magnification within the zone of high dislocation density the “spots” are clearly visible (Figure 76) and well defined. These spots may be associated with very small carbides or interstitial-vacancy pairs which form upon dislocation annihilation [3].

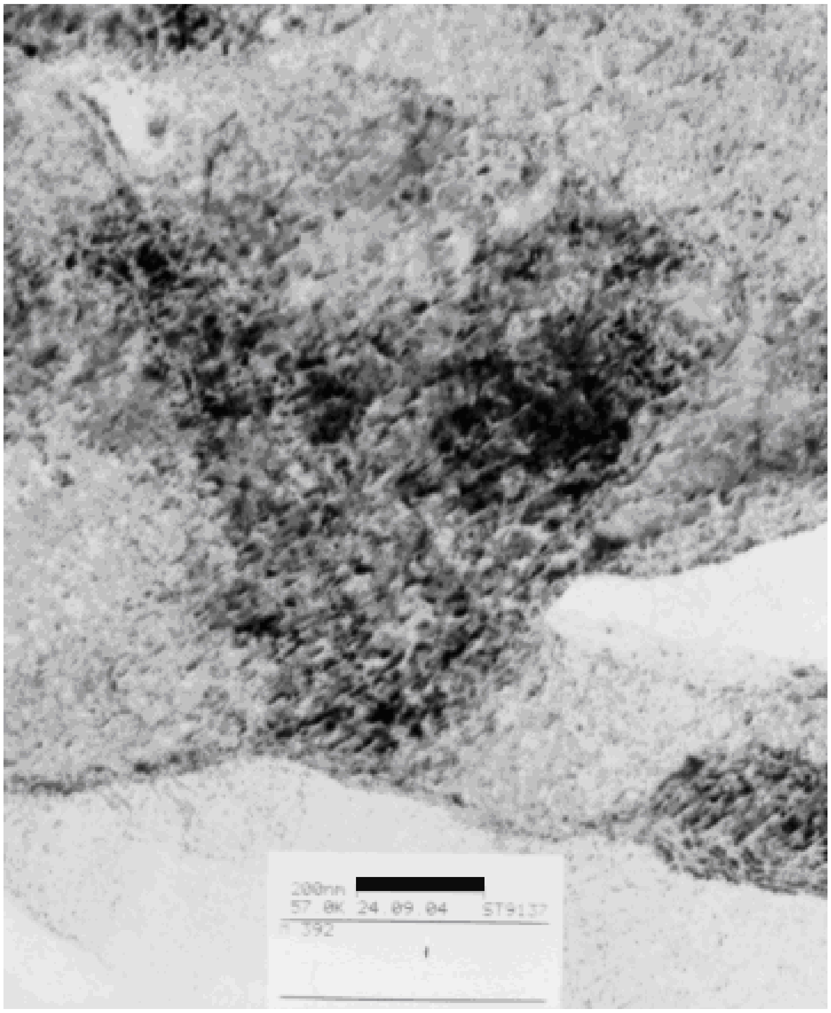

Figure 76: High magnification TEM dark field image of “dark spots” in ECAE 1A (black bar = 200 nm)

Transmission electron microscopy images of ECAE 2A sample material is presented in Figures 77 – 78. At low magnifications the grain structure appears elongated and homogenous.

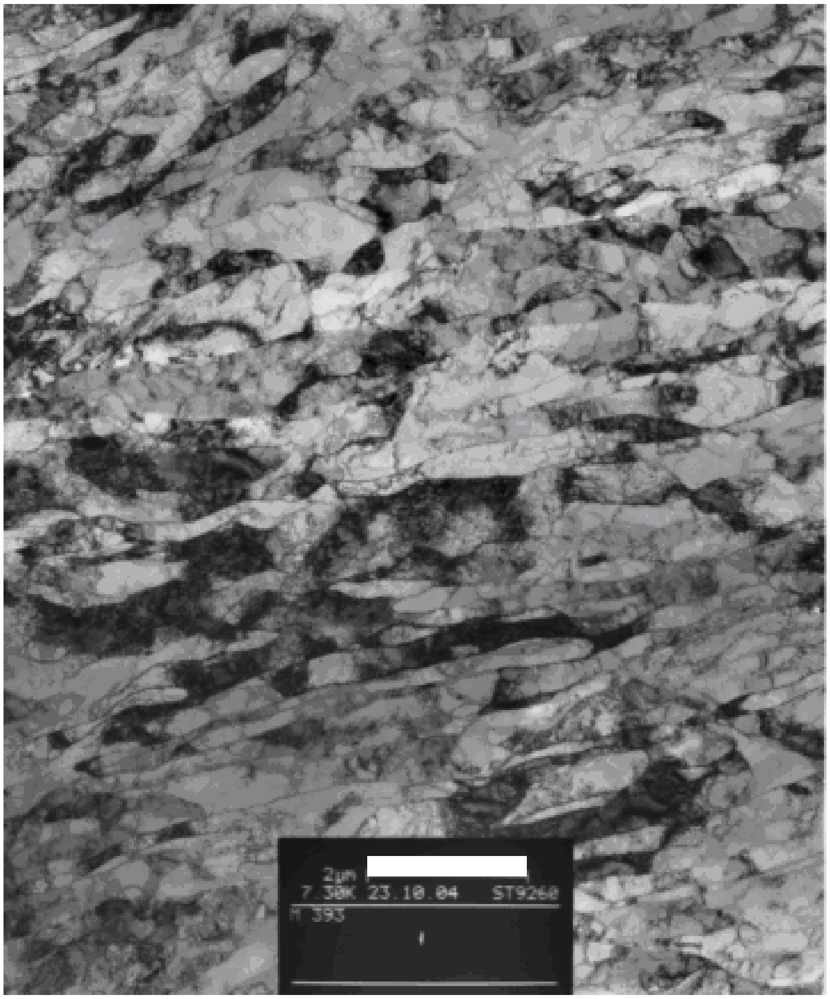

Figure 77: Low magnification TEM image of ECAE 2A IF steel (white bar = 2 µm)

At higher magnifications (Figure 78) it is possible to observe the grains that show moderate dislocation densities and distinguish individual dislocations. It can be seen in the image that dislocations have formed walls and occasional dislocation cells. Grains with lower dislocation density appear lighter in color, while darker grains have a higher dislocation density.

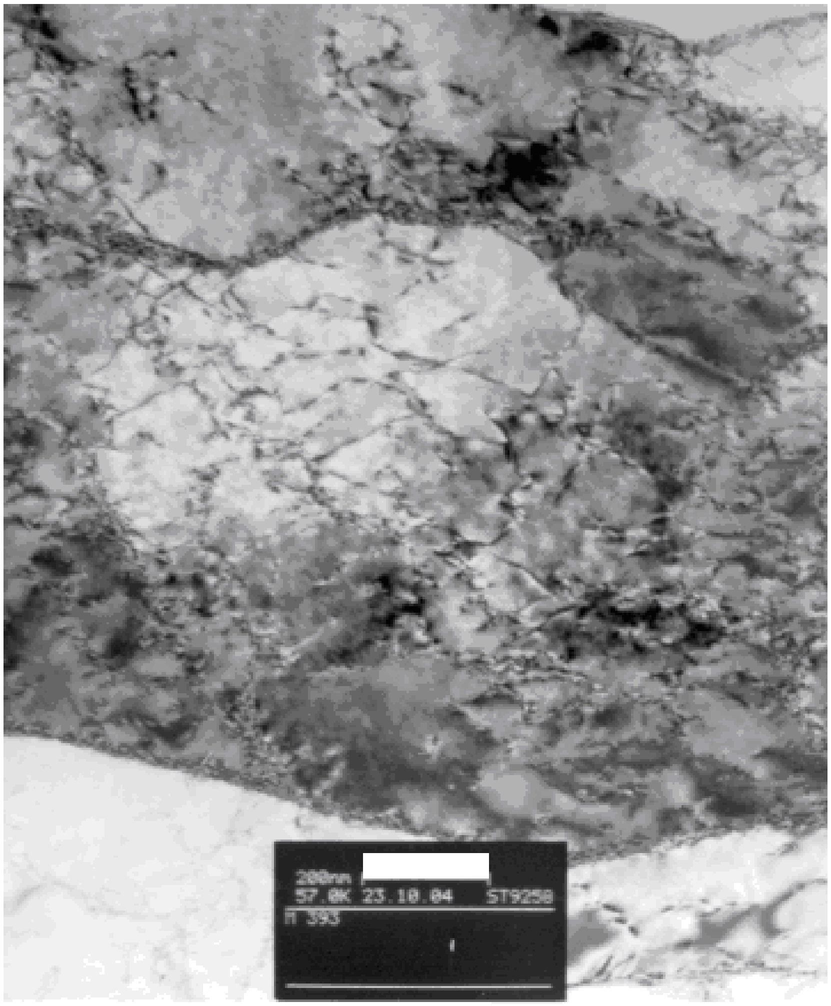

Figure 78: High magnification TEM image of ECAE 2A IF steel (white bar = 200 nm)

Transmission electron micrographs of ECAE 2B sample are shown in Figures 79 – 80. The subgrain structure (Figure 79) is homogeneous and elongated at a low magnification. The low quality of the image is partly caused by the very low magnification.

Figure 79: Low magnification TEM image of ECAE 2B IF steel (white bar = 2 μm)

At very high magnifications it is possible to observe individual dislocations within the subgrains (Figure 80). On the left side of the image is a small cluster of the “dark spots.”

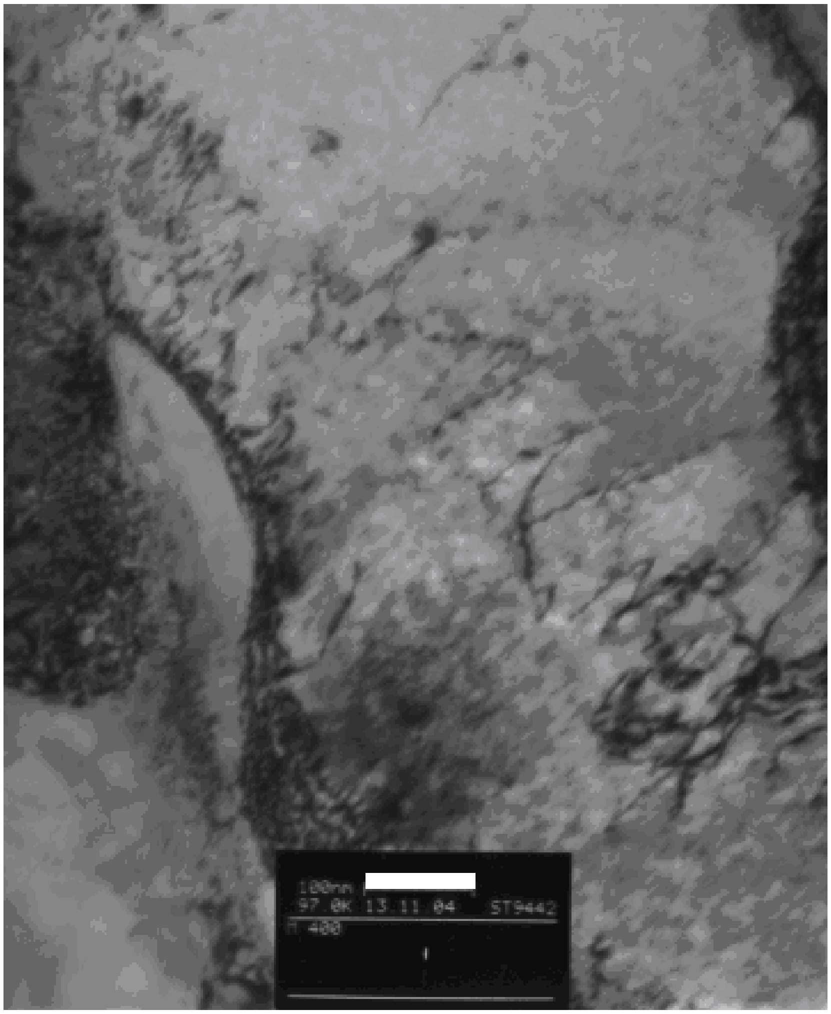

Figure 80: High magnification TEM image of ECAE 2B IF steel (white bar = 100 nm)

Electron micrographs of IF steel processed under ECAE 2C are shown in Figures 81 – 82. At very low magnification the image quality is not optimal, but it is still possible to observe homogenous, elongated subgrains in the foil. The aspect ratio of the subgrains are considerably lower than the 2A and 2B cases. The 2C case is expected to result in equiaxed structures, but it is obvious from the image, and from other Route C and E cases, that the last pass is always the decisive step in final subgrain morphology.

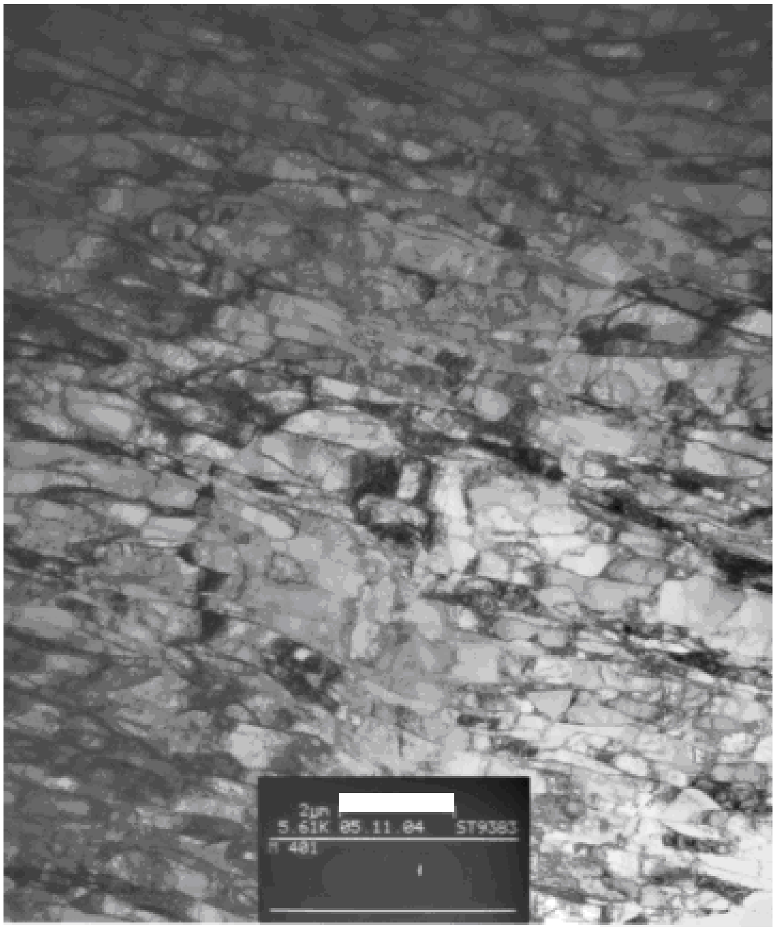

Figure 81: Low magnification TEM image of ECAE 2C IF steel (white bar = 2 µm)

At very high magnification (Figure 82) it is possible to observe the subgrain/cell boundaries, as well as individual dislocations within the subgrains. Subgrain/cell interiors are relatively free of dislocations. The visible refinement is significant.

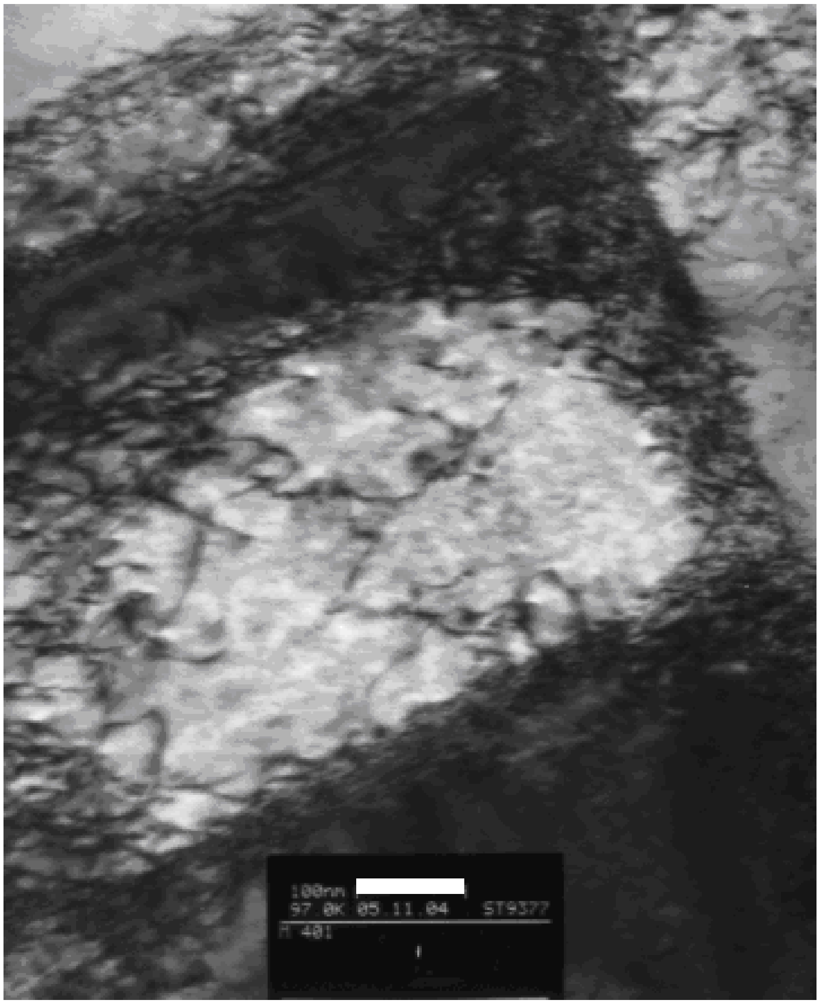

Figure 82: High magnification TEM image of ECAE 2C IF steel (white bar = 100 nm)

Transmission electron microscope images of ECAE 4A IF steel is presented in Figures 83 – 85. A very low magnification micrograph is shown in Figure 83. At such a low magnification the geometry of the foil has a negative impact on image quality. The grains show significant elongation.

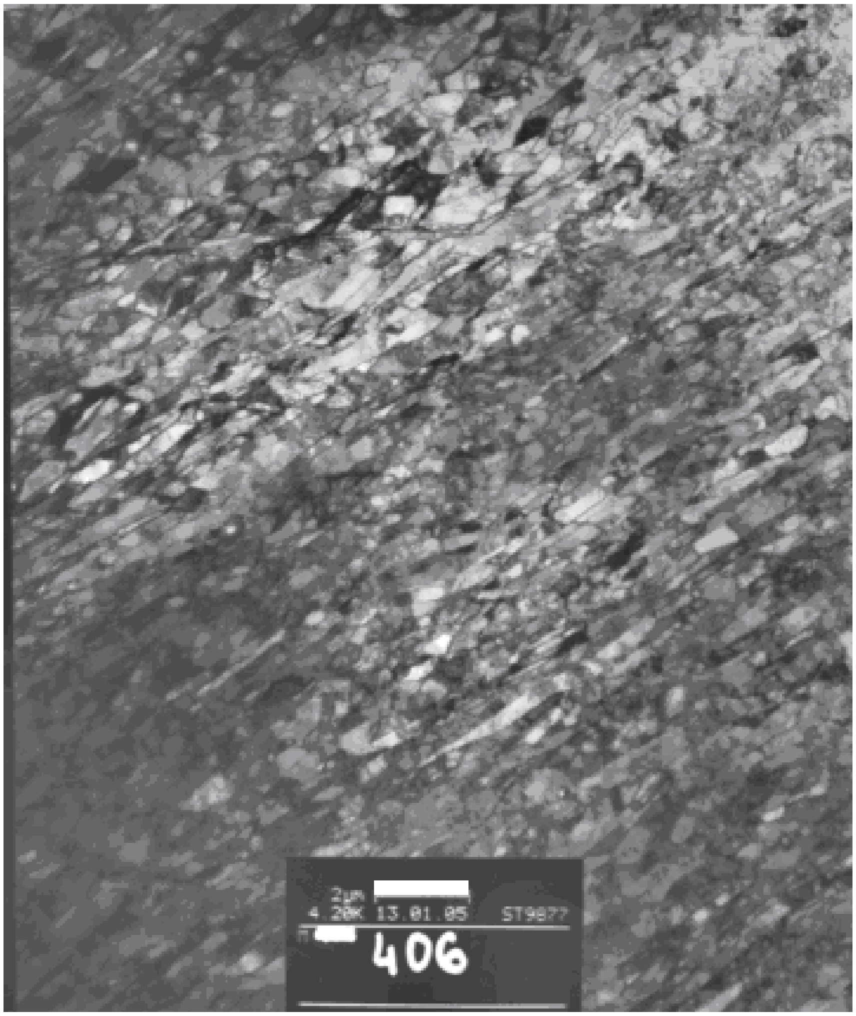

Figure 83: Low magnification TEM image of ECAE 4A IF steel (white bar = 2 µm)

Another region of the foil was examined at slightly higher magnification. This low magnification image (Figure 84) shows an elongated microstructure and somewhat improved image quality. Subgrains seem to be developed further as compared to two pass cases, with more distinguishable subgrain boundaries and clearer interiors.

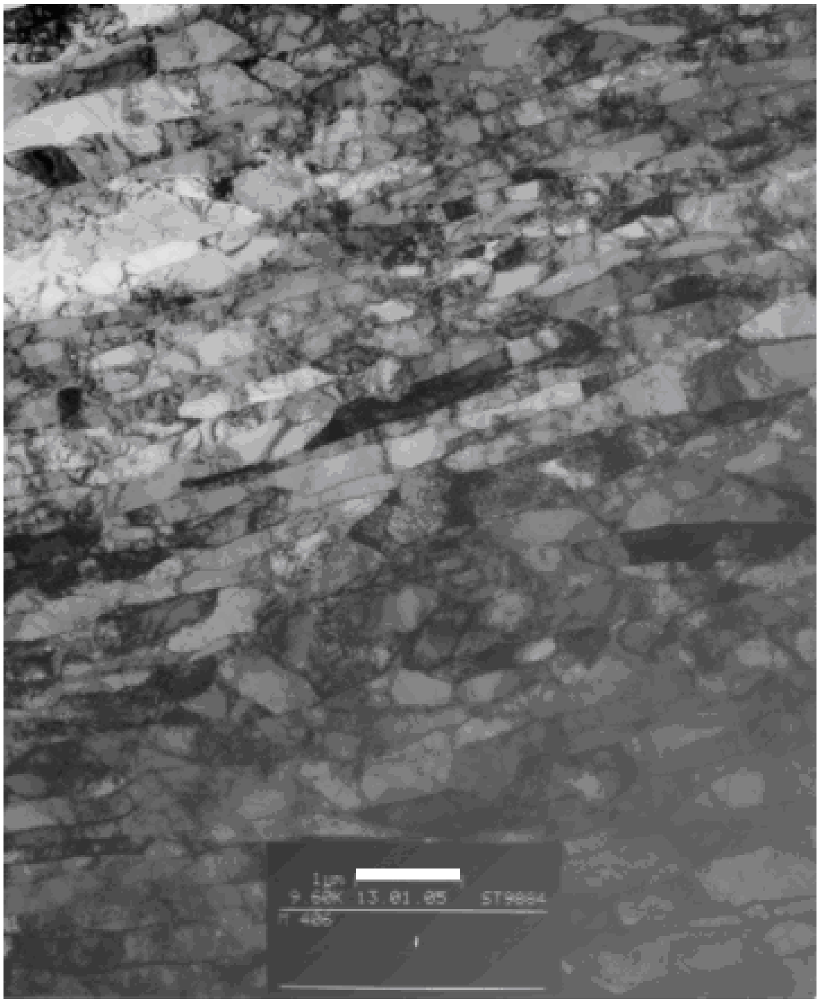

Figure 84: Low magnification TEM image of ECAE 4A IF steel (white bar = 1 µm)

At intermediate magnification, individual cells and the dislocations within them become visible. The TEM micrograph of Figure 85 clearly shows high dislocation density cell walls.

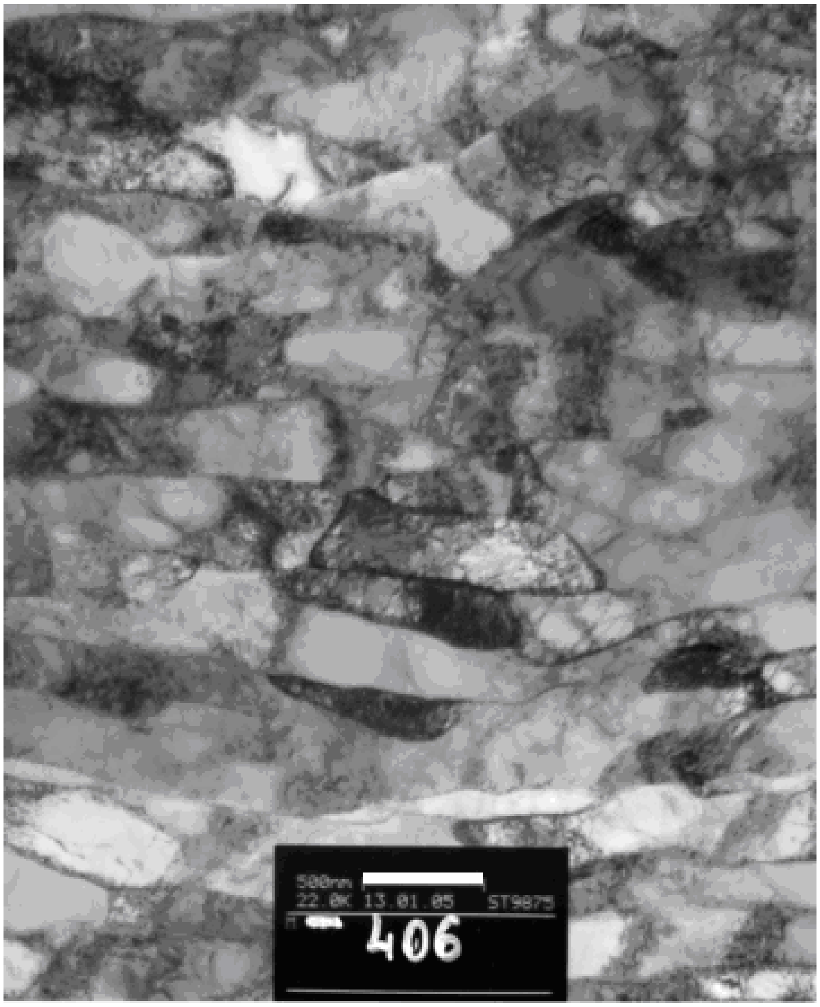

Figure 85: Intermediate magnification TEM image of ECAE 4A IF steel (white bar = 500 nm)

A high magnification TEM micrograph from the elongated cell structures of the ECAE 4A foil is presented in Figure 86. Many dislocations are visible and the cell walls are more distinguishable.

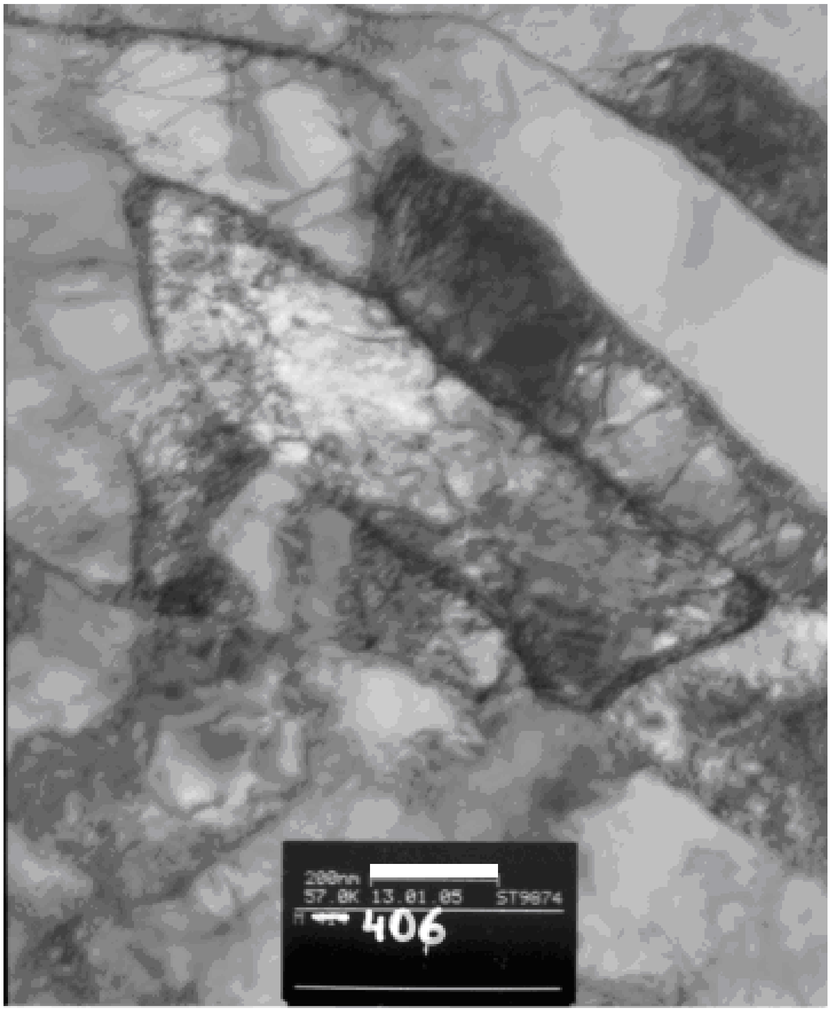

Figure 86: High magnification TEM image of ECAE 4A IF steel (white bar = 200 nm)

Transmission electron microscope images from a sample obtained from ECAE 4B processed IF steel are presented in Figures 87 – 89. At very low magnifications (Figure 87) the image is not of the highest quality. The image shows grains that are not very homogeneous, with some grains being elongated, and others equiaxial in nature. As compared to previous cases, the further microstructural refinement is evident, which is a consequence of cross-shearing between the passes.

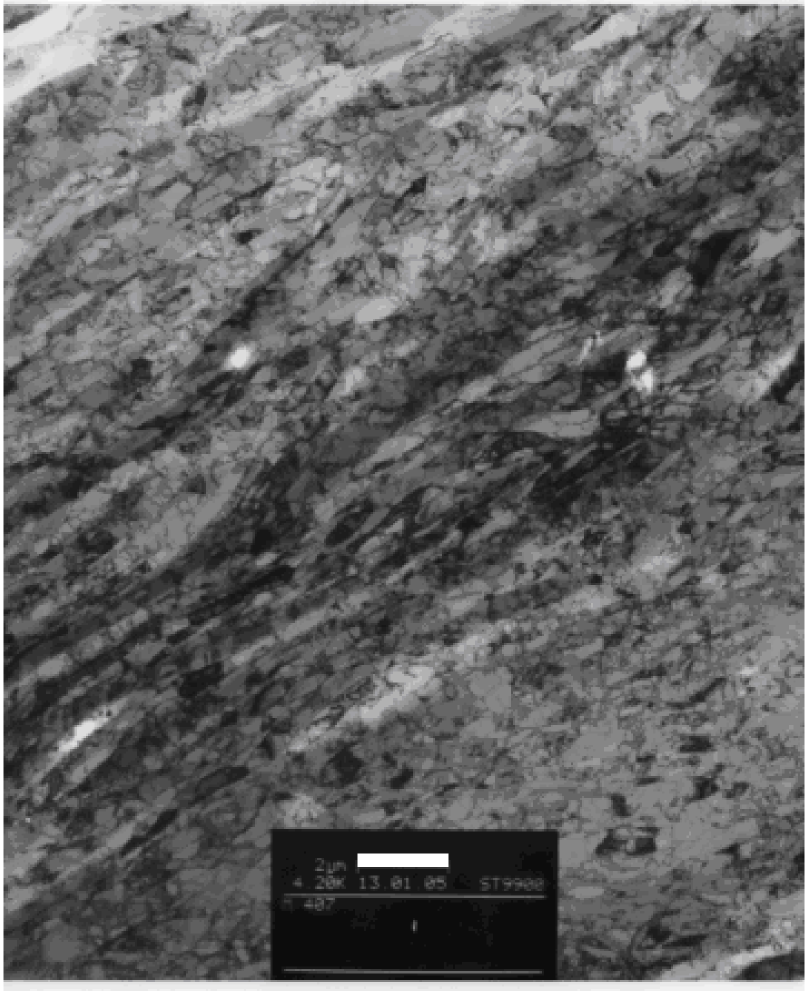

Figure 87: Low magnification TEM image of ECAE 4B IF steel (white bar = 2 µm)

At intermediate magnification within the region of equiaxed grains a high dislocation density is observed (Figure 88). The structure is no longer elongated.

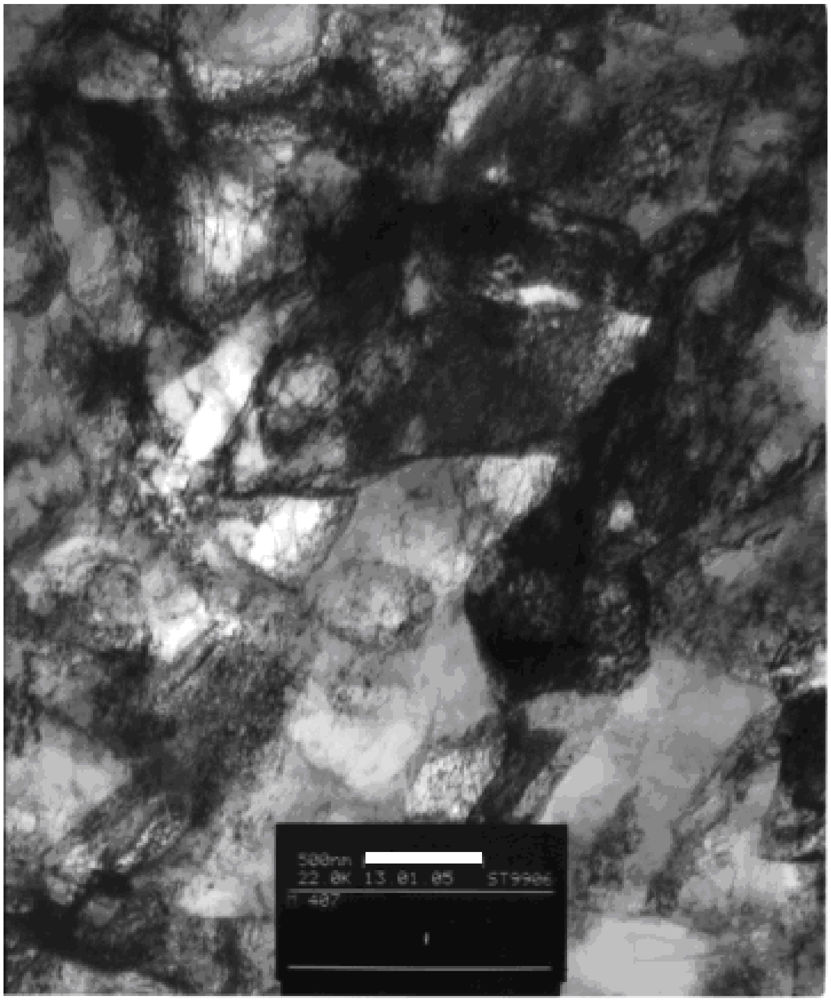

Figure 88: Intermediate magnification TEM image of ECAE 4B IF steel (white bar = 500 nm)

At very high magnifications (Figure 89) it is possible to observe individual dislocations. Dislocation buildups are visible on the left-hand side of the image near the subgrain boundaries. Increasing the magnification is problematic because of the natural magnetic properties of IF steel, which act as a sort of weak lens and interfere with the resolution of the electron microscope.

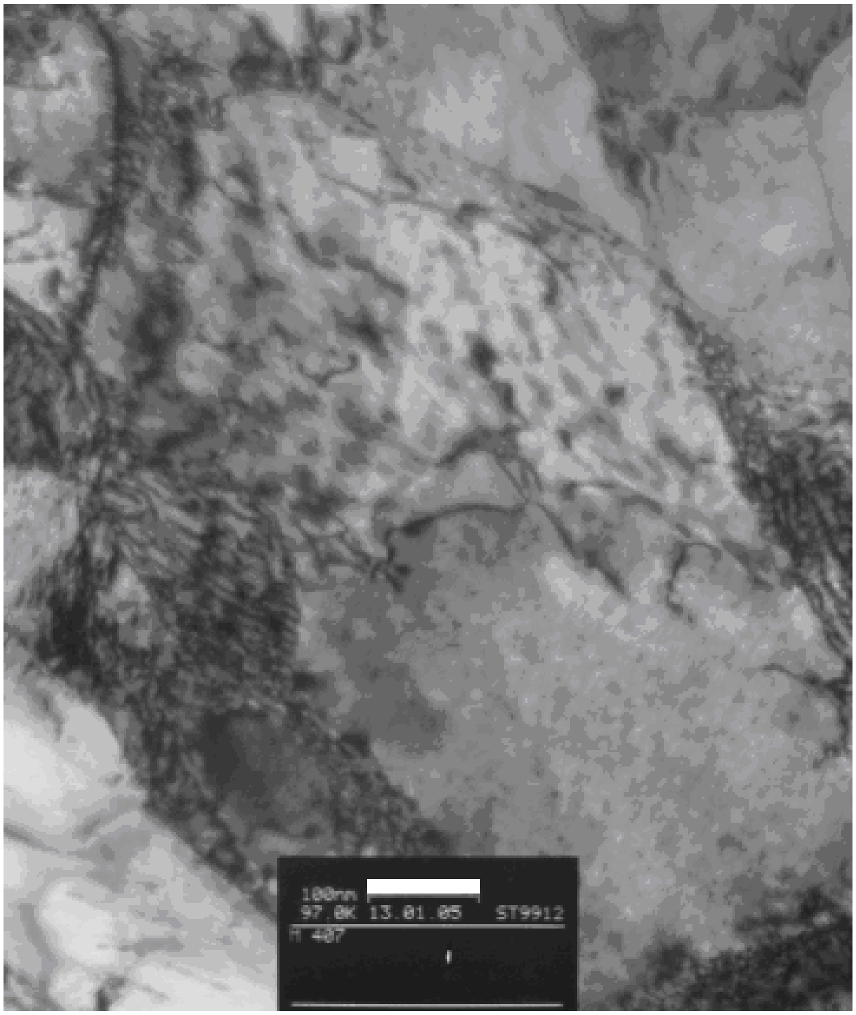

Figure 89: High magnification TEM image of ECAE 4B IF steel (white bar = 100 nm)

Electron micrographs for IF steel processed using ECAE 4C are presented in Figures 90 – 91. At relatively low magnification (Figure 90), the structure of ECAE 4C consists of mixed shapes. There is long band of large, equiaxed cells just below the center of the image. The region is bordered by zones of high dislocation density. There are indications of the formation of subgrains/grains, as shown in the image.

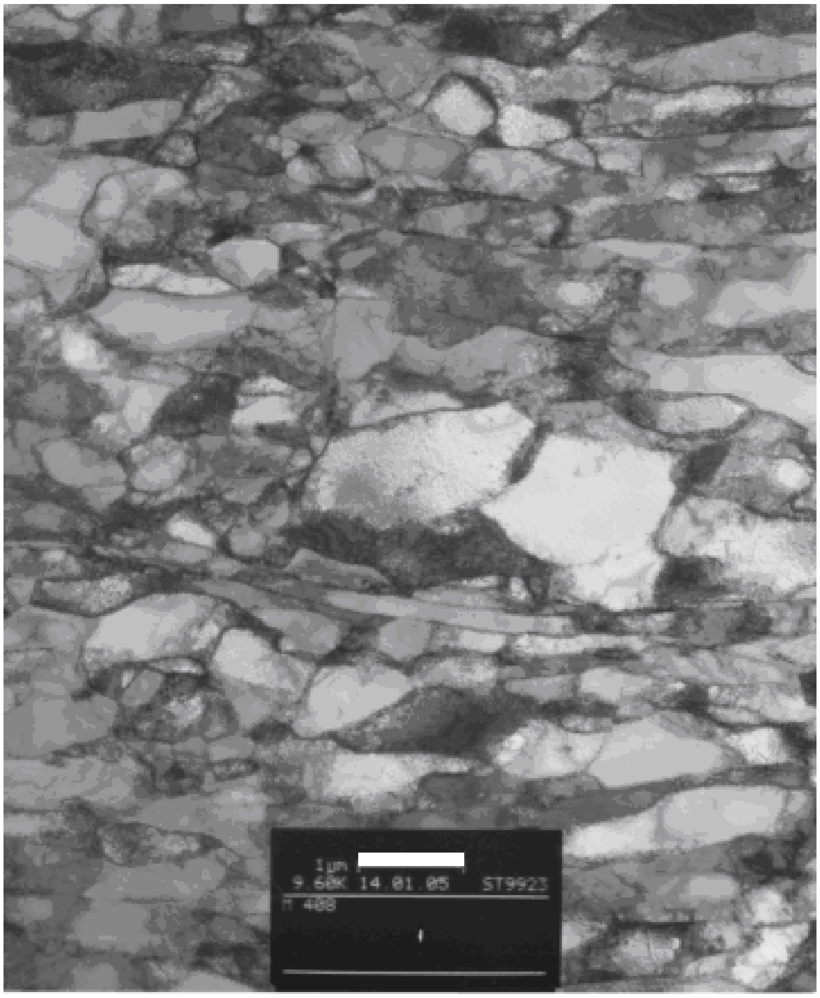

Figure 90: Low magnification TEM image of ECAE 4C IF steel (white bar = 1 µm)

At high magnifications (Figure 91) it is possible to observe the distribution of dislocation densities in a localized area. Some cells do not clearly show dislocations because they are out of contrast in the image. Rotating the sample reveals the dislocations.

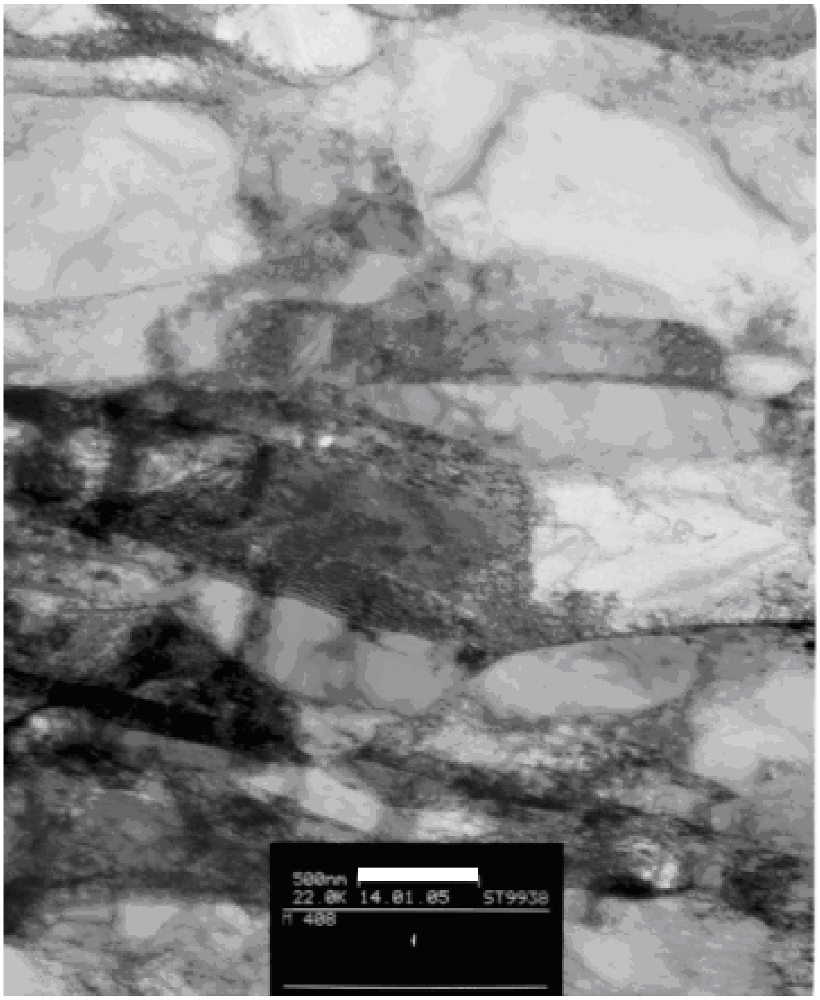

Figure 91: High magnification TEM image of ECAE 4C IF steel (white bar = 500 nm)

Electron micrographs of IF steel processed using ECAE 4E are presented in Figures 92 – 93. At low magnification (Figure 92) the grains appear equiaxial as expected, with little tilt between them.

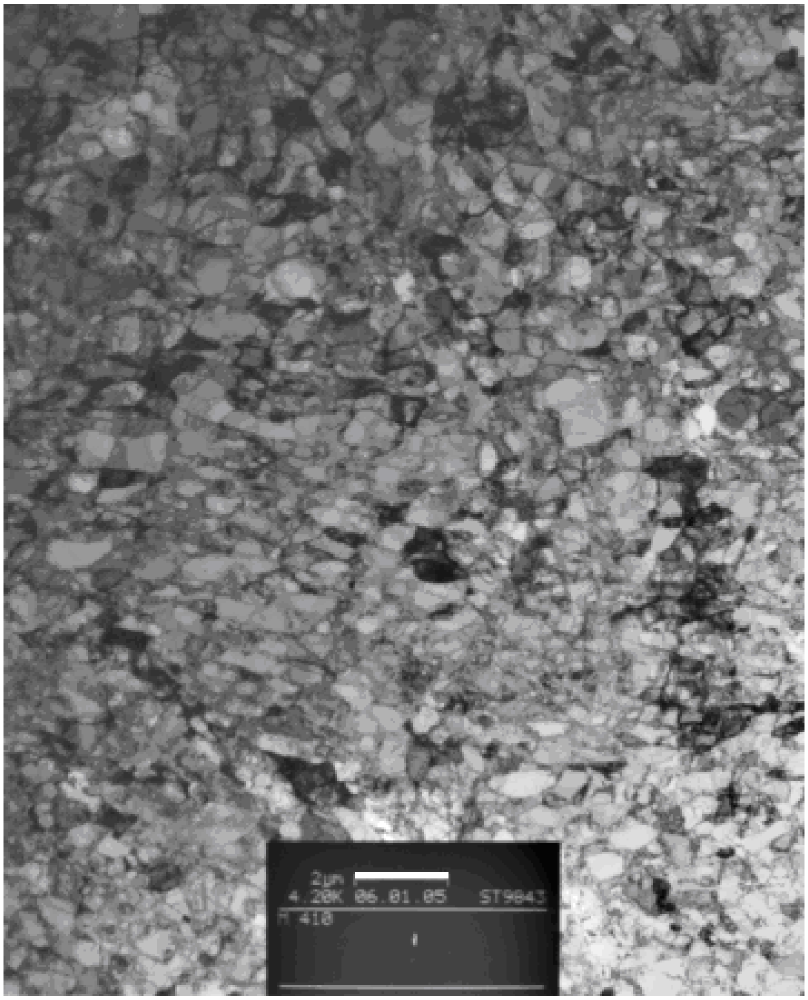

Figure 92: Low magnification TEM image of ECAE 4E IF steel (white bar = 2 μm)

At high magnification (Figure 93) it is possible to observe individual cells and dislocations. The central area of the image shows an area with dislocation cell walls that are not well defined.

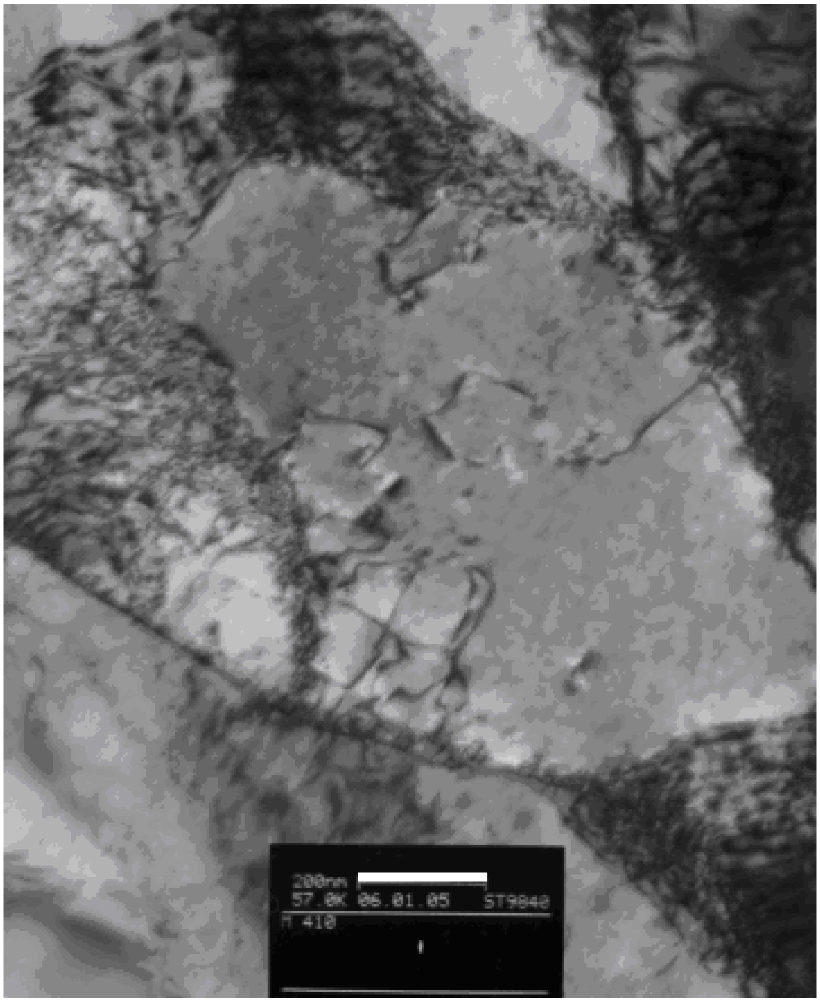

Figure 93: High magnification TEM image of ECAE 4E IF steel (white bar = 200 nm)

Transmission electron micrographs from IF steel samples processed using ECAE 8E are shown in Figures 94 – 96. At very low magnifications (Figure 94) there is a large amount of homogeneity visible with clear refinement as compared to two and four pass cases.

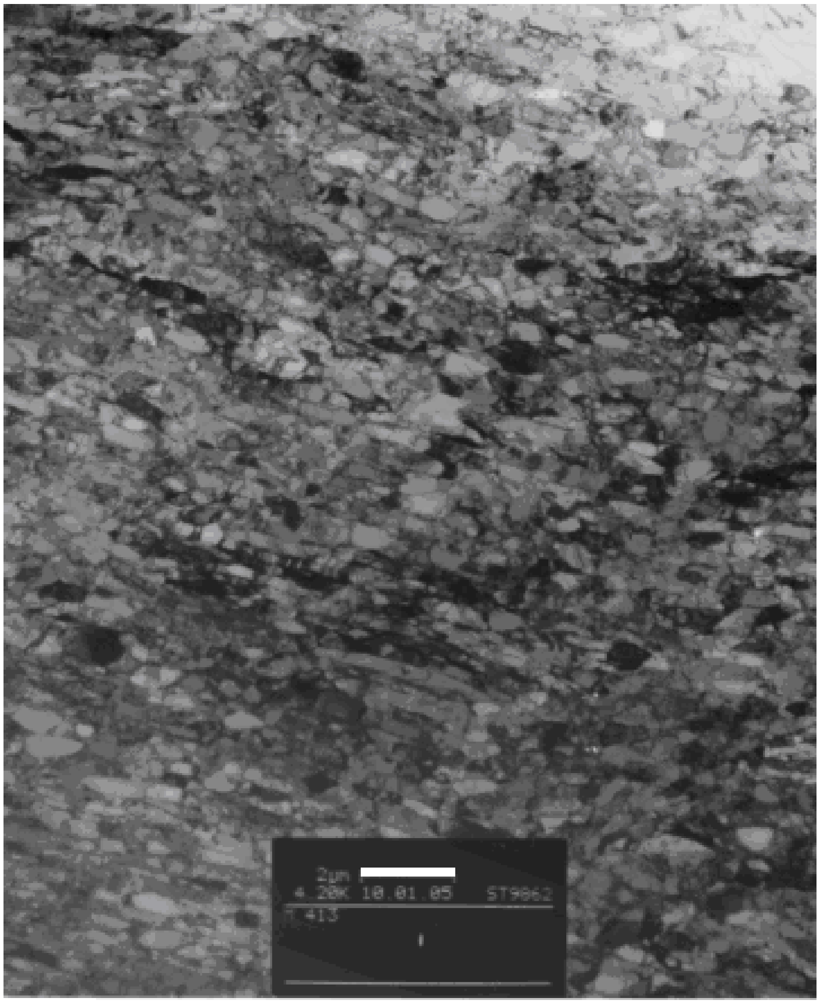

Figure 94: Low magnification TEM image of ECAE 8E IF steel (white bar = 2 μm)

At intermediate magnifications (Figure 95) it is possible to see well defined subgrain boundaries.

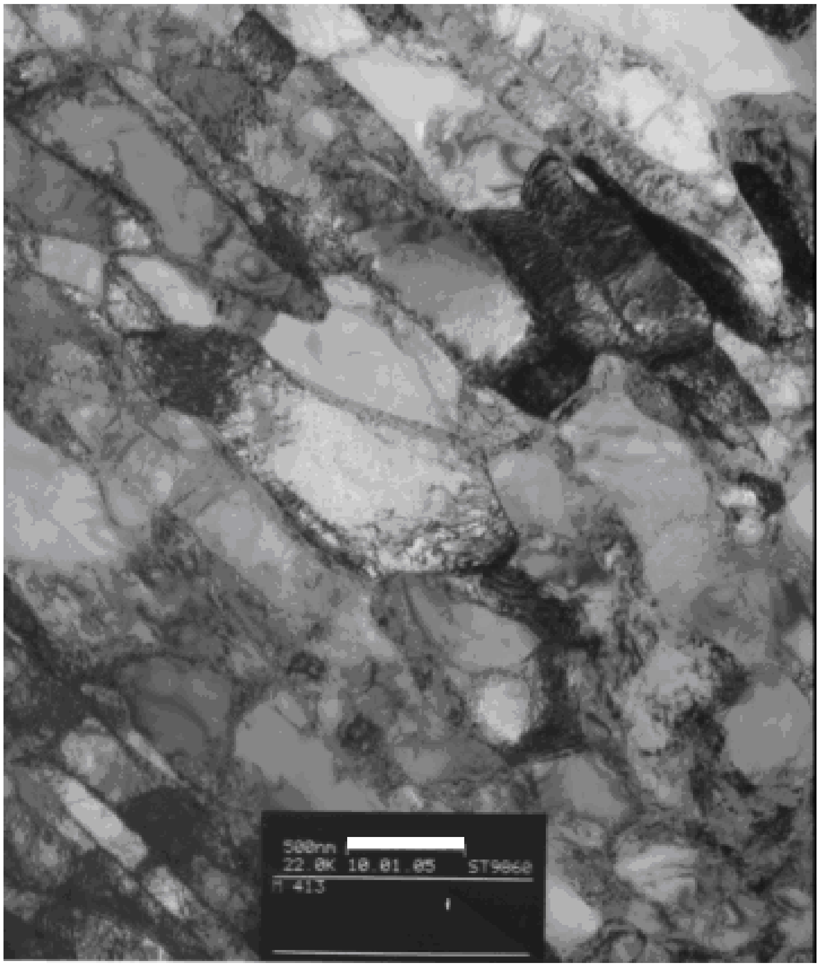

Figure 95: Intermediate magnification TEM image of ECAE 8E IF steel (white bar = 500 nm)

At high magnification (Figure 96) it is possible to observe boundaries that have the appearance of fine subgrains, with well defined dislocation networks. An excellent example of a dislocation network is visible just above center in the image below.

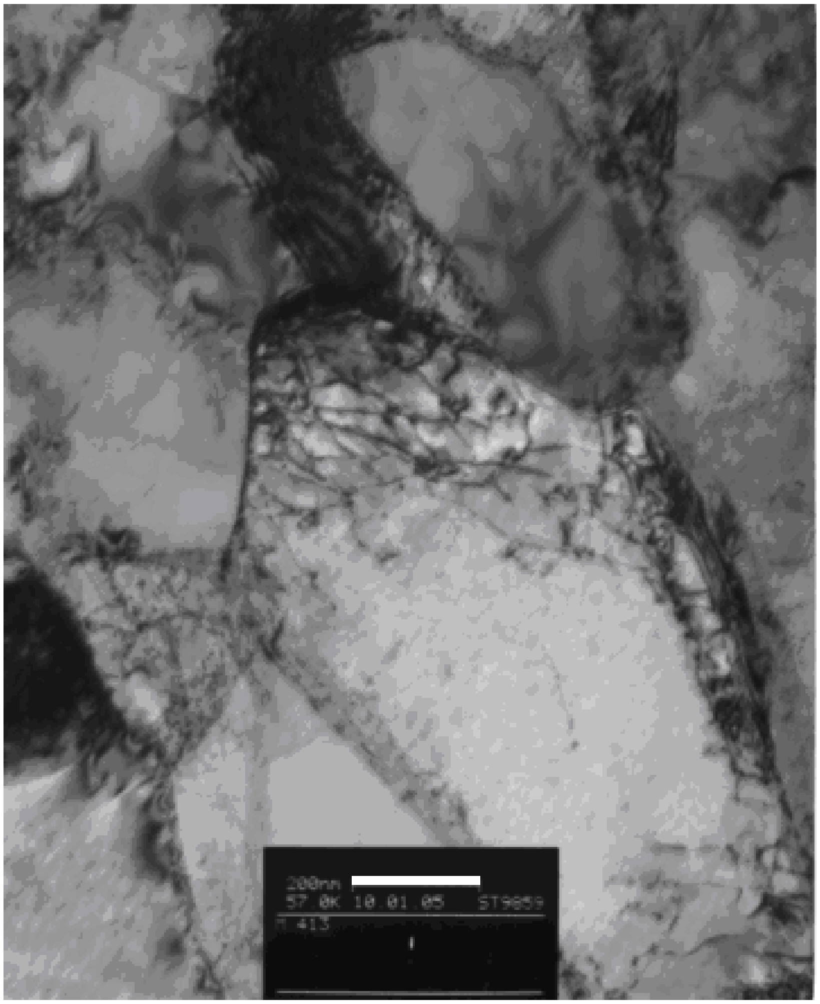

Figure 96: High magnification image of ECAE 8E IF steel (white bar = 200 nm)

Transmission electron microscope images of the sample taken from the IF steel processed using ECAE 16E is presented in Figures 97 – 99. At very low magnification the image quality is poor, due to geometrical issues with the foil previously mentioned. There are no large inhomogeneities present, and the grains are small and equiaxed. As compared to the 8E case, the structure (i.e. subgrain size) seems to be larger. This may be an indication of the saturation of internal energy storage due to new dislocation generation. The material minimizes its energy transformation of more stable dislocation configurations. It is likely that dislocation generation and annihilation occur with similar rates. This behavior is usually observed during SPD of pure metals in which it is difficult to store additional dislocations due to easy annihilation.

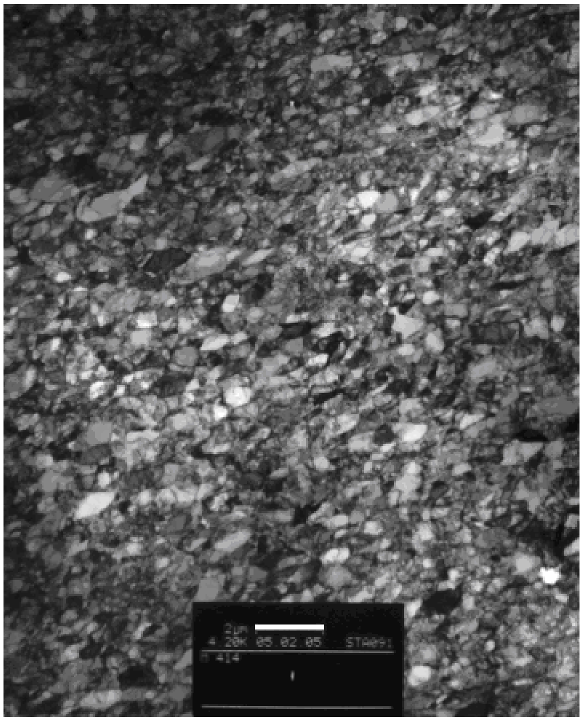

Figure 97: Low magnification TEM image of ECAE 16E IF steel (white bar = 2 µm)

At intermediate magnification (Figure 98) the grains show well developed boundaries. The micrograph shows that many of the grains are in the sub-500 nm size range.

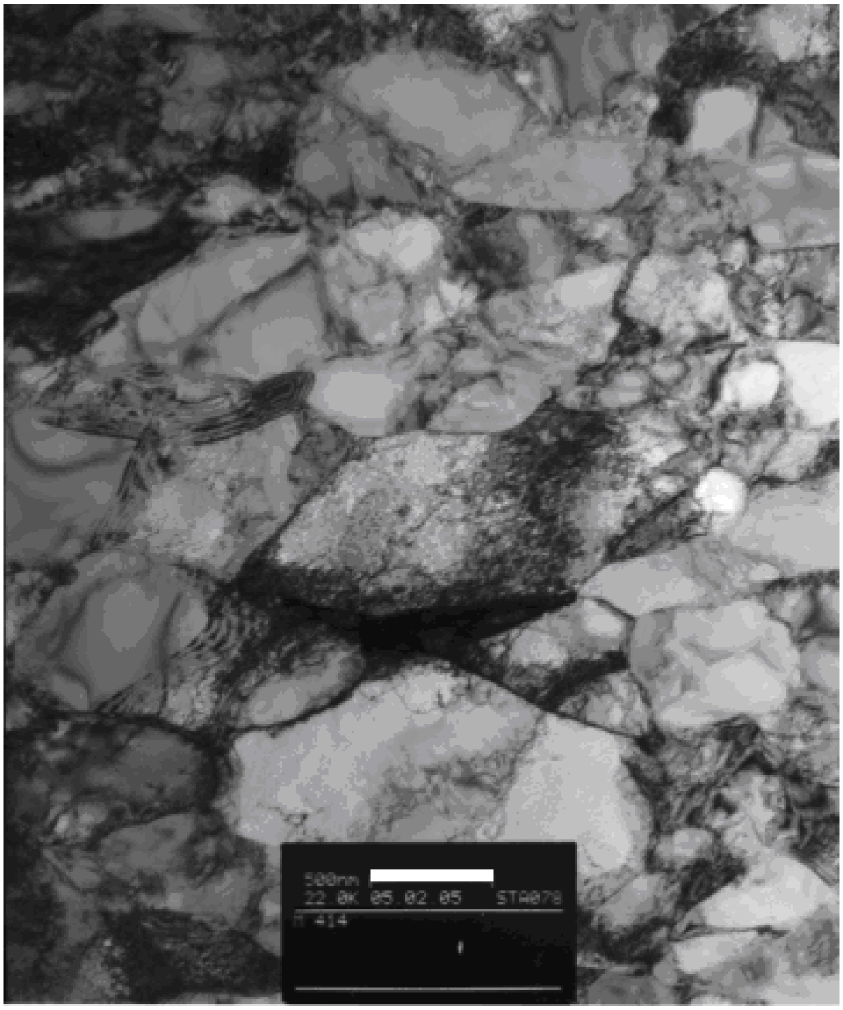

Figure 98: Intermediate magnification TEM image of ECAE 16E IF steel (white bar = 500 nm)

At high magnification (Figure 99) individual dislocations become visible. There is a dislocation network visible in the center of the image.

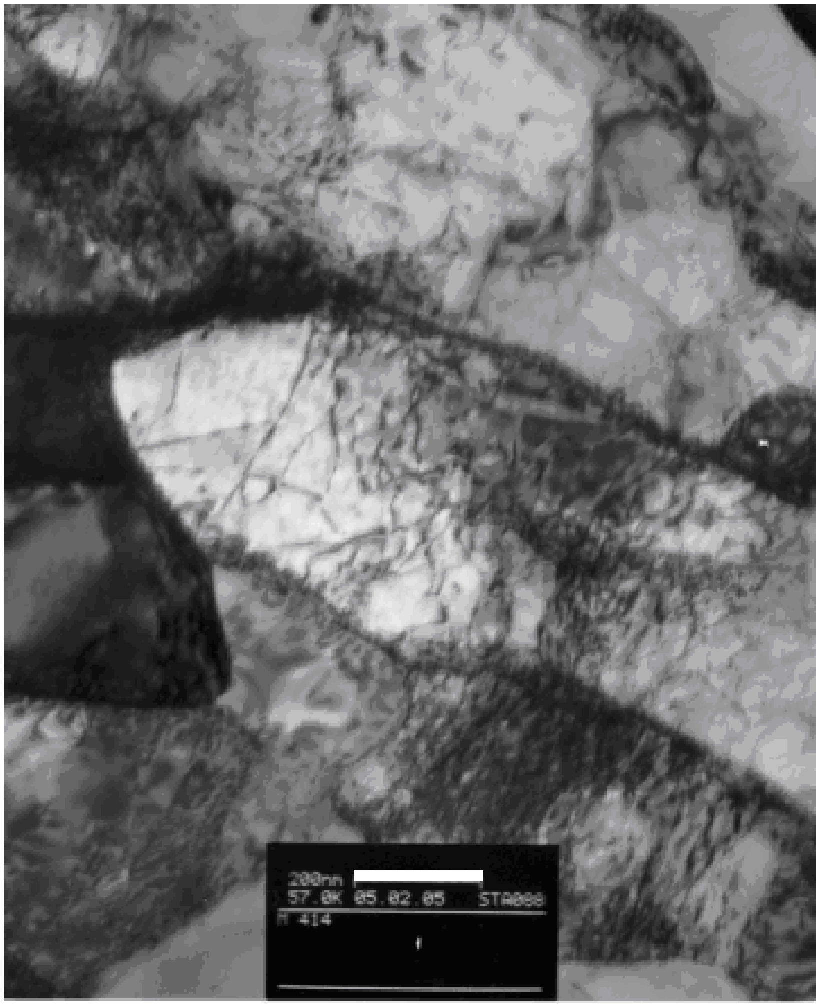

Figure 99: High magnification TEM image of ECAE 16E IF steel (white bar = 200 nm)

4.5. Recrystallization Curves

Measuring the microhardness of each annealed sample from different ECAE routes was the first step in determining the recrystallization temperature. During recrystallization, the material's hardness decreases due to recovery and recrystallization. When a material is annealed at the recrystallization temperature, there is a loss in hardness. Elevating the temperature permits enhanced atomic diffusion, which allows new grains to form. The Vickers hardness measurements taken in this study are presented in Table 6. Eight hardness measurements were taken, and the average and standard deviation are included. The average hardness values are used to construct the recrystallization curves and to identify the recrystallization temperature. The standard deviation shows the uniformity of hardness at a given annealing temperature.

Table 6: Vickers hardness measurements taken for the construction of recrystallization curves

Route	Annealing Temperature (degrees C)	1	2	3	4	5	6	7	8	Average	Deviation
1A	23	171	157	159	150	181	165	179	171	166.6	10.9
	100	185	177	188	177	173	178	186	177	180.1	5.4
	200	180	188	186	174	183	171	177	189	181.0	6.6
	300	177	190	187	188	186	192	181	179	185.0	5.4
	350	162	157	167	149	168	159	169	162	161.6	6.7
	400	169	155	158	166	161	162	168	164	162.9	4.9
	450	160	155	157	157	158	153	160	164	158.0	3.4
	500	167	153	159	154	148	151	154	157	155.4	5.8
	550	145	148	157	154	148	153	151	156	151.5	4.2
	600	81	74	71	68	71	80	84	71	75.0	5.9
	700	71	71	68	66	70	67	69	67	68.6	1.9

Table 6. (continued)

Route	Annealing Temperature (degrees C)	1	2	3	4	5	6	7	8	Average	Deviation
2A	23	172	183	183	180	177	177	175	173	177.5	4.2
	100	193	176	185	183	184	196	196	199	189.0	8.1
	200	171	168	174	180	165	146	170	173	168.4	10.1
	300	157	165	162	160	166	170	159	154	161.6	5.2
	350	199	189	187	177	194	184	191	188	188.6	6.6
	400	178	173	187	171	182	176	185	185	179.6	6.0
	450	144	157	161	158	140	162	159	153	154.3	8.1
	500	153	149	155	151	156	142	149	158	151.6	5.1
	550	141	136	142	134	133	141	143	139	138.6	3.8
	600	75	75	77	78	79	75	75	77	76.4	1.6
	700	68	66	68	66	66	70	66	66	67.0	1.5

Route	Annealing Temperature (degrees C)	1	2	3	4	5	6	7	8	Average	Deviation
2B	23	191	197	190	190	196	189	183	192	191.0	4.3
	100	185	195	204	188	193	198	191	197	193.9	6.0
	200	190	198	196	201	193	191	200	200	196.1	4.3
	300	194	186	197	193	183	190	192	182	189.6	5.4
	350	181	185	183	196	187	187	190	182	186.4	4.9
	400	188	184	180	187	185	185	180	186	184.4	3.0
	450	185	180	175	176	171	180	184	172	177.9	5.2
	500	169	159	164	161	164	164	173	163	164.6	4.4
	550	140	137	135	134	133	142	146	136	137.9	4.5
	600	73	74	74	73	70	74	71	71	72.5	1.6
	700	66	66	65	66	67	67	65	67	66.1	0.8

Route	Annealing Temperature (degrees C)	1	2	3	4	5	6	7	8	Average	Deviation
2C	23	213	186	198	200	201	198	191	199	198.3	7.9
	100	177	196	210	201	198	189	206	196	196.6	10.2
	200	192	193	186	202	196	190	196	195	193.8	4.7
	300	198	189	201	193	192	189	199	194	194.4	4.5
	350	201	187	200	189	200	184	191	188	192.5	6.8
	400	182	180	186	186	182	192	187	189	185.5	4.0
	450	181	174	185	189	178	189	182	184	182.8	5.2
	500	172	162	163	169	161	171	171	169	167.3	4.5
	550	140	131	131	136	141	148	135	148	138.8	6.8
	600	72	70	71	74	74	74	71	74	72.5	1.7
	700	69	69	69	69	67	66	66	68	67.9	1.4

Table 6. (continued)

Route	Annealing Temperature (degrees C)	1	2	3	4	5	6	7	8	Average	Deviation
4A	23	190	205	197	193	204	191	197	197	196.8	5.5
	100	200	202	195	201	199	198	199	202	199.5	2.3
	200	200	193	195	201	196	196	191	203	196.9	4.1
	300	191	195	195	191	205	195	198	199	196.1	4.6
	350	202	199	198	198	200	200	196	197	198.8	1.9
	400	187	185	183	193	189	191	190	192	188.8	3.5
	450	179	184	179	182	181	186	177	183	181.4	3.0
	500	167	156	157	166	165	166	168	161	163.3	4.7
	550	140	140	141	136	147	138	144	142	141.0	3.4
	600	73	73	72	73	73	72	73	72	72.6	0.5
	700	66	67	65	67	66	67	67	67	66.5	0.8

Route	Annealing Temperature (degrees C)	1	2	3	4	5	6	7	8	Average	Deviation
4B	23	204	209	202	201	211	205	209	205	205.8	3.6
	100	196	207	203	205	203	207	207	204	204.0	3.7
	200	202	198	195	206	204	204	201	207	202.1	4.1
	300	193	193	198	201	203	197	197	205	198.4	4.4
	350	201	201	203	199	205	203	206	204	202.8	2.3
	400	192	203	200	204	202	198	207	195	200.1	4.9
	450	186	197	189	195	187	188	186	187	189.4	4.2
	500	174	172	168	173	170	169	167	174	170.9	2.7
	550	128	126	126	130	132	127	130	133	129.0	2.7
	600	77	74	74	75	73	73	76	75	74.6	1.4
	700	68	70	68	68	67	66	65	66	67.3	1.6

Route	Annealing Temperature (degrees C)	1	2	3	4	5	6	7	8	Average	Deviation
4C	23	204	207	208	205	206	207	205	201	205.4	2.2
	100	197	206	217	213	202	203	203	205	205.8	6.4
	200	207	213	208	201	213	213	201	208	208.0	5.0
	300	202	190	202	203	192	202	201	203	199.4	5.2
	350	210	205	206	202	202	209	205	198	204.6	3.9
	400	196	196	199	196	198	197	186	199	195.9	4.2
	450	186	180	180	185	180	188	185	187	183.9	3.4
	500	170	170	162	168	175	177	171	164	169.6	5.0
	550	145	142	144	144	142	143	143	142	143.1	1.1
	600	75	74	75	75	75	76	76	77	75.4	0.9
	700	69	69	69	67	68	70	67	70	68.6	1.2

Table 6. (continued)

Route	Annealing Temperature (degrees C)	1	2	3	4	5	6	7	8	Average	Deviation
4C'	23	212	202	206	205	203	207	216	210	207.6	4.7
	100	204	204	200	200	208	200	202	200	202.3	2.9
	200	219	218	212	198	212	206	200	203	208.5	8.0
	300	208	206	202	208	213	209	204	208	207.3	3.3
	350	213	199	202	204	207	210	208	208	206.4	4.5
	400	201	197	198	196	192	200	193	199	197.0	3.2
	450	191	190	194	187	187	190	187	197	190.4	3.6
	500	169	167	168	170	167	169	169	172	168.9	1.6
	550	131	128	131	136	129	131	131	131	131.0	2.3
	600	78	79	79	80	78	77	79	78	78.5	0.9
	700	67	69	70	69	71	69	71	68	69.3	1.4

Route	Annealing Temperature (degrees C)	1	2	3	4	5	6	7	8	Average	Deviation
4E	23	197	199	201	197	196	197	208	203	199.8	4.1
	100	200	195	187	195	199	199	198	195	196.0	4.2
	200	202	203	201	197	200	200	197	196	199.5	2.6
	300	205	198	188	201	204	189	194	203	197.8	6.7
	350	191	191	194	196	201	188	189	194	193.0	4.2
	400	190	190	185	194	195	189	190	178	188.9	5.4
	450	184	186	179	187	183	180	190	186	184.4	3.7
	500	168	168	166	167	162	165	166	170	166.5	2.4
	550	139	148	128	142	141	124	129	132	135.4	8.3
	600	70	72	73	71	71	72	73	74	72.0	1.3
	700	67	66	65	65	65	67	67	67	66.1	1.0

Route	Annealing Temperature (degrees C)	1	2	3	4	5	6	7	8	Average	Deviation
8C	23	219	222	219	202	213	212	222	220	216.1	6.8
	100	214	212	219	222	222	219	215	216	217.4	3.7
	200	227	220	221	225	220	224	221	217	221.9	3.2
	300	220	213	222	215	223	213	214	210	216.3	4.8
	350	205	213	208	215	206	205	210	218	210.0	4.9
	400	208	210	210	208	214	212	207	208	209.6	2.4
	450	192	193	199	193	195	192	198	197	194.9	2.8
	500	167	176	174	176	170	176	168	174	172.6	3.7
	550	133	131	135	134	136	135	132	137	134.1	2.0
	600	82	81	83	84	83	85	84	82	83.0	1.3
	700	67	68	67	69	67	69	68	67	67.8	0.9

Table 6. (continued)

Route	Annealing Temperature (degrees C)	1	2	3	4	5	6	7	8	Average	Deviation
8C'	23	226	228	231	227	229	227	230	228	228.3	1.7
	100	223	224	226	224	225	224	225	224	224.4	0.9
	200	226	227	230	231	230	231	232	229	229.5	2.1
	300	234	229	233	228	232	236	230	233	231.9	2.7
	350	229	226	227	227	230	229	229	230	228.4	1.5
	400	220	220	218	221	217	220	218	216	218.8	1.8
	450	206	211	210	208	213	210	208	205	208.9	2.6
	500	180	180	181	178	179	181	178	182	179.9	1.5
	550	124	121	123	123	122	123	124	125	123.1	1.2
	600	85	84	83	83	84	86	84	85	84.3	1.0
	700	74	75	74	72	72	74	73	72	73.3	1.2

Route	Annealing Temperature (degrees C)	1	2	3	4	5	6	7	8	Average	Deviation
8E	23	216	210	216	212	213	217	212	221	214.6	3.5
	100	205	210	213	204	211	214	208	205	208.8	3.8
	200	216	211	217	221	211	209	220	207	214.0	5.2
	300	211	214	206	204	209	213	209	211	209.6	3.4
	350	206	208	204	207	208	198	206	205	205.3	3.2
	400	204	203	204	204	200	204	200	203	202.8	1.8
	450	193	190	188	189	195	195	190	193	191.6	2.7
	500	170	176	170	177	175	175	171	178	174.0	3.2
	550	124	129	126	131	125	129	126	125	126.9	2.5
	600	81	80	79	81	79	81	81	81	80.4	0.9
	700	70	69	67	68	66	69	69	69	68.4	1.3

Route	Annealing Temperature (degrees C)	1	2	3	4	5	6	7	8	Average	Deviation
16E	23	202	205	204	200	200	199	199	207	202.0	3.0
	100	198	197	193	199	196	199	192	197	196.4	2.6
	200	209	218	213	211	216	212	220	216	214.4	3.7
	300	199	199	199	201	201	198	198	205	200.0	2.3
	350	209	210	213	207	212	213	209	211	210.5	2.1
	400	213	207	211	210	212	207	208	204	209.0	3.0
	450	200	197	198	198	195	195	196	199	197.3	1.8
	500	162	160	162	159	161	158	158	160	160.0	1.6
	550	127	122	118	128	124	121	121	126	123.4	3.5
	600	79	78	78	79	78	79	81	78	78.8	1.0
	700	72	72	71	69	71	69	68	68	70.0	1.7

It is possible to determine the temperatures at which recrystallization occurs once the hardness tables are converted into graphical format. The recrystallization curves all show similar behavior for the various processing routes that were used in this study. There are three major zones of interest in the hardness curves. The first zone begins at room temperature and ends between 400°C and 450°C. The hardness within this first zone generally remains constant, but may show slight increases or decreases in magnitude, depending on the route and number of passes. Further examination of this first zone will be covered later. The second zone begins where the first zone ends, and ends at approximately 600°C. The hardness values within this second zone decrease due to recrystallization. Beyond the 600°C mark is the third zone, where hardness values decrease gradually or level out. This third zone terminates at 700°C, and corresponds to the zone in which grain growth occurs. The ECAE 1A case stands out in particular, and does not conform to the standard three-zone structure that the other routes follow. In the case of ECAE 1A, the hardness gradually increases from room temperature up to 300°C, then suddenly decreases between 300°C and 350°C, after which it stays almost constant, though with a very gradual negative slope until 550°C. Once ECAE 1A reaches a temperature of 550°C, the hardness values rapidly decrease until the 600°C mark is reached. Beyond 600°C the hardness values are more or less stable, though they do show a slight decrease associated with grain growth. Another processing route that shows unusual behavior is ECAE 2A, which shows an increase in hardness between room temperature and 100°C, a gradual decrease between 100°C and 300°C, followed by a “hump” between 300°C and 450°C. Beyond this “hump” the materials hardness gradually decreases from 450°C to 550°C, after which it shows a sudden decrease in hardness due to recrystallization. Grain growth begins at 600°C and continues through to the 700°C point with the standard gradual decrease in hardness. Route 16E shows a series of “waves” in its hardness values between the temperatures of 100°C and 300°C, and again between 300°C and 450°C, with a normal recrystallization and grain growth behavior following. Figures 100 through 112 show the recrystallization curves for the materials used in this study.

Variations in hardness prior to the onset of recrystallization may be explained by two factors. The first factor is the location of the specimens used for the recrystallization and hardness testing, specifically their location within the billet. Not all of the specimens were cut from exactly the same location in each billet, although they were from theoretically uniformly deformed regions. The variation in hardness after low temperature annealing could simply be an indication of strain localization during extrusion such that the level of strain imposed may vary from specimen to specimen within each case. The second factor is a phenomenon known as polygonization [32], in which dislocations within locally bent crystals rearrange themselves during annealing to form sub-boundaries, producing a more orderly and stable structure. This structure may cause an increase in the measured hardness.

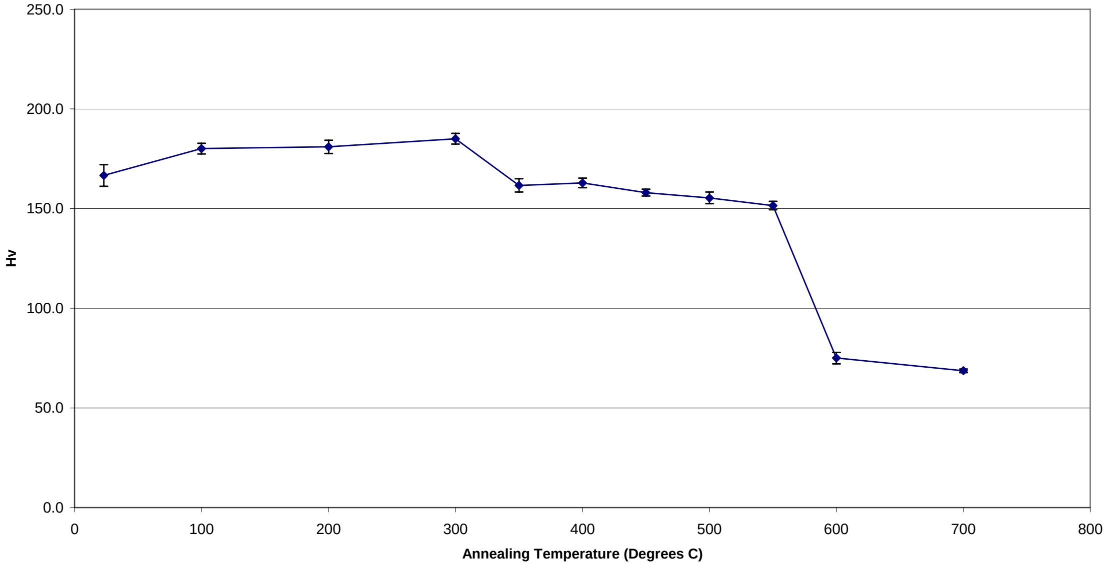

Figure 100: 90-minute recrystallization curve for IF steel processed via ECAE 1A

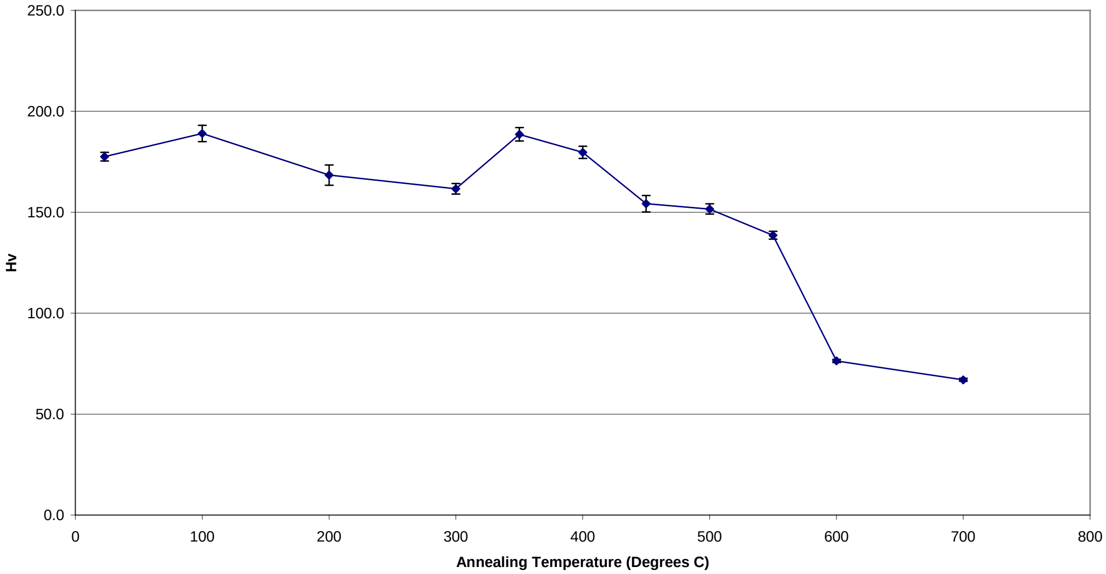

Figure 101: 90-minute recrystallization curve for IF steel processed via ECAE 2A

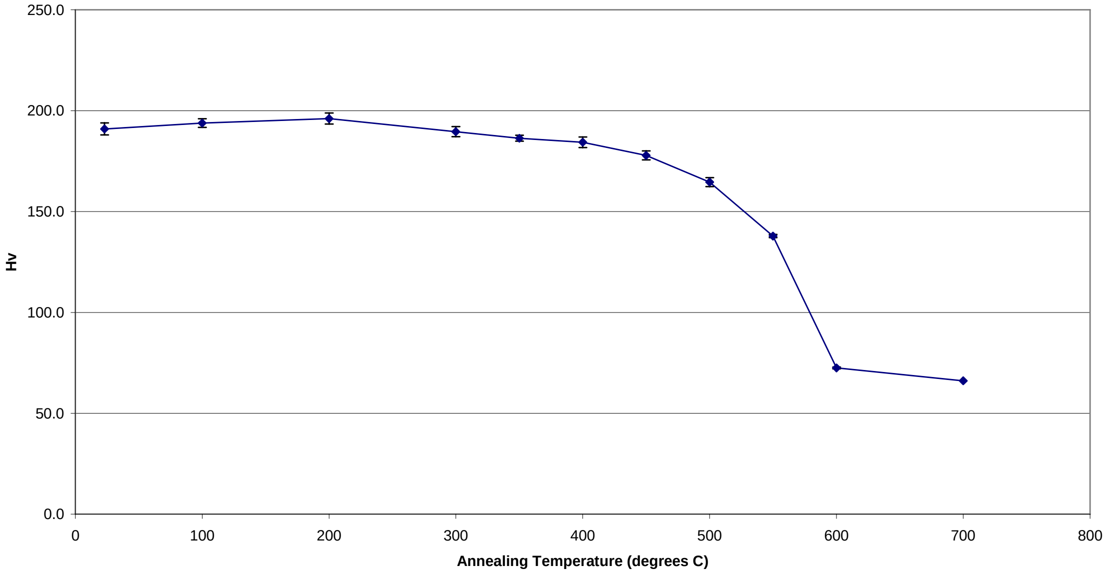

Figure 102: 90-minute recrystallization curve for IF steel processed via ECAE 2B

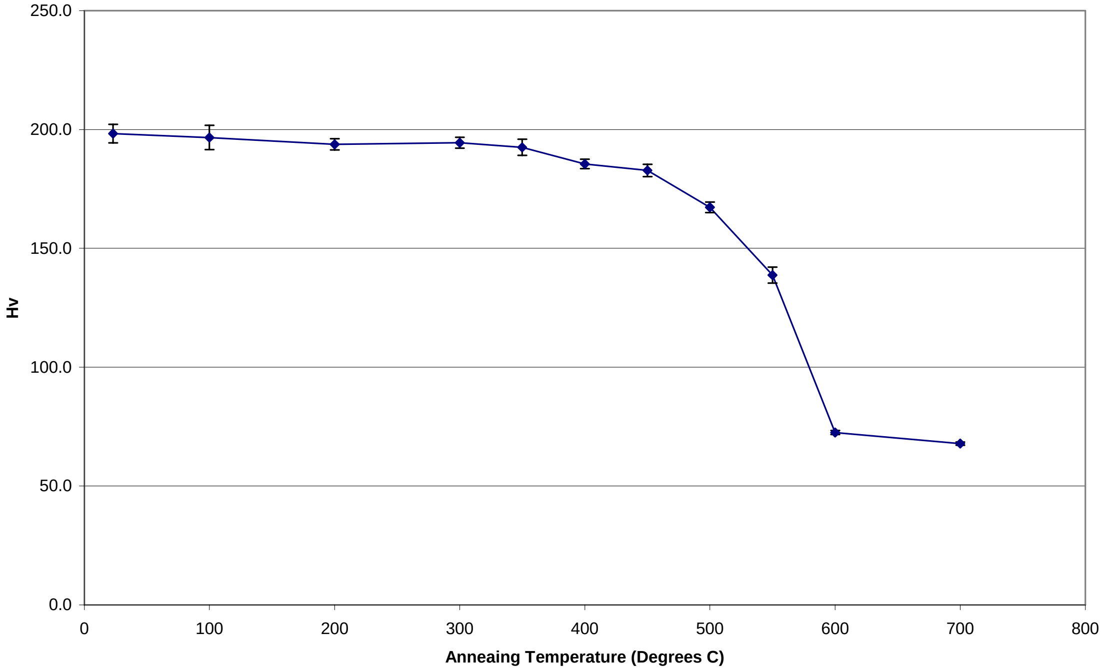

Figure 103: 90-minute recrystallization curve for IF steel processed via ECAE 2C

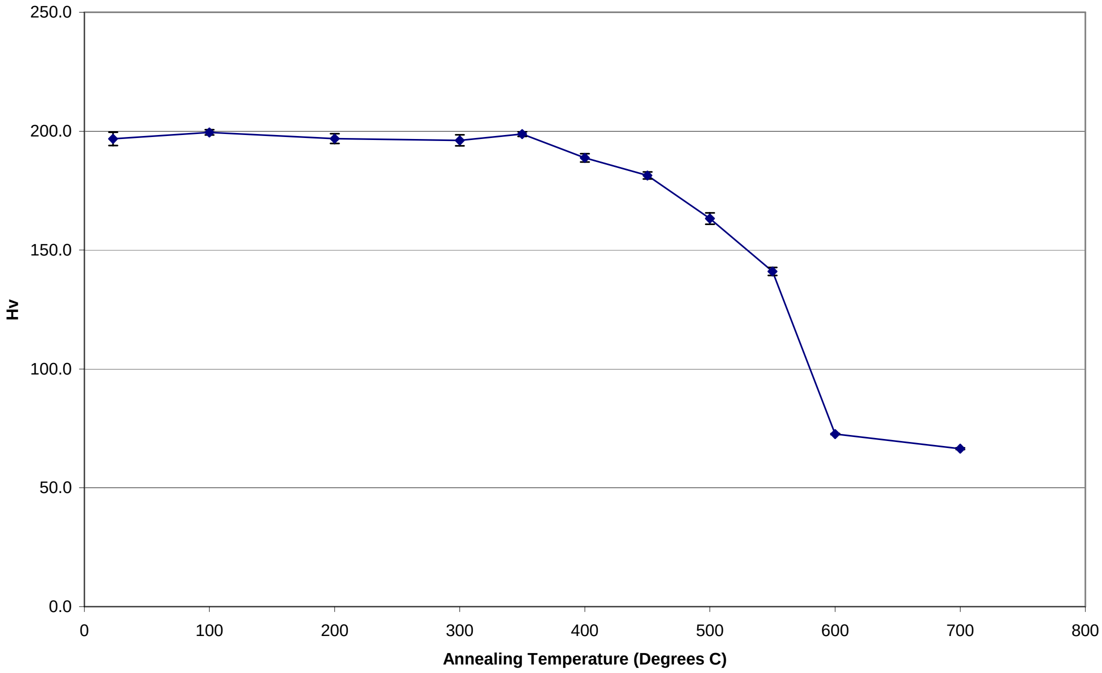

Figure 104: 90-minute recrystallization curve for IF steel processed via ECAE 4A

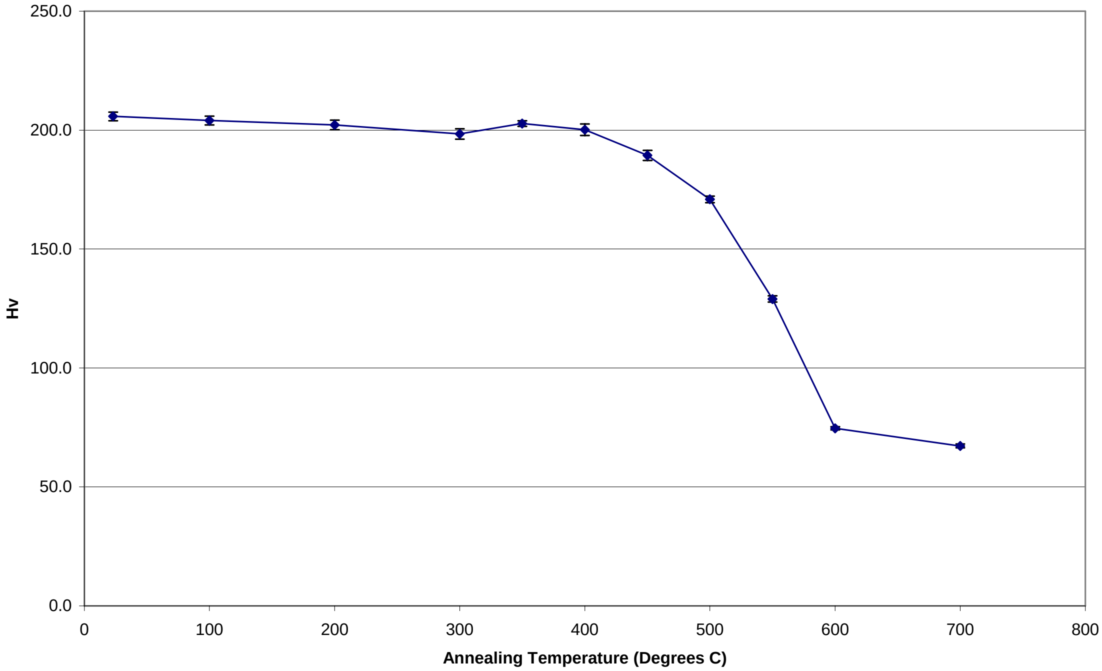

Figure 105: 90-minute recrystallization curve for IF steel processed via ECAE 4B

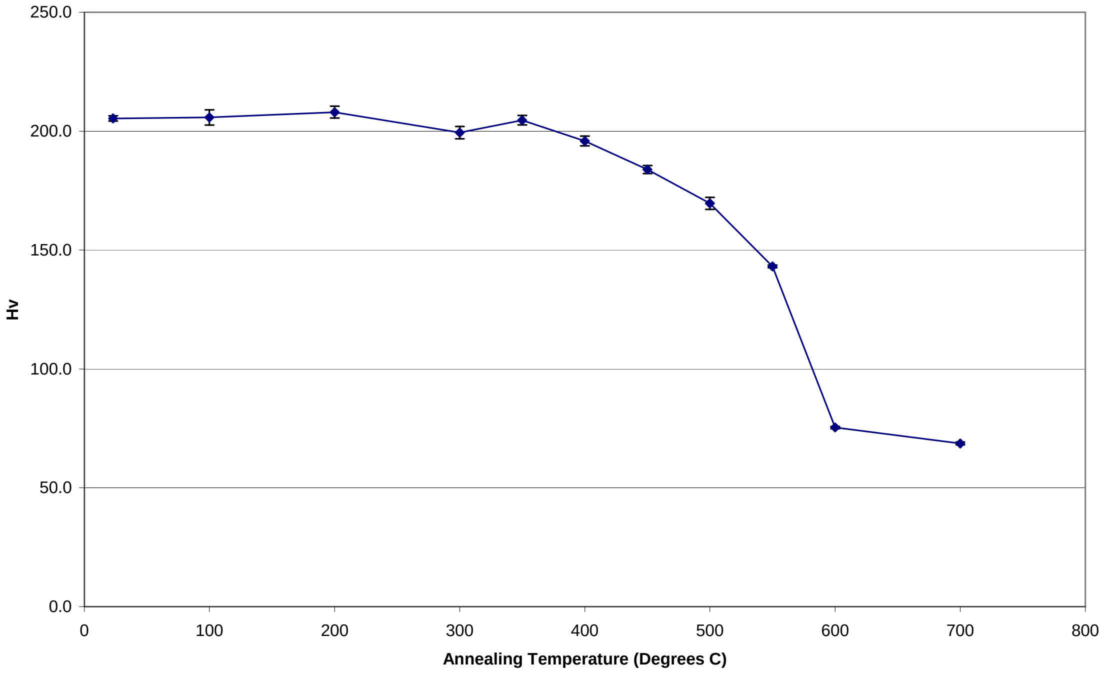

Figure 106: 90-minute recrystallization curve for IF steel processed via ECAE 4C

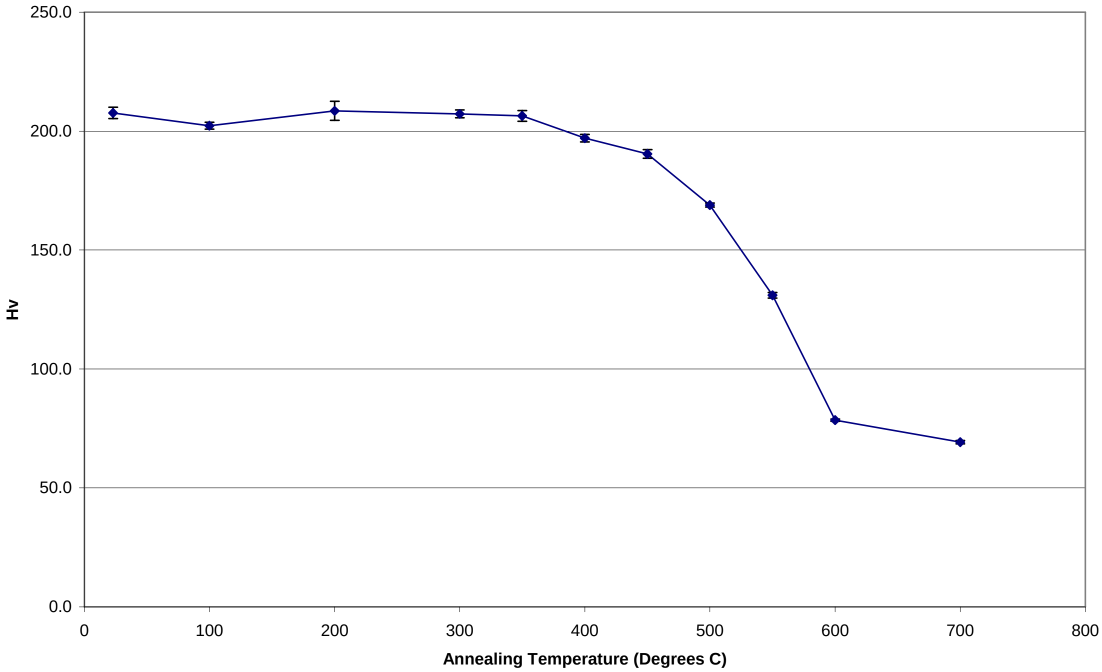

Figure 107: 90-minute recrystallization curve for IF steel processed via ECAE 4C’

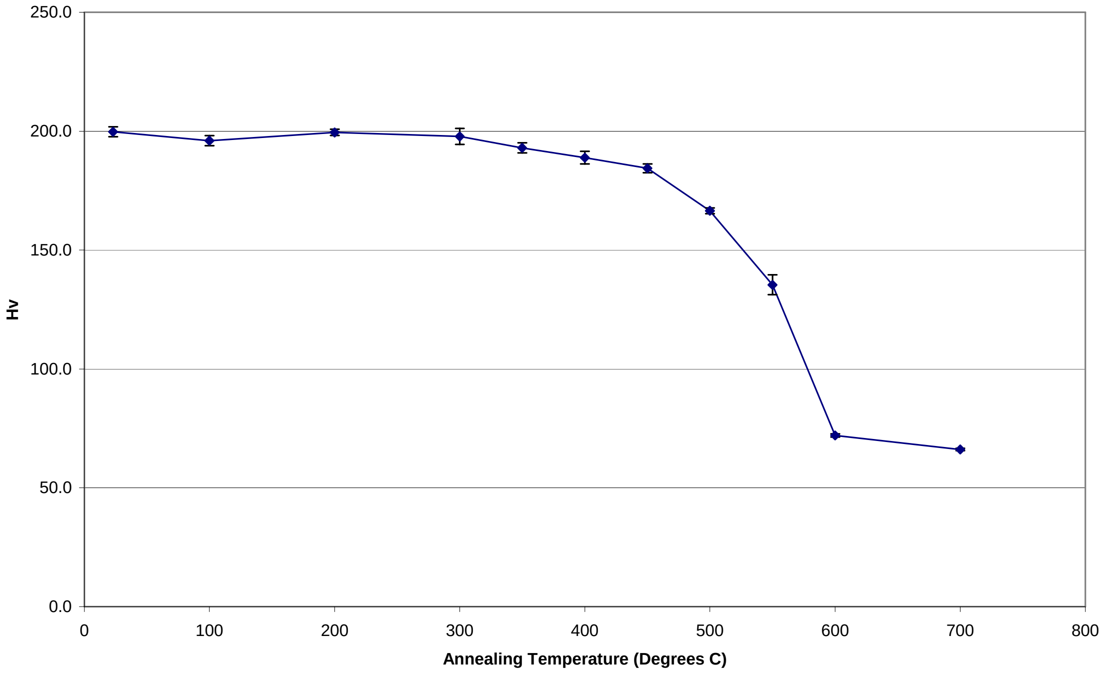

Figure 108: 90-minute recrystallization curve for IF steel processed via ECAE 4E

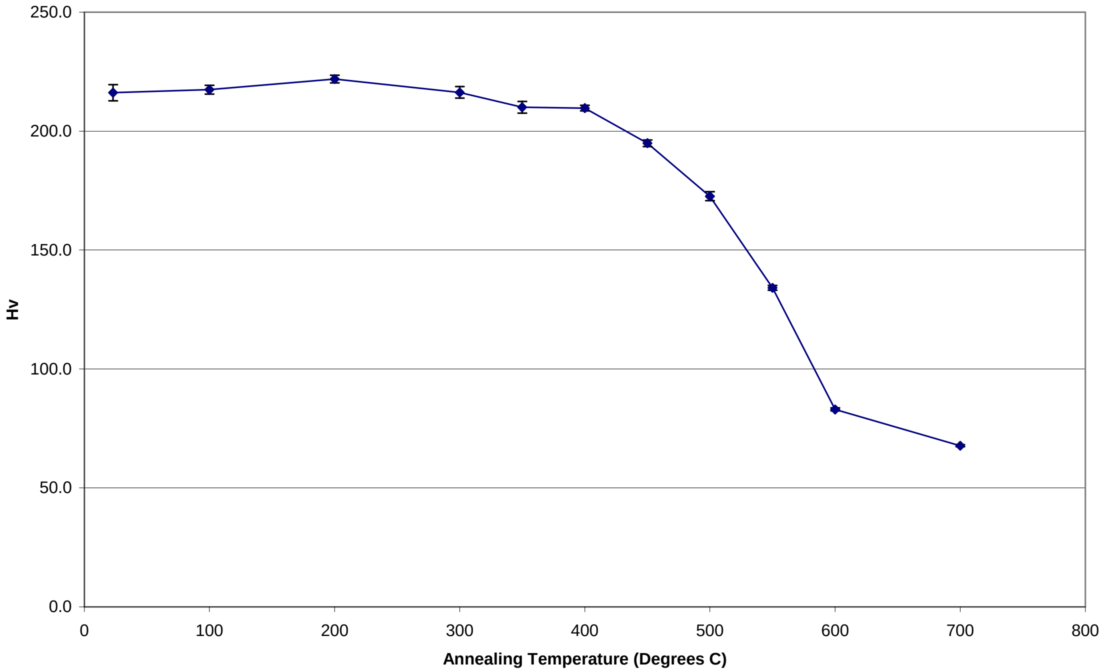

Figure 109: 90-minute recrystallization curve for IF steel processed via ECAE 8C

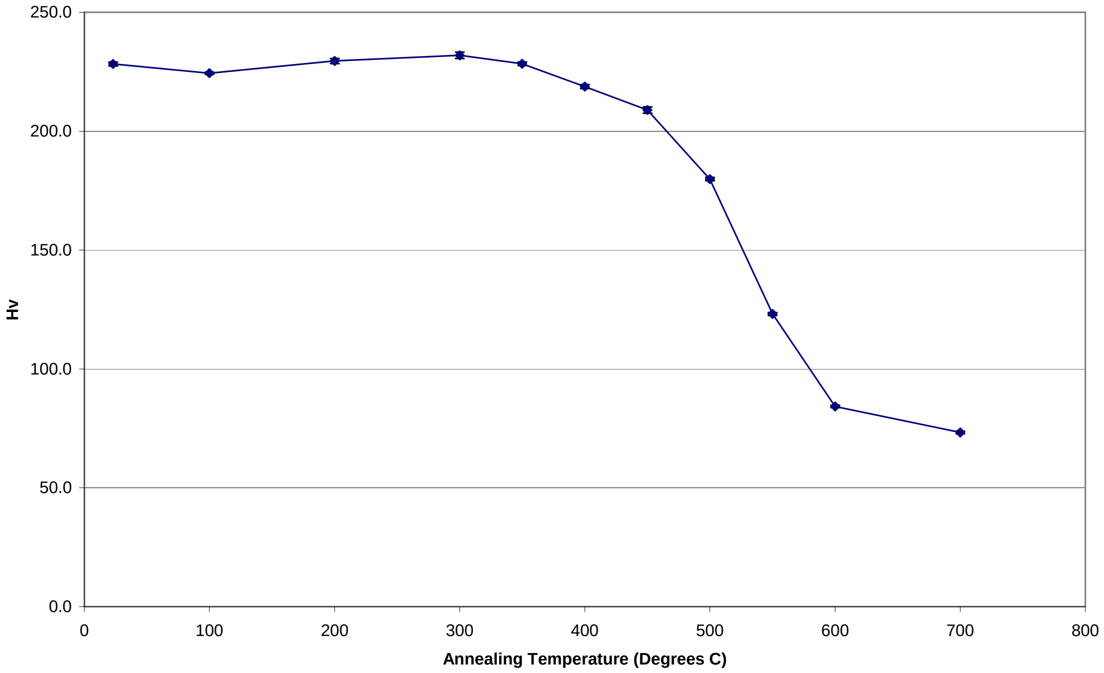

Figure 110: 90-minute recrystallization curve for IF steel processed via ECAE 8C'

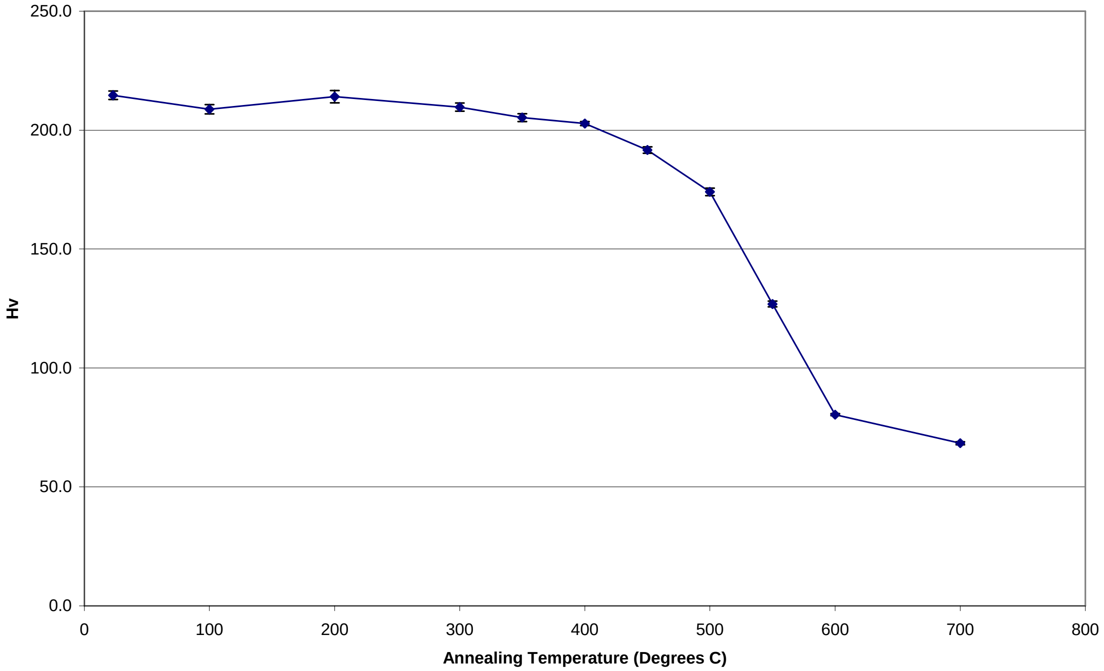

Figure 111: 90-minute recrystallization curve for IF steel processed via ECAE 8E

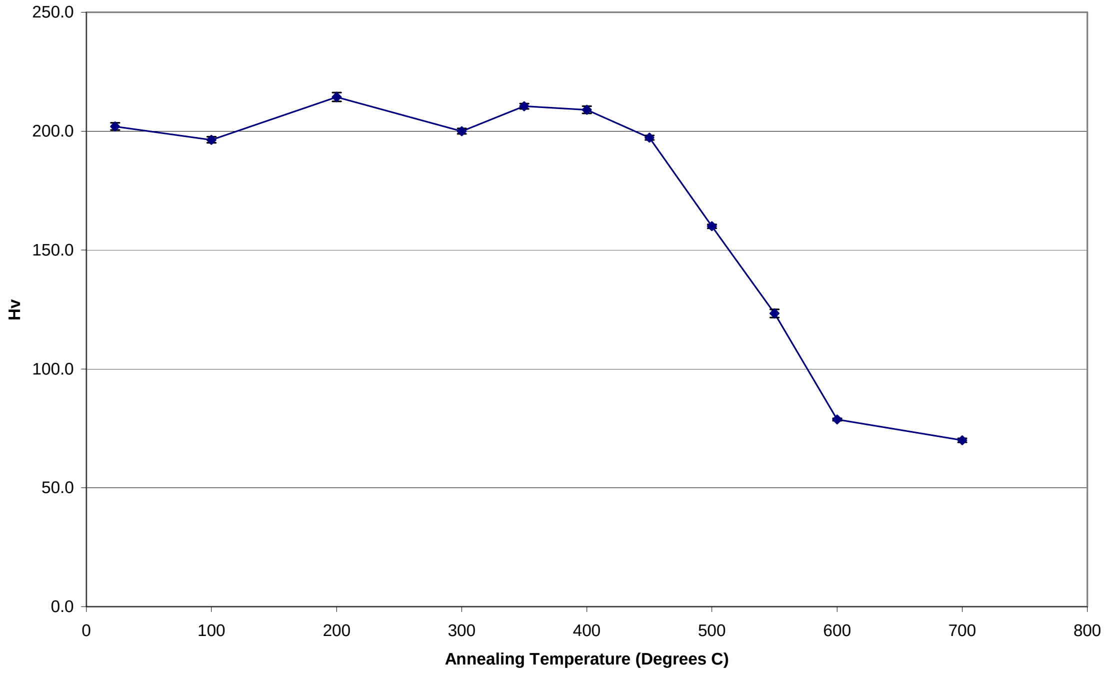

Figure 112: 90-minute recrystallization curve for IF steel processed via ECAE 16E

All of the processing routes examined in this study show a consistent recrystallization temperature of 600°C, although the temperature at which recrystallization begins varies, as shown in Table 7.

Table 7: Temperature ranges of three annealing regimes for the processing routes studied

Route	Recovery Zone	Recrystallization Zone	Grain Growth Zone
1A	RT - 550C	550 - 600C	600 - 700C
2A	RT - 550C	550 - 600C	
2B	RT - 450C	450 - 600C	
2C	RT - 450C	450 - 600C	
4A	RT - 450C	450 - 600C	
4B	RT - 400C	400 - 600C	
4C	RT - 400C	400 - 600C	
4C'	RT - 450C	450 - 600C	
4E	RT - 450C	450 - 600C	
8C	RT - 400C	400 - 600C	
8C'	RT - 400C	400 - 600C	
8E	RT - 400C	400 - 600C	
16E	RT - 450C	450 - 600C	

It is interesting to note the fluctuation in some of the hardness values that were recorded. Cases such as ECAE 1A, ECAE 2A and ECAE 16E, which show fluctuations in their pre-recrystallization hardness values, are of particular interest, since these fluctuations are not seen in the plots of other processing routes. These fluctuations may be attributed to the specimen location within the billet. All hardness specimens were taken from a position close to the centerline of their source billet. The orientation of the shear plane, as shown in Figure 8 in Section 2, and by association the fully worked zone, can change from one pass to another during processing. Hardness values between the fully worked zones and the outer zones would not necessarily be the same after annealing, and this could account for the behavior shown in the pre-recrystallization regions of the samples from ECAE 1A, 2A and 16E.

4.6. Microstructures

Once all of the necessary steps were completed, optical examination of specimens of IF steel that had been subjected to various ECAE routes, as well as post-process annealing, was performed. The specific cases examined were: ECAE 1A, ECAE 2A, ECAE 2B, ECAE 2C, ECAE 4A, ECAE 4B, ECAE 4C’, ECAE 8C’ and ECAE 16E. Material that was in an as-received condition was also examined for comparison purposes. Each case consisted of three specimens, each one corresponding to an annealing condition: one in the as-processed condition; one annealed for 90 minutes at 550°C; and one annealed for 90 minutes at 700°C.

Figures 113 and 114 show two optical micrographs of IF steel in the as-received condition. Figure 113 is a low magnification overview, with large grains of approximately 350 μm clearly visible. Figure 114 is a higher magnification view, showing unusual “fiber” structures. These fibers may be the result of veining, an imperfection in which fcc iron transforms to bcc iron [37], or they may represent another structure within the as-received material, such as an unusual concentration of carbon in the zone of observation. It could also be possible that the structures in question are artifacts of the polishing process.

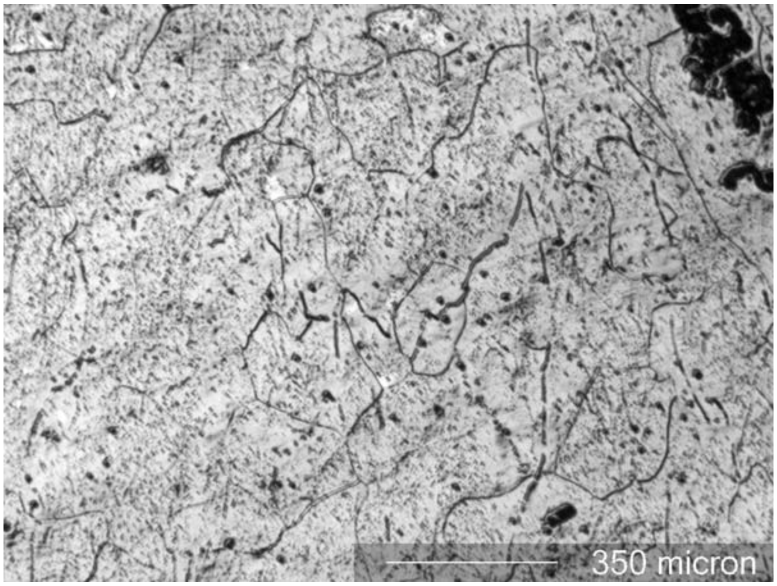

Figure 113: Low magnification optical micrograph of as-received IF steel

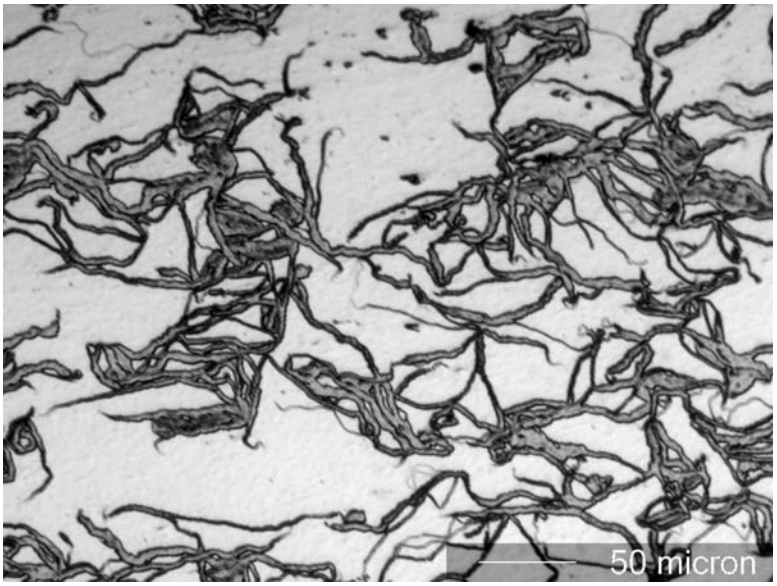

Figure 114: Optical micograph showing "fiber" structures on as-received IF steel

The optical microscopy of the heat-treated samples shows a very noticeable difference in the resulting microstructures between the specimens examined in an as-processed condition and those which were subjected to an annealing heat treatment corresponding roughly to their grain growth temperature. Figures 115 – 116 show representative optical micrographs of IF steel specimens at room temperature and annealed at 700°C for 90 minutes. The micrographs of all samples and annealing schedules can be found in the appendix.

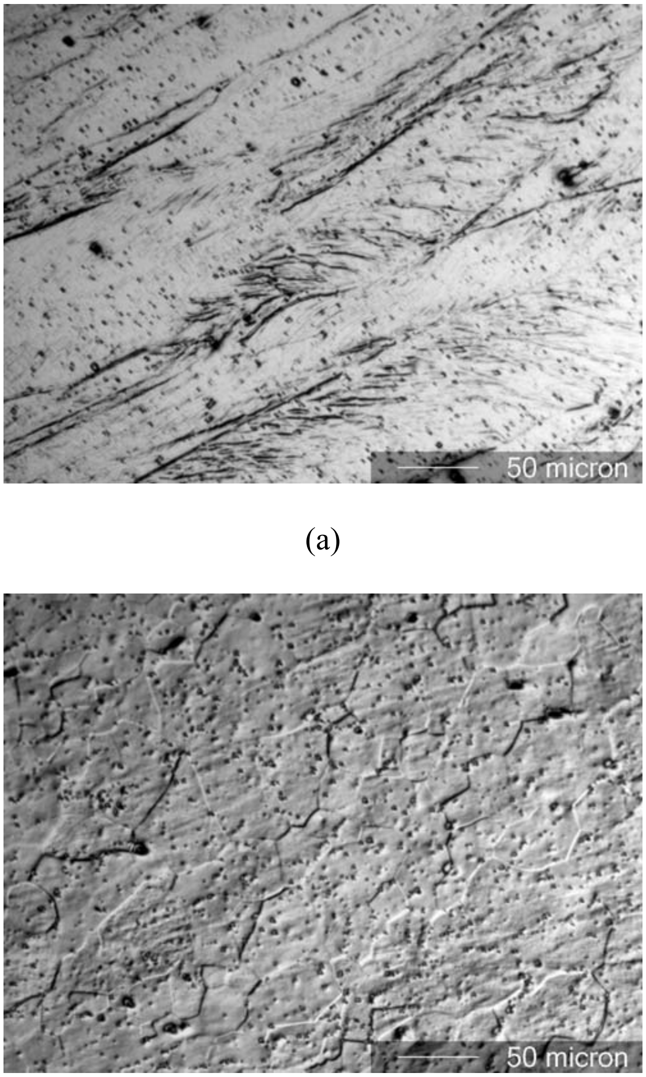

(a)

(b)

Figure 115: Microstructures of ECAE 1A IF steel. (a) as-processed, (b) annealed for 90 minutes at 700°C

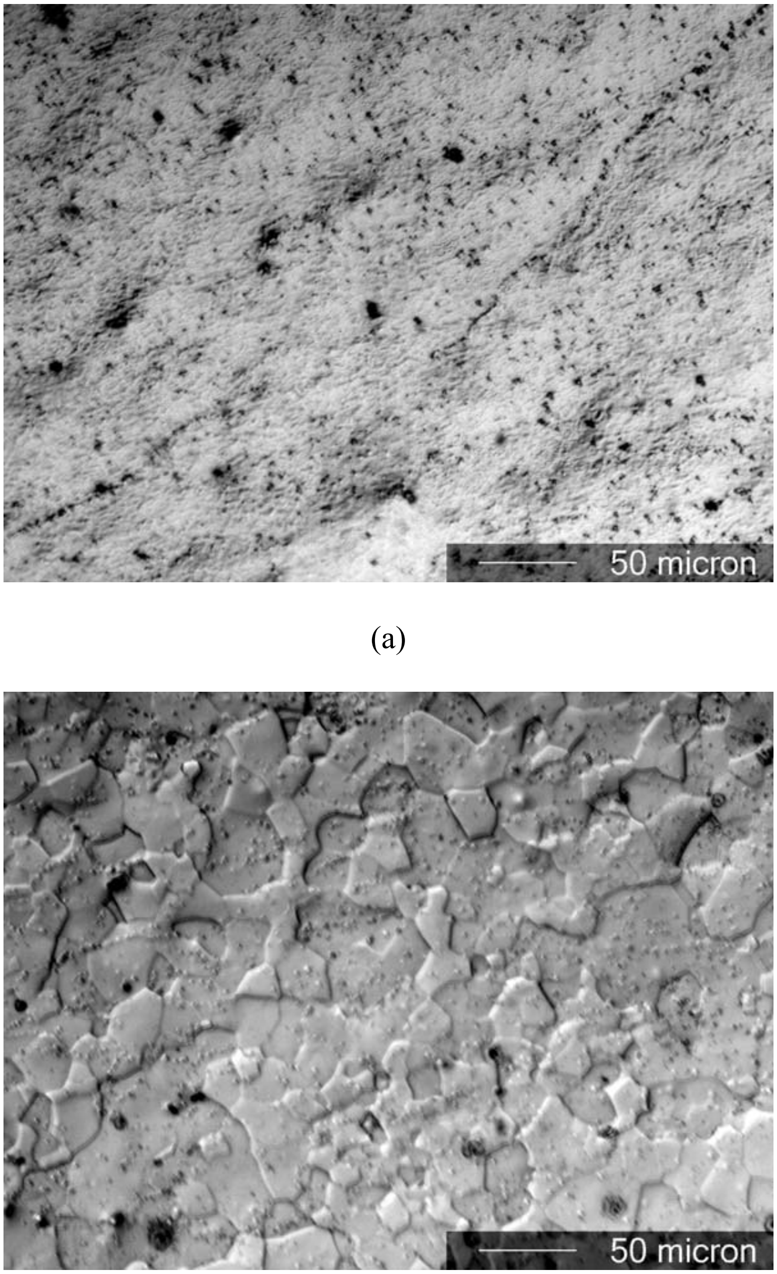

Figure 116: Microstructures of ECAE 8C' IF steel. (a) as-processed, (b) annealed for 90 minutes at 700°C

During the optical examination of the as-processed IF steel specimens, it was observed that in some cases very little clear grain structure could be seen. The severe plastic deformation caused by ECAE resulted in optical images with little or no observable grains (Figure 117).

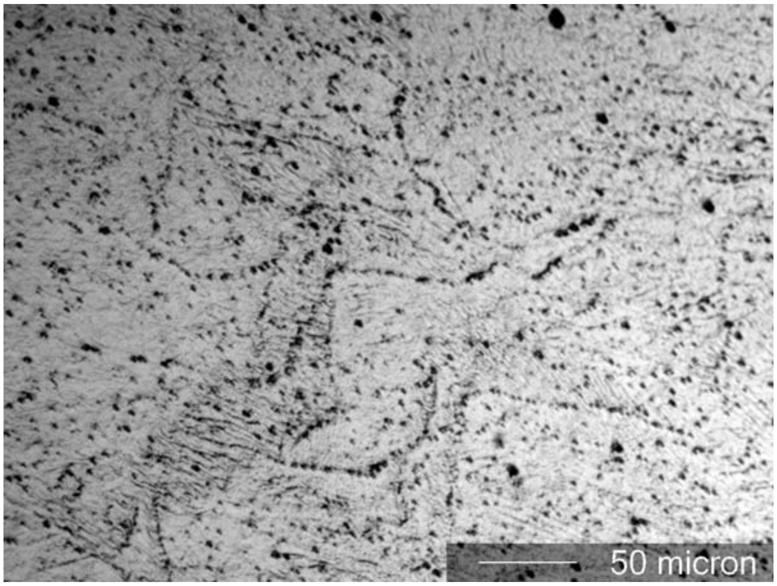

Figure 117: Optical micrograph of ECAE 2C IF steel showing worked structure

Figures 118 – 122 show the microstructures of ECAE processed IF steel following the Routes 1A, 2A, 4A, 4C’, and 8C’. Optical microscopy was performed on the flow plane of these specimens for three different temperature conditions. All heat treatments lasted 90 minutes. Figure 118 shows the microstructures of ECAE 1A processed IF steel. Figure 118 (a) shows the elongated structure associated with Route A. The nucleation of new grains is visible in Figure 118 (b) by 550°C. These nucleation sites appear along the slip lines. The discolored areas in Figure 118 (b) and Figure 119 (b) are artifacts of the etching process. The formation of new crystals from these nuclei occurs mostly in regions of high strain energy, such as the intersections of slip lines and areas near grain boundaries. At 700°C, the structure has been consumed by new grains, as shown in Figure 118 (c). The new grains form in regions of severe localized deformation.

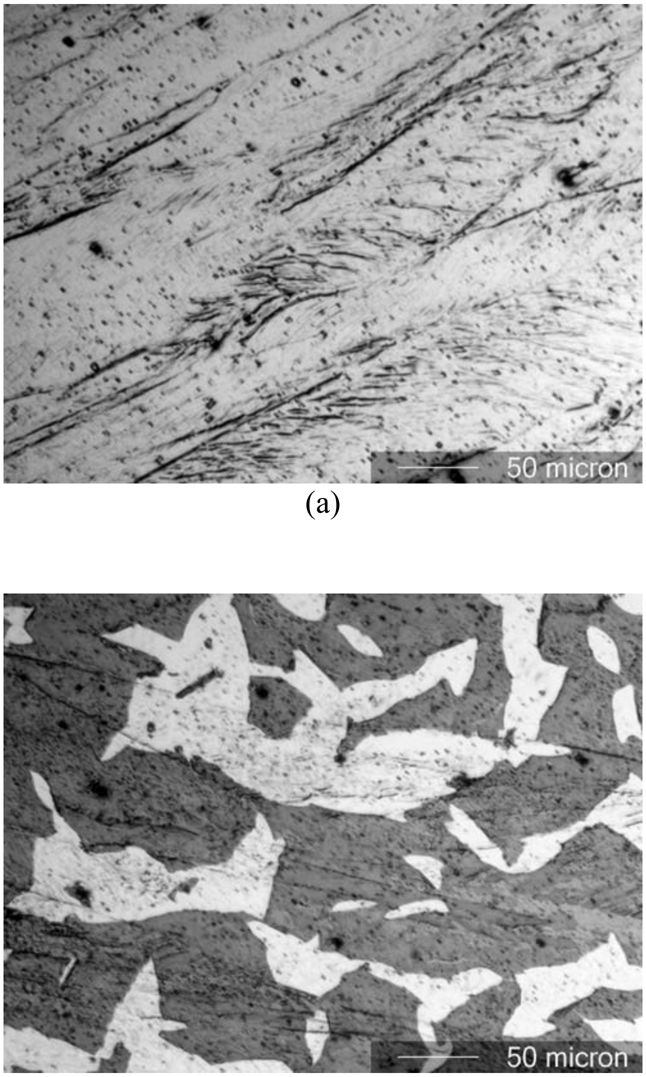

(a)

(b)

Figure 118: Optical micrographs of ECAE 1A IF steel. (a) as-processed, (b) annealed at 550°C

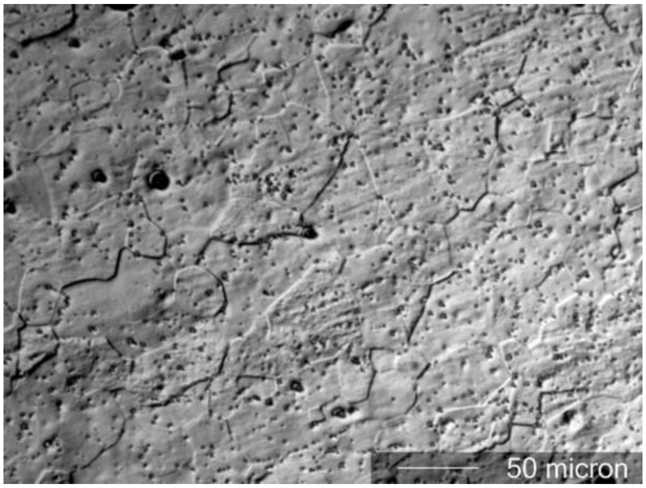

(c)

Figure 118: Continued. (c) annealed at 700°C

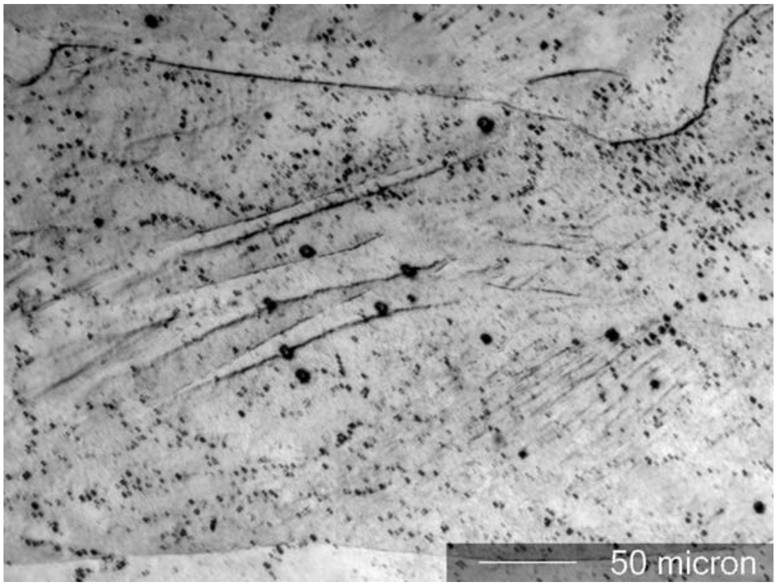

(a)

Figure 119: Optical micrographs of ECAE 2A IF steel. (a) as-processed

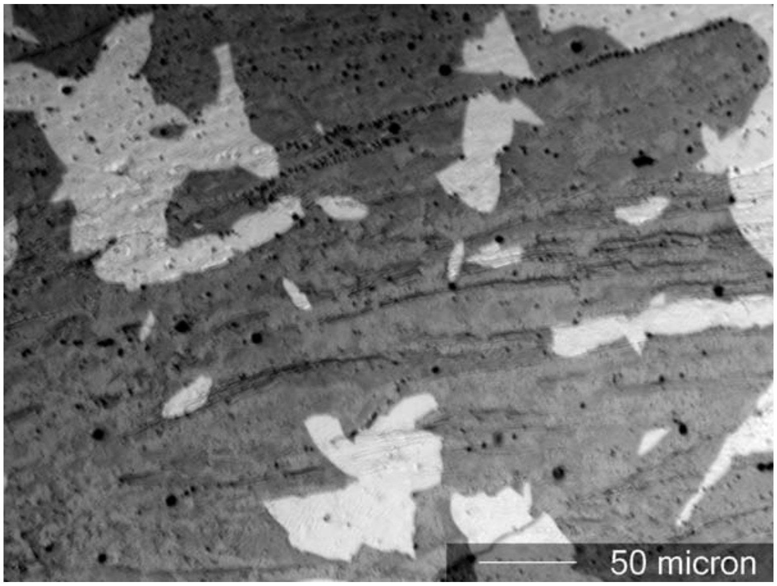

(b)

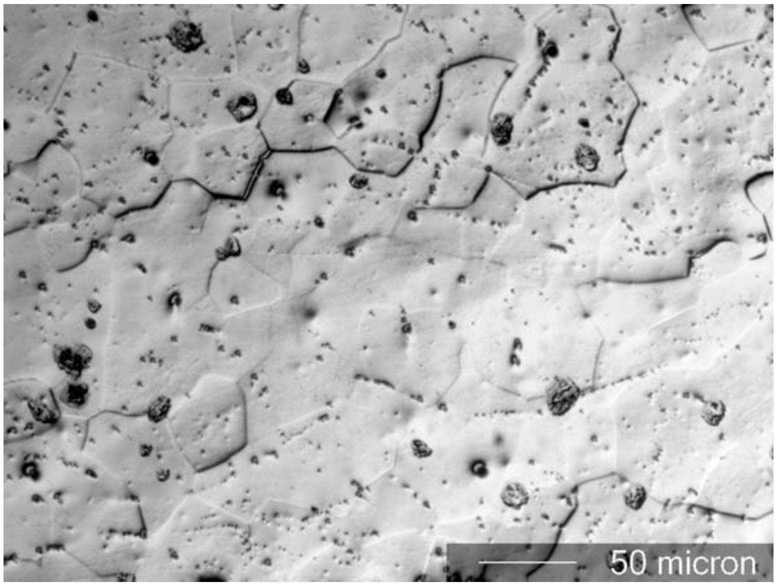

(c)

Figure 119: Continued. (b) annealed at 550°C, (c) annealed at 700°C

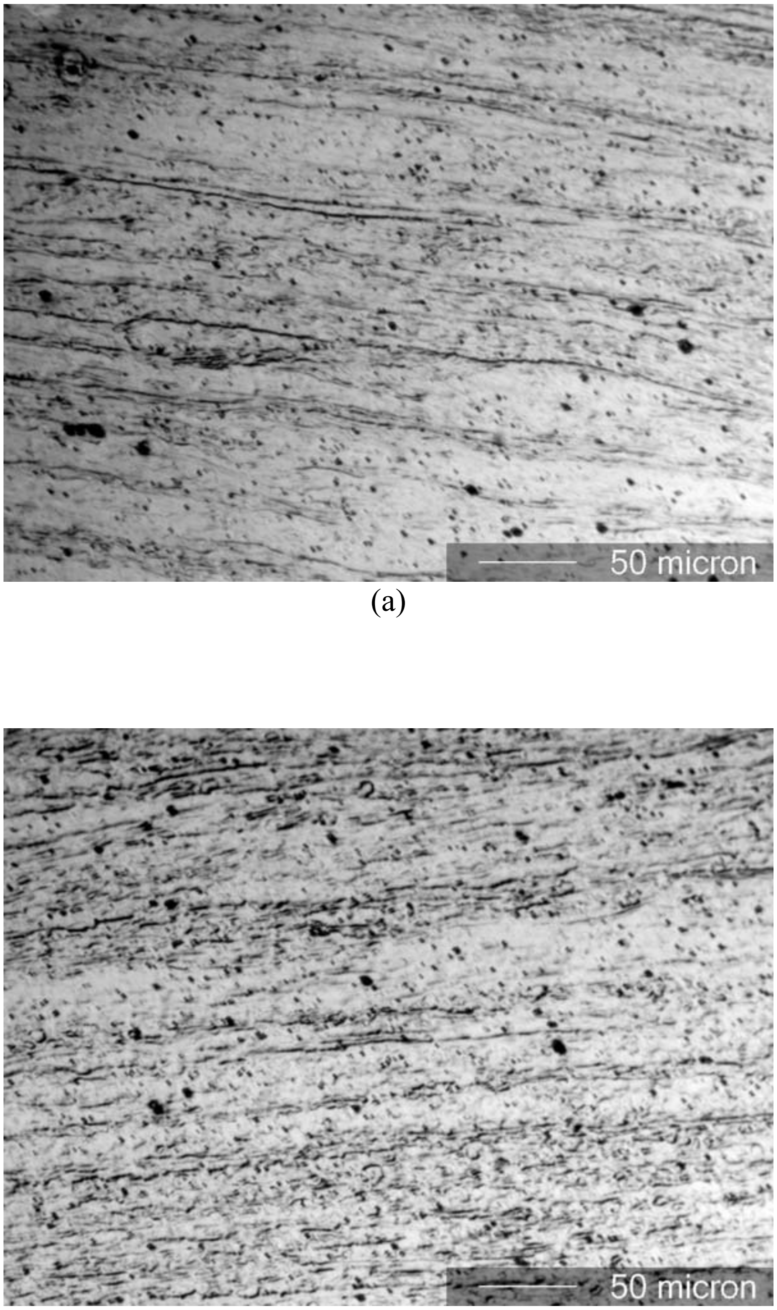

(a)

(b)

Figure 120: Optical micrographs of ECAE 4A IF steel. (a) as-processed, (b) annealed at 550°C

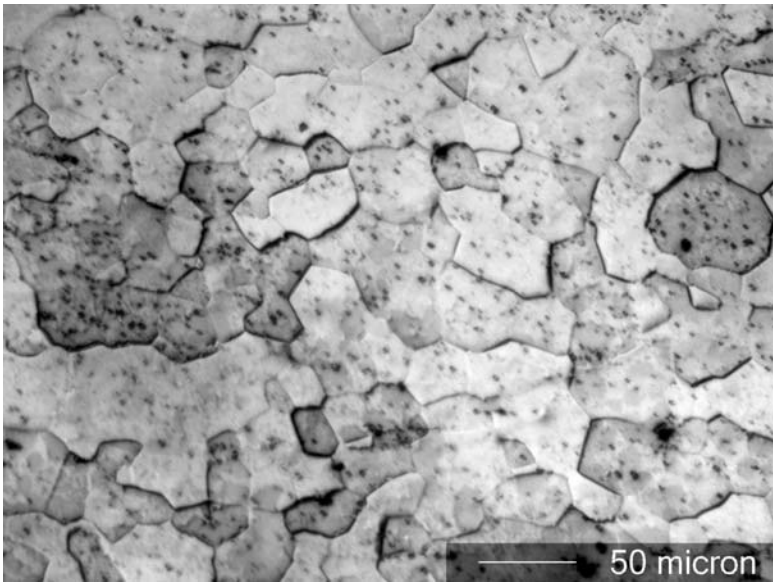

(c)

Figure 120: Continued. (c) annealed at 700°C

Materials processed using Route C' demonstrate a different microstructure. The microstructure obtained at room temperature is more equiaxed in this route, especially at high numbers of passes. At low numbers of passes, i.e. ECAE 4C' (Figure 121), a certain amount of filamentary structure is still visible, but this is almost completely unobservable by ECAE 8C' (Figure 122).

Nucleation of the new grains has started to occur at 550°C, with the nucleation sites developing preferentially along the slip lines of Route C'. As in Route A, grain growth has occurred at 700°C. The grains depicted in Figure 121 (c) and Figure 122 (c) show grains of similar size distribution.

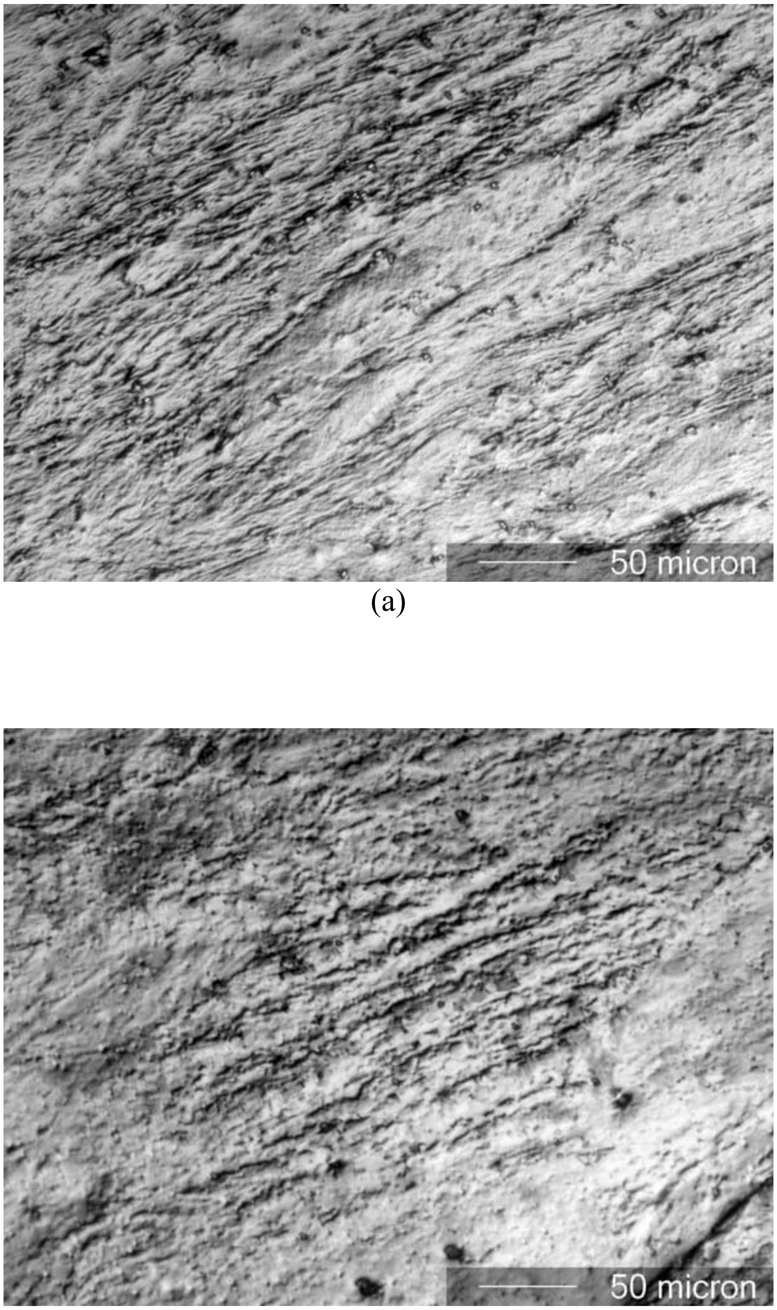

(a)

(b)

Figure 121: Optical micrographs of ECAE 4C' IF steel. (a) as-processed, (b) annealed at 550°C

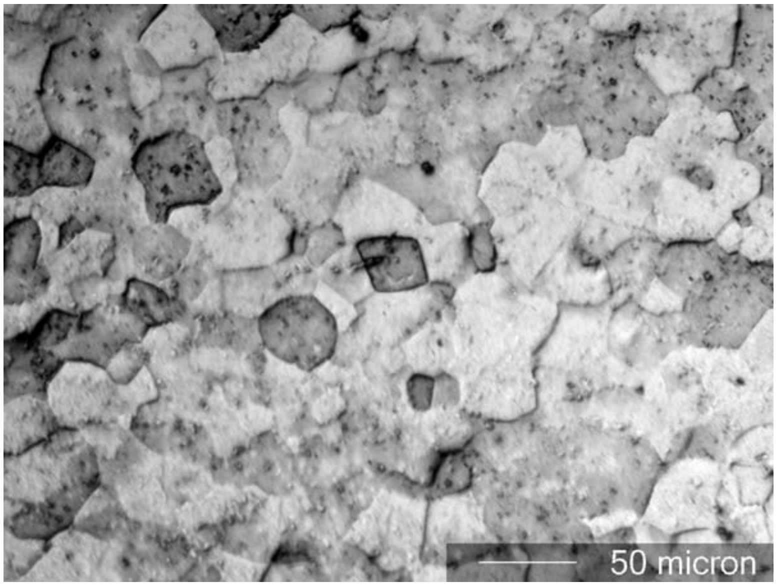

(c)

Figure 121: Continued. (c) annealed at 700°C

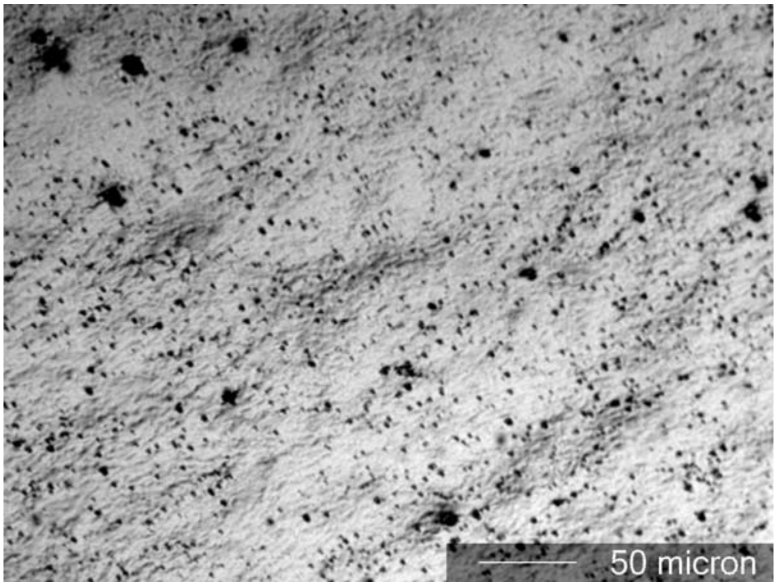

(a)

Figure 122: Optical micrographs of ECAE 8C' IF steel. (a) as-processed

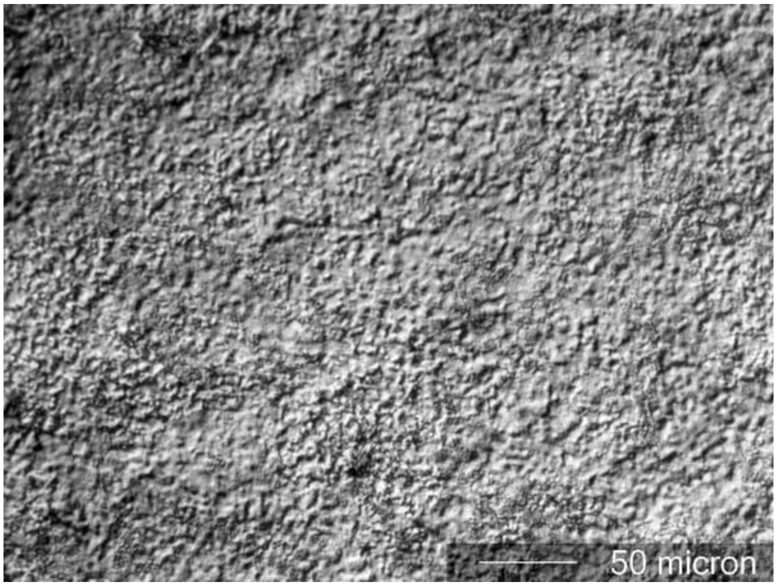

(b)

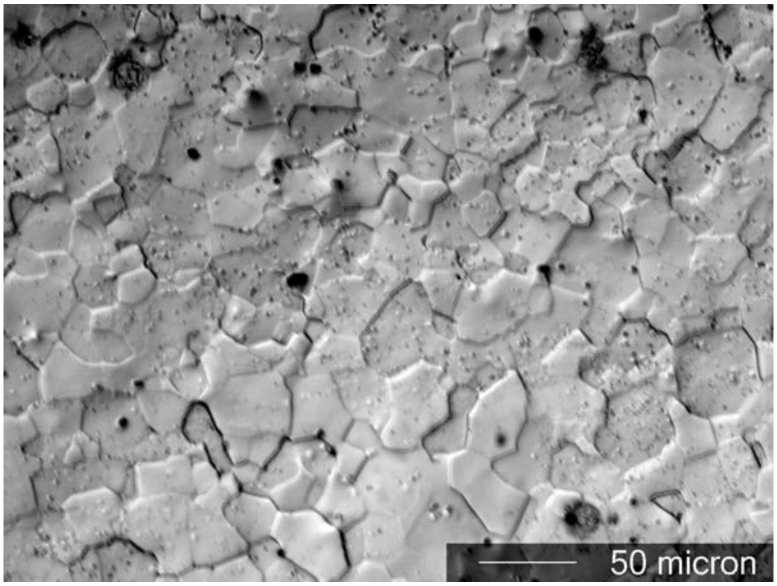

(c)

Figure 122: Continued. (b) annealed at 550°C, (c) annealed at 700°C

Figures 118 – 122 show that grain size increases with increasing temperature, given a constant annealing time. Grain growth lowers surface energy, which means that growth should slow over time given a constant temperature. At high temperatures, samples that were processed with lower levels of strain energy displayed a somewhat inhomogeneous structure. This may be caused by grains that, having already achieved a low surface energy, continue to grow and consume neighboring grains.

Highly worked structures, such as those of ECAE 4C' and ECAE 8C' present numerous sites from which nuclei may form. The subsequent grain growth results in a more homogeneous structure at elevated temperature.

Image manipulation software and a supplemental "plug in" called Image Pro Tool Kit (IPTK) were used to determine the grain area for all specimens that were annealed at 700°C. Calculating grain boundaries was accomplished through a procedure involving the reduction of an optical micrograph to a tracing of grain boundaries (Figures 123 – 124). This "skeleton" image is then put through a global measuring stage within IPTK, resulting in a file containing a large quantity of data relevant to the image.

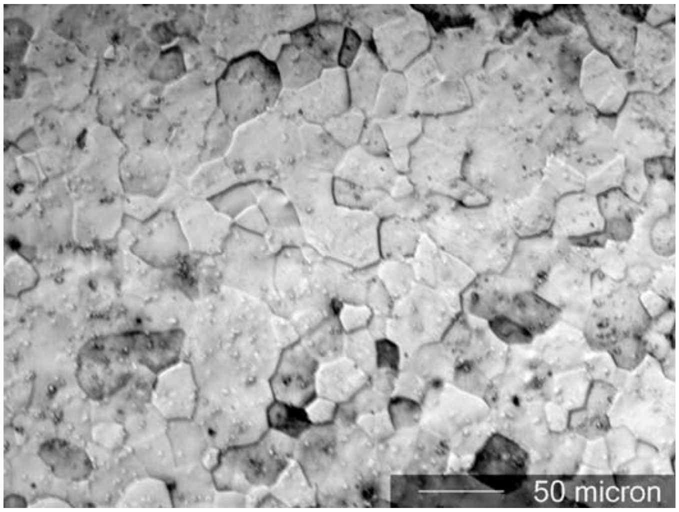

Figure 123: Optical micrograph of ECAE 16E IF steel annealed at 700°C for 90 minutes

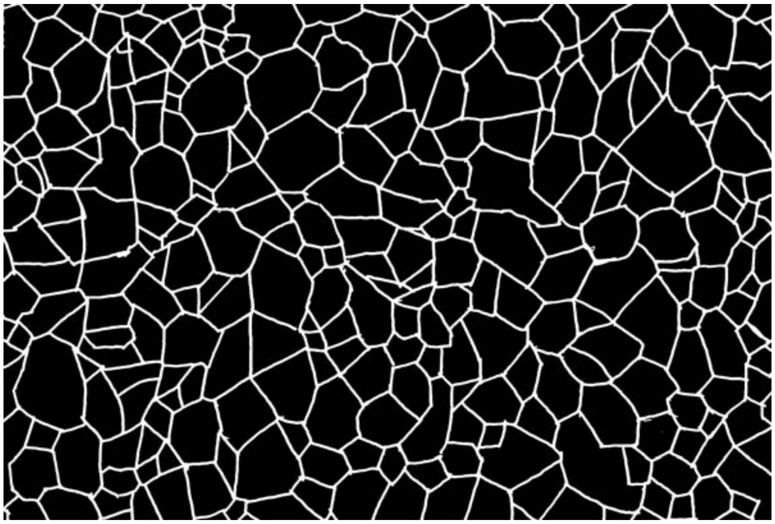

Figure 124: A “skeleton” image of the grain structure of ECAE 16E IF steel annealed at 700°C for 90 minutes

Grain area data was collected from the IPTK output file and imported into Microsoft Excel. With the Excel program, the grain area data was sorted using Boolean operations to produce information that was used to create a histogram of the grain areas. Figures 125 – 133 show the resulting histograms for all of the optical microscopy specimens that were annealed at 700°C for 90 minutes. The grain area, and not its size, was used in this study because the shape of the grains was neither square nor circular.

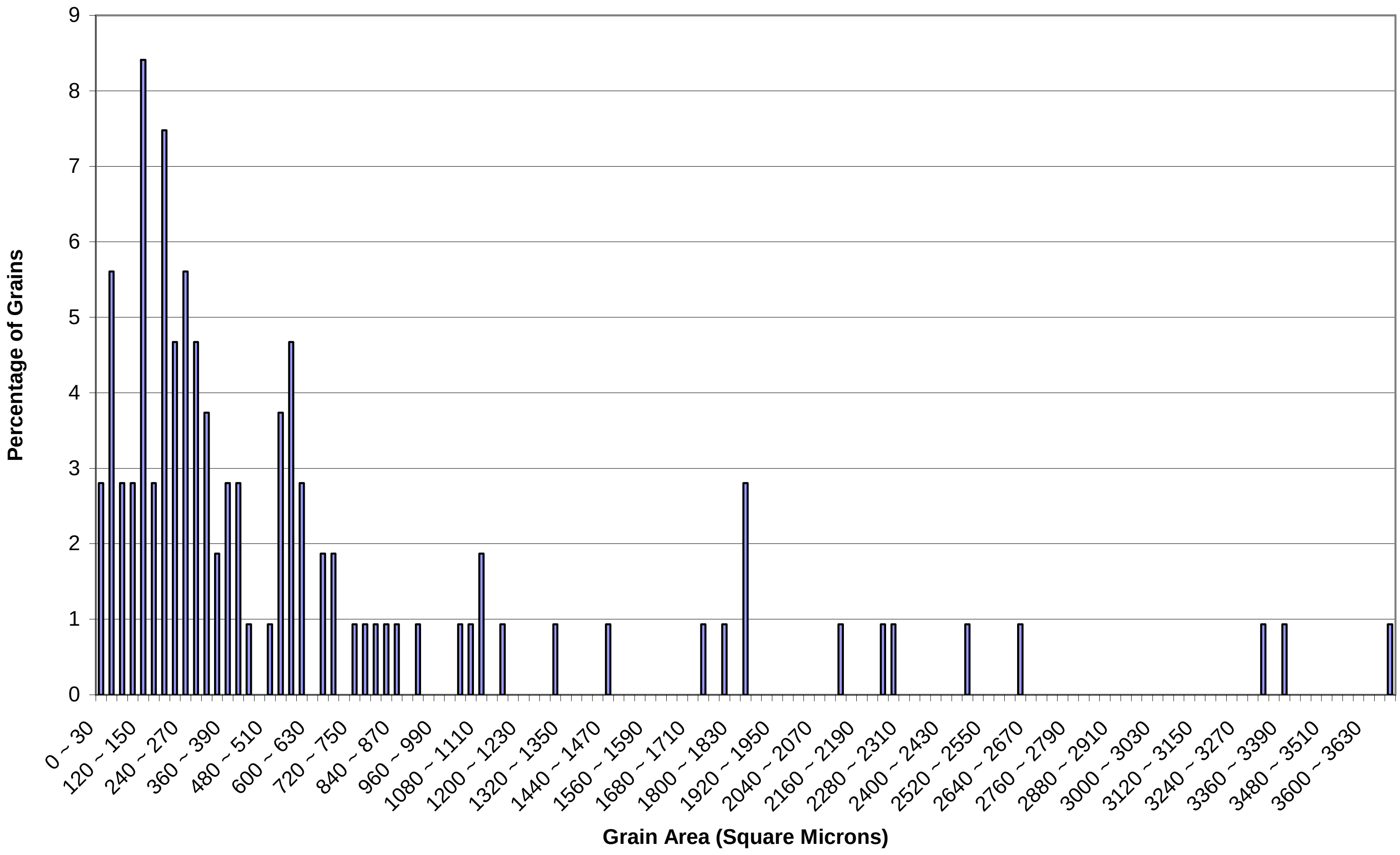

Figure 125: Grain size distribution for ECAE 1A IF steel annealed at 700°C for 90 minutes

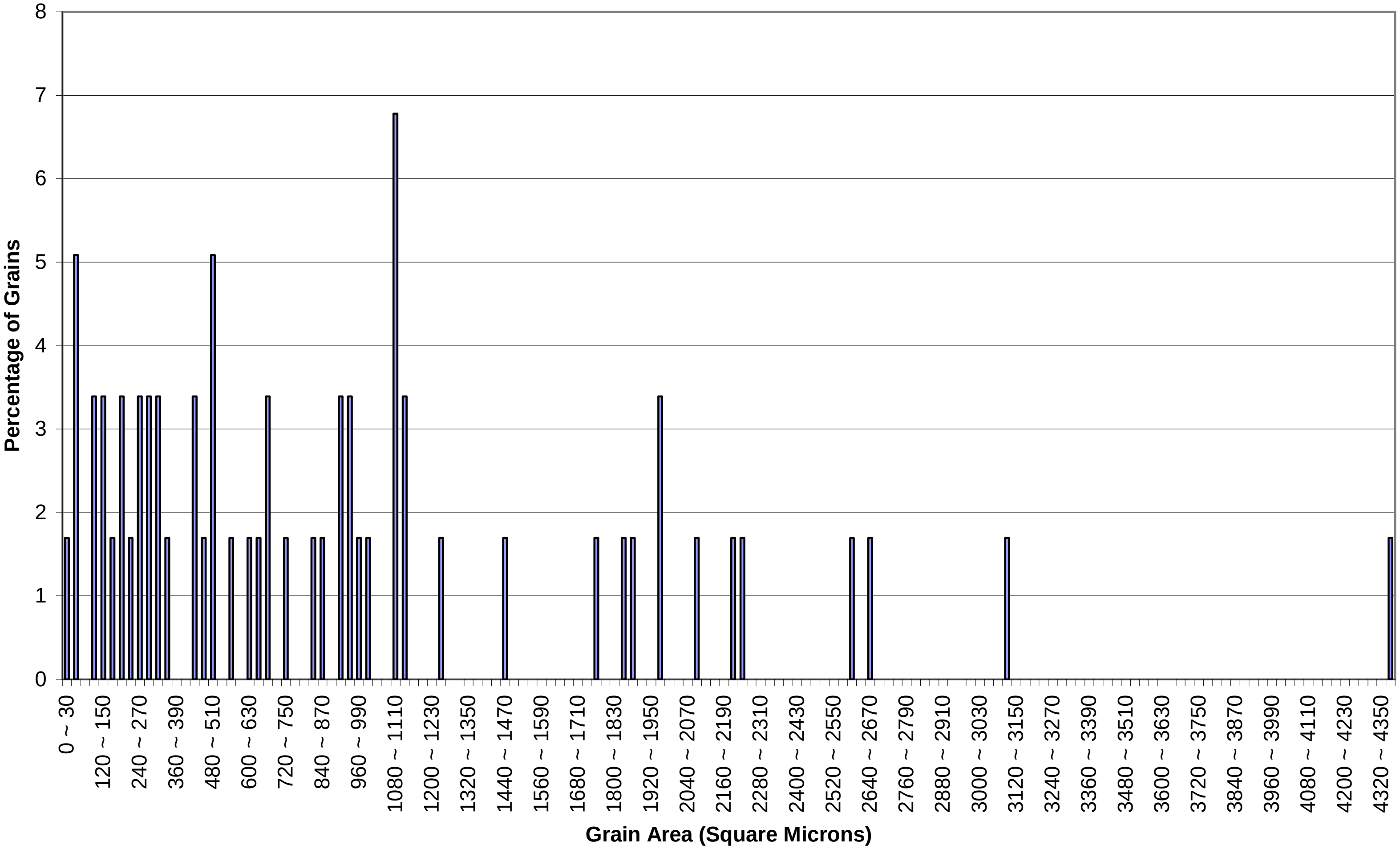

Figure 126: Grain size distribution for ECAE 2A IF steel annealed at 700°C for 90 minutes

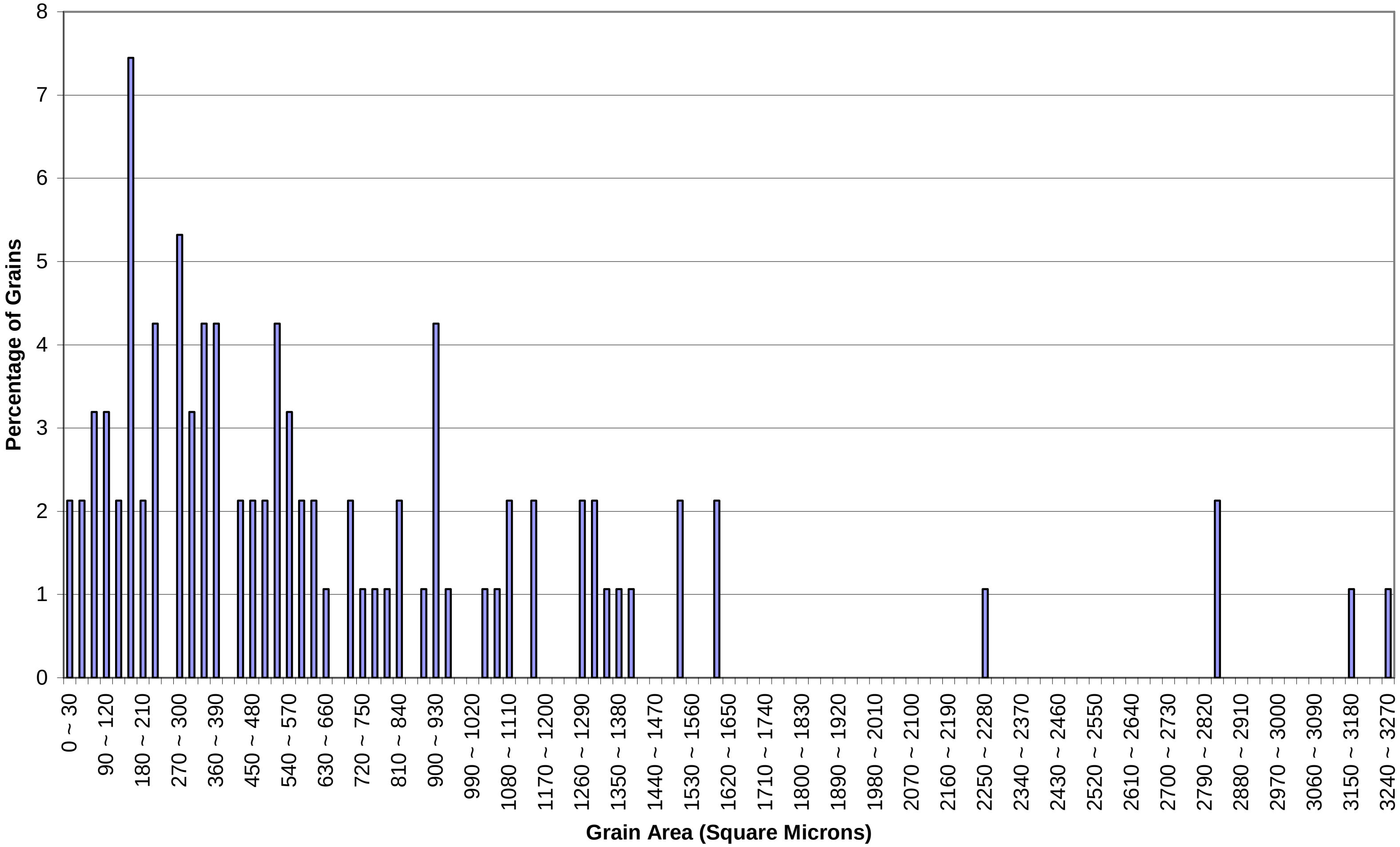

Figure 127: Grain size distribution for ECAE 2B IF steel annealed at 700°C for 90 minutes

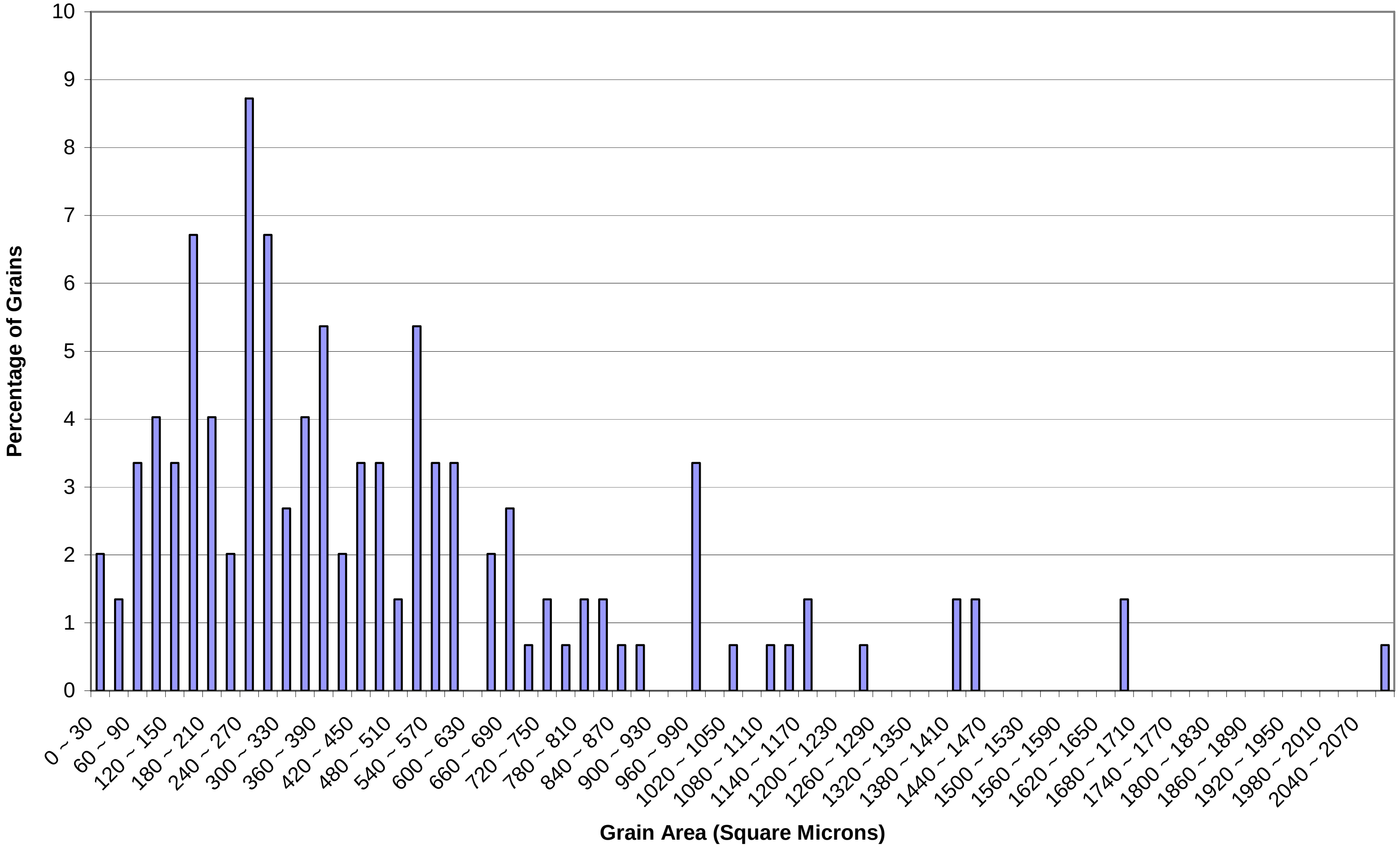

Figure 128: Grain size distribution for ECAE 2C IF steel annealed at 700°C for 90 minutes

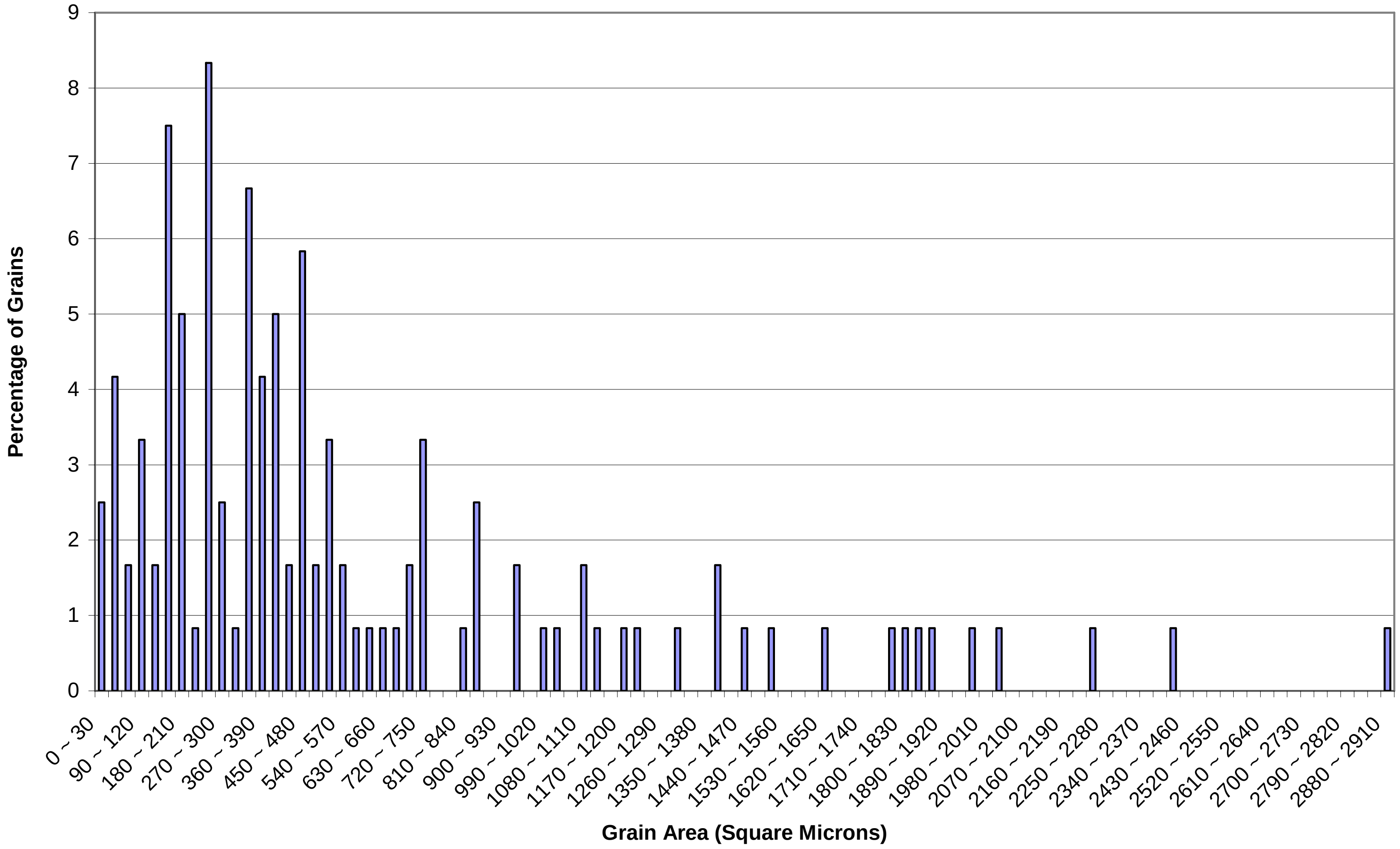

Figure 129: Grain size distribution for ECAE 4A IF steel annealed at 700°C for 90 minutes

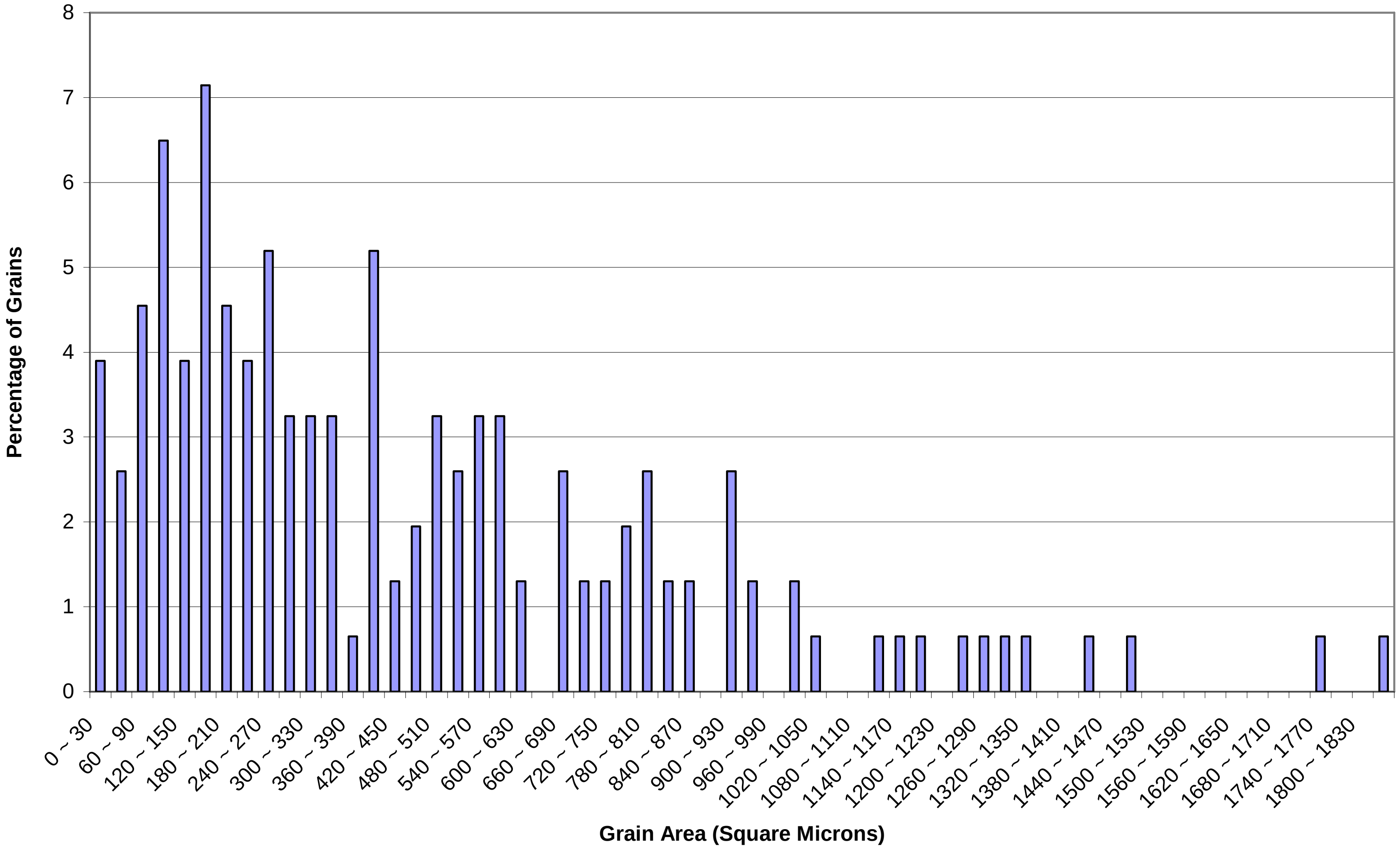

Figure 130: Grain size distribution for ECAE 4B IF steel annealed at 700°C for 90 minutes

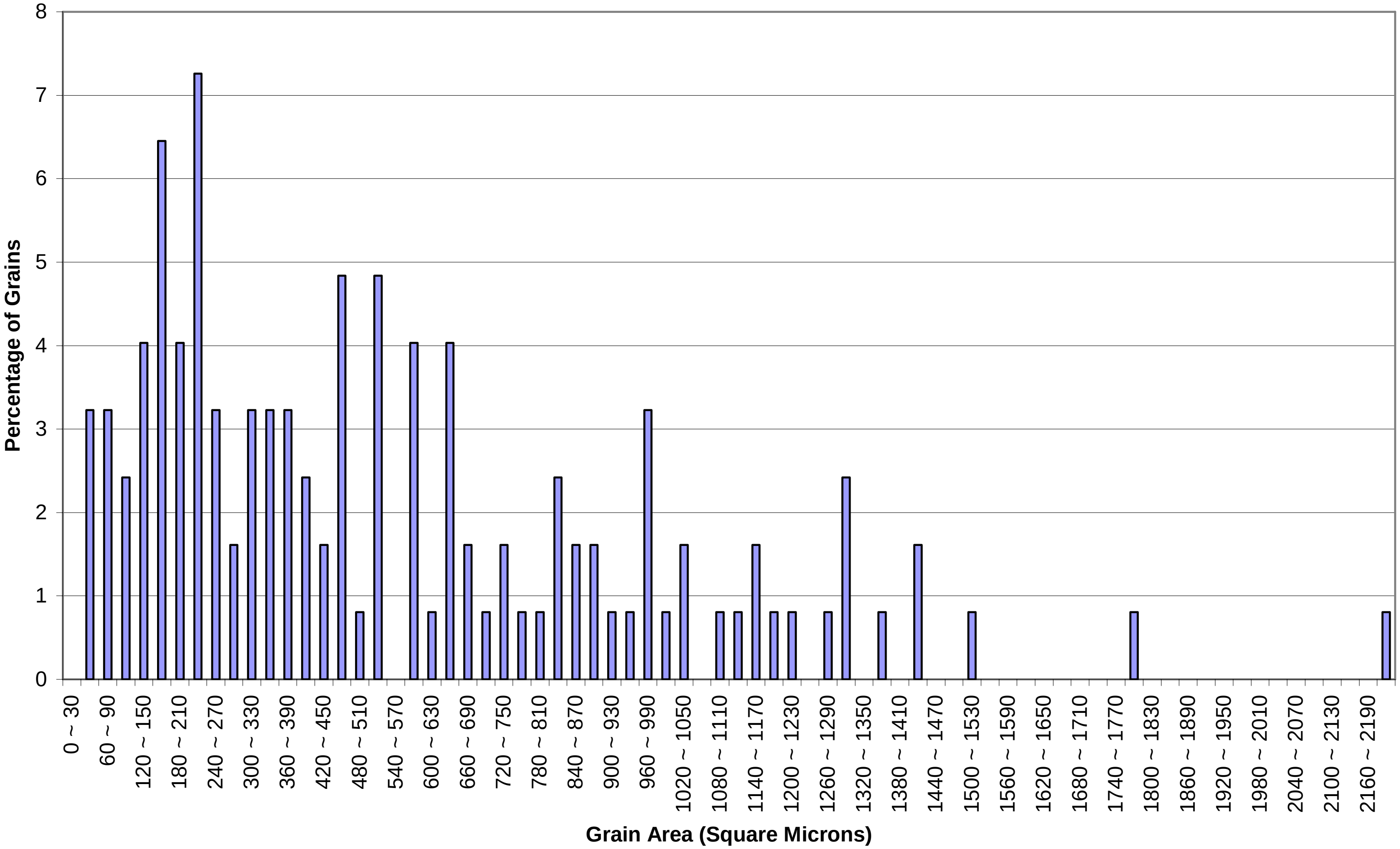

Figure 131: Grain size distribution for ECAE 4C' IF steel annealed at 700°C for 90 minutes

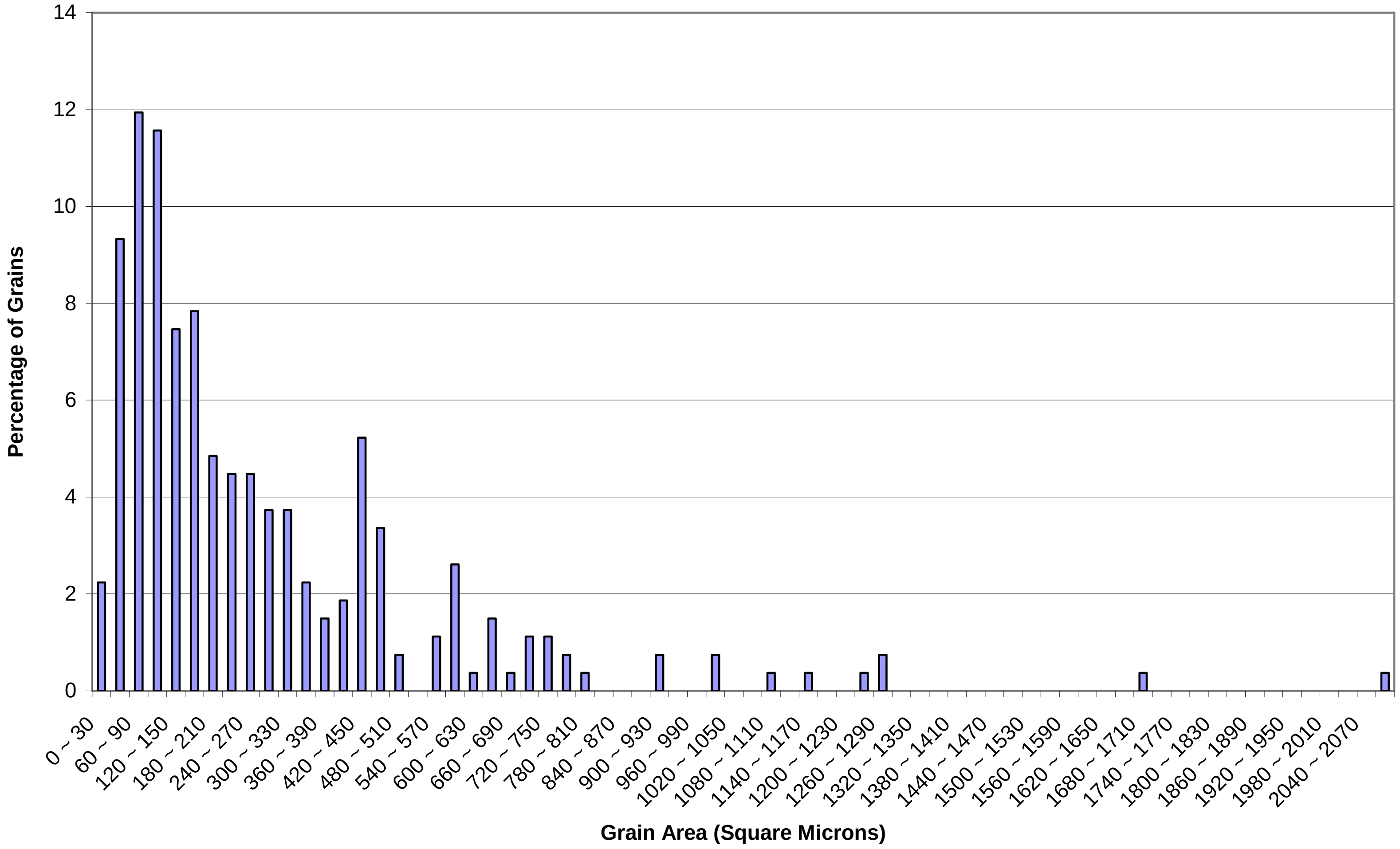

Figure 132: Grain size distribution for ECAE 8C' IF steel annealed at 700°C for 90 minutes

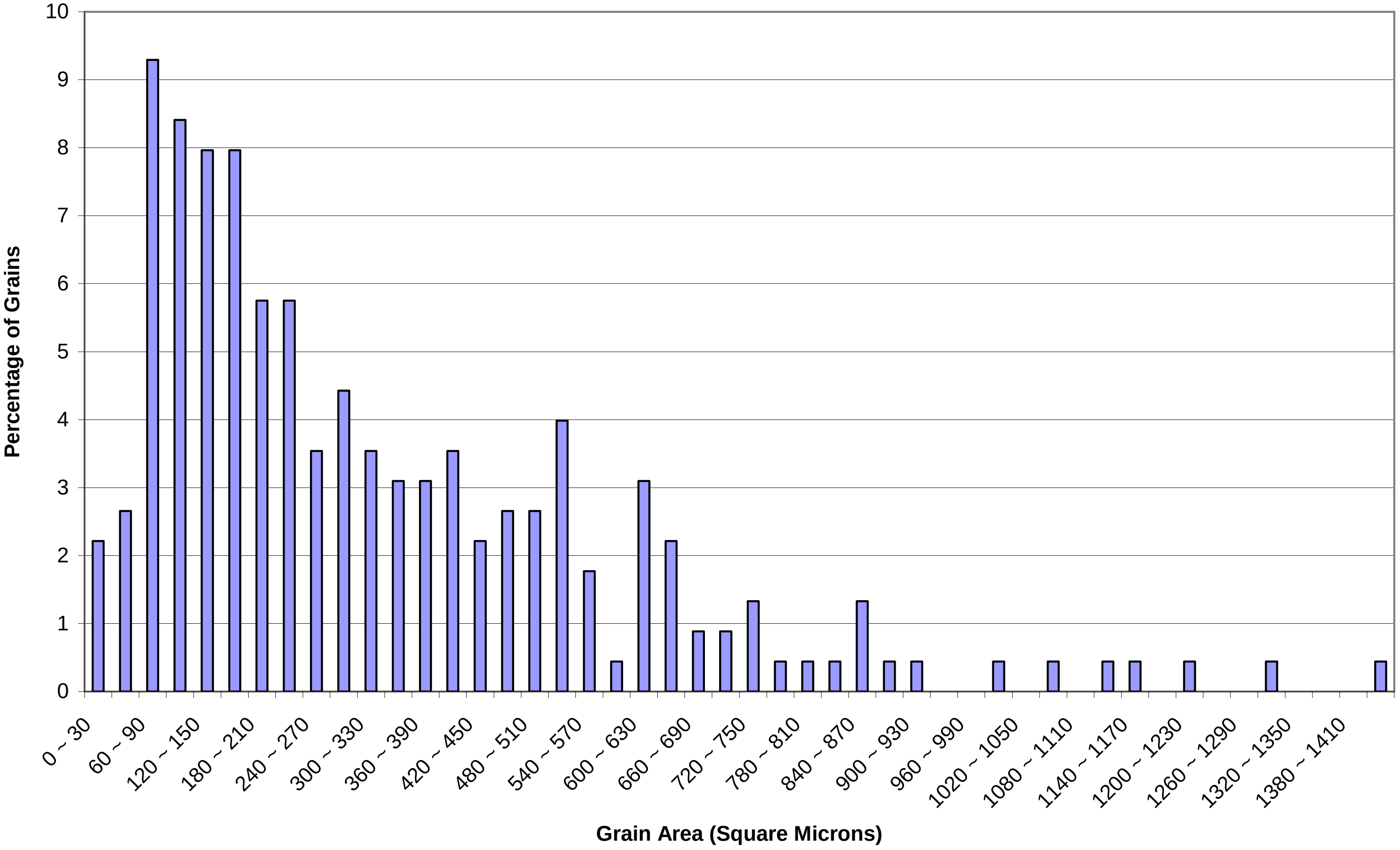

Figure 133: Grain size distribution for ECAE 16E IF steel annealed at 700°C for 90 minutes

When examining the histograms on the previous pages, some features stand out. When the histogram shows a strong, centralized "peak," with few outlying points, the grain area of that specimen is more uniform. A wider histogram peak indicates more variation in the final area of the grains. The histograms of ECAE 8C' and ECAE 16E show relatively uniform grain areas in the ranges of 60 – 90 μm^2 in both cases, while the histogram of ECAE 1A shows a wide variation of grain areas, the majority of which fall into the range of 120 – 150 μm^2. A comparison of the two histograms representing the Route C' cases will demonstrate how the grain area distribution, as well as the grain area, is refined.

5. CONCLUSIONS

Severe plastic deformation through equal channel angular extrusion (ECAE) dramatically improves the yield strength and ultimate tensile strength of interstitial free steel. Ductility at failure, as measured using engineering strain, is generally lowered by SPD, especially at low strain values. Samples of IF steel subjected to many passes of both Route C’ and Route E demonstrated the highest values of yield strength and ultimate tensile strength, and also high ductility at failure. This may be attributed to fine grain structures.

Samples processed using ECAE 8C’ or ECAE 16E demonstrate superior YS and UTS as compared to unprocessed material. In the case of ECAE 8C’, the yield strength is 9.5 times as strong as that of unprocessed material, and 80% as ductile at failure.

Electron microscopy shows that as the strain increases dislocation cells and networks begin to appear. The grains themselves first are elongated, and then begin to evolve based upon which processing route was used. Route A produces elongated grains with high density cell walls. Route B produces a less homogeneous structure of grains that are filamentary and grains that are elongated. Samples processed using Route E result in progressively finer equiaxial grains, ending with grains below 500nm for ECAE 16E.

The recrystallization curves for all samples show that grain growth begins at a temperature of approximately 700°C. Recrystallization for IF steel begins at approximately the same temperature of recrystallization as that of pure iron, 450°C. Vickers microhardness values prior to the point of recrystallization increase as the amount of strain within the specimen increases.

The texture of IF steel is strengthened after ECAE along [111] and [001] and in the direction perpendicular to the transverse plane. Inverse pole figures for Route A show a continuous increase in texture strength along [111] and [001] in the direction perpendicular to the transverse plane. Route B shows a significant increase in texture strength for the same directions, also perpendicular to the transverse plane. In the same directions and orientation, Route C demonstrates a consolidation and strengthening of texture. Route C' produced a varied texture after four passes, but the texture was consolidated along [111] and [001] after eight passes. After eight passes using Route E, the texture strength is at its highest recorded value; Route E after 16 passes yields a highly localized and strong texture along [111] and [001].

When IF steel is annealed it loses much of its as-processed mechanical properties. Yield strength, ultimate tensile strength and, to a lesser extent, ductility at failure, are lowered significantly by annealing. The decrease in mechanical strength is made worse as either the annealing time or temperature is elevated, and the decrease is particularly severe when both are elevated. This behavior is consistent with the results obtained during the analysis of recrystallization in as-processed IF steel.

Interstitial free steel is easy to grind and polish. The softness of the material makes grinding by hand possible, but in order to obtain a uniform polish an automatic polisher/grinder should be used.

The use of Marshall's Reagent as an etchant produced good optical microscopy results. It was determined that an etching time of approximately five to seven seconds after the sample emitted bubbles resulted in the best etch of the material.

Optical microscopy results vary, due to the low carbon content of the material. Good results depend on a high quality polish and proper timing during immersion in the etchant.

Grain structures are most visible in the samples that have been annealed for 90 minutes at a temperature of 700°C, during which grain growth occurs. It is possible to observe nucleation of grains in samples that have been annealed at 550°C.

6. RECOMMENDATIONS FOR FUTURE STUDY

The stress-strain behavior of ECAE-processed IF steel deserves further study.

Additional routes should be examined for their impact on mechanical performance. In particular the routes of C', such as ECAE 16C' deserve further testing.

A systematic analysis of the effect of annealing on processed IF steel should be conducted. Variables of time and temperature need to be evaluated for their impact on mechanical performance.

Optical microscopy of post-process annealed material should be performed in order to examine the grain size distribution.

Specimens should be cut from processed billets in all three planes (flow, transverse and longitudinal) and tested in tension for anisotropic behavior.

Processed specimens should be tested to determine whether there is a relation between the strain path and the Bauschinger effect in IF steel.

REFERENCES

[1] De Messemaeker J, Verlinden B, Van Humbeeck J. Mat Sci Forum 2004;467:1295.

[2] Segal VM. Mat Sci and Eng A 1999;271:322.

[3] Gazder A, Timokhina I, Pereloma E. Mat Sci Forum 2003;426:2693.

[4] De Messemaeker J, Verlinden B, Van Humbeeck J. In: Zhu YT, Langdon TG, Valiev RZ, Semiatin SL, Shin DH, Lowe TC, editors. Ultrafine Grained Materials III. Warrendale, PA: The Minerals, Metals & Materials Society; 2004, p. 595.

[5] De Messemaeker J, Verlinden B, Van Humbeeck J. Mat Let 2004;58:3782.

[6] Jin JH, Huh MY, Chung YH. J Mat Sci 2004;39:5311.

[7] Kim H, Choi M, Chung C, Shin DH. Mat Sci and Eng A 2003;340:243.

[8] Regone W, Jorge Jr AM, Balancin O. Scr Mat 2003;48:773.

[9] Hwang B, Lee HS, Kim YG, Lee S, Ahn BD, Shin DH, Lee CG. Met and Mat Trans A 2005;36A:389.

[10] Haouaoui M, Hartwig KT, Payzant EA. Acta Mater 2005;53:801.

[11] De Messemaeker J, Verlinden B, Van Humbeeck J. Acta Mater 2005;53:4245.

[12] Tsuchida N, Baba E, Nagai K, Tomota Y. Acta Mater 2005;53:265.

[13] Kim HS, Ryu WS, Janecek M, Bail SC, Estrin Y. Adv Eng Mat 2005;7 (No. 1-2):43.

[14] Song R, Ponge D, Kaspar R. Steel Res Int 2004;75 (No. 1):33.

[15] Fukuda Y, Oh-ishi K, Horita Z, Langdon TG. Acta Mater 2002;50:1359.

[16] Shin DH, Park J, Chang SY, Lee Y, Park K. ISIJ Inter 2002;42 (No. 12):1490.

[17] Kim WJ, Kim JK, Choo WY, Hong SI, Lee JD. Mat Lett 2001;51:177.

[18] Shin DH, Kim I, Kim J, Park K. Acta Mater 2001;49:1285.

[19] Shin DH, Seo CW, Kim J, Park K, Choo WY. Scripta Mater 2000;42:695.

[20] Shin DH, Kim W, Choo WY. Scripta Mater 1999;41 (No. 3):259.

[21] Han BQ, Yue S. J Mat Proc Tech 2003;136:100.

[22] Shin DH, Pak J, Kim YK, Park K, Kim Y. Mat Sci and Eng A 2002;325:31.

[23] Kim J, Kim I, Shin DH. Scripta Mater 2001;45:412.

[24] Kim YK, Kim SM, Lee KS, Pak JJ, Shin DH. Met and Mat Int 2001;7 (No. 5):437.

[25] Saito N, Mabuchi M, Nakanishi M, Shigematsu I, Yamauchi G, Nakamura M. J Mat Sci 2001;36:3229.

[26] Barber RE, Dudo T, Yasskin PB, Hartwig KT. Scripta Mater 2004;51:373.

[27] Suś-Ryszkowska M, Wejrzenowski T, Pakiela Z, Kurzydłowski KJ. Mat Sci & Eng A 2004;369:151.

[28] Shin DH, Kim J, Oh Y, Park K. Mat Sci Forum. 2003;426:2801.

[29] Semiatin SL, DeLo DP. Mat & Design. 2000;21:311.

[30] Storojeva L, Ponge D, Kaspar R, Raabe D. Acta Mater 2004;52:2209.

[31] Mughrabi H, Höppel HW, Kautz M, Valiev RZ. Mat Res and Adv Tech2003;94 (No. 10):1079.

[32] Reed-Hill RE, Abbaschian R. Physical Metallurgy Principles. Boston: PWS Publishing Company;1998.

[33] Nave MD, Barnett MR. Mat Sci & Eng A 2004;386:244.

[34] Han BQ, Lavernia EJ, Mohamed FA. Metall and Mat Trans A 2004;35A:1343.

[35] Chen QZ, Duggan BJ. Metall and Mat Trans A 2004;35A:3423.

[36] Ferrasse S, Segal VM, Kalidindi SR, Alford A. Mat Sci & Eng A 2004;368:28.

[37] Metallography: An Introduction. Metallography and Microstructures, Vol. 9, ASM Handbook. Materials Park, OH: ASM International, 2004, p.26.

[38] The Light Alloy Processing Group of University of Manchester (2004), Equal Channel Angular Extrusion. Retrieved September 22, 2005 from http://www2.umist.ac.uk/material/research/lap/ECAE.html

[39] Callister Jr WD. Materials Science and Engineering, an Introduction. New York, NY: John Wiley & Sons, Inc; 1997.

[40] Radiation Safety Office of Indiana University – Bloomington (2003), Radiation safety guide. Retrieved September 22, 2005 from http://www.research.indiana.edu/rschcomp/radsafety/x-ray%20guide%202004.htm

APPENDIX

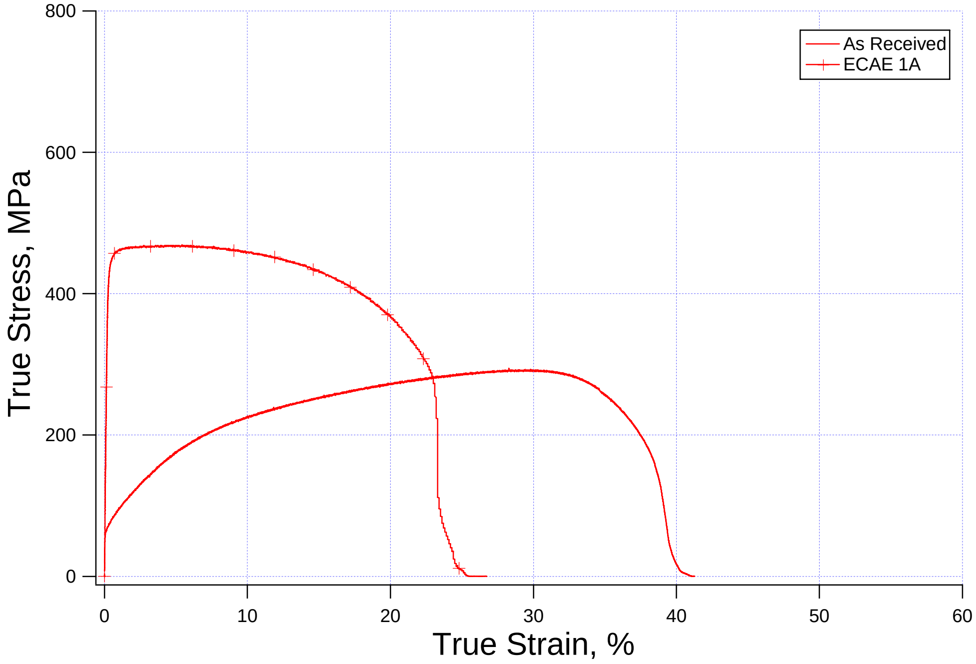

Figure 134: True stress vs. true strain behavior of IF steel after ECAE 1A processing

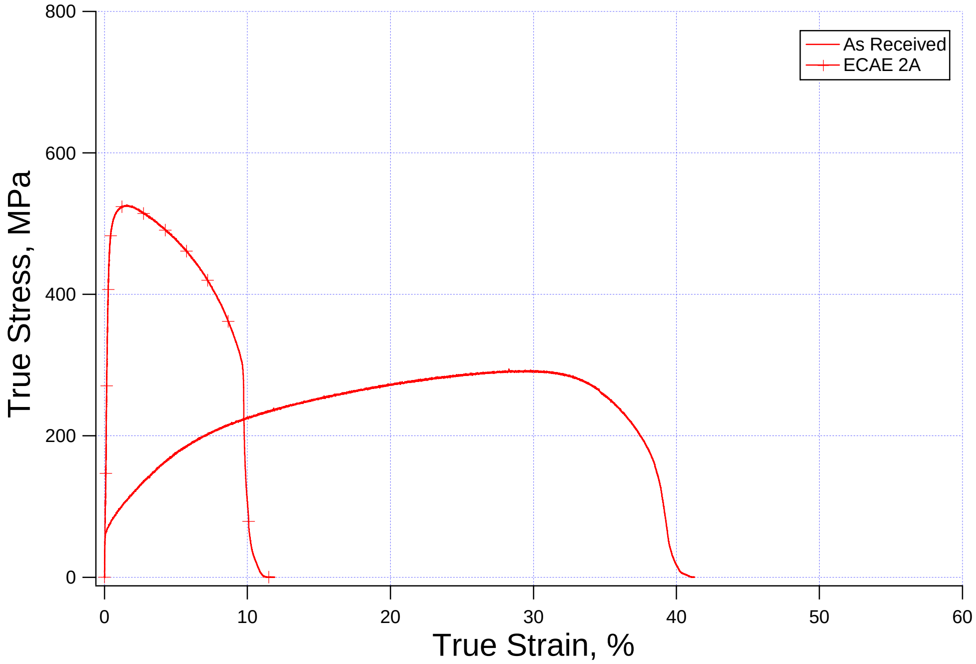

Figure 135: True stress vs. true strain behavior of IF steel after ECAE 2A processing

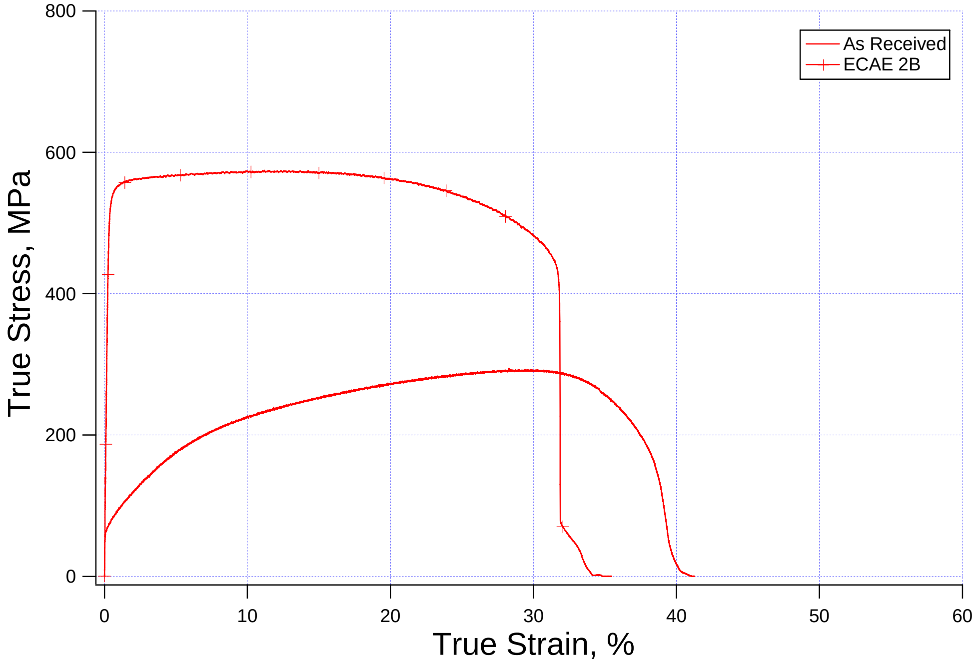

Figure 136: True stress vs. true strain behavior of IF steel after ECAE 2B processing

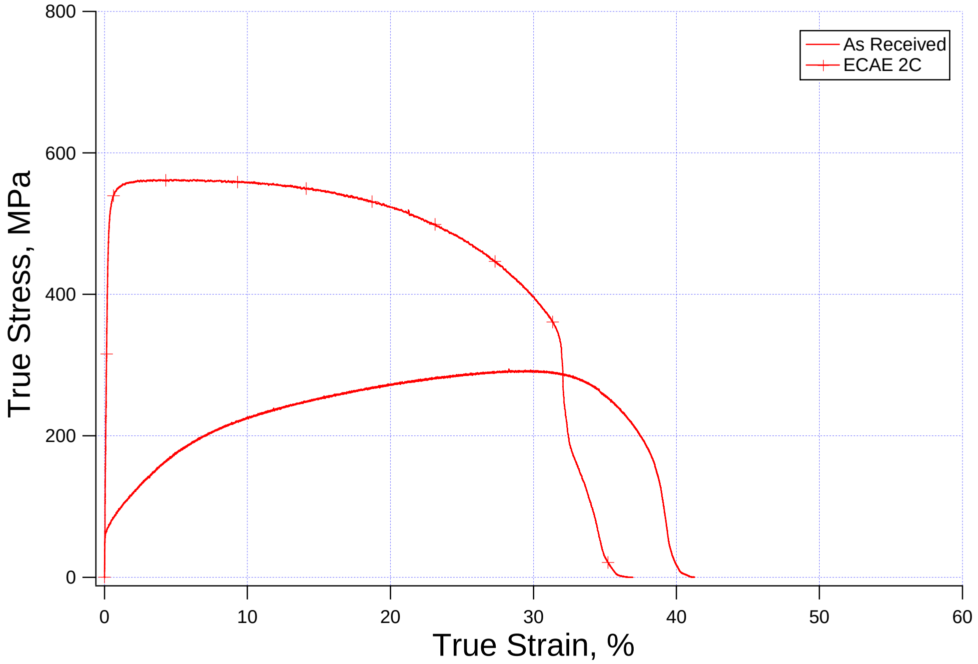

Figure 137: True stress vs. true strain behavior of IF steel after ECAE 2C processing

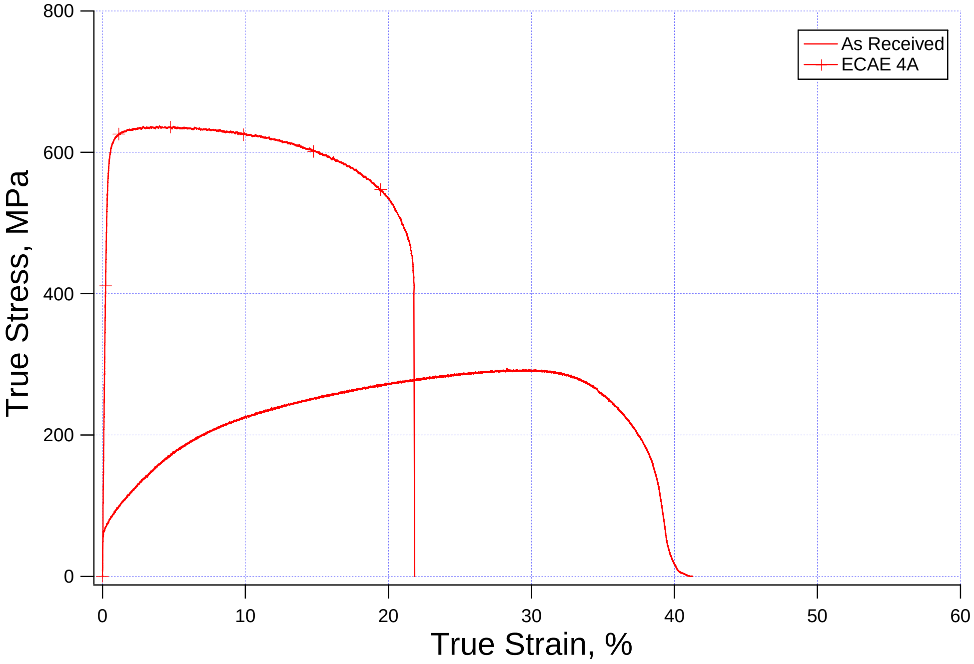

Figure 138: True stress vs. true strain behavior of IF steel after ECAE 4A processing

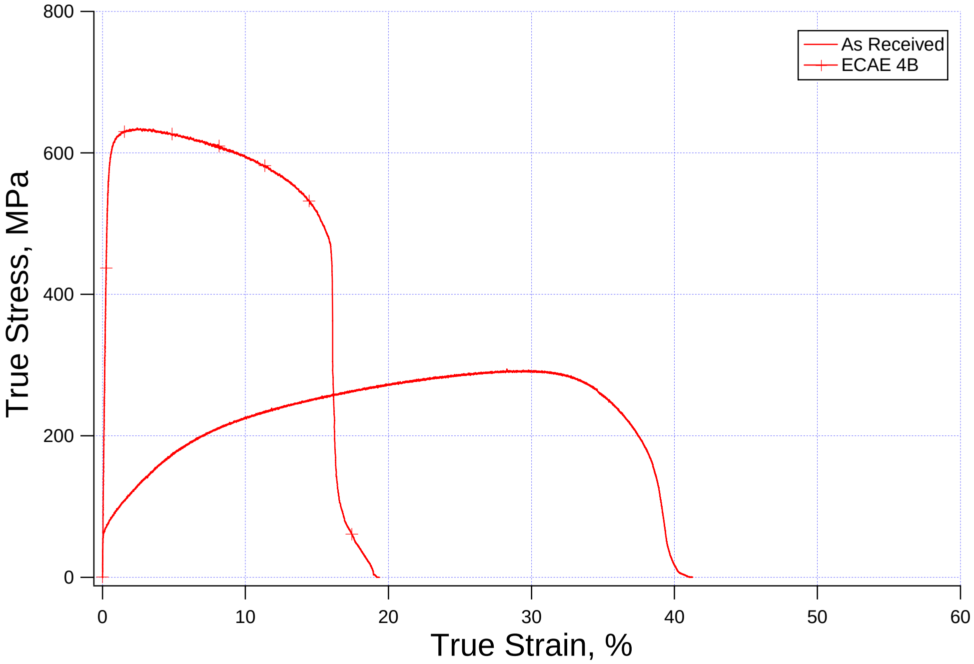

Figure 139: True stress vs. true strain behavior of IF steel after ECAE 4B processing

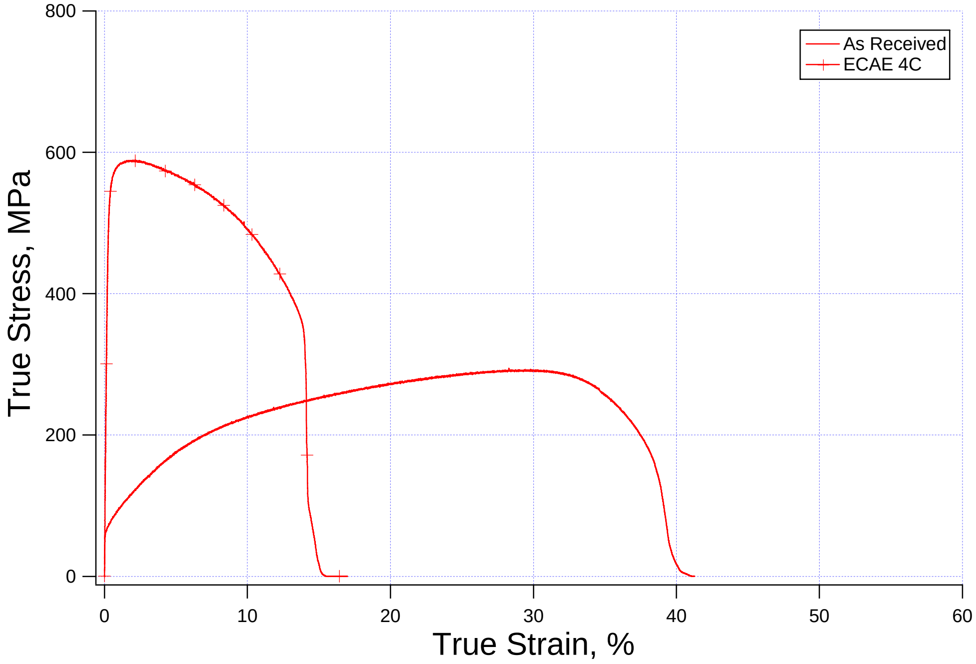

Figure 140: True stress vs. true strain behavior of IF steel after ECAE 4C processing

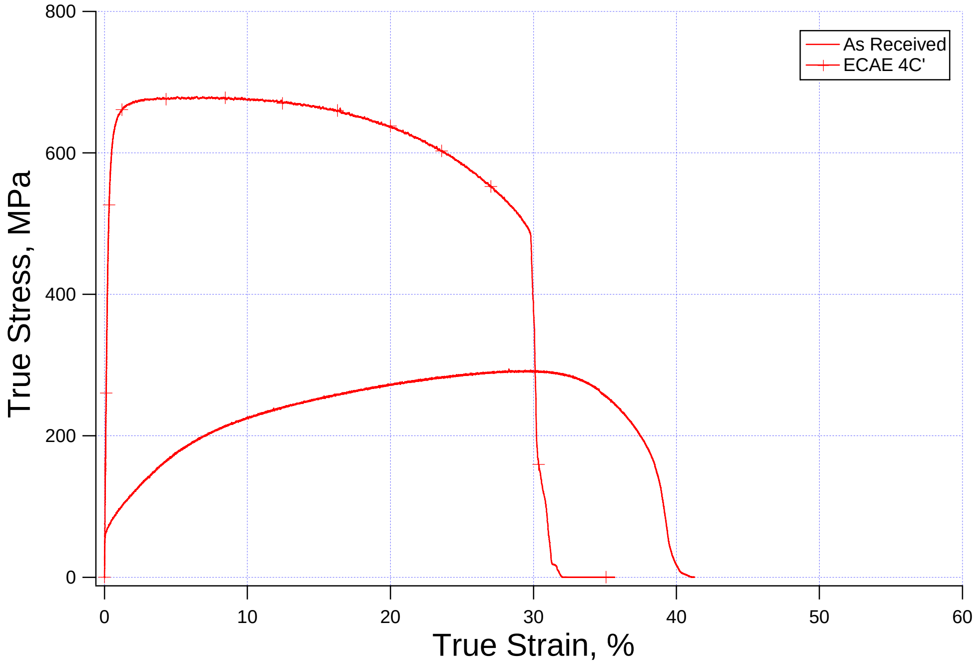

Figure 141: True stress vs. true strain behavior of IF steel after ECAE 4C' processing

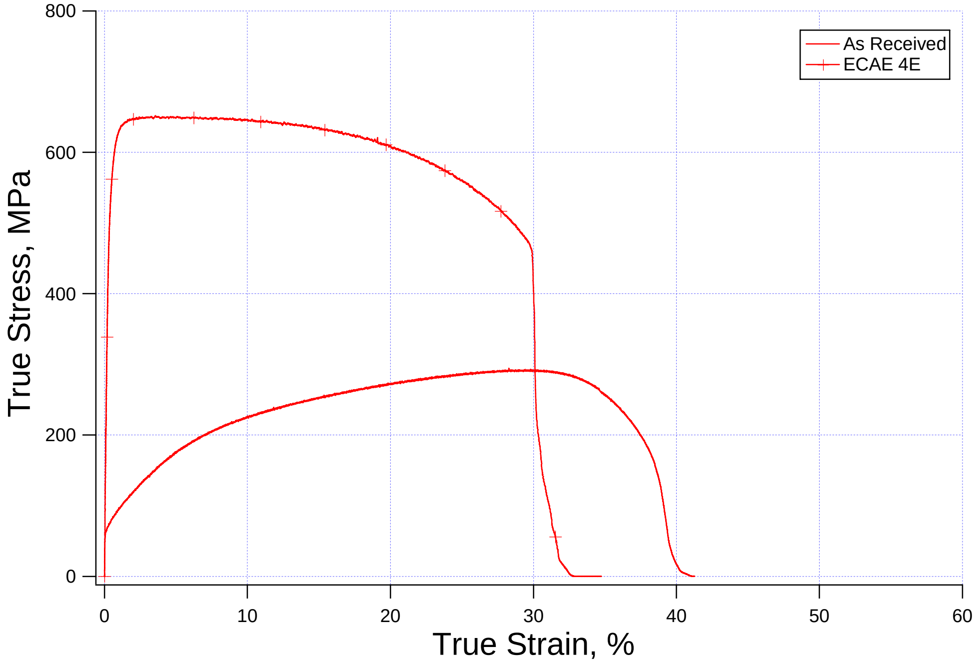

Figure 142: True stress vs. true strain behavior of IF steel after ECAE 4E processing

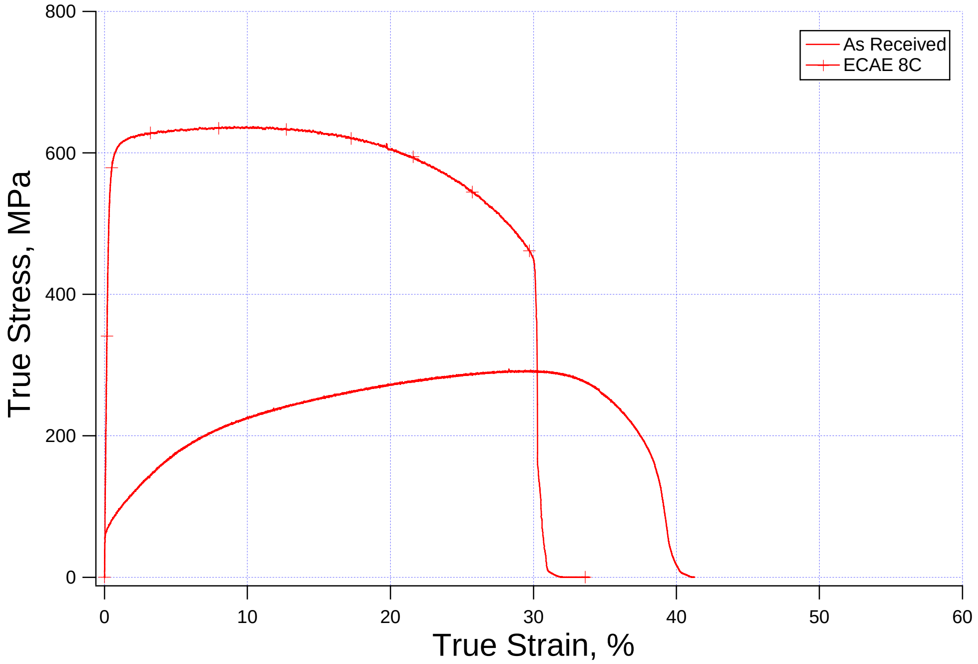

Figure 143: True stress vs. true strain behavior of IF steel after ECAE 8C processing

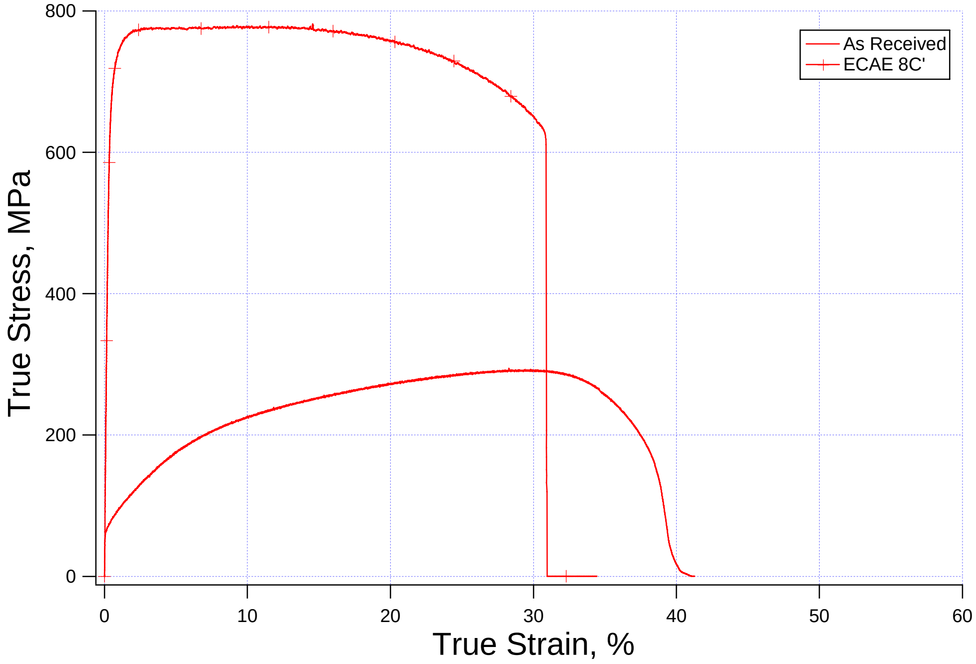

Figure 144: True stress vs. true strain behavior of IF steel after ECAE 8C' processing

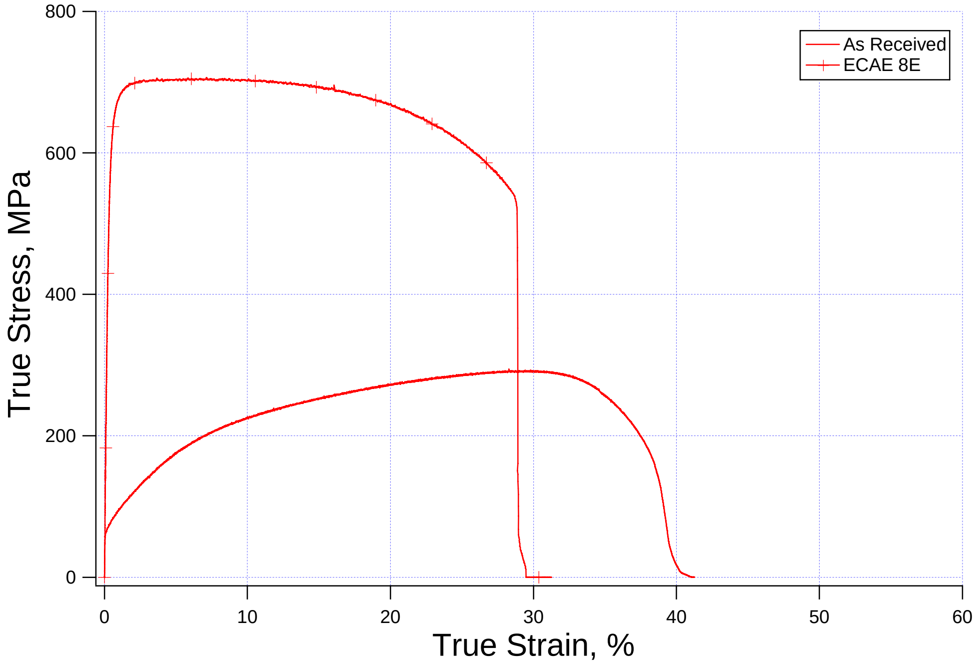

Figure 145: True stress vs. true strain behavior of IF steel after ECAE 8E processing

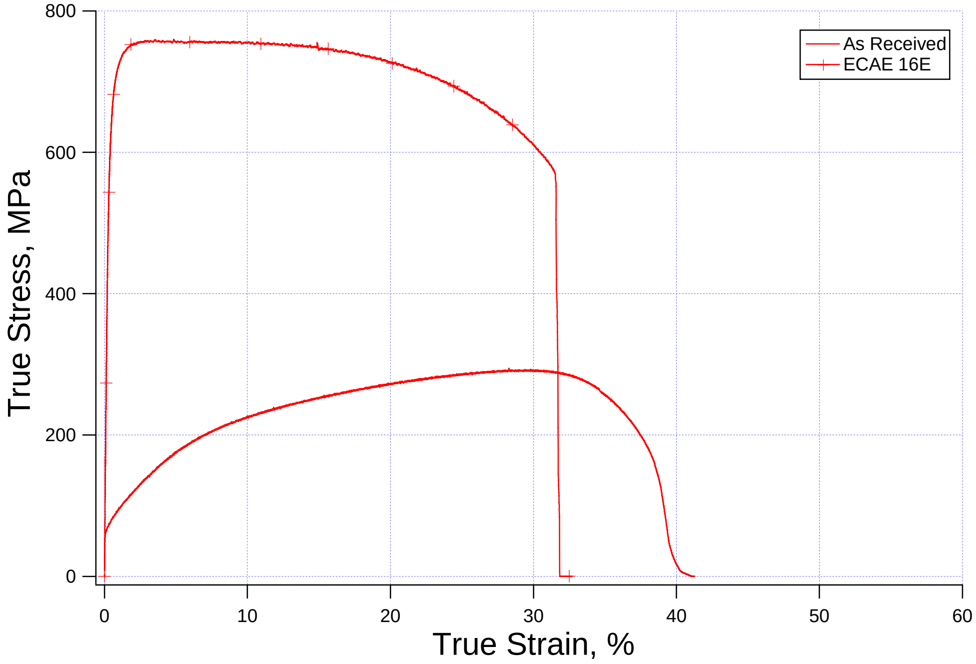

Figure 146: True stress vs. true strain behavior of IF steel after ECAE 16E processing

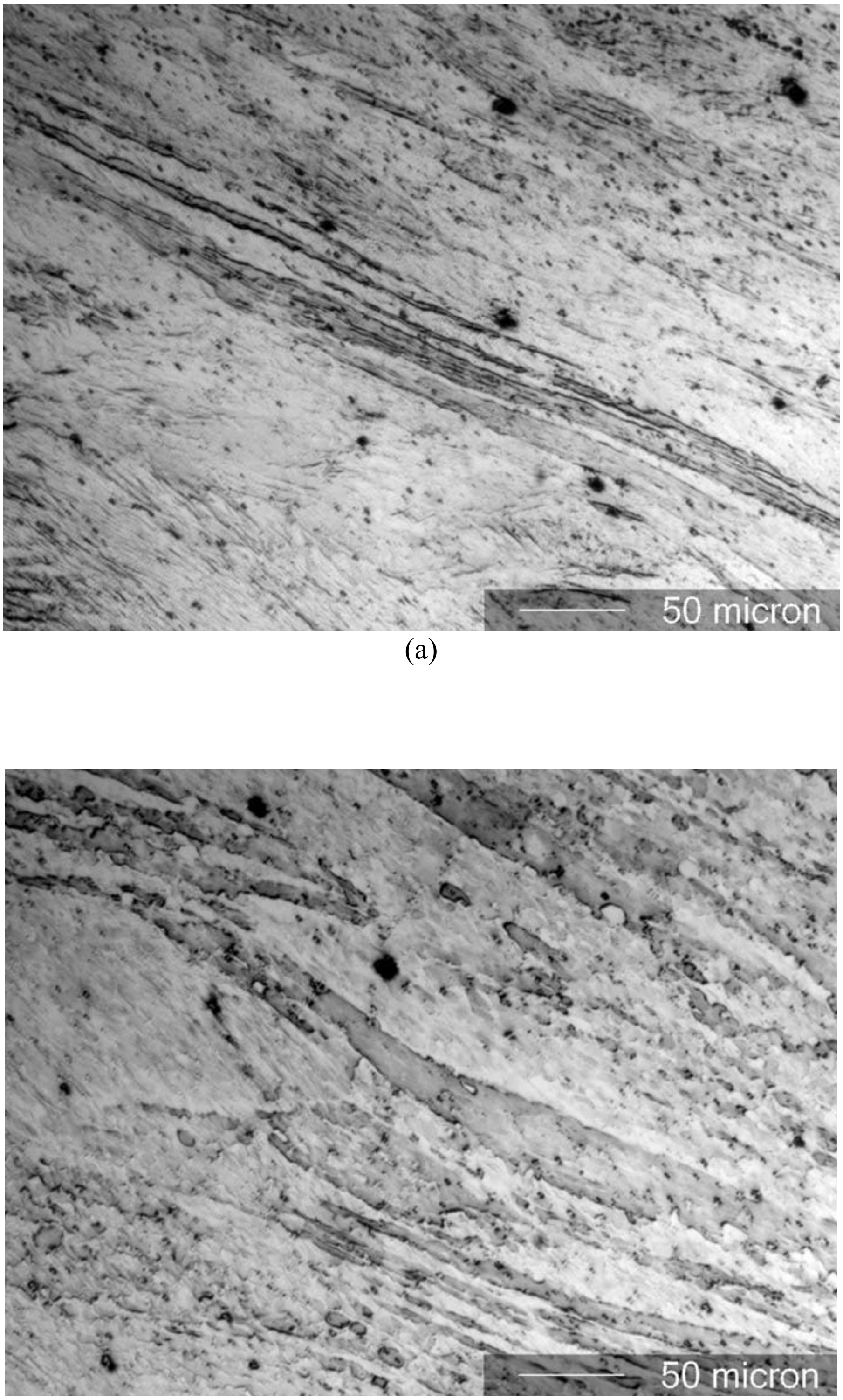

(a)

(b)

Figure 147: Optical micrographs of ECAE 2B IF steel. (a) as-processed, (b) annealed at 550°C

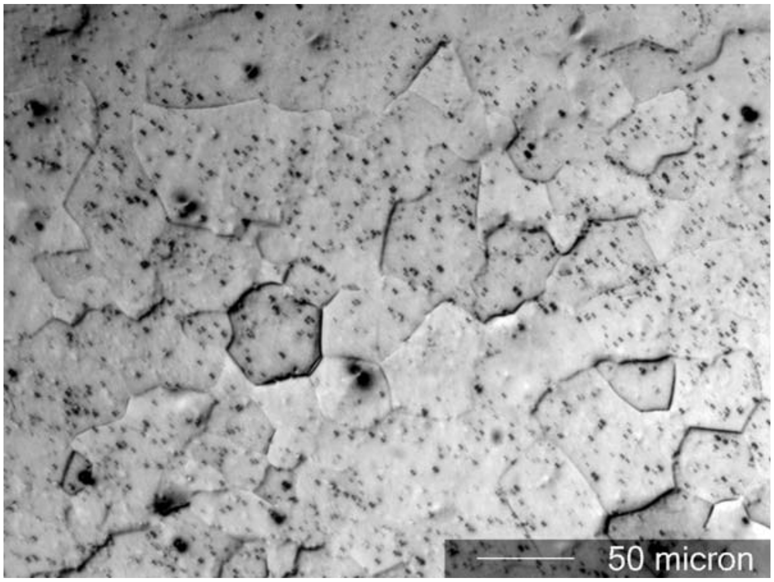

(c)

Figure 147: Continued. (c) annealed at 700°C

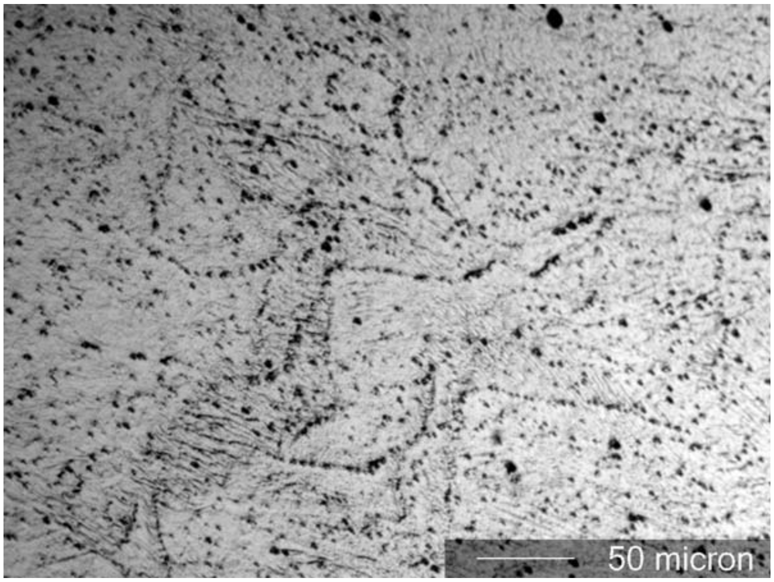

(a)

Figure 148: Optical micrographs of ECAE 2C IF steel. (a) as-processed

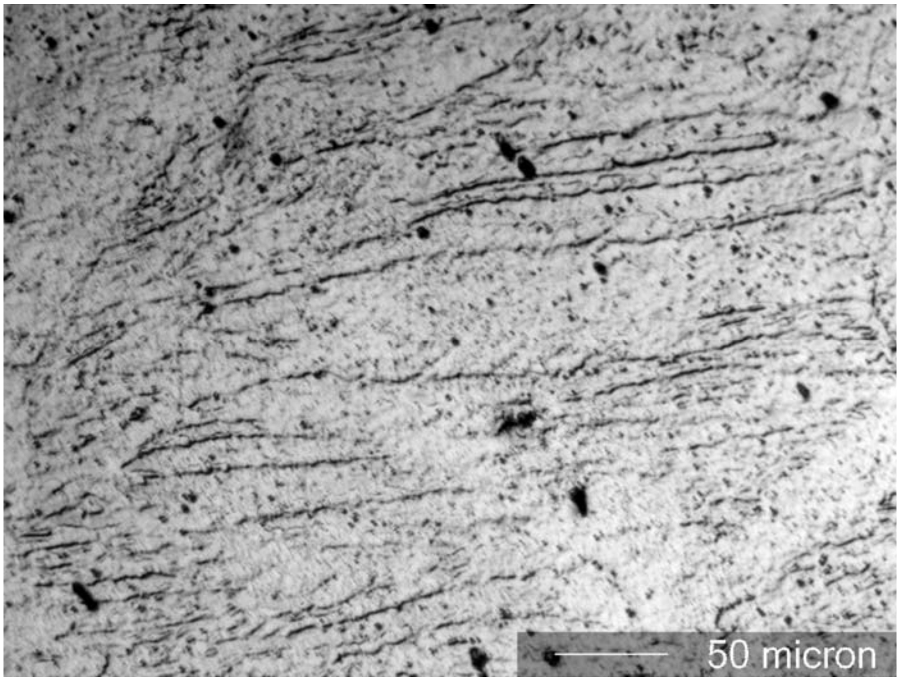

(b)

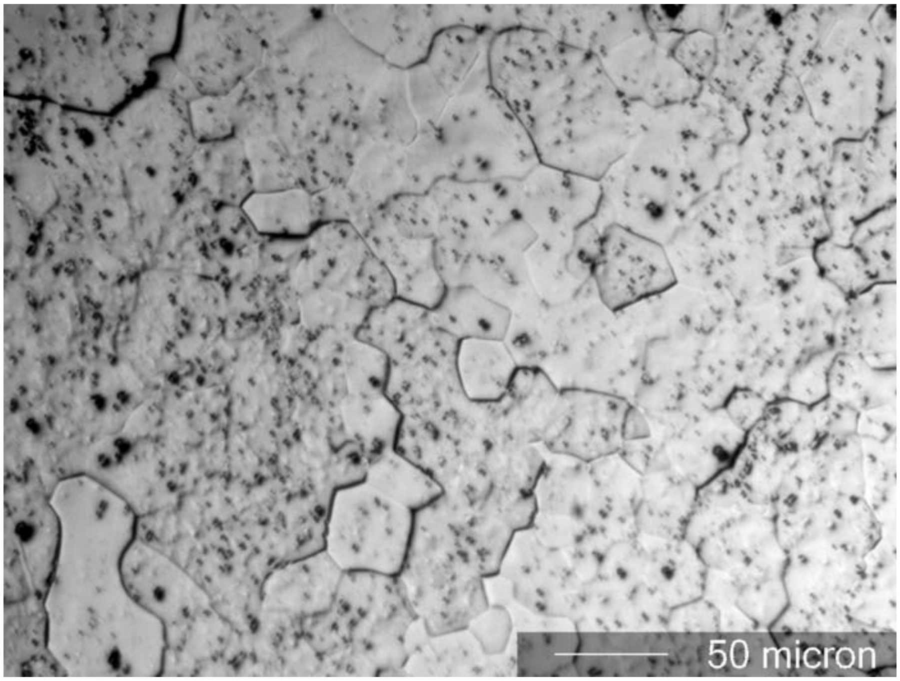

(c)

Figure 148: Continued. (b) annealed at 550°C, (c) annealed at 700°C

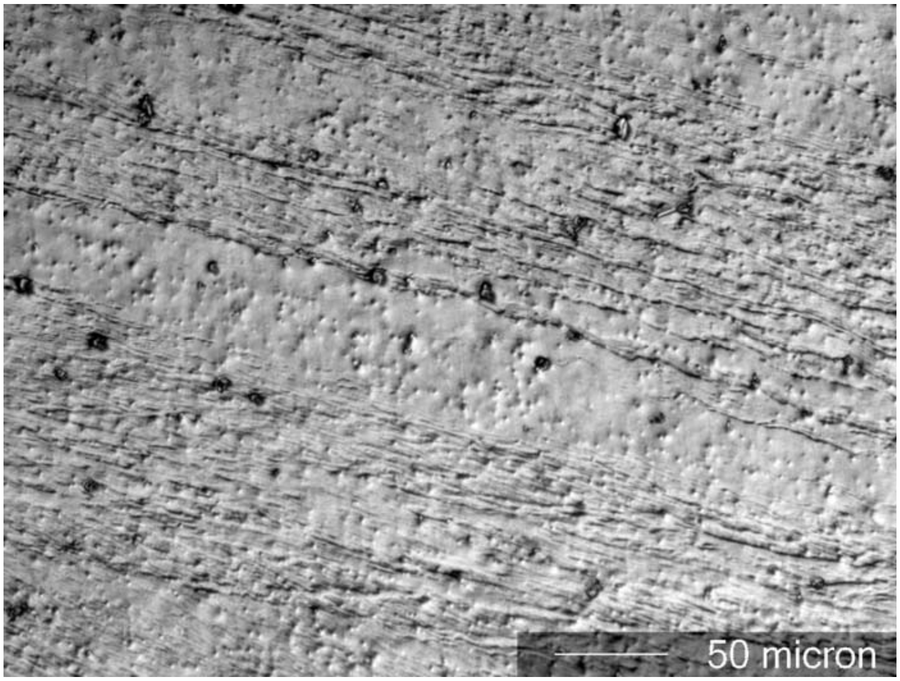

(a)

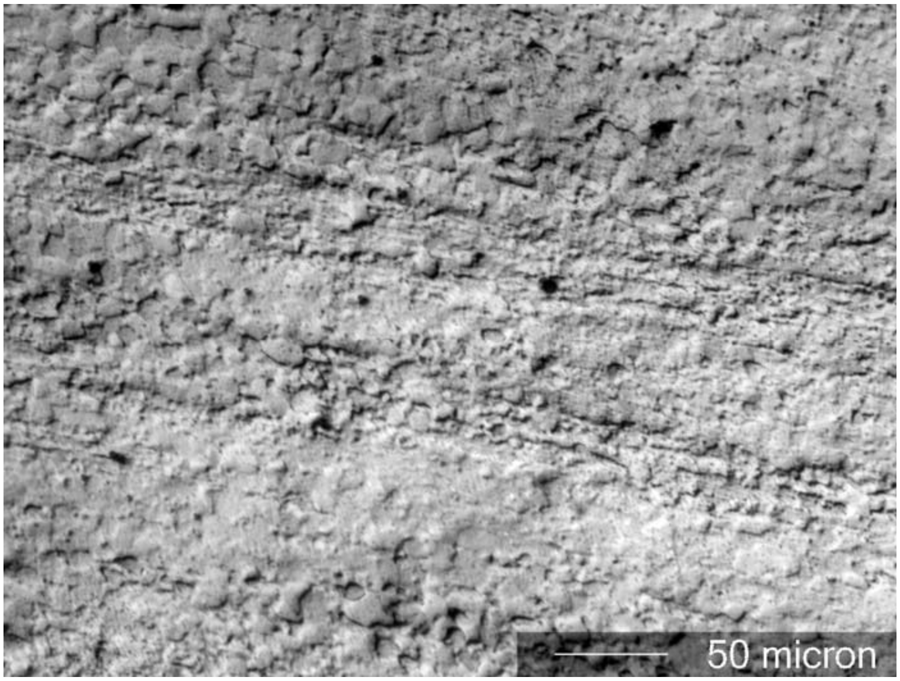

(b)

Figure 149: Optical micrographs of ECAE 4B IF steel. (a) as-processed, (b) annealed at 550°C

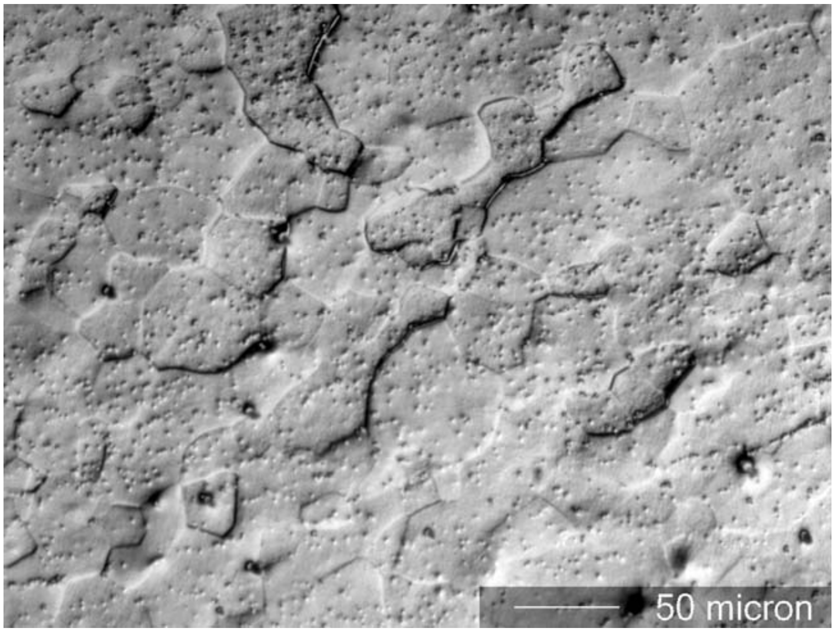

(c)

Figure 149: Continued. (c) annealed at 700°C

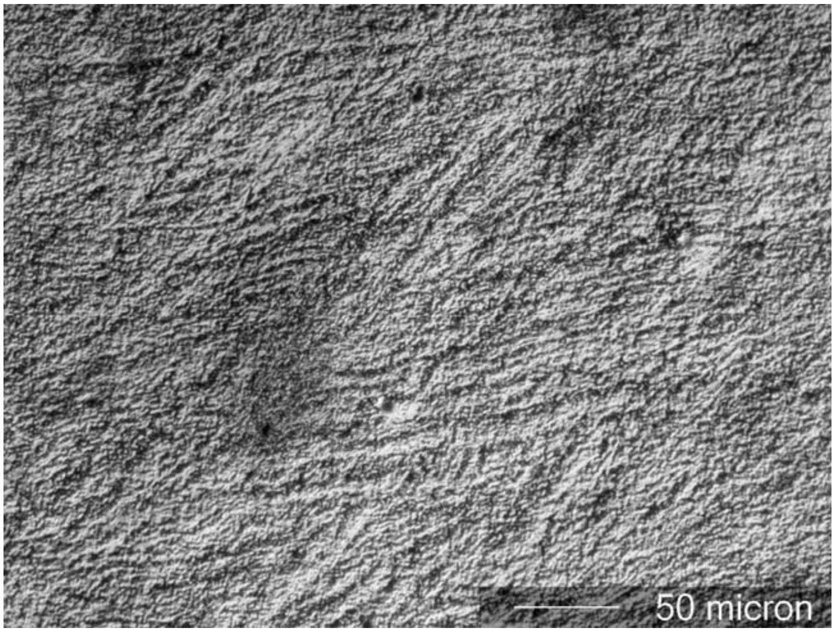

(a)

Figure 150: Optical micrographs of ECAE 16E IF steel. (a) as-processed

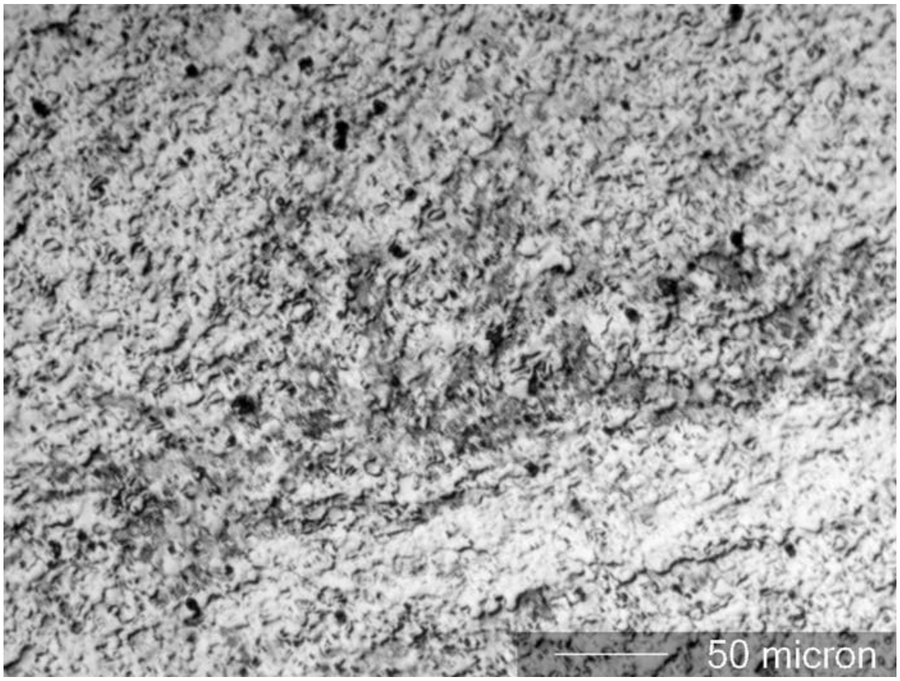

(b)

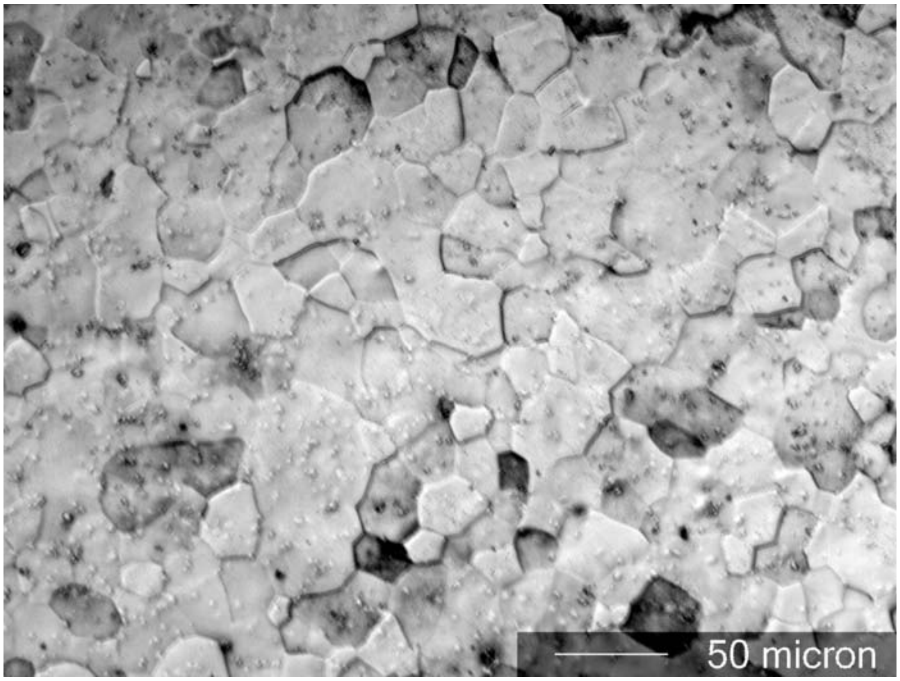

(c)

Figure 150: Continued. (b) annealed at 550°C, (c) annealed at 700°C

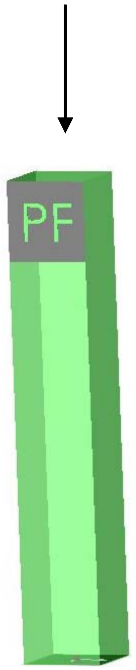

Route A, All passes

All Routes start here

Figure 151: Rotation schematic for Route A. PF refers to punch face

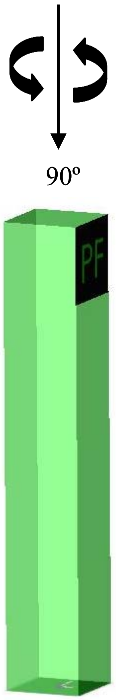

Route C’, all passes

Route B, N=2,4,6….

Route E, N=3,7,11….

Route F, N=2, 6

Figure 152: Rotation schematic for 90° rotations

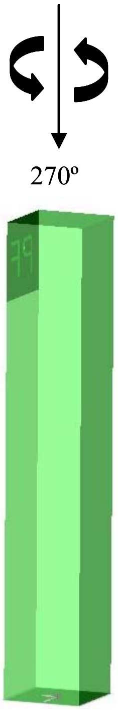

Route B, N=3,5,9….

Route F, N=4,8

Route E, N=5,9,13…

Figure 153: Rotation schematic for 270° rotations

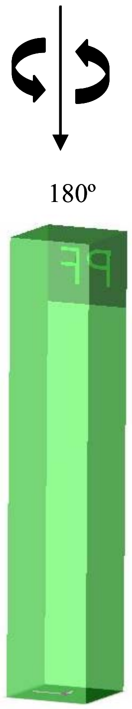

Route C, all passes

Route E, N=2,4,6….

Route F, N=3,5,7

Figure 154: Rotation schematic for 180° rotations

VITA

Steven George Sutter was born on February 20, 1978 in Houston, Texas, and grew up in a neighborhood filled with NASA engineers. He attended elementary and high school in Clear Lake, where he graduated in the top quarter of his class and as a member of the National Honor Society, in 1996.

Having been accepted at Texas A&M University, he pursued a Bachelor of Science degree in mechanical engineering. During his studies, he had the opportunity to work as a co-op engineer with General Electric Power Systems for more than a year, where he was exposed to the application of advanced materials science and the culture of large engineering corporations. He graduated with a degree in mechanical engineering in the summer of 2002.

Upon graduation from undergraduate school, he enrolled in the graduate program at Texas A&M, earning a Master of Science degree in mechanical engineering, with a specialty in materials science, in December 2005. He currently resides at 2110 Airline Drive, Friendswood, TX 77546.